UNIVERSIDADE FEDERAL DO RIO GRANDE DO SUL
INSTITUTO DE GEOCIÊNCIAS
PROGRAMA DE PÓS-GRADUAÇÃO EM GEOCIÊNCIAS

PETROLOGIA E GEOCRONOLOGIA DO COMPLEXO MÁFICO-ULTRAMÁFICO TRINCHEIRA, SUDOESTE DO CRÁTON AMAZÔNICO: IMPLICAÇÕES TECTÔNICAS DO MESOPROTEROZÓICO

GILMAR JOSÉ RIZZOTTO

ORIENTADOR: Prof. Dr. Léo Afraneo Hartmann

Porto Alegre, 2012

UNIVERSIDADE FEDERAL DO RIO GRANDE DO SUL
INSTITUTO DE GEOCIÊNCIAS
PROGRAMA DE PÓS-GRADUAÇÃO EM GEOCIÊNCIAS

PETROLOGIA E GEOCRONOLOGIA DO COMPLEXO MÁFICO-ULTRAMÁFICO TRINCHEIRA, SUDOESTE DO CRÁTON AMAZÔNICO: IMPLICAÇÕES TECTÔNICAS DO MESOPROTEROZÓICO

GILMAR JOSÉ RIZZOTTO

ORIENTADOR: Prof. Dr. Léo Afraneo Hartmann

BANCA EXAMINADORA

Prof. Dr. Moacir José Buenano Macambira – Instituto de Geociências, Universidade Federal do Pará

Prof. Dr. Márcio Martins Pimentel – Instituto de Geociências, Universidade Federal do Rio Grande do Sul

Dr. Wilson Wildner – Serviço Geológico do Brasil (CPRM) – Porto Alegre

Tese de Doutorado apresentada como requisito parcial para a obtenção do Título de Doutor em Ciências.

Porto Alegre – 2012

AGRADECIMENTOS

Aos meus pais e irmãos, que sempre deram apoio incondicional aos meus estudos.

A minha mulher, filhos e enteada, por terem suportado a minha ausência parcial durante esse período, pela compreensão nos momentos críticos e que muito me ajudaram a superar as situações-limite, estimulando-me a seguir em frente. Enfim, pela parceria nos momentos difíceis!

Ao meu orientador, Prof. Dr. Léo Afraneo Hartmann, agradeço as ricas sugestões a este trabalho, seu constante estímulo na busca do conhecimento e o apoio recebido ao longo deste processo de formação acadêmica.

Ao Dr. João Orestes Schneider Santos por sua permanente solicitude na fase de análise laboratorial, pelas facilitações no “abrir portas” da University of Western Austrália, pela amizade e proveitosas discussões e pela atenção e apoio dispensados durante minha estada em Perth.

Ao Serviço Geológico do Brasil – CPRM, na pessoa do Diretor-Presidente, Dr. Manoel Barretto da Rocha Neto, por ter cedido à liberação parcial das minhas atividades profissionais para a execução dessa Tese e, desta forma, ter contribuído para o meu crescimento profissional.

Aos colegas da CPRM – Residência de Porto Velho: Marcos Luiz Quadros, Maria Rosalva Campos Coelho e Pamela Emanuelle Silva, pela inestimável contribuição na preparação das amostras em laboratório; Manoel Rufino, Luiz Rogério e Edcarlos, na assistência as etapas de campo; Helena Costa Bezerra e Alex Silva, pelo aparato logístico sempre prestativo. A todos os colegas da CPRM – Superintendência de Goiânia, em especial a Maria Abadia Camargo, pela cooperação e apoio.

Aos professores do Instituto de Geociências da UFRGS, pelos ensinamentos e orientações oportunas e pela manutenção de um ensino de qualidade. A Secretaria do Programa de Pós-Graduação em Geociências, em especial ao Roberto Martins, pelo prestativo auxílio com as questões burocráticas durante o curso.

Ao Conselho Nacional de Desenvolvimento Científico e Tecnológico (CNPq) pelo auxílio financeiro.

Finalmente, a todos aqueles que, embora não nomeados, me apoiaram em distintos momentos da minha empreitada, o meu reconhecido e carinhoso muito obrigado! Divido com todos vocês mais uma etapa de minha vida.

RESUMO

A ambiência geotectônica das rochas máfico-ultramáficas do sudoeste do Cráton Amazônico é, de uma maneira geral, pouco conhecida. A maioria dos trabalhos desta porção cratônica está enfocada nos estudos geocronológicos em granitóides, de modo que pouco se sabe sobre a origem e significado tectônico destas rochas. Neste contexto, esta pesquisa buscou contribuir para o conhecimento da evolução geotectônica do sudoeste do Cráton Amazônico, através da caracterização de um complexo ofiolítico Mesoproterozóico, correspondente ao Complexo Trincheira, de idade Calimiana. Desta forma, uma nova proposta de modelo tectônico é aqui apresentada, a qual explica muitas das características anteriormente enigmáticas da história Pré-cambriana desta área-chave e possibilita outras alternativas para a reconstrução do supercontinente Columbia. O ofiolito Trincheira é composto de rochas extrusivas (anfibolitos derivados de basaltos maciços e almofadados), intrusivas máfico-ultramáficas, chert, formação ferrífera bandada, pelitos, psamitos e pequena proporção de rochas cálcio-silicáticas. A composição geoquímica das rochas extrusivas e intrusivas máfico-ultramáficas mostra semelhanças com os basaltos toleiíticos modernos, as quais possuem moderado a forte fracionamento de elementos terras-raras leves, padrão quase horizontal dos elementos terras-raras pesados e moderada a forte anomalia negativa dos elementos de alto campo de força (especialmente Nb), uma assinatura geoquímica típica de zona de subducção. As unidades basais do ofiolito Trincheira são quimicamente similares aos modernos basaltos de cadeia meso-oceânica (MORB). Esse comportamento químico muda para as unidades de topo as quais apresentam uma assinatura similar aos toleiítos de arco-de- ilha (IAT). Portanto, o ofiolito Trincheira deve ter sido originado em um ambiente intra-oceânico de supra-subducção composto de um sistema de arco/retro-arco. Os dados isotópicos de Sm, Nd e Sr para essas rochas indicam valores iniciais de ε_{Nd} de moderados a altamente positivos (+2.6 a +8.8) e muito baixa razão inicial de $^{87}Sr/^{86}Sr$ (0,7013 – 0,7033), sugerindo que esses magmas foram originados a partir de uma fonte mantélica empobrecida e nada ou fracamente contaminados por componentes de subducção. O complexo ofiolítico foi deformado, metassomatizado e metamorfisado durante o desenvolvimento da Faixa Móvel Guaporé, um orógeno acrescionário-colisional Mesoproterozóico (1,47-1,35 Ba), constituído pela zona de sutura Guaporé, a qual une o Cráton Amazônico com o Bloco Paraguá. A fase colisional que marca o

encaixe final dessas duas massas continentais ocorreu por volta de 1,35 Ba, onde o metamorfismo atingiu temperaturas entre 780 a 853°C nos granulitos máficos e 680 a 720°C nos anfibolitos, com pressão média de 6,8 kbar. A sutura Guaporé foi reativada no final do Mesoproterozóico e evoluiu para a abertura de um rift intracontinental, com a sedimentação das rochas dos Grupos Nova Brasilândia e Aguapeí, o qual marca a fragmentação final do supercontinente Columbia, por volta de 1,3-1,2 Ba. Granulitos máficos, anfibolitos e trondhjemitos da porção meridional do Cinturão Nova Brasilândia, representativos da última fase compressional que afetou o sudoeste do Cráton Amazônico, forneceram idades U-Pb de 1110 Ma, as quais datam o metamorfismo de alto grau e o fechamento do rift, processo resultante da acresção do microcontinente Arequipa-Antofalla ao Cráton Amazônico. Portanto, a fragmentação do supercontinente Columbia foi seguida rapidamente pela aglomeração de outras massas continentais, formando o supercontinente Rodínia, por volta de 1100 Ma.

Palavras-chave: Complexo máfico-ultramáfico Trincheira, Cráton Amazônico, ofiolito, geocronologia, Mesoproterozóico

ABSTRACT

The tectonic framework of the ultramafic-mafic rocks of the southwestern Amazon Craton is generally little known. Most of work this cratonic portion is focused on the geochronological studies of granitoids, so that little is known about the origin and tectonic significance of these rocks. In this context, this study contributes to the knowledge of the tectonic evolution of the southwestern Amazon Craton, through the characterization of a Mesoproterozoic ophiolitic complex, corresponding to the Trincheira Complex of Calymmian age, and propose a tectonic model that explains many previously enigmatic features of the Precambrian history of this key craton, and discuss its role in the reconstruction of the Columbia supercontinent. The complex comprises extrusive rocks (fine-grained amphibolites derived from massive and pillowed basalts), mafic-ultramafic intrusive rocks, chert, banded iron formation, pelites, psammitic and a smaller proportion of calc-silicate rocks. The geochemical composition of the extrusive and intrusive rocks indicates that all noncumulus mafic-ultramafic rocks are tholeiitic basalts. These rocks display moderately to strongly fractionation of light rare earth elements (LREE), near-flat heavy rare earth elements (HREE) patterns and moderate to strong negative high field strength elements (HFSE) anomalies (especially Nb), a geochemical signature typical of subduction zones. The lowest units of the Trincheira ophiolite are similar to the modern mid-ocean ridge basalt (MORB). This behavior changes to an island arc tholeiites (IAT) signature in the upper units of the Trincheira ophiolite. Therefore, the Trincheira ophiolite appears to have originated in an intraoceanic supra-subduction setting composed of an arc-back-arc system. Mafic-ultramafic rocks of the Trincheira ophiolites display moderate to highly positive initial ε_{Nd} values of +2.6 to +8.8 and very low values for the initial $^{87}Sr/^{86}Sr$ ratio (0.7013 - 0.7033). It is suggested that these magmas originated from a depleted mantle source, which experienced low degree of contamination by variable subduction components.

The ophiolitic sequence was deformed, metasomatized and metamorphosed during the development of the Alto Guaporé Belt, a Mesoproterozoic accretionary-collisional orogen that represents the Guaporé suture zone. Metamorphism was pervasive and reached temperatures of 780-853°C in mafic granulites and 680-720°C in amphibolites under an overall pressure of 6.8 kbar. The Guaporé suture zone is defined by the ESE–WNW trending mafic-ultramafic belt formed during a Mesoproterozoic (ca. 1.47-1.43 Ga) accretionary phase, and overprinted by upper

amphibolite-granulite facies metamorphism during collisional phase in the Ectasian (~1.35 Ga), which mark the docking final of the Amazon craton and Paraguá Block. This suture was reactivated and evolved from the development of an intracontinental rift environment, represented by Nova Brasilândia and Aguapeí Groups, which mark the final breakup of the supercontinent Columbia in the late Mesoproterozoic (ca. 1.3-1.2 Ga). Mafic granulites, amphibolites and trondhjemites in the northernmost portion of the Nova Brasilândia belt yield U-Pb zircon ages ca. 1110 Ma, which dates the high-grade metamorphism and the closure of the rift, due to the accretion of the Arequipa-Antofalla basement to the Amazon craton. Therefore, the breakup of supercontinent Columbia was followed in short sequence by the assembly of supercontinent Rodinia at ca. 1100 Ma.

Keywords: Trincheira mafic-ultramafic Complex, Amazon Craton, ophiolite, geochronology, Mesoproterozoic

SUMÁRIO

1. INTRODUÇÃO

1.1. Apresentação

A investigação de complexos máfico-ultramáficos é importante em vários aspectos. Em relação a sua gênese, podem representar uma origem ofiolítica ou estratiforme intra-placa. Eles também revelam os processos magmáticos relacionados à cristalização fracionada e acumulação de cristal, tanto em litosfera oceânica como continental e o seu entendimento reveste de fundamental importância metalogenética e geodinâmica no sentido de representar a transferência de magma do manto superior para a crosta. Nesse sentido, destacam-se os ofiolitos, os quais são referidos como remanescentes de crosta oceânica e manto superior incorporados no interior dos cinturões orogênicos. Os complexos ofiolíticos tem atraído a atenção de muitos pesquisadores face à importância de serem componentes essenciais dos principais orógenos da Terra e face as suas características petrotectônicas, associados a faixas de *greenstone belts*. Embora ofiolitos possam se formar em muitos ambientes tectônicos, há um consenso geral de que a maioria foi gerada por fechamento de um oceano em zona de subducção. Assim, a acresção de ofiolitos tem sido sugerida como um mecanismo de crescimento continental em inúmeros orógenos Arqueanos, Proterozóicos e Fanerozóicos.

Neste contexto situa-se o presente trabalho dentro da linha temática *Geologia Regional e Geotectônica*. Nele são apresentados os resultados da investigação de um complexo ofiolítico e rochas associadas, além de uma breve revisão do quadro geológico das Províncias Rondônia-Juruena e Sunsás, no sudoeste do Cráton Amazônico. Assim, com base nos dados obtidos no presente trabalho e integrados com as interpretações de pesquisas anteriores, foi possível definir um modelo tectônico em que se insere a evolução do Complexo máfico-ultramáfico Trincheira.

1.2. Objetivos

A presente pesquisa tem como objetivos definir o cenário geológico em que se desenvolveram os ofiolitos da borda sudoeste do Cráton Amazônico e propor modelo geotectônico evolutivo referente à gênese dos protólitos, aqui identificados com pertencentes ao Complexo máfico-ultramáfico Trincheira, envolvendo os aspectos de aglutinação e fragmentação de massas continentais na reconstituição dos supercontinentes. Para atender estes objetivos de amplitude regional, foi dada ênfase aos dados de campo, onde se efetuou uma análise estrutural regional para

reconstituir os ambientes tectônicos, as relações temporais e cinemáticas, regimes e superposição de eventos, e a magnitude dos grandes sistemas de cisalhamento envolvidos na evolução geodinâmica regional.

O estudo petrológico, envolvendo geoquímica em rocha total e química mineral, estudo termo-barométrico e isotópico de rochas de áreas-chave, selecionadas a partir dos levantamentos regionais e de detalhe, como base metodológica para a compreensão dos processos globais da evolução, foi outra meta envolvida nos objetivos da pesquisa.

1.3. Estado da Arte

A área objeto desse estudo está localizada entre as Províncias Rondônia-Juruena e Sunsás (Santos et al., 2008), no sudoeste do Cráton Amazônico (Fig. 1).

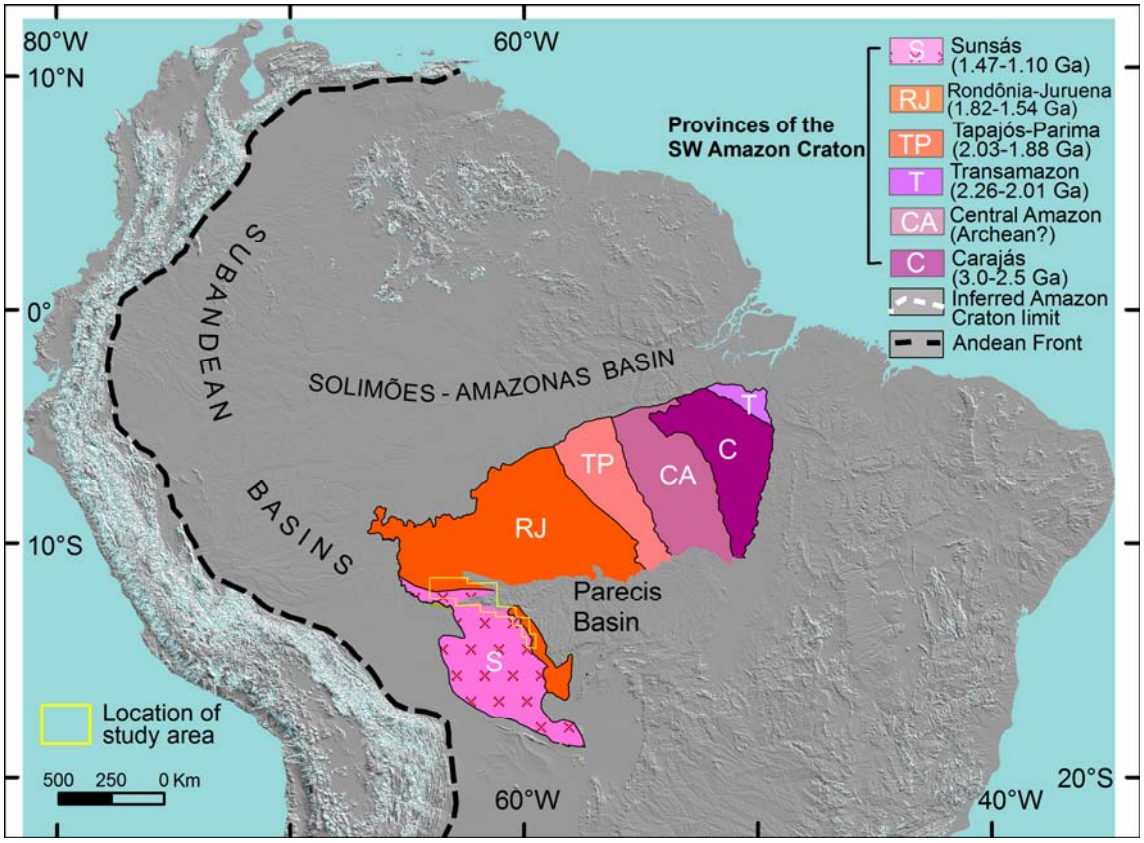

Figura 1- Províncias geocronológicas do sudoeste do Cráton Amazônico e as principais bacias Fanerozóicas (modificado de Santos et. al., 2008).

O Complexo máfico-ultramáfico Trincheira é aqui definido como representante de uma sequência ofiolítica granulitizada que, posteriormente, foi exumada com o evento orogenético do Mesoproterozóico durante o acoplamento tectônico do Bloco Paraguá com o proto-Cráton Amazônico (Fig. 2). A disposição de complexos máfico-

ultramáficos granulitizados junto a proeminentes lineamentos tectono-estruturais e a fortes anomalias magnéticas tem levado à interpretação de que os complexos básicos-ultrabásicos granulitizados representem massas ofiolíticas obductadas.

A origem e o posicionamento dos ofiolitos na história da Terra coincidem com os eventos colisionais que culminaram com a construção de supercontinentes. Nesse contexto insere-se o Cráton Amazônico, o maior dos crátons Neoproterozóicos que constituem o continente Sul-americano. Essa grande massa continental tem participado nas principais reconstruções paleogeográficas, tais como a formação dos supercontinentes Columbia e Rodínia. Na maioria das reconstruções paleogeográficas do Columbia, o Cráton Amazônico está acoplado ao sudoeste do escudo Báltico (Zhao et al., 2002, 2006; Johansson, 2009) e, de acordo com alguns autores, essa conexão deve ter existido desde 1,8 Ba até 800 Ma atrás. Da mesma forma, a hipótese sobre o envolvimento da Amazônia no Rodínia é, em geral, bem aceita (p.ex., Tohver et al., 2002, 2006; Boger et al., 2005; Li et al., 2008; Ibanez-Mejia et al., 2011). O supercontinente Rodínia foi formado no final do Mesoproterozóico ao início do Neoproterozóico pela aglutinação de fragmentos cratônicos pré-existentes, tais como a Amazônia e Laurentia.

A correlação entre Amazônia e Laurentia envolve, especialmente, a comparação de eventos orogênicos que aconteceram por volta de 1200 a 970 Ma. Na Amazônia, os registros dessa aglutinação estão presentes na margem sudoeste do Cráton Amazônico.

Na porção sul e sudoeste do Cráton Amazônico, diversas sínteses geológicas e geocronológicas foram apresentadas nas últimas duas décadas, refletindo avanços significativos no conhecimento geológico. Entretanto, os modelos evolutivos propostos esboçam algumas características que delimitam mega-províncias tectônicas, terrenos e orógenos, mas que ainda exigem um estudo mais aprofundado para avaliar o seu real significado no contexto geotectônico global. Diversos ambientes geotectônicos foram sugeridos para a evolução da margem sudoeste do Cráton Amazônico e, dentre eles, destacam-se aqueles relacionados à amalgamação de arcos magmáticos intra-oceânicos ou retro-arcos e processos de abertura e fechamento de oceanos (orógenos acrescionários). Todas as investigações anteriores foram realizadas em uma escala regional, sem informações detalhadas de campo ou acompanhadas de dados petrológicos, geoquímicos e estruturais, limitando a sua interpretação dos ambientes tectônicos envolvidos,

principalmente, no que diz respeito ao crescimento crustal da borda sudoeste do Cráton Amazônico.

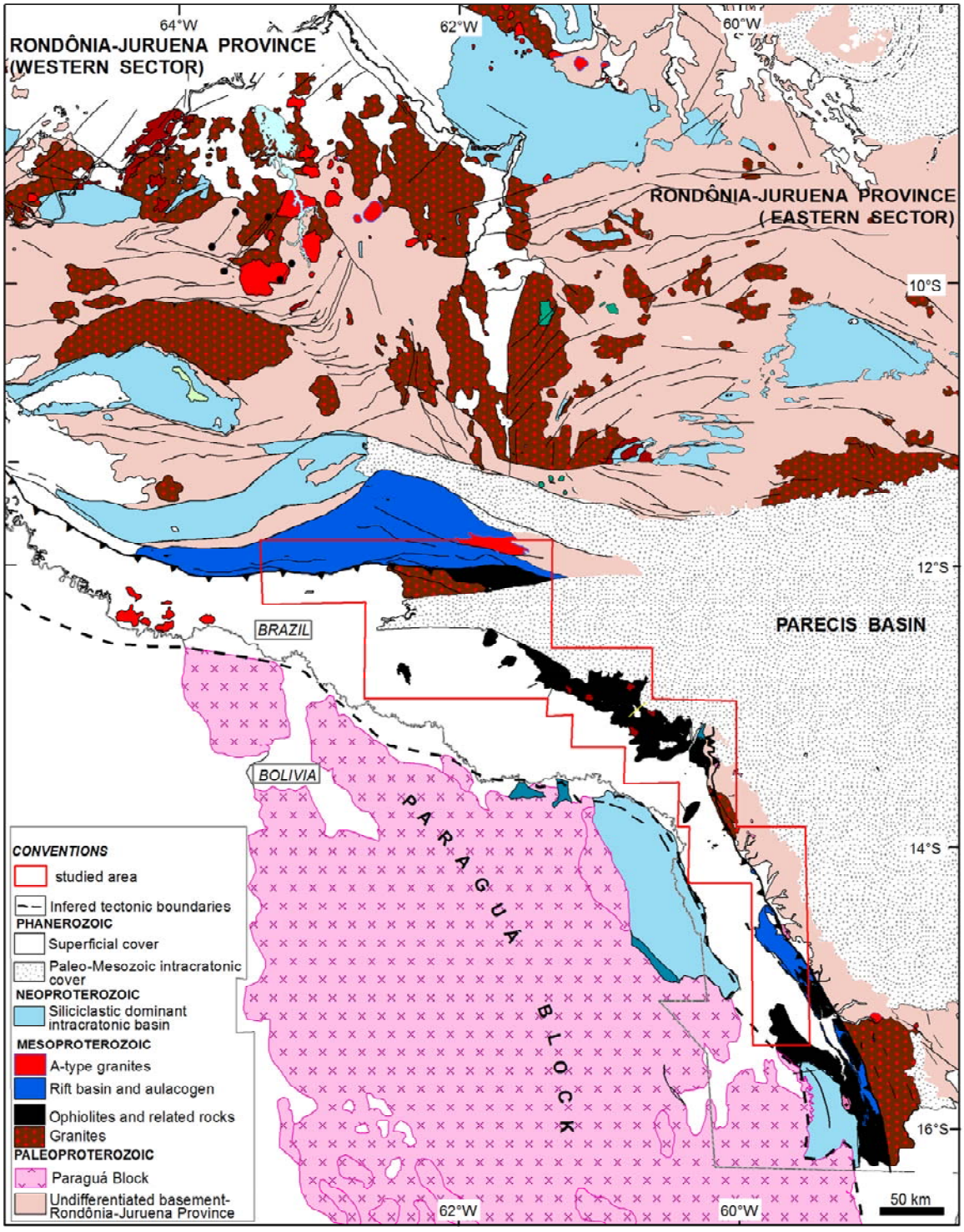

Figura 2- Mapa geológico simplificado do sudoeste do Cráton Amazônico mostrando as unidades litoestratigráficas e os limites aproximados dos terrenos e cinturões. Área estudada em destaque (polígono em vermelho).

Nesse sentido, uma discussão mais detalhada a respeito da evolução geotectônica do sudoeste do Cráton Amazônico, baseada em dados

geocronológicos, estruturais e metamórficos para as rochas do embasamento, foram apresentadas por Tohver et al., (2005) e Boger et al., (2005). Esses autores sugeriram a existência de uma zona de sutura, de direção E-W, representada pelo Cinturão Nova Brasilândia, resultante da acresção do Cráton Paraguá ao Cráton Amazônico durante o final do Mesoproterozóico (cerca de 1,1-1,0 Ba). Esse modelo tectônico de sutura contradiz uma proposta anterior sugerida por Rizzotto (1999), na qual o autor sugere que o Grupo Nova Brasilândia foi formado num ambiente intra-placa, associado a abertura de um proto-oceano, temporalmente sincrônico ao desenvolvimento da Orogenia Grenviliana na Laurentia.

A distinção entre terreno acrescionado, limites de terreno e suturas que separam diferentes crátons ou orógenos envolvidos na colisão continente-continente pode ser difícil, porque a distinção depende da identificação dos terrenos justapostos, os quais apresentam diferentes histórias magmáticas e litotectônicas anteriores à colisão, mas que depois compartilham uma história em comum. Os orógenos acrescionários podem ser referidos como não-colisionais, orógenos exteriores ou zonas de subducção do tipo B, formados em margem de placas convergentes, continental ou intra-oceânica. Eles formam sítios de subducção de litosfera oceânica e incluem zona de supra-subducção, com componentes de arco magmático, retro-arco e frente de arco (ofiolitos). Grandes volumes de rochas dos cinturões acrescionários exibem assinaturas isotópicas tipicamente juvenil, indicando essencialmente magmas parentais derivados do manto.

Os ofiolitos podem fazer parte desses ambientes como remanescentes de antigas crostas oceânicas autóctones ou alóctones que foram incorporados no interior de cadeias de montanhas durante eventos de subducção-acresção. Eles são geralmente encontrados ao longo de zonas de sutura em ambos os tipos de cinturões orogênicos (colisionais e acrescionários) que marcam o limite principal entre placas amalgamadas ou terrenos acrescionários (Lister and Forster, 2009). Nesse sentido, os ofiolitos são de primeira importância para o entendimento de orógenos e são essenciais na definição de uma zona de sutura.

Até o momento, não haviam sido identificados ofiolitos na margem sudoeste do Cráton Amazônico. Nesta investigação nós apresentamos um modelo petrogenético para a formação do ofiolito Trincheira e discutimos as implicações desta nova descoberta, associada com a origem de crosta oceânica Mesoproterozóica. Assim, seguimos a metodologia original que estabeleceu o conceito moderno sobre os ofiolitos (Dilek and Furnes, 2011), baseada

principalmente nos dados de campo, petrológicos e geoquímicos. Como resultado, apresentamos algumas questões fundamentais relacionadas com a reconstrução do supercontinente pré-Rodínia. Essa temática é abordada no artigo que se segue, intitulado de "*Geological and geochemical evolution of the Trincheira Complex, a Mesoproterozoic ophiolite in the southwestern Amazon craton, Brazil*". O artigo em questão foi submetido e aceito pela revista Lithos. Salientamos que os arquivos e apêndices *on line* desse artigo estão inseridos nos anexos da monografia.

Durante o desenrolar da pesquisa, houve aporte significativo de novos conhecimentos e modelos sobre a evolução crustal proterozóica da região e com o reconhecimento de uma sequência ofiolítica e seus fragmentos desmembrados que ocorrem na área de pesquisa nos levaram, por conseguinte, à identificação simultânea de uma zona de sutura. Isto exigiu a ampliação das questões pertinentes à evolução dos ofiolitos como, por exemplo, a abordagem da evolução geotectônica de várias unidades supracrustais e de rochas máficas e félsicas que lhe são intrusivas, justificando, desta maneira, a abrangência colocada no texto que se segue.

Em trabalhos anteriores efetuados na mesma região por Rizzotto et al., (2002), baseados em dados geológicos e geocronológicos, foi caracterizado um evento tectono-magmático de escala regional, com idades no intervalo de 1350 a 1320 Ma. Posteriormente, Rizzotto & Dehler (2007) denominaram o referido evento como Faixa Móvel Alto Guaporé e interpretaram-na como sendo derivada de uma orogenia acrescionária-colisional.

No presente estudo, a definição de uma nova zona de sutura na margem sudoeste do cráton, anterior à formação do Rodínia, trás novas implicações para a evolução geotectônica do Cráton Amazônico. Esta nova interpretação é baseada em dados geocronológicos de U-Pb em zircão e titanita (SHRIMP e LA-ICP-MS), geoquímica isotópica, apoiada pela geologia de campo e dos dados aeromagneto-métricos. Com estes dados foi possível definir a idade de formação do complexo ofiolítico, que integra a zona de sutura Guaporé, uma estrutura tectônica-chave para testar a inferida conexão Mesoproterozóica entre o SW do Cráton Amazônico e o Bloco Paraguá. Este tema é tratado no 2º artigo, intitulado "*The Calymmian/Ectasian Guaporé suture in the SW Amazon craton: geotectonic implications based on field geology, zircon geochronology and Nd-Sr isotopic geochemistry*", o qual foi submetido para a revista Precambrian Research.

Outro objetivo proposto durante a execução da tese foi o de investigar a evolução geotectônica do final do Mesoproterozóico dos cinturões Nova Brasilândia, Aguapeí e Sunsás, do extremo sul do Cráton Amazônico. Para essa região do cráton, há uma proposta de arcabouço tectônico sugerida por Tohver et al., (2004, 2005, 2006), na qual os autores comparam o SW do Cráton Amazônico com a porção meridional da Laurentia e propõem que durante o final do Mesoproterozóico, o sudeste do Cráton Amazônico foi submetido a atuação de dois eventos tectônicos separados temporalmente. O primeiro, relacionado à colisão com o sul da Laurentia (cerca de 1,2 a 1,15 Ba) e o segundo, foi aquele que possibilitou o acoplamento do Cráton Amazônico com o Bloco Paraguá (cerca de 1,09 Ba). Esses pesquisadores também fizeram referência para a existência de uma sutura (representada pelo Cinturão Nova Brasilândia) indicando que o encaixe final do Cráton Amazônico com o sul da Laurentia se deu em torno de 1,0 Ba, nos estágios finais da evolução do Rodínia.

Sugestões alternativas para a evolução do Cráton Amazônico no final do Mesoproterozóico foram previstas na tentativa de acomodar pequenos fragmentos crustais dispersos, tais como o microcontinente Arequipa-Antofalla (p.ex., Keppie and Ortega-Gutierrez, 1999, Loewy et al., 2004, Casquet et al., 2006). Nesse sentido, Boger et al., (2005) apresenta três diferentes cenários para a acresção do Bloco Paraguá e o microcontinente Arequipa-Antofalla com a margem SW do Cráton Amazônico. Portanto, as inconsistências existentes em relação ao arranjo dos blocos crustais envolvidos numa colisão e sua evolução geodinâmica durante o final do Mesoproterozóico estão ainda sob avaliação. Dessa forma, as principais questões ainda existentes a respeito da história tectônica da borda SW do Cráton Amazônico, as quais envolvem os cinturões Nova Brasilândia e Aguapeí, podem ser descritas como: (1) Foram esses cinturões geograficamente contíguos; eles se formaram e evoluíram no mesmo intervalo de tempo, ou eram cinturões geologicamente distintos? Será que se formaram numa crosta já estabilizada (cráton), ou eles representam uma zona de sutura que marca um limite crustal no Cráton Amazônico?

Em função das dúvidas e controvérsias existentes, nós apresentamos uma contribuição para tentar resolver algumas destas questões, utilizando-se de novos dados geocronológicos de U-Pb em zircão e titanita, relacionados às rochas que compõem os Grupos Nova Brasilândia e Aguapeí, juntamente com dados de campo. Estes resultados colocam novas delimitações sobre a evolução geológica da

margem sudoeste do Cráton Amazônico e fornecem mais evidências para a correlação paleogeográfica entre a Amazônia e Laurentia. Nesse aspecto, a temática abordada no 3º artigo trata dos assuntos relacionados com a evolução geotectônica da borda sudoeste do Cráton Amazônico, mais especificamente, durante o final do Mesoproterozóico. Portanto, o artigo submetido aos Anais da Academia Brasileira de Ciências, intitulado ¨*Tectonic evolution of the southern margin of the Amazon craton in the late Mesoproterozoic based on field relationships and zircon U–Pb geochronology*" procura estabelecer uma nova visão sobre a história geológica dessa porção cratônica.

1.4. Resultados

Discussões e os resultados por completo das pesquisas são apresentados nos três artigos que compõem o corpo da Tese. Entretanto, alguns dos resultados mais significativos desta investigação são descritos abaixo.

- O Complexo máfico-ultramáfico Trincheira é composto por várias fatias de rochas máficas e ultramáficas, imbricadas e desmembradas por uma tectônica de empurrão, constituindo uma seqüência ofiolítica incompleta. A seqüência inclui camadas de rochas cumuláticas, extrusivas e intrusivas máfico-ultramáficas, intercaladas com uma unidade sedimentar clasto-química.

- Com base na análise e interpretação dos dados geológicos e geoquímicos obtidos no presente estudo, sugere-se que as rochas máfico-ultramáficas do Complexo Trincheira foram derivadas de um magma híbrido do tipo MORB e Toleiíto de Arco-de-Ilha (IAT). Sua origem está vinculada a um sistema de supra-subducção, em ambiente de arco-de-ilha intra-oceânico e bacia retroarco.

- A composição isotópica de Sm, Nd e Sr indica que o magma original do Complexo Trincheira foi extraído de uma fonte mantélica empobrecida, com fraco enriquecimento metassomático de elementos-traço incompatíveis, característico de crosta oceânica em ambiente de supra-subducção.

- Esta crosta oceânica reliquiar pode representar um fragmento de litosfera oceânica que obductou durante a colisão do Bloco Paraguá com a borda ocidental do proto-Cráton Amazônico durante o Mesoproterozóico, por volta de 1470-1350 Ma.

- A fase acrescionária na borda SW do proto-Cráton Amazônico é representada pelo magmatismo Trincheira, rochas quartzo-dioríticas e tonalíticas-trondhjemíticas associadas, que ocorreu entre 1,47 e 1,43 Ba, enquanto que a fase colisional que marca o encaixe final do proto-Cráton Amazônico com o Bloco Paraguá é

representada pela intrusão de diversos corpos graníticos sintectônicos, que ocorreu por volta de 1350 a 1330 Ma.

- Os dados termo-barométricos obtidos nas rochas máfico-ultramáficas indicam que o metamorfismo, durante a fase colisional, atingiu temperaturas de 820-853°C nos granulitos máficos e 680-720°C nos anfibolitos, sob pressão de 6,8 kbar.

- Os ofiolitos do Complexo Trincheira caracterizam uma zona de sutura Mesoproterozóica (zona de sutura Guaporé) entre o proto-Cráton Amazônico e o Bloco Paraguá. Esse contexto tectônico explica muitas das questões previamente enigmáticas da história Pré-Cambriana do Cráton Amazônico e possibilita acrescentar novos ingredientes nos modelos de reconstrução do supercontinente Columbia.

- Os dados integrados de campo e os dados geocronológicos apresentados nessa investigação, juntamente com a interpretação dos dados geofísicos aeromagnetométricos, são uma forte evidência na comprovação da continuidade física entre os cinturões orogênicos intra-placa Nova Brasilândia e Aguapeí, os quais foram precedidos com a abertura de um rift intracontinental no final do Mesoproterozóico, por reativação da paleo-sutura Guaporé. A abertura do rift se deu por volta de 1150 Ma e o fechamento em 1110 Ma.

- Sugere-se que a formação dos cinturões orogênicos Nova Brasilândia, Aguapeí e Sunsás esteja vinculada diretamente com a acresção do micro-continente Arequipa-Antofalla ao proto-Cráton Amazônico.

- Os últimos movimentos tectônicos, antes da efetiva cratonização da margem sudoeste do proto-Cráton Amazônico, ocorreram por volta de 1,0 Ba quando a reativação de antigas zonas de fraqueza permitiu a instalação de zonas transcorrentes e a colocação simultânea de diversos corpos graníticos. Após essa fase, processos de soerguimento, exumação e extensão crustal se sucederam no tempo e culminaram com a implantação de bacias intracontinentais (p.ex. Formação Palmeiral, Grupo Huanchaca).

1.5. Referências

BOGER, Steven et al. U–Pb age data from the Sunsas region of eastern Bolivia, evidence for the allochtonous origin of the Paraguá Block. **Precambrian Research**, v.139, p.121–146, 2005.

CASQUET, César et al. U–Pb SHRIMP zircon dating of Grenvillian metamorphism in Western Sierras Pampeanas (Argentina): correlation with the Arequipa-Antofalla

Craton and constraints on the extent of the Precordillera Terrane. **Gondwana Research**, v. 9, n. 4, p. 524–529, 2006.

DILEK, Yildirim; FURNES, Harald. Structure and geochemistry of Tethyan ophiolites and their petrogenesis in subduction rollback systems. **Lithos,** v. 113, p. 1-20, 2009.

IBANEZ-MEJIA, Maurício et al. The Putumayo Orogen of Amazonia and its implications for Rodinia reconstructions: New U-Pb geochronological insights into the Proterozoic tectonic evolution of northwestern South America. **Precambrian Research**, v. 191, p. 58-77, 2011.

JOHANSSON, Ake. Baltica, Amazonia and the SAMBA connection—1000 million years of neighbourhood during the Proterozoic? **Precambrian Research**, v. 175, p. 221-234, 2009.

KEPPIE, John; ORTEGA-GUTIÉRREZ, Fernando. Middle American Precambrian basement: a missing piece of the reconstructed 1 Ga orogen. **Geological Society of America**, Special Paper, v. 336, p. 199–210, 1999.

LI, Zengh et al. Assembly, configuration, and break-up history of Rodinia: a synthesis. **Precambrian Research**, v. 160, p. 179–210, 2008.

LOEWY, Staci, CONNELLY, James., DALZIEL, Ian. An orphaned basement block: the Arequipa-Antofalla Basement of the central Andean margin of South America. **Geological Society of America Bulletin**, v. 116, p. 171–187, 2004.

RIZZOTTO, Gilmar. **Petrologia e Geotectônica do Grupo Nova Brasilândia, Rondônia**, 1999. Dissertação (Mestrado em Geociências) - Instituto de Geociências, Curso de Pós-Graduação em Geociências, Universidade Federal do Rio Grande do Sul, Porto Alegre, 1999.

RIZZOTTO, Gilmar et al. Geologia e Geocronologia da Suíte Metamórfica Colorado e suas encaixantes, SE de Rondônia: implicações para a evolução mesoproterozóica do Craton Amazônico. GEOLOGIA USP, Série Científica, v. 2, p. 41-56, 2002.

RIZZOTTO, Gilmar; DEHLER, Nolan.. Arcabouço Estrutural da Faixa Alto Guaporé e o Regime Tectônico do Ectasiano na borda SW do Craton Amazônico. XI Simpósio Nacional de Estudos Tectônicos – V International Symposium on Tectonics of the SBG, Natal, p.130-132, 2007.

SANTOS, João Orestes et al. 2008. Age and autochthonous evolution of the Sunsás Orogen in West Amazon Craton based on mapping and U-Pb geochronology. **Precambrian Research**, v.165, p. 120-152, 2008.

TOHVER, Eric et al. Significance of the Nova Brasilândia metasedimentary belt in western Brazil: redefining the mesoproterozoic boundary of the Amazon Craton. **Tectonics**. doi:10.1029/2003TC001563 (TC6004), 2004.

TOHVER, Eric et al. Late Mesoproterozoic deformation of SW Amazonia (Rondonia, Brazil): geochronological and structural evidence for collision with Southern Laurentia. **Journal of Geology**, v. 113, p.309–323, 2005.

TOHVER, Eric et al. Restored transect across the exhumed Grenville orogen of Laurentia and Amazonia, with implications for crustal architecture. **Geology**, v. 34, p. 669-672, 2006.
ZHAO, Guochun et al. Review of global 2.1-1.8 Ga orogens: implications for a pre-Rodinia supercontinent. **Earth and Science Reviews**, v. 59, p. 125-162, 2002.

ZHAO, Guochun et al. Implications based on the first SHRIMP U–Pb zircon dating on Precambrian granitoid rocks in North Korea. **Earth and Planetary Science Letters**, v. 251, p. 365-379, 2006.

2. ARTIGOS

2.1. Artigo I

Rizzotto, G.J., Hartmann, L.A. 2012. Geological and geochemical evolution of the Trincheira Complex, a Mesoproterozoic ophiolite in the southwestern Amazon craton, Brazil. **Lithos**, (aceito).

Lithos 148 (2012) 277–295

Contents lists available at SciVerse ScienceDirect

Lithos

journal homepage: www.elsevier.com/locate/lithos

Invited review article

Geological and geochemical evolution of the Trincheira Complex, a Mesoproterozoic ophiolite in the southwestern Amazon craton, Brazil

Gilmar José Rizzotto [a,*], Léo Afraneo Hartmann [b]

[a] Geological Survey of Brazil (CPRM), Rua 148, no. 485; 74170-110 Goiânia, Goiás, Brazil
[b] Instituto de Geociências, Universidade Federal do Rio Grande do Sul, Avenida Bento Gonçalves, 9500; 91501-970 Porto Alegre, Rio Grande do Sul, Brazil

ARTICLE INFO

Article history:
Received 1 December 2011
Accepted 23 May 2012
Available online 4 June 2012

Keywords:
Amazon craton
Ophiolite
Mafic–ultramafic complex
Trincheira Complex
Arc-back-arc system

ABSTRACT

We document the first-known Mesoproterozoic ophiolite from the southwestern part of the Amazon craton, corresponding to the Trincheira Complex of Calymmian age, and propose a tectonic model that explains many previously enigmatic features of the Precambrian history of this key craton, and discuss its role in the reconstruction of the Columbia supercontinent. The complex comprises extrusive rocks (fine-grained amphibolites derived from massive and pillowed basalts), mafic–ultramafic intrusive rocks, chert, banded iron formation (BIFs), pelites, psammitic and a smaller proportion of calc-silicate rocks. This sequence was deformed, metasomatized and metamorphosed during the development of the Alto Guaporé Belt, a Mesoproterozoic accretionary orogen. The rocks were deformed by a single tectonic event, which included isoclinal folding and metamorphism of the granulite–amphibolite facies. Layered magmatic structures were preserved in areas of low strain, including amygdaloidal and cumulate structures. Metamorphism was pervasive and reached temperatures of 780–853 °C in mafic granulites and 680–720 °C in amphibolites under an overall pressure of 6.8 kbar.

The geochemical composition of the extrusive and intrusive rocks indicates that all noncumulus mafic–ultramafic rocks are tholeiitic basalts. The mafic–ultramafic rocks display moderate to strong fractionation of light rare earth elements (LREE), near-flat heavy rare earth element (HREE) patterns and moderate to strong negative high field strength element (HFSE) anomalies (especially Nb), a geochemical signature typical of subduction zones. The lowest units of mafic granulites and porphyroblastic amphibolites in the Trincheira ophiolite are similar to the modern mid-ocean ridge basalt (MORB), although they locally display small Ta, Ti and Nb negative anomalies, indicating a small subduction influence. This behavior changes to an island arc tholeiite (IAT) signature in the upper units of fine-grained amphibolites and amphibole rich-amphibolites, characterized by progressive depletion in the incompatible elements and more pronounced negative Ta and Nb anomalies, as well as common Ti and Zr negative anomalies. Tectono-magmatic variation diagrams and chondrite-normalized REE and primitive mantle normalized patterns suggest a back-arc to intra-oceanic island arc tectonic regime for the eruption of these rocks. Therefore, the Trincheira ophiolite appears to have originated in an intraoceanic supra-subduction setting composed of an arc-back-arc system. Accordingly, the Trincheira Complex is a record of oceanic crust relics obducted during the collision of the Amazon craton and the Paraguá block during the Middle Mesoproterozoic. Thus, the recognition of the Trincheira ophiolite and suture significantly changes views on the evolution of the southern margin of the Amazon craton, and how it can influence the global tectonics and the reconstruction of the continents.

Contents

* Corresponding author. Tel.: +55 62 99725559; fax: +55 62 32401417.
E-mail address: grgilmarjose@gmail.com (G.J. Rizzotto).

0024-4937/$ – see front matter © 2012 Elsevier B.V. All rights reserved.
doi:10.1016/j.lithos.2012.05.027

1. Introduction

The paleogeographic continental reconstructions of the Mesoproterozoic commonly propose a link between eastern Laurentia and the western margin of the Amazon craton (Cawood et al., 2007; Dalziel, 1991; Hoffman, 1991; Keppie et al., 2001; Santos et al., 2008; Tohver et al., 2004a,b; Weil et al., 1998). The link between Amazonia and Laurentia is a key issue for the reconstruction of the Mesoproterozoic paleogeography. Over the past decade, different scenarios have been proposed for the evolution of the SW margin of the Amazon craton, primarily based on geochronological data (Bettencourt et al., 2010; Boger et al., 2005; Cordani and Teixeira, 2007; D'Agrella-Filho et al., 2008; Litherland et al., 1989; Sadowski and Bettencourt, 1996; Santos et al., 2000, 2008; Teixeira and Tassinari, 1984; Tohver et al., 2002, 2004a,b). All these previous investigations were conducted on a regional scale, without detailed field information or petrological, geochemical and structural data, limiting their interpretation of tectonic environments involved in the crustal growth of the southwestern Amazon craton. Several tectonic environments have been suggested and are related to the amalgamation of intra-oceanic magmatic arcs or back-arc and Wilson Cycle processes of ocean opening and closing (accretionary orogens). However, thus far, only Tohver et al. (2004a, 2006) have indicated the location of a suture zone between the adjoining Amazonia and Laurentia. In this work, we provide detailed field information and geochemical data which allow advancements in understanding the tectonic setting of the southwestern margin of the Amazon craton.

Distinguishing between accreted-terrane and terrane boundaries and sutures that separate different cratons or orogens involved in continent–continent collisions may be difficult because the distinction depends on identifying juxtaposed terranes that had significantly different magmatic and lithotectonic histories prior to collision but share a common history afterwards. Accretionary orogens may also be referred to as non-collisional, exterior orogens or zones of type-B subduction formed at intraoceanic and continental margin convergent plate boundaries. They form at sites of subduction of the oceanic lithosphere and include the supra-subduction zone forearc, magmatic arc and back-arc components (ophiolites) (Cawood et al., 2009). A large proportion of juvenile mafic to silicic calc-alkaline igneous rocks are involved, as well as their volcanosedimentary products. Large volumes of rocks from accretionary belts exhibit typical juvenile isotopic signatures, indicating essentially mantle-derived parental magmas. Ophiolites can be part of these environments as remnants of an allochthonous or autochthonous ancient oceanic crust and upper mantle incorporated into an orogenic belt. Thus, ophiolites are of prime importance to an understanding of orogens and are essential to the definition of a suture zone. One of the difficulties in the study of ophiolite complexes in deformed regions is that they are generally emplaced early and undergo considerable deformation and alteration during subsequent orogenic events.

Therefore, the identification of oceanic crust relicts in ophiolites along a suture zone at which the Amazon craton collided with the Laurentia or Paraguá block to form a supercontinent has remained enigmatic for many years, despite intense study of the poorly exposed SW portion of the Amazon craton. Tohver et al. (2004a) believe that the E–W trending Nova Brasilândia belt marks the limit between the Amazon and Paraguá cratons and formed during the late Mesoproterozoic. However, the Nova Brasilândia belt has no petrotectonic association compatible with a suture zone and was interpreted as a rift-passive margin (Rizzotto, 1999). To date, there are no known ophiolites in the southwestern margin of the Amazon craton.

Most modern ophiolites have subduction zone chemical characteristics, indicating their magmatic and tectonic association with supra-subduction zone processes (Dilek et al., 1999; Ishikawa et al., 2002; Shervais, 2001; Stern and Bloomer, 1992). The well-studied Tethyan ophiolites show a common geochemical progression in their magmatic evolution from initially MORB-like to IAT to boninites. In general, these ophiolitic complexes show an internal stratigraphy and chemical composition represented by a lower suite of relatively evolved IAT lavas, a middle suite of depleted arc tholeiite rocks, and a stratigraphically higher suite of highly depleted boninitic rocks (Dilek and Furnes, 2009). The evolution in the geochemical behavior of magma from MORB-type to IAT is characterized by a progressive depletion of the incompatible elements and more pronounced negative Ta and Nb anomalies, as well as negative anomalies of Ti and Zr.

The recognition of ancient tectonic environments based on only their geochemical characteristics is restricted by chemical similarity and alteration. The uncertainty about the tectonic setting where such ophiolites formed is due to the common occurrence of MORB-like lavas, in addition to those more indicative of a suprasubduction zone setting (IAT). Likewise, several examples in the literature show us that the geochemical characteristics of Archean mafic–ultramafic volcanic rocks provide important information for understanding the evolution of the initial mantle–crust system (Arndt et al., 1997; Jochum et al., 1991; Polat et al., 1998; Puchtel et al., 1998; Sun, 1987). Similarly, the geochemical characteristics of modern volcanic rocks of different tectonic environment are distinct in terms of the behavior of HFSE, LFSE and REE (Pearce and Cann, 1973; Sun and McDonough, 1989).

In the case of the oceanic crust, studies of modern island arc basalts suggest that subduction of the oceanic lithosphere, with or without associated sediment, can continuously modify the chemical, isotopic and mineralogical composition of the overlying mantle wedge. The release of fluids and hydrous silicate melts from the down-going altered oceanic crust can result in the enrichment of incompatible elements in the mantle wedge above the subduction zone. In this context, back-arc basin basalts are MORB-like, with a subtle subducted slab flux component made evident by elevated large ion lithophile element (LILE) abundances. These abundances exhibit the typical spiked pattern of subduction-related arc basalts on multi-element plots, but the pattern is more subdued than that of arc basalts (Hawkins et al., 1994; Jenner et al., 1987). More recently, this geochemical duality (MORB to IAT) has been ascribed to the progressive depletion and metasomatism of a common melt source over the course of ophiolite formation (Dilek and Furnes, 2009). In other words, all magmatic components (i.e., MORB, IAT, and boninite) may have formed in the same oceanic environment, which witnessed the eruption of MORB-like lavas followed by IAT and boninites.

Our proposal of the existence of an ancient ocean crust in the southwestern Amazon craton represented by the Trincheira Complex is supported by field data, mineral chemistry and whole-rock geochemistry (mainly REE and trace elements). Thus, we follow the original methodology that established the ophiolite concept, based largely on field, petrological, and geochemical studies.

In this study, we present field data, mineral chemistry and whole-rock geochemistry to test this hypothesis. We emphasize trace elements and REE content to characterize the geotectonic environment and the evolution of magmatism that generated the Trincheira Complex. The result of this study is the recognition of ophiolites and their dismembered fragments and the concurrent identification of chemically distinct island-arc/back-arc volcanic and plutonic complexes. Preserved oceanic lithosphere commonly occurs along major tectonic sutures. The presence of oceanic lithosphere in the Alto Guaporé Belt and the evaluation of its origin establish constraints for tectonic reconstructions of the southwestern Amazon craton and provide some key issues related to reconstruction of the pre-Rodinia supercontinent.

2. Geological framework and field characteristics

The studied area is located on the boundary between the Sunsás and Rondônia–Juruena Provinces (Santos et al., 2008), southwestern Amazon craton (Fig. 1). Rizzotto et al. (2002) used geological and geochronological data to characterize a regional tectono-magmatic event with ages in the range of 1350 to 1320 Ma. Rizzotto and Dehler (2007) later called the resulting orogen the Alto Guaporé Mobile Belt (AGB) and interpreted it as having been derived from an accretional–collisional orogeny under conditions of medium to high metamorphic grade. The belt has the same temporal delimitation as the San Ignacio Orogeny in eastern Bolivia (Litherland et al., 1986) and the Rondonian (Teixeira and Tassinari, 1984) and Candeias (Santos et al., 2002) orogenies. This study reports new data that indicate that the Alto Guaporé Belt contains juvenile magmatism aged 1468–1447 Ma that was reworked at 1350–1320 Ma (Rizzotto et al. unpublished data).

The Alto Guaporé Belt (WNW–ESE trend) is a large geotectonic feature extending from the southeastern portion of Rondônia to the southwestern portion of Mato Grosso, integrating an area of 1900 km^2, 95 km long by 20 km wide. The southern part of the complex is covered by the Cenozoic sediments of the Guaporé basin. Interpretation of the aeromagnetic data suggests a continuity of the Alto Guaporé Belt to the west–northwest along at least 400 km below the Phanerozoic cover, but geological observations suggest that it may extend up to 1000 km, reaching the Andean Cordillera. Its northern boundaries are the Nova Brasilândia Terrane, Uopianes Basin, and Rondônia–Juruena Province. To the south, the boundaries are hidden below the Phanerozoic sedimentary rocks of the Guaporé basin (Fig. 2).

The Alto Guaporé Belt is primarily represented by the Trincheira Complex of mafic–ultramafic rocks initially described by Romanini (2000) and the Rio Galera Complex of dioritic–tonalitic rocks, in addition to various bodies of mafic–felsic intrusives (granitoids and gabbros) (Fig. 3). Typically of the oceanic domain the Trincheira Complex is composed of several disrupted, highly dismembered imbricate thrust slices forming an incomplete ophiolite sequence (Fig. 4).

The disrupted complex has an apparent stratigraphic sequence of layered mafic–ultramafic cumulates, intrusive mafic–ultramafic and extrusive mafic rocks with interbedded sedimentary clastic and chemical sequences. The deformation is heterogeneous, as indicated by highly deformed zones adjacent to areas with poorly developed foliation or a partly preserved primary texture. Although the original stratigraphy is not recovered here because of its structural complexity, superimposed metamorphism and sparsity of outcrops, the complex is divided into three units: a) Lower Unit: layered mafic–ultramafic (granulite-facies metamorphism): mafic granulites that has as protolith olivine orthopyroxenite, bronzitite, and websterite; b) Intermediate Unit: intrusive mafic (amphibolite-facies metamorphism): banded amphibolites which has as protolith norite, gabbronorite, gabbro, anorthosite, gabbroanorthosite and rare plagiogranite; and c) Upper Unit: extrusive mafic rocks (amphibolite-facies metamorphism): fine-grained amphibolites (massive and pillowed basalt) with intercalations of chemical and sedimentary sequences consisting of metachert (BIFs), calc-silicate rocks and aluminous schist/quartzite. The close spatial relationship between the mafic intrusives of the intermediate unit and the extrusive rocks with comparable deformation and metamorphism suggests that they are cogenetic. Granulite-facies metamorphism ranges from the basal portions of the complex to amphibolite-facies in the upper zone of the complex with retrogression to middle amphibolite facies in an anastomosing network of mylonitic shear zones (Fig. 5a).

Mafic–ultramafic cumulates of the lower unit in the southern part of the complex have mostly anhydrous granulite-facies parageneses of olivine–orthopyroxenite, bronzitite and websterite protoliths. These are interlayered with rare plagiogranites and show transposed igneous banding into vertical structures. Narrow mylonitic shear bands cut granulitic rocks and turn them into amphibolites or tremolitites, actinolitites, serpentinites and actinolite-talc schists in variable proportions, derived from the deformation of the ultramafic components. Locally, these cumulate rocks are intruded by coarse-grained granitic dikes and dioritic–tonalitic rocks. The textures of the mafic–ultramafic granulites (Vernon, 1970) are fine-grained granoblastic aggregates with polygonal grain boundaries and common triple junctions. The characteristic mineral assemblage of metamorphosed mafic rocks is orthopyroxene + clinopyroxene ± plagioclase ± olivine throughout the entire granulite zone, with minor Ti-biotite, brown hornblende and ilmenite.

Norite, gabbronorite, gabbro, anorthosite and gabbroanorthosite intercalated in the lower sequence display cumulate textures commonly cut by high-angle, mm- to cm-scale mylonitic shear zones that have diffuse to sharp boundaries with the surrounding, slightly deformed or undeformed gabbros. These are usually present as layered bodies with primary compositional banding transposed into vertical structures by tectonic superposition and transformed into banded amphibolites. Additional observations include millimeter- to centimeter-thick alternate felsic layers composed of plagioclase and rare amphibole and mafic bands of amphibole cumulates (originally pyroxene), and intermediate layers rich in plagioclase + amphibole + ilmenite ± titanite ± epidote ± quartz (Fig. 5b).

Amphibolites become predominant upward in the plutonic sequence, where multiple and mutually intrusive relations between granoblastic amphibolites (deformed small bodies of pyroxenites) and leucocratic metagabbros are common. The mylonitic foliation has a high dip (>60°) to the SSW and a mineral lineation down-dip (>50°).

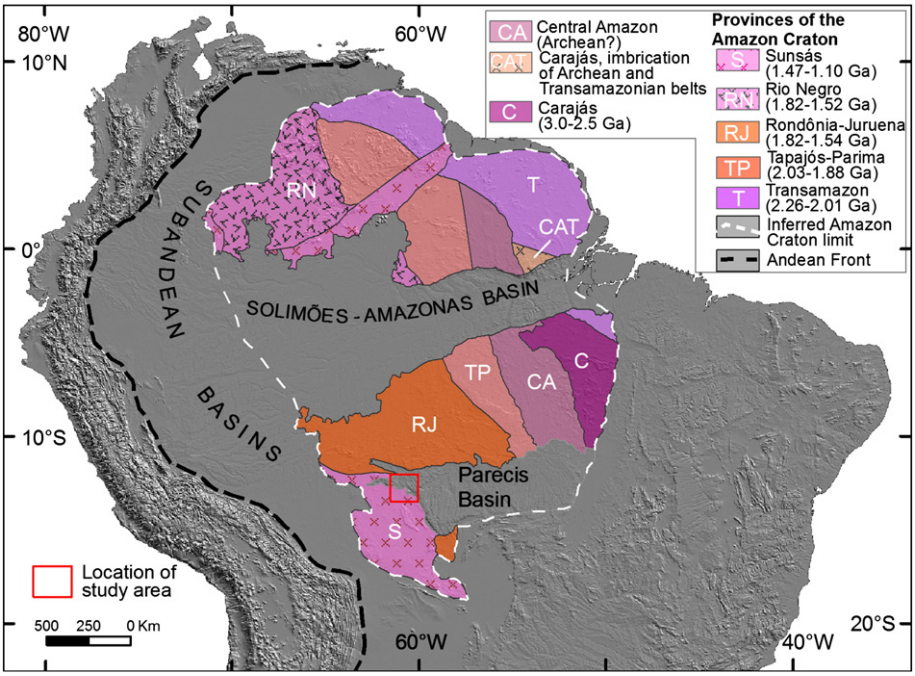

Fig. 1. Major geochronological provinces of the Amazon craton and main Phanerozoic basins. Modified from Santos et al. (2008).

Metamorphic banding and closed-isoclinal and asymmetric folds are generally associated with tectonic foliation (Fig. 5c). The adjacent amphibolites and metasedimentary rocks are structurally conformable.

The amphibolites occur in the southeastern sector of the mafic–ultramafic complex. They are usually mylonitic, banded and folded, and fine-grained; rarely isotropic; commonly tectonically interlayered with dioritic–tonalitic gneiss, banded metagabbro, metagabbronorites, leucometagabbros and metapyroxenites. The units show a strong to vertical tectonic transposition. In zones of high strain, the amphibolites are fine-grained, with regular and uniform banding in the centimeter–millimeter scale displayed as a heterogeneous segregation of felsic bands of plagioclase and quartz alternating with mafic bands composed of amphibole. These lenses of amphibolites occur in sub-vertical positions as a result of compressive deformation. Isoclinal folds are frequent, as well as thin quartz veinlets that define ptigmatic and intrafolial folds. In some locations, isoclinal folding and thickening of the hinge zone can be observed (Fig. 5c). In a few places, centimetric to metric pegmatoidal veins composed of K-feldspar, quartz and amphibole are observed, which were likely generated by the late segregation of hydrothermal fluids.

The upper unit is distributed in the northwestern sector and represented predominantly by fine-grained, gray amphibolites, which locally present partially preserved igneous textures and structures and can be characterized as metabasalts. These show a pervasive sub-horizontal jointing with centimeter spacing, representing subaerial volcanism (Fig. 5d). Millimeter- to centimeter-sized cavities are filled with an aggregate of epidote, garnet and quartz and may correspond to deformed amygdules (Fig. 5e) in relict pillow lavas. Likewise, bands of fine-grained, white material composed of quartz + plagioclase + epidote ± carbonate ± sulfide (interpillow material) bordering the better-preserved cores of the metabasalts resemble pillow structures (Fig. 5f). However, the high strain makes this identification questionable. Restricted bands with high sulfidation are common in fine-grained amphibolites affected by late, low-grade metamorphism (retrometamorphism), which transformed the rock into an assembly composed of actinolite + epidote + albite + quartz + pyrite ± chalcopyrite.

Pods of mafic–ultramafic rocks occur as bodies of several tens of meters contained in fine-grained amphibolites and suggesting intrusions in the form of sills. They occur as subrounded to elongated blocks with preserved cores and sheared edges, usually distributed along the direction of the regional metamorphic foliation. They are mostly massive, coarse-grained, have a dark green to black color and outcrop as metric subangular boulders and a few bodies that are hundreds of meters in length (Fig. 6a). The pods occur along the zones with least deformation where the flow of metamorphic fluids is concentrated in low-pressure areas, often in the hinges of folds in pyroxenite and melagabbro protoliths. They often exhibit granoblastic aggregates of amphibole as well as porphyroblasts (up to 8 cm) surrounded by irregularly shaped grains of plagioclase (Fig. 6b). They are classified as porphyroblastic amphibolite with partially preserved igneous texture and structure. Nevertheless, they show a heterogeneous pattern in the behavior of the flow direction of metamorphism, with variation in the foliation trend depending on the rheology of the rock (Fig. 6c). Therefore, some outcrops contain megapods surrounded by shear bands in which the original rock has been partly transformed into ultramafic schist (actinolite schist, talc schist, and tremolitite) (Fig. 6d). Metamorphic foliation rarely develops in the central parts of larger bodies, indicating a greater strength in relation to the same strain.

The fine-grained amphibolites are overlain by supracrustal rocks consisting of metacherts, calc-silicate rocks, banded iron formations (Fig. 7a), mylonitic gneiss, pelitic schists and aluminous quartzite. The clastic and chemical supracrustal rocks occur as lenses with elongated and sigmoidal forms and dimensions ranging from a few meters to kilometers in length. They are composed of biotite–muscovite–quartz schist, garnet–sillimanite–biotite schist, sillimanite–staurolite–biotite–quartz schist, sillimanite–garnet gneiss (Fig. 7b), hematite–magnetite quartzite, metamarls, and scarce kyanite quartzite. Generally, schists show pervasive ptigmatic folds constituted primarily of quartz and feldspar and lenses of quartz boudin, which are often generated by metamorphic segregation (Fig. 7c). Polycrystalline aggregates of quartz form less altered cores which were preserved from deformation along the sigmoidal foliation (Fig. 7d). Associated with the schists is a striking presence of metric veins (more rarely decametric) of white quartz with

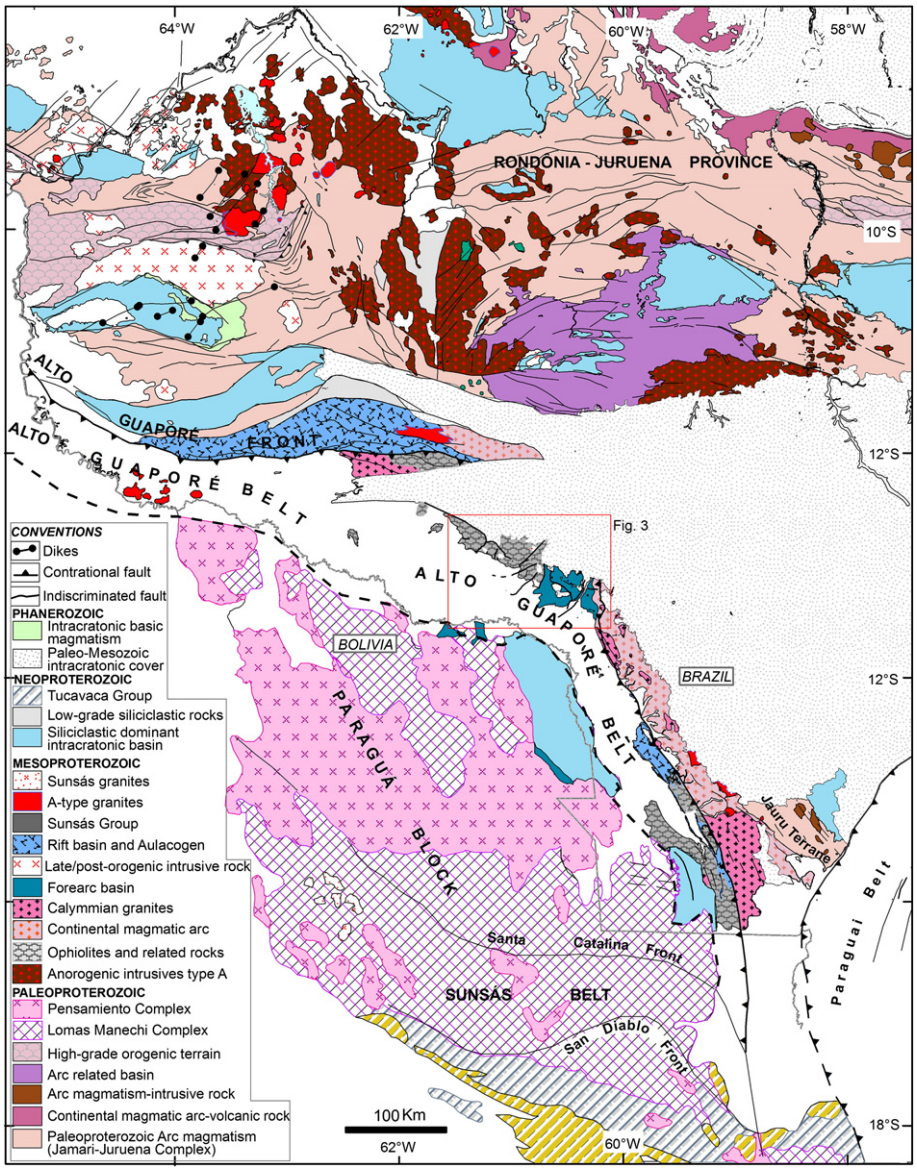

Fig. 2. Simplified map of the southwestern Amazon craton showing the approximate boundaries of the main terranes and belts, tectonic elements, and lithologic units. Modified after Rizzotto (2010) and Schobbenhaus (2001).

sporadic centimeter muscovite plates, which form small ridges aligned along the regional foliation.

Farther to the southeast, two more bodies of ultramafic rocks may be part of the ophiolitic sequence; they are referred to as Morro sem Boné and Morro do Leme. They consist of strongly serpentinized ultramafic rocks that are exposed discontinuously as two bodies layered within the metavolcanic–sedimentary sequence. The Morro sem Boné is a unique body elongated in a NE–SW trend and is approximately 5.5 km long and 1.0 km wide. It is intrusive into pelitic–psamitic supracrustal rocks. Its upper portion is predominantly composed of serpentinites, which exhibit strong sub-horizontal fracturing and intercalations of laterite and siliceous silcrete layers. The serpentinite grades at a lower topography into dunite, which is strongly fractured and transformed into a network of aggregates of serpentine, magnesite, silica and microcrystalline garnierite. Lenses of pyroxenite are intercalated with the dunite. Narrow lenses of amphibolites and actinolite schist were generated by shearing the pyroxenites.

In general, the rocks have a brittle–ductile foliation of an approximately N20E direction, subconcordant with the general direction of the massif. In the serpentinite, the original rock has been completely transformed because iron–magnesium minerals were leached and replaced by microcrystalline silica and iron oxides. In some places, the rock is porous and has low density, depending on its degree of alteration. A mesh-like texture was formed by the aggregate of fibrous serpentine surrounding the olivine. In drill cores, granite intrusions were observed in the layered dunites.

3. Petrography and mineral chemistry

The mineralogical characteristics and interpreted protoliths of the different types of mafic–ultramafic rocks are presented in Table 1. These rocks show metamorphic assemblages with penetrative foliation. The primary igneous mineralogy and texture are preserved in some rocks. Based on the mineral assemblages of the metamorphosed mafic–ultramafic rocks, two metamorphic zones are distinguished: a granulite zone (orthopyroxene + clinopyroxene + plagioclase ± olivine) and a large amphibolite zone (hornblende + plagioclase ± clinopyroxene + ilmenite + titanite ± epidote) resultant from retrogressive metamorphism of the granulite by continuous deformation during uplift and

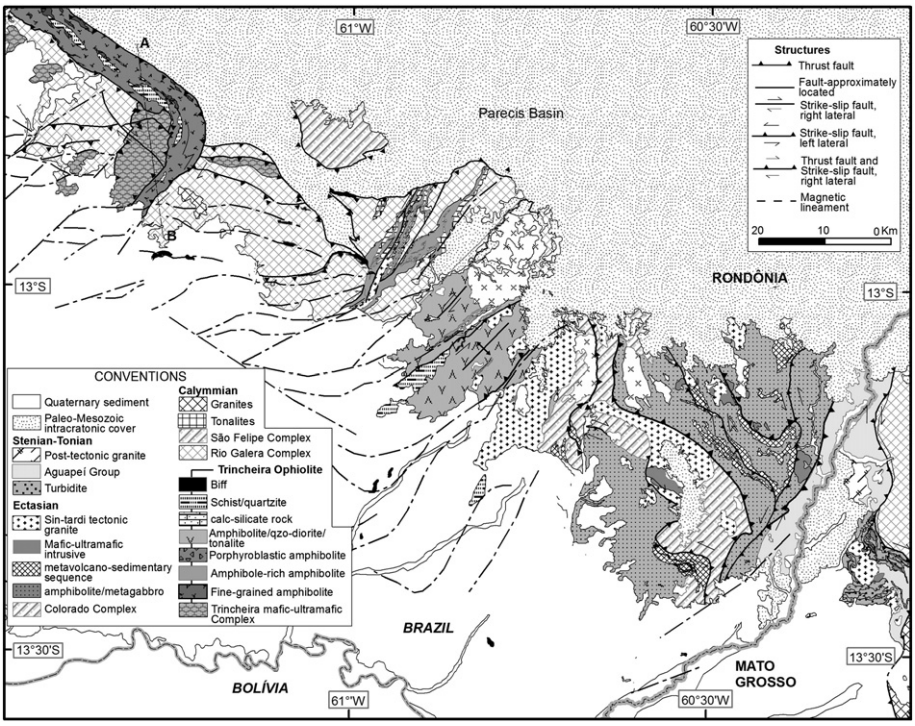

Fig. 3. Simplified geological map of our study area in southeastern region of Rondônia and southwestern of Mato Grosso, Brazil. A–B depicts the profile line for the structural cross-section shown in Fig. 4.

exhumation. Igneous and metamorphic minerals are not easily distinguished on textural grounds in granulite-facies metamorphic rocks in the region.

Mafic granulites have relict igneous textures consisting of elongated and curved, wedge-shaped and plane twinning crystals (<2 mm) of plagioclase. The crystals are surrounded by a granoblastic, polygonal and isogranular matrix (<1 mm) consisting of plagioclase, diopside and orthopyroxene. Relict igneous porphyroclasts (orthopyroxene + plagioclase) (Fig. 8a) are usually deformed, elongate crystals partially replaced by metamorphic minerals. In contrast with the metamorphic pyroxene, the igneous pyroxene has ubiquitous exsolution lamellae, while metamorphic orthopyroxene recrystallizes in granoblastic polygonal aggregates. The contacts are polygonal, with angles of 120°. The orthopyroxene is partially transformed along the rims into tschermakitic hornblende. In shear micro-zones, magnesio-hornblende forms intergrowths with cummingtonite, carbonate and rare quartz.

Magnesio-hornblende in fine-grained amphibolites occurs as prismatic aggregates; together with epidote, they define the penetrative foliation of the rock. Amygdules elongated by deformation are filled with prismatic crystals of epidote and a fine granoblastic aggregate of quartz + albite + ilmenite ± sulfides (Fig. 8b). The preserved igneous features are represented in amygdaloidal zones (Fig. 8c), suggesting a basaltic protolith (pillowed basalt).

Amphibole-rich amphibolites are spatially associated with fine-grained amphibolites. The mineral assemblage is shown in Table 1 and Fig. 8d. Prismatic crystals and acicular actinolite surround the porphyroclasts of magnesio-hornblende in some areas. The presence of ghost crystals as porphyroclasts of pyroxene partially replaced by magnesio-hornblende is also common. The sigmoidal penetrative foliation is defined by the elongated prisms of amphibole and rare chlorite (Fig. 8e). Relict igneous texture (ophitic texture) is observed locally and granoblastic aggregates of plagioclase + quartz occur between the interstitial spaces of the amphibole.

Porphyroblastic amphibolites are less abundant than amphibole rich-amphibolites. The porphyroblastic aggregates of magnesio-hornblende with subrounded to elongated inclusions and fillets of quartz along the planes of cleavage suggest the replacement of igneous pyroxene by amphibole (Fig. 8f). Plagioclase and quartz aggregates in a mosaic of 120° occur between amphibole porphyroblasts.

Metaultramafic rocks are represented by orthopyroxene cumulates (Fig. 8g), which exhibit an adcumulate texture represented by their imbrication in a triple junction at angles of 120° of large crystals of orthopyroxene. Rare post-cumulus crystals of plagioclase, magnetite and cummingtonite make up approximately 1%.

The metagabbros are coarse-grained and have the best-preserved primary igneous features among the rocks (Fig. 8h). Metagabbro bodies often escape pervasive internal deformation and this, in turn, prevents the access of water, hampers recrystallization and hinders hydratation of the igneous minerals. Ophitic and intergranular textures are present. However, plagioclase simplectites + hornblende develop at the edges of the pyroxene. Throughout shear micro-zones the primary minerals (plagioclase) are transformed to albite + epidote + quartz and the pyroxene is partially transformed into amphibole. The metamorphic changes are most evident at the edges

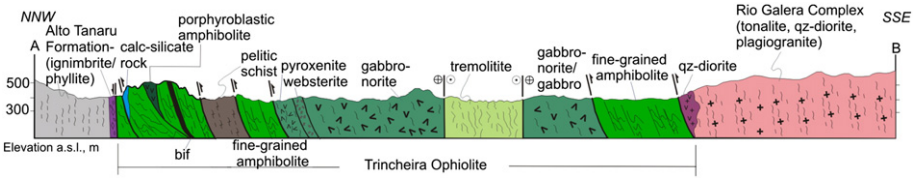

Fig. 4. Structural cross-sections (A–B) across the Trincheira ophiolite.

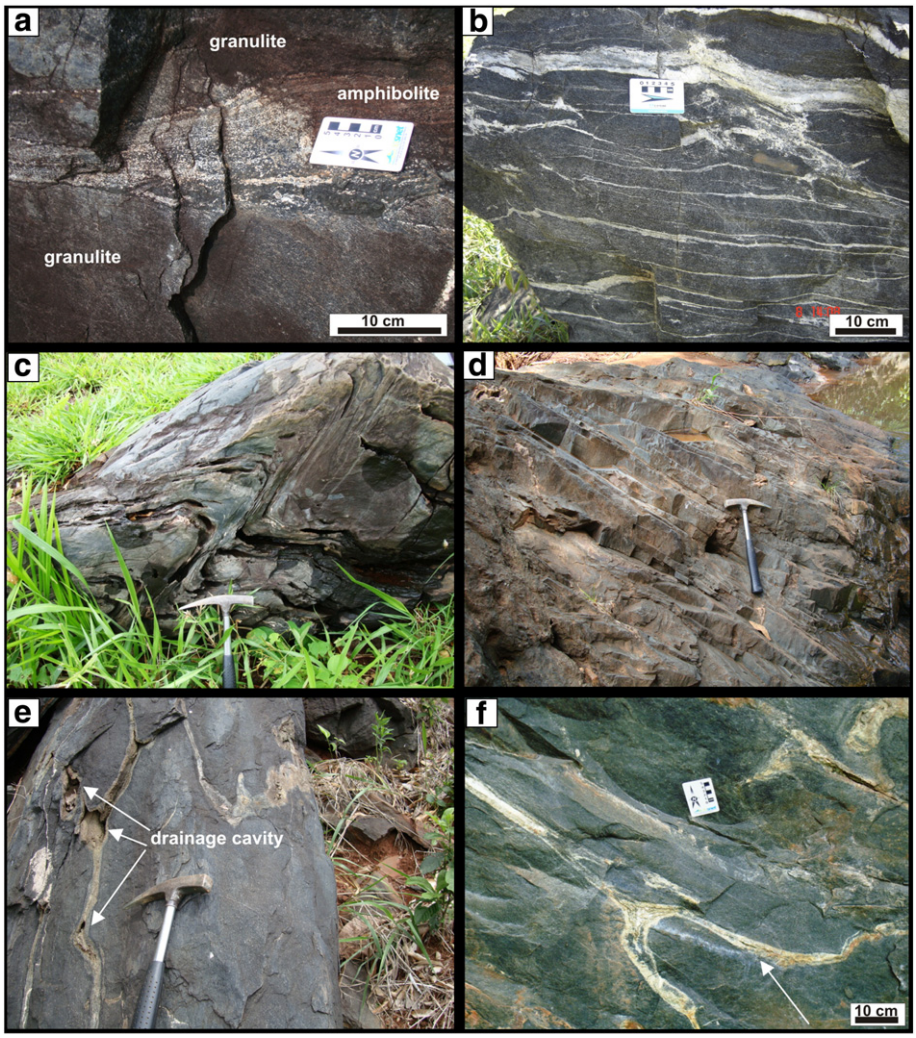

Fig. 5. Mafic and ultramafic rocks of the Trincheira Complex. (a) Mafic granulite cross-cutting for amphibolite shear band; (b) banded amphibolite; (c) tight fold in amphibolite into zone of high strain; (d) subhorizontal jointing in amphibole rich-amphibolite; (e) drainage cavities in fine-grained amphibolite; (f)) structures similar to stretched pillow lavas. On the arrow, interpillow material.

of the clinopyroxenes, where there is simplectitic intergrowth of magnesio-hornblende + plagioclase. Crystals of orthopyroxene are pseudometamorphosed to cummingtonite and magnesio-hornblende.

3.1. Analytical methods

Mineral analyses of mafic–ultramafic rocks were performed on polished thin sections of orthopyroxene, clinopyroxene, amphibole and plagioclase using a JEOL JXA-8530F EPMA five-spectrometer electron microprobe at the University of Western Australia. Online Table 1 presents representative compositions of these minerals. The analytical conditions were an accelerating voltage of 15 kV and a beam current of 20 nA. The elements analyzed and their standards were as follows: Na (jadeite), Mg (periclase), Al (corundum), Si (wollastonite), K (orthoclase), Ca (wollastonite), Ti (rutile), Cr (Cr metal), Mn (Mn metal) and Fe (Fe metal). All analytical X-ray lines were K alpha; counting times were 20 s for both peaks and backgrounds.

3.2. Results

3.2.1. Amphibole

The mafic granulites contain brown and greenish-brown amphiboles. According to Leake's (1978) classification, brown amphibole is ferro-tschermakitic hornblende and greenish-brown amphibole is tschermakite (Fig. 9a), with magnesium number (Mg#) between 0.47 and 0.72 and high TiO_2 and Al_2O_3 contents. Their Al^{iv}/Al^{vi} ratios are <3.3, suggesting a secondary (metamorphic) origin. Although amphibole crystals are generally unzoned, they rarely show a lamellar intergrowth between tschermakite and cummingtonite. Green amphibole (magnesio-hornblende) occurs in close microshear zones that cut granoblastic mafic granulites. These amphiboles are similar to those of the adjacent amphibolites. The porphyroblastic amphibolite, fine-grained amphibolites and amphibole rich-amphibolite contain greenish-brown and green amphiboles, which vary from tschermakitic hornblende to magnesio-hornblende (Fig. 9a). Its Mg# value varies between 0.46 and 0.60, with TiO_2 and Al_2O_3 contents between 0.22 and 0.91 wt.% and between 5.5 and 16.4 wt.%, respectively.

3.2.2. Orthopyroxene

Metamorphic orthopyroxene and Ca-clinopyroxene coexist in the mafic granulites of the Trincheira Complex. To distinguish between the igneous orthopyroxene and metamorphic orthopyroxene, we utilized a graphic that uses the ratio $Fe_{total} + MgO$ versus Al_2O_3 (Bhattacharyya, 1971) (Fig. 9b), which is from unambiguously metamorphic orthopyroxene.

Orthopyroxene in mafic granulites has an enstatite to ferrosillite composition (Fig. 9c). The compositions of pyroxene are listed in

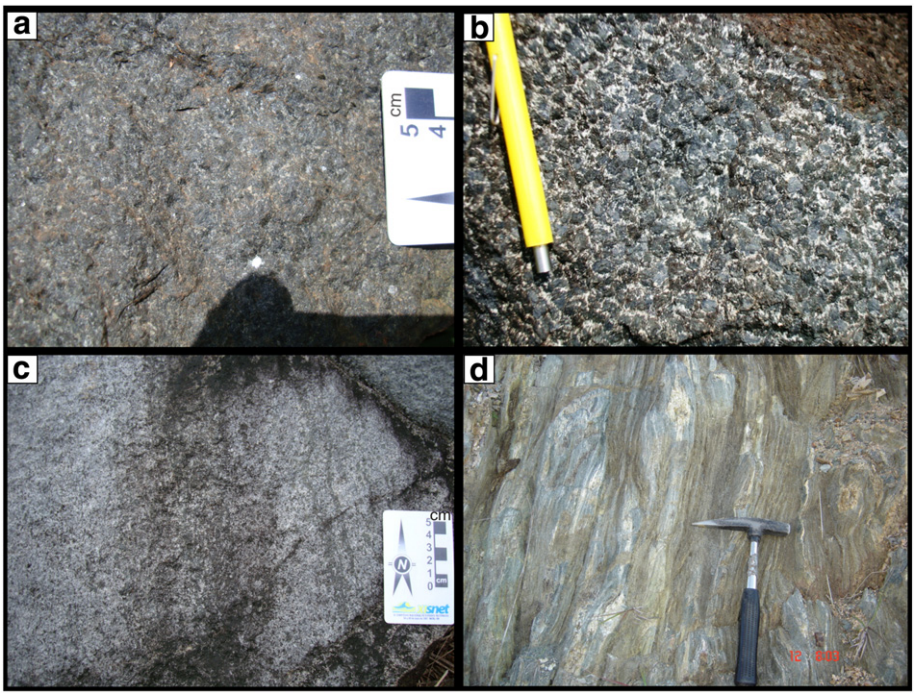

Fig. 6. Rocks of the Trincheira Complex. (a) massive, coarse-grained, ultramafic rock; (b) granoblastic texture of the porphyroblastic amphibolite; (c) metamorphic microbanded in metapyroxenite; (d) shear bands, where the original rock has been partly transformed for ultramafic schist.

the Online Table 1. The Mg# ranges between 0.48 and 0.61, with Cr_2O_3 and TiO_2 contents varying between 0 and 0.03 and 0 and 0.08 wt.%, respectively. Al_2O_3 decreases from the core (1.92 wt.%) to the overgrowth rim (1.08 wt.%).

3.2.3. Clinopyroxene

Clinopyroxene in the mafic granulites ($En_{25–35}$, $Wo_{45–47}$, $Fs_{18–30}$) is diopside; in one analysis, it is hedenbergite (Fig. 9d). It has an Mg# between 0.85 and 1.90 and Cr_2O_3 and NiO contents between 0 and 0.09 wt.% and 0 and 0.019 wt.%, respectively. Al_2O_3 and TiO_2 contents range from 0.62 to 2.35 wt.% and 0.01 to 0.26 wt.%, respectively (Online Table 1).

3.2.4. Plagioclase

Plagioclase in both mafic granulites and amphibolites is almost unzoned. Although twinning is completely destroyed in most cases,

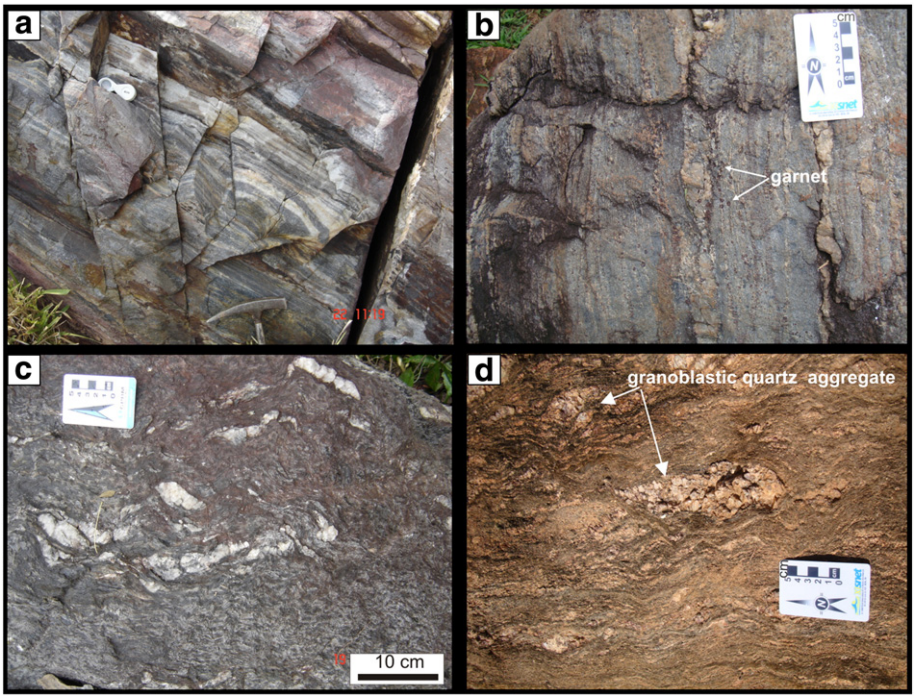

Fig. 7. Field pictures of various types of supracrustal rocks of the Trincheira ophiolite. (a) Alternating layers of chert and magnetite (BIFs) in transpressional zone; (b) aluminous banded gneiss; (c) lenses of the quartz boundin in pelitic schist; (d) biotite–quartz schist with quartz polycrystalline aggregates preserved in sigmoidal shape.

Table 1
Characteristics mineralogical and protolith interpreted of the main rock types Trincheira Complex.

Lithology	Mineralogical composition	Protolith
Mafic granulite	Plagioclase (40–50%) + orthopyroxene (20–25%) + diopside (15–20%) + tschermakitic hornblende (3–5%) + ilmenite (<1%) ± olivine ± cummingtonite	Gabbronorite, norite
Fine-grained amphibolite	Tschermakite or magnesio-hornblende (60–65%) + plagioclase (15–20%) + quartz (5–10%) + epidote (7–10%) ± magnetite ± titanite ± garnet	Basalt
Amphibole-rich amphibolite	Magnesio-hornblende or tschermakite (65%) + plagioclase (20%) + quartz (9%) + epidote (2%) ± titanite ± ilmenite ± actinolite	Hornblende gabbro/melagabbro
Porphyroblastic amphibolite	Magnesio-hornblende (70–80%) + plagioclase (15–20%) + quartz (3–6%) + magnetite (1–2%) ± augite ± ilmenite ± apatite ± epidote	Gabbronorite
Metaultramafic rock	Orthopyroxene (90–95%) + clinopyroxene (5–10%) ± cummingtonite ± plagioclase ± olivine	Pyroxenite, websterite
Metagabbro	Plagioclase (50–60%) + clinopyroxene (25–30%) + orthopyroxene (10–15%) + tschermakite or magnesio-hornblende (5%) ± ilmenite ± titanite ± scapolite	Gabbro

it is still discernible in some crystals. In the mafic granulites, the plagioclase is labradorite (An_{61-67}). In one sample, the plagioclase is bytownite (An_{75}), while in the amphibolites it varies from andesine to labradorite (An_{36-65}) (Fig. 9e). In amphibole rich-amphibolites, the plagioclase medium grains in the matrix are zoned, with core compositions of An_{62} decreasing to An_{36} toward the rims. Plagioclase is often transformed to epidote in the amphibole-rich amphibolites and fine-grained amphibolites.

3.3. P–T estimates

The temperatures and pressure during the metamorphism of the Trincheira mafic–ultramafic Complex have been estimated using the hornblende-plagioclase thermometer of Holland and Blundy (1994) and the aluminum-in-hornblende geobarometry (in the absence of garnet) of Schmidt (1992), respectively. The temperatures were calculated for plagioclase_amphibole pairs that show clear contacts at their boundaries from samples of both granulites and amphibolites. For the specific pressure of 6.8 kbar, temperatures of 820–853 °C and 680–720 °C were estimated for mafic granulites and amphibolites, respectively. Also, we use clinopyroxene–orthopyroxene (two-pyroxene geothermometer) in the mafic granulites to establish a solvus temperature, based on the miscibility gap and the distribution of Ca and Na between both pyroxenes and Fe–Mg exchange reaction between the mineral phases of the geothermometer, according to the empirical calibrations of Wood and Banno (1973). Phase chemistry calculations on granulites show ambient P–T conditions to have been in the range 780–820 °C (clinopyroxene–orthopyroxene equilibria), a temperature value close to those calculated by hornblende-plagioclase thermometer of Holland and Blundy (1994).

The above P–T estimates in both geothermometers are in agreement with an overall metamorphic overprint under granulite (c. 780–853 °C and 6.8 kbar) and amphibolite (c. 680–720 °C and 6.4 kbar) facies conditions. The peak metamorphic conditions (i.e., 850 °C and 6.8 kbar) correspond to a burial depth of c. 20–30 km.

4. Whole-rock chemistry

4.1. Analytical methods

The samples were pulverized using an agate mill at a 150-mesh fraction in the laboratory of Geological Survey of Brazil-CPRM, and the analyses were performed at Acme Analytical Laboratories Ltd. (Vancouver, Canada). The samples were mixed with lithium metaborate and lithium tetraborate and fused at 1000 °C in an induction furnace. The molten beads were rapidly digested in a solution of 5% HNO_3 containing an internal standard and mixed continuously until complete dissolution. The loss on ignition (LOI) was determined by measuring the weight lost during heating at 1000 °C over a three-hour period.

Major elements and several minor elements were determined by emission spectrometry (ICP), while the trace elements and REE were determined by mass spectrometry (inductively coupled plasma mass spectrometry—ICP-MS). Additionally, a fraction of 0.5 g was removed for digestion in aqua regia (heated to 95 °C) and analyzed for base metals and precious metals by mass spectrometry (ICP-MS). The accuracy and precision of the geochemical data are presented in the Online Appendix.

Selected elements were normalized to primitive mantle (pm) (Hofmann, 1988) and chondrite (cn) (Sun and McDonough, 1989). Nb (Nb/Nb*), Zr (Zr/Zr*), Ti (Ti/Ti*) and Eu (Eu/Eu*) ratios were calculated with respect to the neighboring immobile elements, following the method developed by Taylor and McLennan (1985). The samples were recalculated to a 100% anhydrous basis for intercomparisons. Mg numbers (Mg#) were calculated with a molecular ratio of 100 $Mg/(Mg + Fe^{2+})$, assuming that $Fe_2O_3/FeO = 0.15$.

4.2. Results

The data of major elements, trace elements, REE and inter-element ratios of the most significant mafic–ultramafic rocks of Trincheira Complex are presented in Table 2 and Online Table 2. Based on the characteristics of the field, petrographic study and the abundance of major elements (e.g., SiO_2 and MgO), the metavolcano-plutonic rocks can be divided into five main groups: (1) fine-grained amphibolite, (2) amphibole rich-amphibolite, (3) porphyroblastic amphibolite, (4) mafic granulite, and (5) mafic–ultramafic cumulate.

Before considering a petrogenetic interpretation, an investigation was conducted to evaluate the geochemical mobility of elements by hydrothermal alteration, amphibolite to granulite facies metamorphism, polyphase deformation and the metasomatism eventually suffered by the mafic–ultramafic rocks of the sequence.

Many petrochemical studies have demonstrated that Zr is one of the least mobile elements in the geochemical system (Pearce and Peate, 1995; Pearce et al., 1992; Winchester and Floyd, 1977). This element has been used as an independent index of geochemical variation for studies of both the geochemical behavior of modern volcanic rocks (Murton et al., 1992) and Archean rocks (Polat et al., 2002). Therefore, we adopted a similar procedure in this study to evaluate the effects of the changes in the mafic–ultramafic rocks.

The mobility of K, Rb, Na, Ba, Sr, Ca, P and Fe has been demonstrated in studies of metamorphosed volcanic rocks (Arndt, 1994; Brunsmann et al., 2000; Frei et al., 2002). In contrast, REE, HFSEs, Al, Cr and Ni have lower mobility (Jochum et al., 1991; Ludden et al., 1982). However, the mobility of the elements of each case must be tested. An effective method was proposed by Cann (1970), in which an immobile element is plotted on the horizontal axis of a diagram of bivariate variation and the element to be evaluated is plotted on its vertical axis. This was used as a criterion to evaluate the effects of alteration and the magnitude of correlation of Zr in binary diagrams (Fig. 10). Elements with a

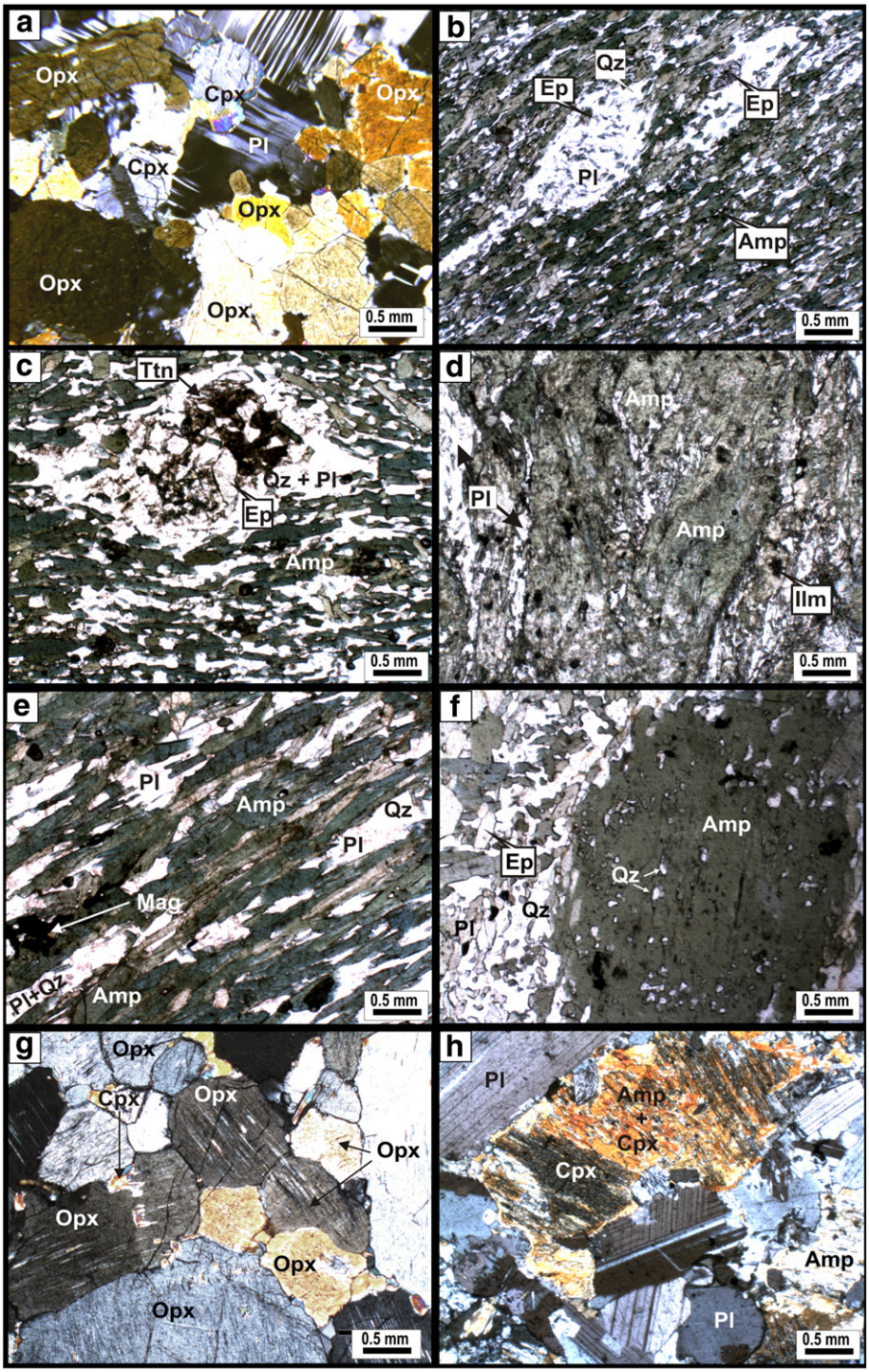

Fig. 8. Photomicrographs of mafic–ultramafic rocks (see Table 1). (a) Mafic granulite with granoblastic texture; (b) fine-grained amphibolite with stretched amygdules; (c) fine-grained amphibolite showing amygdule filled by Pl + Ep + Qz + Ttn; (d) amphibole rich-amphibolite with nematoblastic sigmoidal texture; (e) amphibole rich-amphibolite with penetrative foliation; (f) porphyroblastic amphibolite with small inclusion of quartz in amphibole; (g) ultramafic rock with granoblastic texture; (h) metagabbro with granoblastic texture. Plane polarized light (b, c, d, e, f) and cross-polarized light (a, g, h). Abbreviations: Ep—epidote; Ilm—Imenite; Pl—plagioclase; Qz—quartz, Cpx—clinopyroxene, Opx—orthopyroxene, Amp—amphibole; Ttn—titanite; Mag—magnetite.

correlation coefficient (R) <0.75 were regarded as mobile (Polat et al., 2004) and will not be used for petrogenetic interpretation. Therefore, we have assessed the effect of alteration on these elements in all sample mafic–ultramafic rocks. The abundance of the elements Si, K, Na, Sr and Ba show moderate variations (e.g., $K_2O = 0.13–1.2$ wt.%; $Na_2O = 0.33–3.8$ wt.%; Sr = 71–301 ppm and Ba = 20–420 ppm), which do not correlate well with Zr abundances (Fig. 10), and show weak correlations with MgO contents (Appendix B — Fig. 1). Accordingly, these elements were screened out and not used for petrogenetic interpretation.

On the diagrams of Zr vs. Ti, Nb, Y and REE, most samples display systematic correlation consistent with a relatively low mobility of these elements in the Trincheira mafic–ultramafic rocks (Fig. 10). Similarly, despite its weak dispersion, there is a good correlations for these elements on MgO variation diagrams (Appendix B —

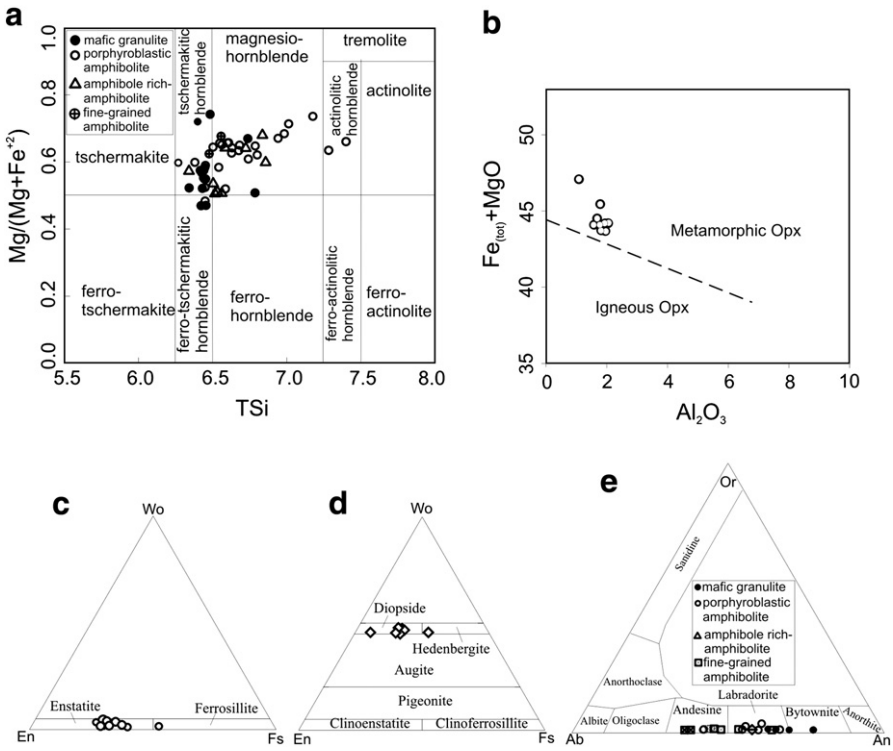

Fig. 9. (a) Compositional ranges of Ca-amphiboles from the Trincheira mafic–ultramafic Complex, expressed in the classification diagram of Leake (1978); (b) orthopyroxene compositions plotted in Fe(tot) + MgO x Al_2O_3 diagram of Bhattacharyya, (1971); (c and d) compositional variability of the composition of orthopyroxene and clinopyroxene from Trincheira mafic–ultramafic rocks, expressed in the diagram wollastonite–enstatite–ferrosilite; (e) chemical classifications of plagioclase in Or–Ab–An diagram.

Fig. 1). In addition, the evidence suggesting low mobility of Ti, Nb, Zr, Th and REE (except Ce) includes the following: (1) Th–Nb–La–Gd inter-element relationships do not correlate with loss on ignition (LOI) (Appendix B — Fig. 2); (2) the samples have consistent and coherent primitive mantle-normalized trace element patterns (Fig. 11). Thus, these elements are widely considered to be immobile and have not been significantly affected by post-magmatic alteration, and variation in their abundances can be attributed to olivine and/or pyroxene fractionation.

There is no evidence for any crustal contamination, according to initial Sr–Nd composition, by significantly older rocks in the Trincheira Complex (Rizzotto et al. unpublished data). Likewise, the absence of xenocrystic zircons in the Trincheira mafic–ultramafic rocks is also consistent with the absence of the continental crust in their geodynamic setting. The granitoids and felsic dykes in the region are younger than the Trincheira mafic–ultramafic rocks.

Most of mafic–ultramafic rocks plot in the basalts field on a Zr/Ti versus Nb/Y diagram, and only three samples are basaltic andesite composition (Fig. 12a). In variation diagrams with Zr (Fig. 10), mafic–ultramafic rocks show collinear trends for the HFSE, REE and transition metals, indicating their comparable composition. The mafic–ultramafic rocks were divided into five main groups (mafic–ultramafic cumulates are not shown), depending on the chemical characteristics of trace elements when normalized to chondrite and primitive mantle, according to Hofmann (1988) and Sun and McDonough (1989), respectively (Fig. 11, Table 2).

4.2.1. Fine-grained amphibolites

Fine-grained amphibolites are characterized by variable contents of SiO_2 and MgO; high Fe_2O_3 and Al_2O_3; moderate TiO_2 and CaO; and Mg# ranging from 34 to 52. Al_2O_3/TiO_2 ratios are sub-chondritic, whereas Ti/Zr and Zr/Y range from sub-chondritic to super-chondritic (Table 2 and Online Table 2). Additionally, the fine-grained amphibolites show: (1) weak depletion to slightly fractionated LREE patterns ($La/Sm_{cn} = 0.62–1.15$); near-flat REE patterns ($La/Yb_{cn} = 0.74–1.40$); (2) flat to weak enrichment HREE pattern ($Gd/Yb_{cn} = 1.1–1.4$) with moderate negative Nb, Ti, Zr anomalies; and no negative Eu anomalies (Fig. 11a–b, Table 2).

4.2.2. Amphibole rich-amphibolites

Amphibole rich-amphibolites have higher contents of MgO and Fe_2O_3, but low Zr and Ni and moderate to variable SiO_2, CaO and TiO_2 contents compared to modern average mid-ocean ridge basalt (MORB) (see Hofmann, 1988). Their Mg# range from 37 to 62 and their Al_2O_3/TiO_2 ratios are slightly sub-chondritic, whereas the Zr/Y ratios are sub-chondritic to slightly super-chondritic and Ti/Zr ranges from sub-chondritic to super-chondritic (Table 2 and Online Table 2). On chondrite and primitive mantle-normalized diagrams they have: (1) weak to moderate fractionation LREE patterns ($La/Sm_{cn} = 0.85–1.27$; $La/Yb_{cn} = 0.86–2.17$); slight fractionation HREE patterns ($Gd/Yb_{cn} = 1.02–1.67$); moderate to large negative Nb, Ti, Zr anomalies; and very weak or absent negative Eu anomalies (Fig. 11c–d, Table 2).

4.2.3. Porphyroblastic amphibolites

Porphyroblastic amphibolites have Zr/Y (1.9–3.0) ratios comparable to modern tholeiitic basalts ($Zr/Y = 1.3–3.1$) (Barrett and MacLean, 1994). They have Mg# ranging from 52 to 62 and small variations of SiO_2, TiO_2, Fe_2O_3, Al_2O_3, MgO, Zr and REE contents (Fig. 8 and Table 2). The Al_2O_3/TiO_2 ratios are slightly sub-chondritic, whereas the Zr/Y ratios are sub-chondritic to slightly super-chondritic. The Ti/Zr ratio ranges from sub-chondritic to super-chondritic.

On the chondrite and primitive mantle-normalized diagrams, they have: (1) near-flat total REE patterns, slight depletion LREE patterns ($La/Sm_{cn} = 0.50–1.0$); near-flat HREE patterns ($Gd/Yb_{cn} = 0.93–1.4$);

Table 2
Representative major (wt.%) and trace element (ppm) concentrations and significant element ratios for mafic–ultramafic rocks. Major elements oxides in wt.%. FeO_t is total Fe expressed as Fe^{2+}. Mg# = 100 Mg/(Mg + Fe^{2+}) assuming $Fe_2O_3/FeO = 0.15$. LDL = lower than detection limit.

	Fine-grained amphibolites		Amphibole-rich amphibolites		Porphyroblastic amphibolites		Mafic granulites		Ultramafic cumulus (metapyroxenites)		Mafic cumulus (metagabbros)	
	GR 730	GR 738	NM 141	NM 54	GR 694	GR 710	GR 558	SJ 2562	GR-759	GR-760	GR-18	GR-761
$SiO_{2(wt.\%)}$	49.74	48.94	50.34	46.10	48.06	46.90	47.88	48.57	47.27	49.11	46.46	48.94
TiO_2	1.30	1.50	1.13	1.44	1.02	1.08	1.65	1.27	0.42	0.50	0.58	0.23
Al_2O_3	16.32	13.85	14.58	15.09	14.01	15.15	15.74	15.68	6.67	6.48	16.72	20.03
Fe_2O_3	11.42	13.47	12.84	11.33	11.68	12.88	12.98	12.30	11.38	11.79	9.71	6.31
MnO	0.19	0.21	0.20	0.15	0.29	0.20	0.20	0.19	0.19	0.18	0.18	0.14
MgO	5.65	7.51	6.55	9.34	7.22	7.89	6.26	6.90	19.16	19.24	10.51	7.98
CaO	11.44	9.76	10.22	12.50	12.57	10.99	11.18	11.30	8.85	7.58	12.93	13.08
Na_2O	2.60	2.94	2.80	2.36	2.27	1.88	2.54	2.39	0.38	0.33	1.49	1.99
K_2O	0.33	0.28	0.43	0.27	0.15	0.12	0.26	0.20	0.07	0.05	0.18	0.09
P_2O_5	0.15	0.17	0.24	0.12	0.107	0.12	0.16	0.12	0.02	0.10	0.06	0.01
LOI	0.60	1.10	0.60	1.20	2.40	2.50	0.90	0.80	4.90	3.90	1.10	1.00
Total	99.79	99.77	99.94	99.97	99.81	99.76	99.74	99.77	99.62	99.61	100	99.81
Mg#	49	52	50	62	55	55	49	53	77	76	68	71
Sc (ppm)	42	54	45	37	35	38	42	44	38	27	29	39
V	283	377	279	229	230	242	334	283	128	145	192	122
Cr	274	260	55	328	171	178	205	281	1875	1608	294	123
Co	45	50	47.3	53.1	48.4	57	50.4	51.5	70.7	75.9	61.2	34.1
Ni	64	93	58	171	100	114	69	70	461	546	294	36
Ga	18	17	18.1	15.4	15.9	15.4	19.2	17.7	8.8	8.8	14.4	16.2
Rb	6	8	7.7	14.4	1.8	3.8	4.2	3.8	2.8	2.4	4.4	1
Sr	164	101	299.4	250.6	178.5	158.1	207.3	211.1	55.6	71.9	165.6	301.1
Y	33.7	35.8	28	33.4	18.7	19.7	32.3	25.5	24.3	21.5	15.3	8.5
Zr	104.5	87.5	78	78.3	47.2	58.2	98.4	60.8	63.3	56.7	30.2	10.2
Nb	3.8	4.5	2.3	0.9	1.2	1	2.1	1.3	3.0	2.6	0.9	0.5
Ba	97	60	138.9	112.6	32	32	60	29	77	90	32.2	33
Ta	0.3	0.3	0.2	0.2	0.05	0.05	0.1	0.08	0.1	0.1	0.8	LDL
Th	0.8	0.8	1.3	0.5	0.1	0.1	0.3	0.2	0.8	1.5	0.4	0.16
Hf	3.4	2.9	2.2	2.7	1.5	1.3	2.9	1.8	2.1	1.5	1	0.2
U	0.4	0.2	0.4	LDL	LDL	LDL	0.2	0.1	0.3	0.6	0.3	LDL
La	6.2	3.6	5.9	2.6	2.3	2	4.4	2.9	8.4	11	1.6	1.7
Ce	16.4	8.4	15.3	8.6	6.2	7.6	14.2	9.5	13	19.7	4.3	3.7
Pr	2.6	1.82	2.26	1.65	1.13	1.28	2.35	1.56	3.57	3.1	0.71	0.58
Nd	12.9	10.7	11.1	10.3	6.1	9.5	12.2	8.7	17	13.9	3.4	3.3
Sm	3.89	3.76	3.1	3.8	1.92	2.57	3.94	2.79	4.14	3.19	1.2	1.08
Eu	1.27	1.39	1.1	1.46	0.81	0.95	1.46	1.17	1	0.82	0.59	0.56
Gd	4.89	5.24	3.92	4.95	2.65	2.99	5.28	3.96	4.06	3.41	1.96	1.27
Tb	0.93	0.97	0.65	0.93	0.52	0.57	0.94	0.71	0.73	0.57	0.38	0.25
Dy	5.8	6.12	4.31	6.31	3.08	3.79	5.39	3.92	4.47	3.55	2.5	1.43
Ho	1.23	1.32	0.97	1.33	0.69	0.76	1.12	0.88	0.85	0.74	0.52	0.33
Er	3.51	3.83	2.91	3.91	2.02	2.29	3.43	2.58	2.32	2	1.69	0.89
Tm	0.55	0.56	0.44	0.57	0.32	0.29	0.51	0.40	0.35	0.3	0.22	0.14
Yb	3.39	3.47	2.57	3.31	1.9	2.14	3.15	2.40	2.14	1.79	1.36	0.92
Lu	0.51	0.53	0.4	0.49	0.29	0.26	0.49	0.37	0.31	0.28	0.24	0.14
La/Yb_{cn}	1.31	0.74	1.65	0.56	0.87	0.67	1	0.87	2.82	4.41	0.84	1.33
La/Sm_{cn}	1.03	0.62	1.15	0.44	0.77	0.5	0.72	0.67	1.31	2.23	0.86	1.02
Gd/Yb_{cn}	1.19	1.25	1.26	1.24	1.15	1.16	2.63	2.42	1.57	1.58	1.19	1.14
$(Eu/Eu^*)_{cn}$	0.89	0.96	0.92	1.03	1.1	1.05	0.98	1.08	0.75	0.76	1.18	1.46
Al_2O_3/TiO_2	12.55	9.23	12.90	10.48	14	14	10	12	16	29	29	87
Zr/Y	3.1	2.44	2.79	2.34	2.5	3.0	3.05	2.38	2.60	1.97	1.97	1.20
Ti/Zr	75	103	87	110	130	111	101	125	40	53	115	135
$(Nb/Nb^*)_{pm}$	0.06	0.13	0.02	0.06	0.42	0.40	0.13	0.18	0.04	0.01	0.11	0.15
$(Zr/Zr^*)_{pm}$	0.10	0.10	0.11	0.09	0.19	0.11	0.10	0.12	0.04	0.06	0.35	0.14
$(Ti/Ti^*)_{pm}$	0.08	0.08	0.13	0.08	0.21	0.17	0.11	0.15	0.04	0.08	0.20	0.21

Notes: $Eu/Eu^* = (Eu)_{cn}/[(Sm)_{cn} + (Gd)_{cn}]^{1/2}$; $Nb/Nb^* = Nb_{pm}/(Th_{pm} \times La_{pm})$; $Ti/Ti^* = Ti_{pm}/(Tb_{pm} \times Dy_{pm})$; $Zr/Zr^* = Zr_{pm}/(Nd_{pm} \times Sm_{pm})$.

moderate to large negative Nb, Ti, and Zr anomalies; and no Eu ($Eu/Eu^* = 0.96–1.12$) anomalies (Fig. 11e–f and Table 2).

4.2.4. Mafic granulites

Mafic granulites are chemically very similar to porphyroblastic amphibolites. They are compositionally uniform in SiO_2, Fe_2O_3, CaO, MgO, Al_2O_3 and TiO_2 contents, while their Mg# range from 49 to 60. There is a large variation in Ni, and moderate variations in Co, V, Zr, Y and REE concentrations (Table 2). The Al_2O_3/TiO_2 ratios are sub-chondritic, whereas the Ti/Zr ratios are sub-chondritic to super-chondritic. In addition, the Zr/Y ratios are super-chondritic (Table 2 and Online Table 2). On chondrite and primitive mantle-normalized diagrams they have: (1) slightly depleted LREE patterns ($La/Sm_{cn} = 0.67–0.98$); flat to slightly fractionated HREE patterns; large negative Nb, Ti, and Zr anomalies; and no Eu anomalies (Fig. 11g–h and Table 2).

4.2.5. Mafic–ultramafic cumulates

The mafic–ultramafic cumulates were divided into two groups: (a) those with pyroxene rich-cumulates and (b) those with plagioclase rich-cumulates. The first show variable SiO_2, Fe_2O_3 and CaO; high MgO (16.3–19.2 wt.%); and low Al_2O_3 and TiO_2 contents. Their Mg# range from 76 to 80. Additionally, the first group has high Ni (423–546 ppm) and Cr (1608–3770 ppm) and moderate Co, V, Zr, Y and REE contents (Table 2 and Online Table 2). The Al_2O_3/TiO_2

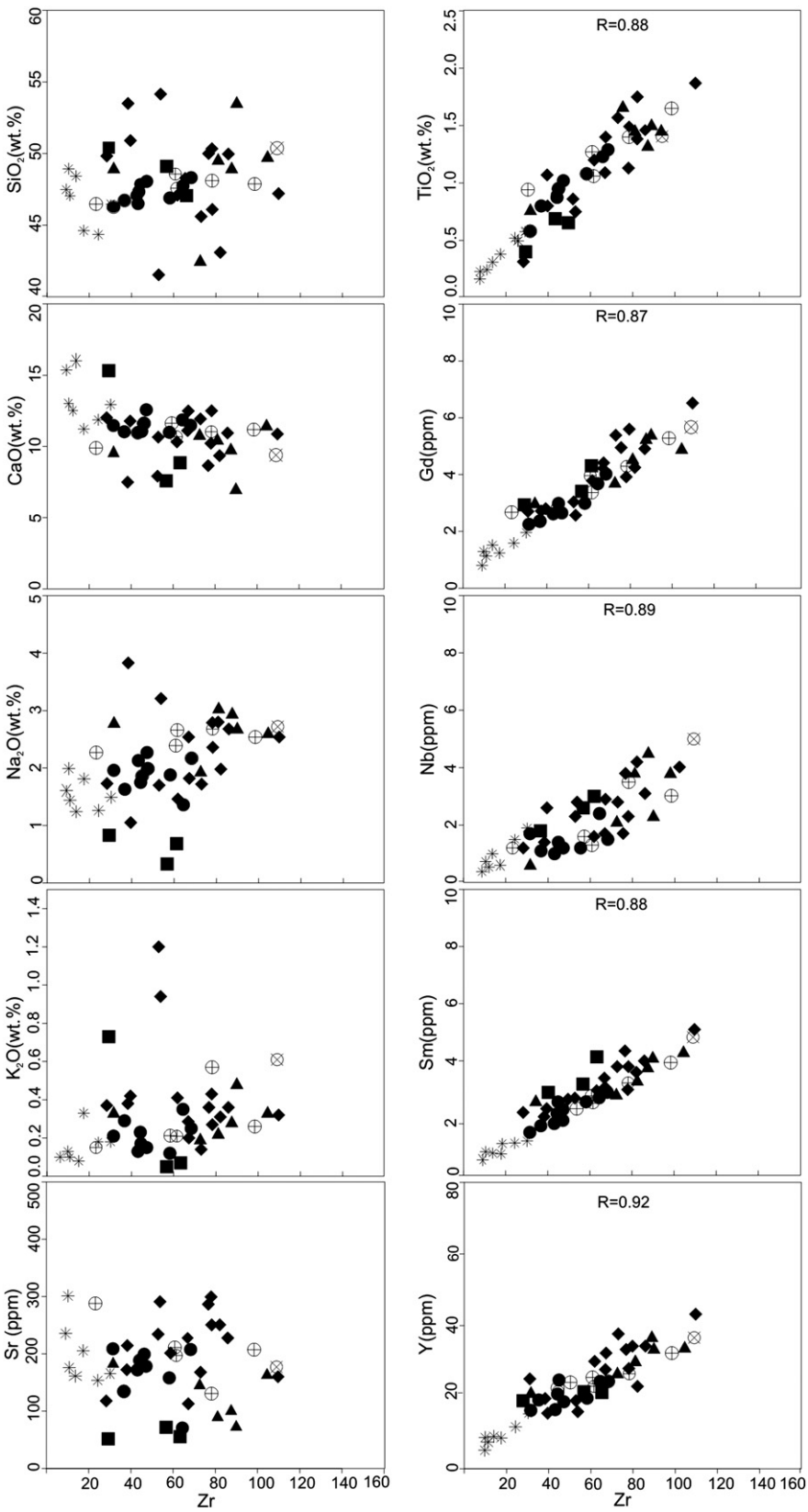

Fig. 10. Variation diagrams for a selected element plotted against the immobile element, Zr. Symbols: 4 — fine-grained amphibolite; ♦ — amphibole rich-amphibolite; ● porphyroblastic amphibolite; ⊕ — mafic granulite; ∗ — plagioclase cumulus; ■ pyroxene cumulus; ⊗ — gabbro.

(13–16) and Ti/Zr (40–82) ratios are sub-chondritic, whereas the Zr/Y (1.5–2.6) ratios are sub-chondritic to super-chondritic. In addition, they display the following trace element characteristics in chondrite and primitive mantle-normalized diagrams: (1) LREE enriched patterns; moderately fractionated HREE patterns; large negative Nb, Ti, and Zr anomalies; and variably negative Eu anomalies (Table 2).

In comparison to pyroxene rich-cumulates, plagioclase rich-cumulates have similar SiO_2 but lower Fe_2O_3, MgO and TiO_2 and

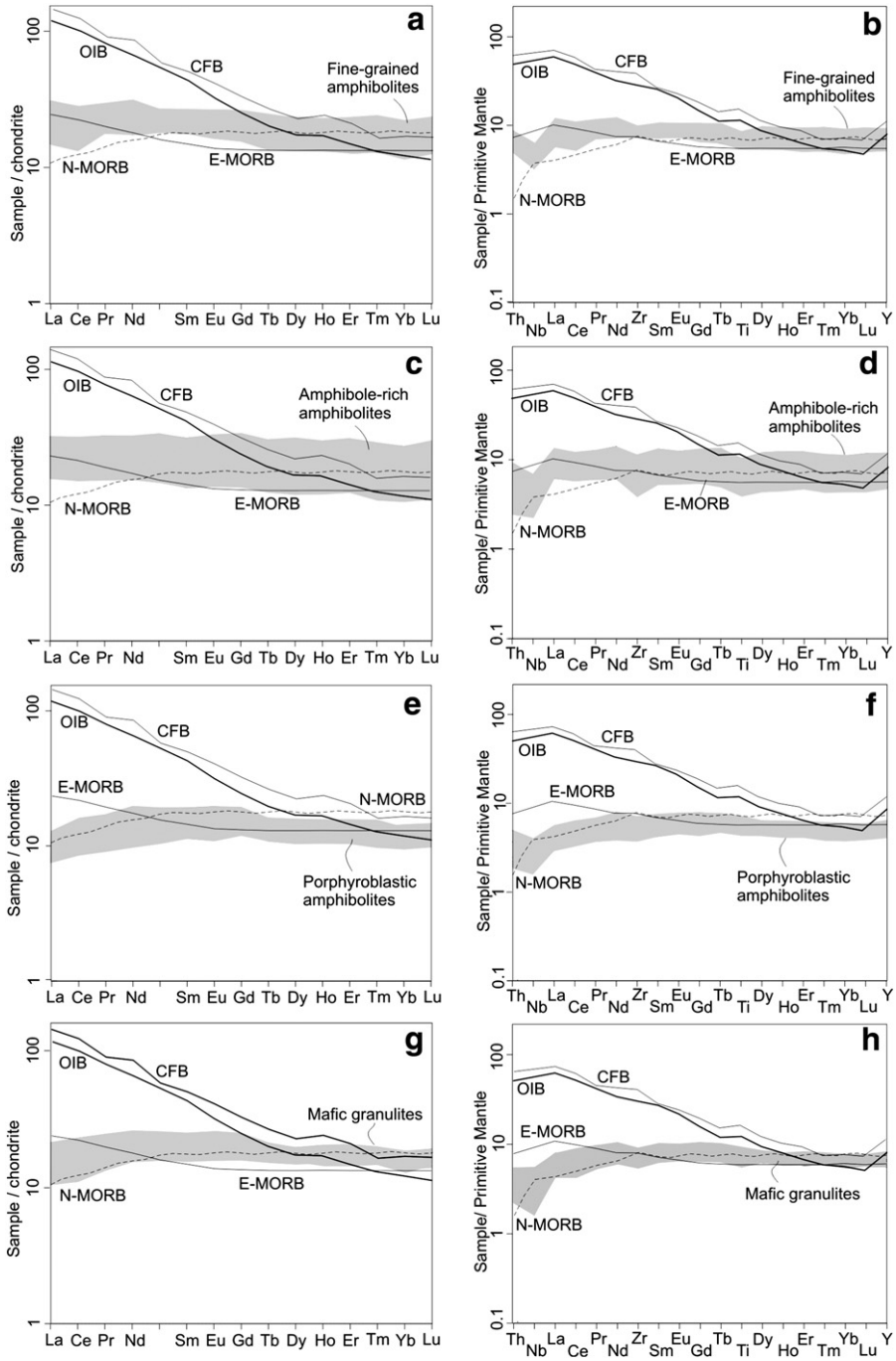

Fig. 11. Chondrite-normalized REE and primitive mantle-normalized trace element patterns for mafic–ultramafic rocks. Chondrite normalization values are from Sun and McDonough (1989) and primitive mantle normalization values are from Hofmann (1988). N-MORB, E-MORB, OIB e CFB standards for comparison.

higher CaO and Al_2O_3 contents. Their Mg-numbers are slightly lower, ranging from 68 to 79. They display lower and variable Ni and Cr; low Co, V, and Zr; and variable Y contents (Table 2 and Online Table 2). The plagioclase rich-cumulates also have Al_2O_3/TiO_2 and Ti/Zr ratios that are super-chondritic, while the Zr/Y ratios are sub-chondritic.

On chondrite and primitive mantle-normalized diagrams, they have: (1) near-flat LREE patterns; slightly fractionated HREE patterns; pronounced negative Nb, Ti, and Zr anomalies; and moderately positive Eu anomalies (Table 2 and Online Table 2).

5. Geodynamic setting and petrogenesis

This study documents an association of mafic–ultramafic rocks that were deformed, metasomatized and metamorphosed during the development of an accretionary orogen. Its extrusive rocks are predominantly massive basalts (now fine-grained amphibolites). Together with porphyroblastic amphibolites, mafic granulites, ultramafic rocks, chert, BIFs, pelites, psammitic and smaller proportion calc-silicate rocks, this association represents an ophiolitic sequence. While the rocks do not outcrop continuously due to the thick weathered material and the development of lateritic crusts in the tropical weather conditions that are characteristic of the hot and humid Amazon region, a continuous phase of deformation, including isoclinal folding and metamorphism of the granulite-amphibolite facies have been recognized. However, amygdaloidal, cumulate and layered magmatic structures have been preserved in areas of low strain in the rocks that comprise the Trincheira Complex. The presence of these primary structures provides a unique opportunity to study the characteristics of hydrothermal alteration, magma

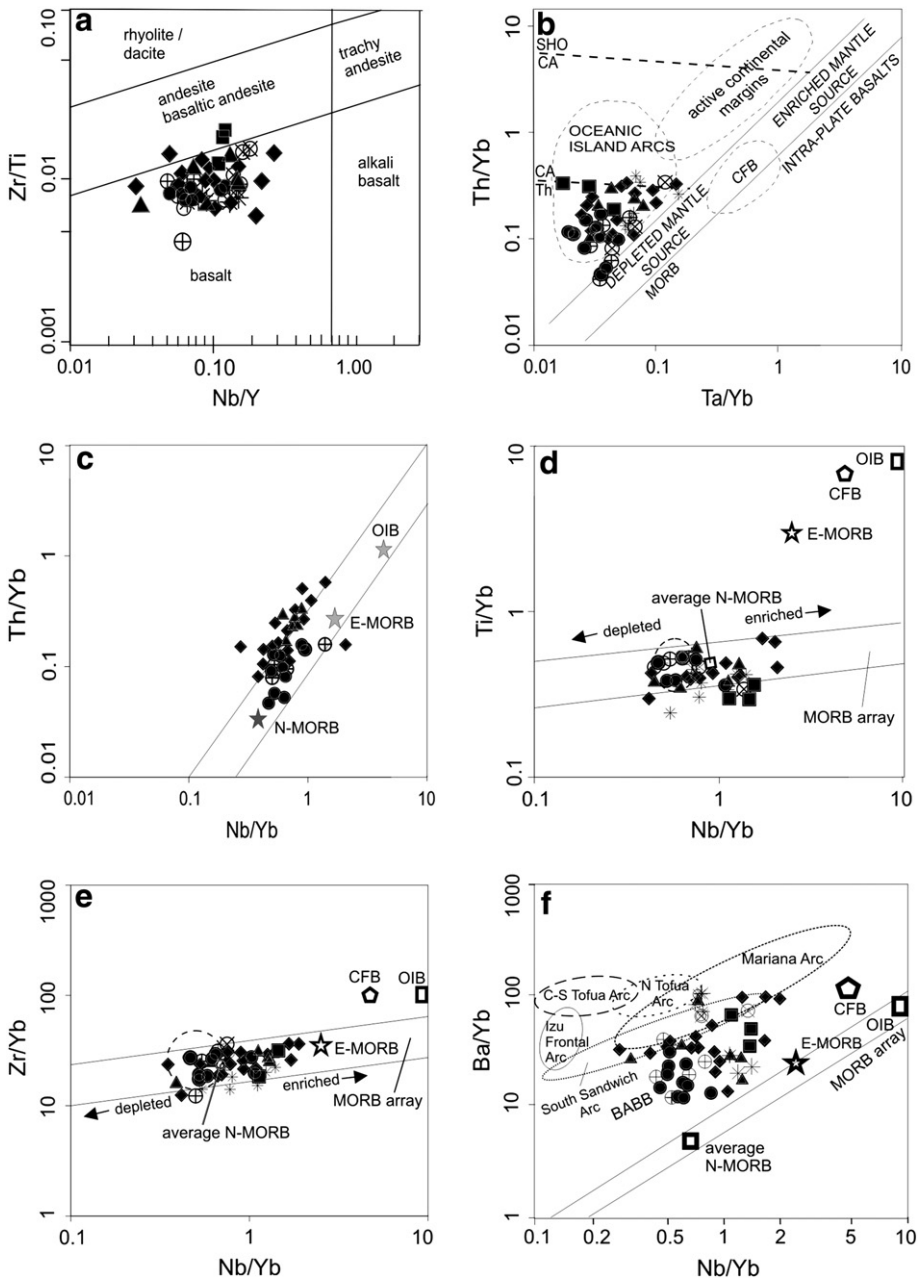

Fig. 12. (a) Distribution of mafic–ultramafic rocks of the Trincheira Complex, which occupy predominantly the field of basalts. Diagram modified from Pearce, 1996; (b) Th/Yb versus Ta/Yb and (c) Nb/Yb plots to show the distribution of the mafic–ultramafic rocks of the Trincheira Complex compared with oceanic island basalts (OIB), basalts derived from depleted sources (MORB), enriched source (E-MORB), uncontaminated intracontinental plate basalts and basalts derived from active continental margins; (d–e) distribution of samples of mafic granulites and porphyroblastic amphibolites (dotted area) in the field delimited by back-arc basin basalts of Pearce and Peat (1995); (f) distribution of samples of porphyroblastic amphibolites and mafic granulites in the field of BABB; and fine-grained amphibolites and amphibole rich-amphibolites in arc environment defined by Pearce and Stern (2006).

genesis and geodynamic processes. In this way, magmatism in the back-arc basins appears to result from the same basic processes responsible for the production of mid-ocean ridge basalt (MORB), or rifting of the oceanic crust leads to the passive uplift and partial melting of the upper mantle. Therefore, in many compositional aspects, back-arc basin basalts (BABB) are similar to MORBs (Taylor and Martinez, 2003). In detail, however, the evolution of back-arc basins is closely related to the processes of plate subduction, and the magmatism of back-arc basins is chemically and physically more variable than the magmatism generated at mid-ocean ridges. Specifically, the center of the spreading back-arc basin is positioned relatively close to active volcanic arcs and trench, and thus they are inevitably influenced by "components" derived from the subducted slab. It is believed that the water derived from the dehydration of the subducted slab should be the main carrier of such components, and many studies have shown that the role and methods of transport by water and fusion differ systematically, mainly in back-arc basins and on mid-ocean ridges (Pearce and Stern, 2006).

The mafic–ultramafic rocks of Trincheira Complex represent mid-ocean ridge basalts (MORB) and island arc tholeiites. In general, the HFSE concentrations in the volcano-plutonic rocks of the Trincheira Complex are lower than those of modern N-MORBs (Table 2), indicating that the Mesoproterozoic mantle that originated the rocks of Trincheira Complex was more depleted in these elements when compared to modern N-MORB upper mantle. In addition, the mafic–ultramafic rocks have low Ni contents, which suggests that they are not derived from primary magmas that have undergone the fractionation of olivine.

The chemical characteristics presented above indicate that fine-grained amphibolites and amphibole rich-amphibolites, on the one

hand, and porphyroblastic amphibolites and mafic granulites, on the other, show specific characteristics of trace elements and REE, suggesting different sources and petrogenetic origins for these spatially and temporally associated groups of rocks. However, as a whole, the chemical differences when comparing the concentrations of REE and trace elements are subtle. Both groups show collinear trends of trace elements, HFSE, REE and transition metals in Zr variation diagrams showing broadly similar compositions (Fig. 10 and Table 2). However, when observed in detail, there are small differences between the groups formed by fine-grained amphibolites and amphibole rich-amphibolites. These trace element patterns show weak enrichment in LREE, enrichment in LILE (e.g., Rb, Ba, Sr and K) and a strong depletion of HFSE (e.g., negative Nb, Ti and Zr anomalies) consistent with a subduction zone geochemical signature (Saunders et al., 1991; Hawkesworth and Hooper, 1993; Pearce and Peate, 1995).

Additionally, the strong signature of the arc is evidenced by the enrichment of Pb and LILE relative to HFSE, which would involve a substantial amount of the subduction components having been present in the mantle source during the generation of fine-grained amphibolites and amphibole rich-amphibolites.

The igneous activity in island-arcs and back-arc basins are similar in some respects, although arc crustal growth is dominantly thickening due to the accumulation of lava and intrusion by magmatic underplating, while the crustal growth in the back-arc basin is caused by seafloor spreading (Hawkins et al., 1994). Flows of the intra-oceanic arc are characterized by high Ba/La and low Ce/Pb, combined with low $(La/Yb)_{cn}$ and moderate K/Rb ratios.

When studying suites of subduction-related basalts, Pearce (1982) found bivariate diagrams based on trace elements ratios to be useful in separating subduction-related from mantle components in the petrogenesis of the magmas. Fig. 12b is such a diagram, showing the variations of Th/Yb versus those of Ta/Yb. Compared to mid-ocean ridge basalts (MORB) and uncontaminated intra-plate basalts, the majority of the Trincheira Complex data plot within the field defined by oceanic island-arc basalts, where fine-grained amphibolites and amphibole-rich amphibolites show higher Th/Yb ratios in relation to mafic granulites and porphyroblastic amphibolites, presumably reflecting the influence of subduction-zone fluids enriched in Th in their petrogenesis. In addition, the MORB affinity for mafic granulites and porphyroblastic amphibolites and the island arc-related character of the fine-grained amphibolites and amphibole-rich amphibolites are well demonstrated on a Nb/Yb–Th/Yb diagram (Fig. 12c). The MORB and OIB domains form a diagonal mantle array on this discriminant diagram, whereas magmas that have a subduction component are displaced to higher Th/Yb values.

In the remaining two discriminant diagrams (HFSEs), mafic granulites and porphyroblastic amphibolites show weak depletion in LREE and variable degrees of depletion of HFSE (Nb, Ti, and Zr), as shown in the diagrams of conservative elements in subduction systems (Pearce and Peate, 1995) (Fig. 12d and e) and similarly to modern back-arc basin basalts (BABB). Likewise, the diagrams show the influence of components derived from the subducted slab as enrichments in Rb, Ba and Sr, but lower quantities to fine-grained amphibolites and amphibole rich-amphibolites. The elements with low ionic potential are most readily mobilized by a fluid phase, and their enrichment in island-arc basalts has been attributed to the metasomatism of their mantle source region by hydrous fluids derived from the subducted oceanic crust.

On Fig. 12f most samples of mafic granulites and porphyroblastic amphibolites of the Trincheira Complex are plotted in the BABB field, while the fine-grained amphibolites and amphibole-rich amphibolites are distributed in the field delimited by the rocks' arc setting, some of which are transitional to BABB.

5.1. Trincheira Complex: implications for Columbia supercontinent

Ophiolites represent fragments of upper mantle and oceanic crust that were incorporated into mountain belts during subduction–accretion events. They are generally found along suture zones in both collisional-type and accretionary-type orogenic belts that mark major boundaries between amalgamated plates or accreted terranes (Lister and Forster, 2009). Thus, subduction-related lithosphere and ophiolites develop during the closure of ocean basins. Some of the main processes of ophiolite genesis and emplacement overlap in time with major orogenic events that led to the construction of supercontinents. Likewise, the formation of supercontinents is commonly explained by the coalescence of numerous continental fragments (cratons, microcontinents) along sutures formed by the closure of ocean basins between them (Unrug, 1992). Examples of Phanerozoic orogenic events include the Famatian and Caledonian (Baltica–Laurentia collision) orogens in the early Paleozoic, which collectively formed the Gondwana and Laurasia supercontinents, and the Appalachian–Hercynian and Altaid–Uralian orogens later in the Paleozoic, which built the Pangea supercontinent (Moores et al., 2000). These Phanerozoic ophiolites commonly show MORB to IAT geochemical affinities. Similar tectonic processes probably occurred in the Proterozoic through which supercontinents were formed by the amalgamation of pre-existing continental masses, with the concomitant disappearance of the intervening oceans.

Many alternative configurations have been proposed for the Paleo- to Mesoproterozoic Columbia supercontinent, although its configuration is based on the available paleomagnetic data that are normally affected by large uncertainties, especially regarding paleolongitudes (Bispo-Santos et al., 2008; D'Agrella-Filho et al., 2012; Hou et al., 2008; Johansson, 2009; Kusky et al., 2007; Meert, 2002; Pesonen et al., 2003; Rogers and Santosh, 2002; Zhao et al., 2002, 2004, 2006). The possibility that this phase of Earth history involved assembly of a supercontinent was suggested by the abundance of orogenic activity between about 1.8 Ga and 1.6 Ga (Rogers and Santosh, 2004). According to previous work there is considerable to evidence show that, following its assembly at circa 1.8 Ga, the Columbia supercontinent underwent long-lived (1.8–1.2 Ga) accretion along some of its continental margins. In our view, the configuration of Columbia implies subduction-related outgrowth along the southwestern margin of the Amazon craton around 1.47 to 1.35 Ga.

The age and the character of the Paleo- to Mesoproterozoic belts of SW Amazon craton permit correlation with the Svecofennian domain and the Transcandinavian igneous belt within Baltica and also with the Mid-continent region of Laurentia. These similarities led several authors to propose a possible link between the north-northeastern Amazon craton and southwestern Baltica (e.g., Cordani et al., 2009; Geraldes et al., 2001; Johansson, 2009; Sadowski and Bettencourt, 1996; Zhao et al., 2002, 2004, 2006). Both cratons show subduction-related accretionary belts, which evolved throughout the Mesoproterozoic at the margins of such contiguous cratonic nuclei. In contrast, paleomagnetic data presented by Bispo-Santos et al. (2008) and Pesonen et al. (2003) indicate that these cratons were not linked. New paleomagnetic data from D'Agrella-Filho et al. (2012) provides a test for the longevity of the previously proposed Columbia paleogeography and led the authors to suggest that the break-up of Columbia must have taken place before 1420 Ma. But the paleogeography of the Amazon craton closer to Baltica in the Mesoproterozoic is also allowed by the paleomagnetic data.

In this work, the recognition of the Trincheira ophiolite and suture significantly changes views on the evolution of the southern margin of the Amazon craton, and how it can influence the global tectonics and the reconstruction of the continents. It also modifies current ideas about Amazonia's role in plate reconstructions of the Columbia supercontinent.

The relation of Amazonia, Laurentia and Baltica is a key issue for the continental reconstruction of the Mesoproterozoic. The eastern margin of Laurentia was a site of continued continental-margin orogeny with subduction-related outgrowth. This outgrowth is well shown by the Yavapai, Labradorian and Mazatzal provinces of southwestern United States, which developed from ~1.8–1.5 Ga. The western part of the Amazon craton also underwent marginal growth from

~1.8–1.3 Ga, when subduction beneath Amazonia progressively formed the Rio Negro–Juruena and Alto Guaporé belts. The Alto Guaporé belt is partly formed by the small Paraguá crustal block that possibly was originally part of older continents. From ~1.47 Ga to 1.35 Ga compressional orogeny occurred along the southwestern margin of the Amazon craton, subduction below Amazonia followed by granulite-facies metamorphism. In our view, the juvenile rocks of the Trincheira Complex and related magmatic arcs (Rio Alegre terrane), dated between 1470 and 1350 Ma, could well correspond to the accreted intra-oceanic material that attests the existence of a large ocean that separated Amazonia from Laurentia. The final closure of the ocean was marked by the accretion of the Paraguá microcontinent around 1.35 Ga. Thus, the discovery of the Mesoproterozoic Trincheira ophiolite supplies important evidence for the existence of an oceanic basin on the southern margin of the Amazon craton, and demonstrates that the Amazon craton had its growth, first by accretion of oceanic crust and later by collision with Paraguá Block on its southwestern margin. Additionally, petrotectonic studies in the Trincheira Complex are consistent with a belt that grew along a northward dipping subduction zone through accretion of oceanic island arc and back-arc. Therefore, growth of the southwestern Amazon craton was through subduction-related magmatism during continued accretion of juvenile material in Mesoproterozoic times. This implies that in the Columbia supercontinent, at ~1.5–1.3 Ga, the southern margin of the proto-Amazon craton was not connected to any other continent, but was bordered by an active supra-subduction zone. This scenario can be related to the reconstruction of Paleo-Mesoproterozoic supercontinent Columbia proposed by Zhao et al. (2004). In contrast, D'Agrella-Filho et al. (2012), based on paleomagnetic data proposed the Columbia reconstruction at ~1460 Ma and suggest that there was no major ocean between the Paraguá Block and proto-Amazon craton at roughly this time. However, this new scenario for Mesoproterozoic Columbia supercontinent proposed by the authors mentioned above, does not address the oceanic lithosphere that existed between the proto-Amazon craton and Paraguá Block, represented by the Trincheira Complex.

Details on the life cycle duration of Columbia have yet to be reliably established. Therefore, any attempt to reconstruct the supercontinent must take into account the existence of oceanic crust during the Mesoproterozoic in the southern border of the proto-Amazon craton. Therefore, it is necessary paleomagnetic studies in this important belt of mafic–ultramafic rocks to better understand the paleogeographic reconstruction for the supercontinent that preceded Rodinia.

At about 1.35–1.25 Ga, in South America, Mesoproterozoic rapakivi granites younger than 1.35 Ga, such as the Teotônio Intrusive Suite (~1.34 Ga), Santo Antônio Intrusive Suite (~1.36 Ga), Alto Candeias Intrusive Suite (1.33 Ga), and associated intracontinental rifting represented by sedimentary and igneous rocks of the Nova Brasilândia Group (>1.25 Ga) (Bettencourt et al., 1999, 2010; Rizzotto, 1999), coupled with the intrusions of many mafic dike swarms and associated basaltic extrusions in other places worldwide marks a major episode of plate-wide extension and rifting, and signaled the final breakup of the Columbia supercontinent.

6. Conclusions

The Trincheira mafic–ultramafic Complex is composed of several disrupted, highly dismembered imbricate thrust slices forming an incomplete ophiolitic sequence. The sequence includes layered mafic–ultramafic cumulates and intrusive mafic–ultramafic and extrusive mafic rocks with an interbedded sedimentary clast-chemical sequence. The deformation is heterogeneous, as indicated by highly deformed zones adjacent to areas with poorly developed foliation or a partially preserved primary texture. Based on the characteristics of the field, petrographic, geophysical and geochemical, was suggested a division of the complex into three units: a) Lower Unit: layered mafic–ultramafic rocks (granulite-facies metamorphism): mafic granulites which has as protolith olivine–orthopyroxenite, bronzitite, and websterite; b) Intermediate Unit: intrusive mafic rocks (amphibolite-facies metamorphism): banded amphibolites that has as protolith norite, gabbronorite, gabbro, anorthosite, gabbroanorthosite and rare plagiogranite; and c) Upper Unit: extrusive mafic rocks (amphibolite-facies metamorphism): fine-grained amphibolites (basalt massive and pillow) with intercalations of sedimentary sequence consisting of metachert (BIFs), calc-silicate rocks and aluminous schist/quartzite.

Metamorphism is pervasive. It attained temperatures of 820–853 °C and 680–720 °C for mafic granulites and amphibolites, respectively, and a pressure of 6.8 kbar.

The presence of layers of chert, BIFs and amygdaloidal basalt is consistent with an oceanic setting for the eruption of volcanic rocks and associated intrusions. Therefore, the analysis of the new geological and geochemical data presented here indicates that the mafic–ultramafic rocks of the Trincheira Complex have a hybrid mixture of MORB-like and arc-like element signatures and are part of a supra-subduction system formed by an intra-oceanic island arc and back-arc basin. Its fine-grained amphibolites and amphibole rich-amphibolites have a closer similarity to arc tholeiites, while the mafic granulites and porphyroblastic amphibolites are chemically compatible with the modern BABB. The participation of a subduction component is implicit in the high Rb, Sr, Ba and K contents in proportion to immobile elements (HFSE), such as Nb and Ta. The water derived from the dehydration of the subducted slab is the main carrier of such components. In summary, the behavior of trace elements suggests that the mantle source of lavas and intrusive of Trincheira Complex was affected by subduction components. This relict oceanic crust may represent a fragment of oceanic lithosphere that obducted during what remained of the collision of the Paraguá block with the western border of the Amazon craton during the Middle Mesoproterozoic period, between 1470 and 1350 Ma. This tectonic model explains many previously enigmatic features of the Precambrian history of this key craton, and discusses its role in the reconstruction of the Columbia supercontinent.

Acknowledgments

This work was supported by CNPq (Conselho Nacional de Desenvolvimento Científico e Tecnológico) grant 140917/2008-0. The authors thank Dr. Janet Muhling from the Centre for Microscopy, Characterisation and Analysis (CMCA) at the University of Western Australia for her assistance in the microprobe work and the CPRM/Geological Survey of Brazil for its assistance in the fieldwork and access to the analytical preparation. The insightful comments from editor and of the two reviewers were greatly appreciated and as they helped improve the final version of this manuscript.

Appendix A. Supplementary data

Supplementary data to this article can be found online at doi:10.1016/j.lithos.2012.05.027.

References

Arndt, N.T., 1994. Archean komatiites. In: Condie, K.C. (Ed.), Archean Crustal Evolution. Elsevier, Amsterdam, pp. 11–44.

Arndt, N.T., Albarbde, E., Nisbet, E.G., 1997. Mafic and ultramafic magmatism. In: de Wit, M.J., Ashwal, L.D. (Eds.), Greenstone Belts. Clarendon Press, Oxford, pp. 233–254.

Barrett, T.J., MacLean, W.H., 1994. Chemostratigraphy and hydrothermal alteration in exploration for VHMS deposits in greenstones and younger volcanic rocks. In: Lenz, D.R. (Ed.), Alteration and Alteration Processes Associated with Ore-forming Systems. Geological Association of Canada, Short Course Notes, vol. 11, pp. 433–467.

Bettencourt, J.S., Tosdal, R.M., Leite Jr., W.B., Payolla, B.L., 1999. Mesoproterozoic rapakivi granites of Rondonia Tin Province, southwestern border of the Amazonian Craton, Brazil—I. Reconnaissance U–Pb geochronology and regional implications. Precambrian Research 95, 41–67.

Bettencourt, J.S., Leite Jr., W.B., Ruiz, A.S., Matos, R., Payolla, B.L., Tosdal, R.M., 2010. The Rondonian–San Ignacio Province in the SW Amazonian Craton: an overview. Journal of South American Earth Sciences 29, 28–46.

Bhattacharyya, C., 1971. An evaluation of the chemical distinctions between igneous and metamorphic orthopyroxenes. American Mineralogist 56, 499–506.
Bispo-Santos, F., D'Agrella-Filho, M.S., Pacca, I.I.G., Janikian, L., Trindade, R.I.F., Elming, S., Silva, J.A., Barros, M.A.S., Pinho, F.E.C., 2008. Columbia revisited: paleomagnetic results from the 1790 Ma Colíder volcanics (SW Amazonian Craton, Brazil). Precambrian Research 164, 40–49.
Boger, S.D., Raetz, M., Giles, D., Etchart, E., Fanning, C.M., 2005. U–Pb age data from the Sunsas region of eastern Bolivia, evidence for the allochtonous origin of the Paraguá Block. Precambrian Research 139, 121–146.
Brunsmann, A., Franz, G., Erzinger, Landwehr, D., 2000. Zoisite- and clinozoisite-segregations in metabasites (Tauern Window, Austria) as evidence for high-pressure fluid–rock interaction. Journal of Metamorphic Geology 18, 1–21.
Cann, J.R., 1970. Rb, Sr, Y, Zr and Nb in some ocean floor basaltic rocks. Earth and Planetary Science Letters 10, 7–11.
Cawood, P.A., Nemchin, A.A., Strachan, R., Prave, T., Krabbendam, M., 2007. Sedimentary basin and detrital zircon record along East Laurentia and Baltica during assembly and breakup of Rodinia. Journal of the Geological Society 164, 257–275.
Cawood, P.A., Kroner, A., Collins, W.J., Kusky, T.M., Mooney, W.D., Windley, B.F., 2009. Accretionary orogens through Earth history. Geological Society, London, Special Publications 318, 1–36.
Cordani, U.G., Teixeira, W., 2007. Proterozoic accretionary belts in the Amazonian Craton. In: Hatcher, R.D., Carlson Jr., M.P., McBride, J.H., Martinez Catalan, J.R. (Eds.), 4-D framework of continental crust: Geological Society of America Memoir, 200, pp. 297–320.
Cordani, U.G., Teixeira, W., D'Agrella-Filho, M.S., Trindade, R.I., 2009. The position of the Amazonian Craton in supercontinents. Gondwana Research 15, 396–407.
D'Agrella-Filho, M.S., Tohver, E., Santos, J.O.S., Elming, S.A., Trindade, R.I.F., Pacca, I.G., Geraldes, M.C., 2008. Direct dating of paleomagnetic results from Precambrian sediments in the Amazon Craton: evidence for Grenvillian emplacement of exotic crust in SE Appalachians of North America. Earth and Planetary Science Letters 267, 188–199.
D'Agrella-Filho, M.S., Trindade, R.I.F., Elming, S., Teixeira, W., Yokoyama, E., Tohver, E., Geraldes, M.C., Pacca, I.I.G., Barros, M.A.S., Ruiz, A.S., 2012. The 1420 Ma Indiavaí Mafic Intrusion (SW Amazonian Craton): paleomagnetic results and implications for the Columbia supercontinent. Gondwana Research. http://dx.doi.org/10.1016/j.gr.2012.02.022.
Dalziel, I.W.D., 1991. Pacific margins of Laurentia and East-Antarctica–Australia as a conjugate rift pair: evidence and implications for an Eocambrian supercontinent. Geology 19, 598–601.
Dilek, Y., Furnes, H., 2009. Structure and geochemistry of Tethyan ophiolites and their petrogenesis in subduction rollback systems. Lithos 113, 1–20.
Dilek, Y., Thy, P., Hacker, B., Grundvig, S., 1999. Structure and petrology of Tauride ophiolites and mafic dike intrusions (Turkey): implications for the Neo-Tethyan ocean. Geological Society of America Bulletin 111, 1192–1216.
Frei, R., Rosing, M., Waight, T.E., Krogstad, E.J., Storey, M., Ulfbeck, D.G., Albarde, E., 2002. Hydrothermal–metasomatic and tectono-metamorphic processes in the Isua greenstone belt (West Greenland): a multi-isotopic investigation of their effects on the Earth's oldest oceanic crustal sequence. Geochimica et Cosmochimica Acta 66, 467–486.
Geraldes, M.C., Van Schmus, W.R., Condie, K.C., Bell, S., Teixeira, W., Babinski, M., 2001. Proterozoic Geologic Evolution of the SW part of the Amazonian Craton in Mato Grosso State, Brazil. Precambrian Research 111, 91–128.
Hawkesworth, C.J., Hooper, P.R., 1993. Isotopic and geochemical constraints on the origin and evolution of the Columbia River Basalt. Journal of Petrology 34, 1203–1246.
Hawkins, J.W., Bloomer, S.H., Evans, C.A., Melchior, J.T., 1994. Evolution of intra-oceanic arc–trench systems. Tectonophysics 102, 174–205.
Hoffman, P.F., 1991. Did the breakout of Laurentia turn Gondwanaland inside-out? Science 252, 1409–1412.
Hofmann, A.W., 1988. Chemical differentiation of the Earth: the relationships between mantle, continental crust, and oceanic crust. Earth and Planetary Science Letters 90, 297–314.
Holland, T.J.B., Blundy, J., 1994. Non-ideal interactions in calcic amphiboles and their bearing on amphibole-plagioclase thermometry. Contributions to Mineralogy and Petrology 116, 433–447.
Hou, G., Santosh, M., Qian, X., Lister, G.S., Li, J., 2008. Configuration of the Late Paleoproterozoic supercontinent Columbia: insights from radiating mafic dyke swarms. Gondwana Research 14, 395–409.
Ishikawa, T., Nagaishi, K., Umino, S., 2002. Boninitic volcanism in the Oman ophiolite: implications for thermal conditions during transition from spreading ridge to arc. Geology 30, 899–902.
Jenner, G.A., Cawood, P.A., Rautenschlein, M., White, W.M., 1987. Composition of back-arc basin volcanics, Valu Fa Ridge, Lau Basin: evidence for a slab-derived component in their mantle source. Journal of Volcanology and Geothermal Research 32, 209–222.
Jochum, K.P., Arndt, N.T., Hofmann, A.W., 1991. Nb–Th–La in komatiites and basalts: constraints on komatiite petrogenesis and mantle evolution. Earth and Planetary Science Letters 107, 272–289.
Johansson, A., 2009. Baltica, Amazonia and the SAMBA connection — 1000 million years of neighbourhood during the Proterozoic? Precambrian Research 175, 221–234.
Keppie, D., Dostal, J., Ortega-Gutiérrez, F., Lopez, R., 2001. A Grenvillian arc on the margin of Amazonia: evidence from the southern Oaxacan Complex, southern Mexico. Precambrian Research 112, 165–181.
Kusky, T.M., Li, J., Santosh, M., 2007. The Paleoproterozoic North Hebei Orogen: North China craton's collisional suture with the Columbia supercontinent. Gondwana Research 12, 4–28.
Leake, B.E., 1978. Nomenclature of amphiboles. American Mineralogist 63, 1023–1052.
Lister, G., Forster, M., 2009. Tectonic mode switches and the nature of orogenesis. Lithos 113, 274–291.
Litherland, M., Annels, R.N., Appleton, J.D., Berrange, J.P., Bloomfield, K., Darbyshire, D.P.F., Fletcher, C.J.N., Hawkins, M.P., Klinck, B.A., Mitchell, W.I., O'Connor, E.A., Pitfield, P.E.J., Power, G., Webb, B.C., 1986. The geology and mineral resources of the Bolivian Precambrian Shield. Overseas Memoir British Geological Survey 9 (153 pp.).
Litherland, M., Annels, R.N., Darbyshire, D.P.F., Fletcher, C.J.N., Hawkins, M.P., Klink, B.A., Mitchell, W.I., O'Connor, E.A., Pitfield, P.E.J., Power, G., Webb, B.C., 1989. The Proterozoic of eastern Bolivia and its relationship to the Andean mobile belt. Precambrian Research 43, 157–174.
Ludden, J.N., Gélinas, L., Trudel, P., 1982. Archean metavolcanics from the Rouyn–Noranda district, Abitibi greenstone belt, Québec. 2. Mobility of trace elements and petrogenetic constraints. Canadian Journal of Earth Sciences 19, 2276–2287.
Meert, J.G., 2002. Paleomagnetic evidence for a Paleo-Mesoproterozoic supercontinent Columbia. Gondwana Research 5, 207–215.
Moores, E.M., Kellogg, L., Dilek, Y., 2000. Tethyan ophiolites, mantle convection, and tectonic "historical contingency": a resolution of the "ophiolite conundrum. In: Dilek, Y., Moores, E.M., Elthon, D., Nicolas, A. (Eds.), Ophiolites and Oceanic Crust: New Insights from Field Studies and Ocean Drilling Program: Geological Society of America Special Paper, 349, pp. 3–12.
Murton, B.J., Peate, D.W., Arculus, R.J., Pearce, J.A., Van Der Laan, S.R., 1992. Trace-element geochemestry of volcanic rocks from Site 786: the Izu–Bonin forearc. In: Fryer, P., Pearce, J.A., Stokking, L.B., et al. (Eds.), Proceedings of the Ocean Drilling Program, Scientific Results 125, 211–235.
Pearce, J.A., 1982. Trace element characteristics of lavas from destructive plate boundaries. In: Thorpe, R.S. (Ed.), Andesites. John Wiley and Sons, pp. 525–548.
Pearce, J.A., Cann, J.R., 1973. Tectonic setting of basic volcanic rocks determined using trace element analyses. Earth and Planetary Science Letters 19, 290–300.
Pearce, J.A., Peate, D.W., 1995. Tectonic implications of the composition of volcanic arc magmas. Annual Review of Earth and Planetary Science 23, 251–285.
Pearce, J.A., Stern, J.R., 2006. The Origin of Back-arc Basin Magmas: Trace Element and Isotopic Perspectives. In: Christie, D.M., Fisher, C.R., Lee, S.-M., Givens, S. (Eds.), Back-arc spreading systems: geological, biological, chemical, and physical interactions: AGU monograph, American Geophysical Union. Geophysical Monograph, Washington DC, pp. 63–86.
Pearce, J.A., Van Der Laan, S.R., Arculus, R.J., Murton, B.J., Ishii, T., 1992. Boninite and harzburgite from Leg 125 (Bonin–Mariana forearc): a case study of magma genesis during the initial stages of subduction. In: Fryer, P., Pearce, J.A., Stokking, L.B., et al. (Eds.), Proceedings of the Ocean Drilling Program, Scientific. Texas A&M University, College Station, pp. 623–659.
Pesonen, L.J., Elming, S., Mertanen, S., Pisarevsky, S., D'Agrella-Filho, M.S., Meert, J.G., Schmidt, P.W., Abrahamsen, N., Bylund, G., 2003. Palaeomagnetic configuration of continents during the Proterozoic. Tectonophysics 375, 289–324.
Polat, A., Kerrich, R., Wyman, D.A., 1998. The late Archean Schreiber–Hemlo and White River–Dayohessarah greenstone belts, Superior Province: collages of oceanic plateaus, oceanic arcs, and subduction–accretion complexes. Tectonophysics 289, 295–326.
Polat, A., Hofmann, A.W., Rosing, M.T., 2002. Boninite-like volcanic rocks in the 3.7–3.8 Ga Isua greenstone belt, West Greenland: geochemical evidence for intra-oceanic subduction zone processes in the early Earth. Chemical Geology 184, 231–254.
Polat, A., Hofmann, A.W., Appel, P.W.U., 2004. Geochemical diversity in volcanic rocks of the 3.7–3.8 Ga Isua Greenstone belt, southwest Greenland: implications for mantle composition. In: Eriksson, P.G., Altermann, W., Nelson, D.R., Mueller, W.U., Catuneanu, O. (Eds.), Tempos and Events in Precambrian Time. Development in Precambrian Geology, vol.12. Elsevier, pp. 74–88.
Puchtel, I.S., Hofmann, A.W., Mezger, K., Jochum, K.P., Shchipansky, A.A., Samsonov, A.V., 1998. Oceanic plateau model for continental crustal growth in the Archaean: a case study from the Kostomuksha greenstone belt, NW Baltic Shield. Earth and Planetary Science Letters 155, 57–74.
Rizzotto, G.J., 1999. Petrologia e geotectônica do Grupo Nova Brasilândia, Rondônia. MSc. Dissertation. Federal University of Rio Grande do Sul. Porto Alegre, Brazil, p. 131 (in Portuguese).
Rizzotto, G.J., 2010. Geologia e Recursos Minerais da Folha Pimenteiras (SD.20-X-D). Sistema de Informação Geográfica-SIG. CPRM, Rondônia, Brazil. 136 pp. (in Portuguese).
Rizzotto, G.J., Dehler, N., 2007. Arcabouço Estrutural Da Faixa Alto Guaporé e o Regime Tectônico do Ectasiano na Borda SW do Cráton Amazônico. XI Simpósio Nacional de Estudos Tectônicos, Natal. ANAIS XI Simpósio Nacional de Estudos Tectônicos (in Portuguese).
Rizzotto, G.J., Bettencourt, J.S., Teixeira, W., Pacca, I.G., D'Agrella-Filho, M.S., Vasconcelos, P.M., Basei, M.A.S., Onoe, A.T., Passarelli, C.R., 2002. Geologia e geocronologia da Suite Metamórfica Colorado e suas encaixantes, SE de Rondônia: implicações para a evolução mesoproterozóica do SW do Craton Amazônico. Revista do Instituto de Geociências USP: Série Científica, 2, pp. 41–55 (in Portuguese).
Rogers, J.J.W., Santosh, M., 2002. Configuration of Columbia, a Mesoproterozoic supercontinent. Gondwana Research 5, 5–22.
Rogers, J.J.W., Santosh, M., 2004. Continents and Supercontinents. Oxford University Press, New York. 289 pp.
Romanini, S.J., 2000. Programa Nacional de Prospecção de Metais do Grupo da Platina. Geologia e prospecção geoquímica/aluvionar da área Corumbiara/ Chupinguaia-Rondônia. Informe de Recursos Minerais. Serie Metais do Grupo da Platina e Associados, 6. CPRM, Porto Alegre (in Portuguese).
Sadowski, G.R., Bettencourt, J.S., 1996. Mesoproterozoic tectonic correlations between eastern Laurentia and western border of the Amazon Craton. Precambrian Research 76, 213–227.
Santos, J.O.S., Hartmann, L.A., Hartmann, L.A., Gaudette, H.E., Groves, D.I., McNaughton, N.J., Fletcher, I.R., 2000. A new understanding of the provinces of Amazon craton

based on integration of field mapping and U–Pb and Sm–Nd geochronology. Gondwana Research 3, 489–506.
Santos, J.O.S., Rizzotto, G., Easton, M.R., Potter, P.E., Hartmann, L.A., McNaughton, N.J., 2002. The Sunsás Orogen in Western Amazon Craton, South America and correlation with the Grenville Orogen of Laurentia, based on U–Pb isotopic study of detrital and igneous zircons. Geological Society of America, 2002 Denver Annual Meeting, Precambrian Geology, pp. 122–128.
Santos, J., Rizzotto, G.J., Potter, P., Mcnaughton, N., Matos, R., Hartmann, L., Chemale Jr., F., Quadros, M., 2008. Age and autochthonous evolution of the Sunsás Orogen in West Amazon Craton based on mapping and U Pb geochronology. Precambrian Research 165, 120–152.
Saunders, A.D., Norry, M.J., Tarney, J., 1991. Fluid influence on the trace element compositions of subduction zone magmas. Philosophical Transactions of the Royal Society of London 335, 377–392.
Schmidt, M.W., 1992. Amphibole composition in tonalites as a function of pressure: an experimental calibration of the Al-in-hornblende barometer. Contributions to Mineralogy and Petrology 110, 304–310.
Schobbenhaus, C., 2001. Geological map of south America, scale 1:5000000, CGMW-CPRM-DNPM-UNESCO, Brasilia, Brazil.
Shervais, J.W., 2001. Birth, death and resurrection: the life cycle of suprasubduction zone ophiolites. Geochemistry, Geophysics, Geosystems 2 (Paper 2000GC000080).
Stern, R.J., Bloomer, S.H., 1992. Subduction zone infancy: examples from the Eocene Izu–Bonin–Mariana and Jurassic California. Geological Society of America Bulletin 104, 1621–1636.
Sun, S.S., 1987. Chemical composition of Archaean komatiites: implications for early history of the Earth and mantle evolution. Journal of Volcanology and Geothermal Research 32, 67–82.
Sun, S.S., McDonough, W.E., 1989. Chemical and isotopic systematics of oceanic basalts: implications for mantle composition and processes. In: Saunders, A.D., Norry, M.J. (Eds.), Magmatism in the Ocean Basins: Geological Society London, Spec. Publ., 42, pp. 313–345.
Taylor, B., Martinez, F., 2003. Back-arc basin basalt systematics. Earth and Planetary Science Letters 210, 481–497.
Taylor, S.R., McLennan, S.M., 1985. The continental crust: its composition and evolution. Blackwell Scientific Publication, Oxford, p. 312.
Teixeira, W., Tassinari, C.C.G., 1984. Caracterização geocronológica da província Rondoniana e suas implicações geotectônicas. Simpósio Amazônico. Manaus, 2. SBG/DNPM, Atas, pp. 87–91 (in Portuguese).
Tohver, E., van der Pluijm, B.A., Van der Voo, R., Rizzotto, G., Scandolara, J.E., 2002. Paleogeography of the Amazon craton at 1.2 Ga: early Grenvillian collision with the Llano segment of Laurentia. Earth and Planetary Science Letters 199, 185–200.
Tohver, E., van der Pluijm, B., Mezger, K., Essene, E., Scandolara, J., Rizzotto, G., 2004a. Significance of the Nova Brasilândia metasedimentary belt in western Brazil: redifining the Mesoproterozoic boundary of the Amazon craton. Tectonics 23, TC6004.
Tohver, E., Bettencourt, J.S., Tosdal, R., Mezger, K., Leite, W.B., Payolla, B.L., 2004b. Terrane transfer during the Grenville orogeny: tracing the Amazonian ancestry of southern Appalachian basement through Pb and Nd isotopes. Earth and Planetary Science Letters 228, 161–176.
Tohver, E., Teixeira, W., van der Pluijm, B., Geraldes, M., Bettencourt, J.S., Rizzotto, G.J., 2006. Restored transect across the exhumed Grenville orogen of Laurentia and Amazonia, with implications for crustal architecture. Geology 34, 669–672.
Unrug, R., 1992. The supercontinent cycle and Gondwana assembly: component cratons and the timing of suturing events. Journal of Geodynamics 16, 215–246.
Vernon, R.H., 1970. Comparative grain-boundary studies in some basic and ultrabasic granulites, nodules and cumulates. Scottish Journal of Geology 6, 337–351.
Weil, A.B., Van der Voo, R., Niocaill, C.M., Meert, J.G., 1998. The Proterozoic supercontinent Rodinia: paleomagnetically derived reconstructions for 1100 to 800 Ma. Earth and Planetary Science Letters 154, 13–24.
Winchester, J.A., Floyd, P.A., 1977. Geochemical discrimination of different magma series and their differential products, using immobile elements. Chemical Geology 20, 325–344.
Wood, B.J., Banno, S., 1973. Garnet–orthopyroxene and orthopyroxene–clinopyroxene relationships in simple and complex systems. Contributions to Mineralogy and Petrology 4, 109–124.
Zhao, G.C., Cawood, P.A., Wilde, S.A., Sun, M., 2002. Review of global 2.1–1.8 Ga orogens: implications for a pre-Rodinia supercontinent. Earth Science Reviews 59, 125–162.
Zhao, G.C., Sun, M., Wilde, S.A., Li, S.Z., 2004. A Paleo-Mesoproterozoic supercontinent: assembly, growth and breakup. Earth Science Reviews 67, 9–123.
Zhao, G.C., Cao, L., Wilde, S.A., Sun, M., Choe, W.J., Li, S.Z., 2006. Implications based on the first SHRIMP U–Pb zircon dating on Precambrian granitoid rocks in North Korea. Earth and Planetary Science Letters 251, 365–379.

2.2. Artigo II

Rizzotto, G.J, Santos, J.O.S., Hartmann, L.A., Tohver, E., Pimentel, M.M., McNaughton, N., 2012. The Calymmian/Ectasian Guaporé suture in the SW Amazon craton: geotectonic implications based on field geology, zircon geochronology and Nd-Sr isotopic geochemistry. **Precambrian Research** (Submetido).

Dear Mr Rizzotto,

Your submission entitled "The Calymmian/Ectasian Guaporé suture in the SW Amazon craton: geotectonic implications based on field geology, zircon geochronology and Nd-Sr isotopic geochemistry" has been assigned the following manuscript number: **PRECAM3485**.

You will be able to check on the progress of your paper by logging on http://ees.elsevier.com/precam/ as Author.

Thank you for submitting your work to this journal.

Kind regards,

D. Jones
Administrative Support Agent [16-Mar-11]

Elsevier Editorial System(tm) for Precambrian Research
Manuscript Draft

Manuscript Number: PRECAM3485

Title: The Calymmian/Ectasian Guaporé suture in the SW Amazon craton: geotectonic implications based on field geology, zircon geochronology and Nd-Sr isotopic geochemistry

Article Type: Research Paper

Keywords: Suture zone, Amazon craton, ophiolite, geochronology, Mesoproterozoic

Corresponding Author: Mr Gilmar José Rizzotto, M.D.

Corresponding Author's Institution: Geological Survey of Brazil (CPRM)

First Author: Gilmar J Rizzotto, M.D.

Order of Authors: Gilmar J Rizzotto, M.D.; João O Santos, Dr; Léo A Hartmann, Dr; Eric Tohver, Dr;Márcio M Pimentel, Dr; Neal J McNaughton, Dr

Abstract: New U-Pb zircon (SHRIMP) and isotopic geochemistry data document the existence of apreviously unrecognized Calymmian/Ectasian suture zone, herein termed the Guaporé suture zone, which has implications for Proterozoic tectonic reconstructions of Amazonia predating the formation of the supercontinent Rodinia. The suture has been identified by the presence of mafic granulites and a large volume of mafic-ultramafic rocks (ophiolitic fragments) that are associated with strong contrasts in magnetic signatures between two crustal blocks. The Guaporé suture zone is defined by the ESEWNW trending mafic-ultramafic belt formed during a Mesoproterozoic (ca. 1.47-1.43 Ga) accretionary phase, and overprinted by upper amphibolite-granulite facies metamorphism during collisional phase in the Ectasian (~1.35 Ga), which mark the docking final of the proto-Amazon craton and Paraguá Block. The identification of a fossil ophiolite-decorated suture zone in the southwestern Amazon craton enables us to constrain the timing of generation of oceanic crust formed as early as ca. 1470-1435 Ma; however, the Amazon craton reached its terminal orogenic phase as late as ca. 1350 Ma.
A mafic granulite (1468±24 Ma) associated with and banded mafic granulite (1447±12 Ma), yields the oldest zircon ages for the plutonic part of the ophiolite. A banded amphibolite (1435±6 Ma) and a finegrained amphibolite (metabasalt; 1435±9 Ma) yielded the younger age of the ophiolitic sequence. The ophiolites were intruded by tonalitic-plagiogranitic syntectonic plutons. The ages of tonalitethrondhjemite gneiss (1433±2 Ma) and tonalitic gneiss (1435±2 Ma) are suggestive of a metamorphic growth. Mafic-ultramafic rocks of the Trincheira ophiolites display moderate to highly positive initial values of +2.6 to +8.8 and very low values for the initial 87Sr/86Sr ratio (0.7013 - 0.7033). It is suggested that these magmas originated from a depleted mantle source, which experienced low degree of contamination by variable subduction components. The gabbros and granites syntectonic plutons, dated around 1350-1340 Ma, record the collisional phase of orogeny.
This study contributes significantly to our understanding of the operation of Mesoproterozoic plate tectonics in the southwestern Amazon craton, here inferred to involve accretionary orogen involving the subduction of oceanic lithosphere.

The Calymmian/Ectasian Guaporé suture in the SW Amazon craton: geotectonic implications based on field geology, zircon geochronology and Nd-Sr isotopic geochemistry

Gilmar José Rizzotto [a,*], João Orestes S. Santos [b], Léo Afraneo Hartmann [c], Eric Tohver [d], Márcio Martins Pimentel [c], Neal J. McNaughton [e]

[a] Geological Survey of Brazil (CPRM), Rua 148, nº 485; 74170-110 Goiânia, Goiás, Brazil;

[b]Redstone Resources, Suite 3 – 110 East Parade, East Perth, WA, 6004, Australia;

[c] Instituto de Geociências, Universidade Federal do Rio Grande do Sul, Avenida Bento Gonçalves, 9500; 91501-970 Porto Alegre, Rio Grande do Sul, Brazil;

[d] School of Earth and Environment, University of Western Australia (M004) 35, Stirling Highway, Crawley, WA, 6009, Australia;

[e] Curtin University of Technology, GPO Box U1987, Bentley, WA, 6845, Australia

Abstract

New U-Pb zircon (SHRIMP) and isotopic geochemistry data document the existence of a previously unrecognized Calymmian/Ectasian suture zone, herein termed the Guaporé suture zone, which has implications for Proterozoic tectonic reconstructions of Amazonia predating the formation of the supercontinent Rodinia. The suture has been identified by the presence of mafic granulites and a large volume of mafic-ultramafic rocks (ophiolitic fragments) that are associated with strong contrasts in magnetic signatures between two crustal blocks. The Guaporé suture zone is defined by the ESE–WNW trending mafic-ultramafic belt formed during a Mesoproterozoic (ca. 1.47-1.43 Ga) accretionary phase, and overprinted by upper amphibolite-granulite facies metamorphism during collisional phase in the Ectasian (~1.35 Ga), which mark the docking final of the proto-Amazon craton and Paraguá Block. The identification of a fossil ophiolite-decorated suture zone in the southwestern Amazon craton enables us to constrain the timing of generation of oceanic crust formed as early as ca. 1470-1435 Ma; however, the Amazon craton reached its terminal orogenic phase as late as ca. 1350 Ma.

A mafic granulite (1468±24 Ma) associated with and banded mafic granulite (1447±12 Ma), yields the oldest zircon ages for the plutonic part of the ophiolite. A banded amphibolite (1435±6 Ma) and a fine-grained amphibolite (metabasalt; 1435±9 Ma) yielded the younger age of the ophiolitic sequence. The ophiolites were intruded by tonalitic-plagiogranitic syntectonic plutons. The ages of tonalite-throndhjemite gneiss (1433±2 Ma) and tonalitic gneiss (1435±2 Ma) are suggestive of a metamorphic growth. Mafic-ultramafic rocks of the Trincheira ophiolites display moderate to highly positive initial ε_{Nd} values of +2.6 to +8.8 and very low values for the initial $^{87}Sr/^{86}Sr$ ratio (0.7013 - 0.7033). It is suggested that these magmas originated from a depleted mantle source, which experienced low degree of contamination by variable subduction components. The gabbros and granites syntectonic plutons, dated around 1350-1340 Ma, record the collisional phase of orogeny.

This study contributes significantly to our understanding of the operation of Mesoproterozoic plate tectonics in the southwestern Amazon craton, here inferred to involve accretionary orogen involving the subduction of oceanic lithosphere.

Keywords: Suture zone, Amazon craton, ophiolite, geochronology, Mesoproterozoic

1. Introdution

The Amazon craton is the largest of the Neoproterozoic cratons that constitute the South America continent and its important role in the agglutination of the continental landmass in supercontinent formation has long been recognized by several authors (Sadowski and Bettencourt, 1996; Tassinari and Macambira, 1999; Cordani and Teixeira, 2007; Santos et al., 2008; Cordani et al., 2009, D'Agrella Filho et al., 2012). The first proposal for a link between Amazonia and Baltica was advanced by Almeida (1974). Following the same idea, Geraldes et al., (2001) proposed lateral correlation of Amazonia and Baltica during the late Paleoproterozoic (1.6-1.5 Ga) based on their paired accretionary-rapakivi suites. In most reconstructions of Columbia, the north-northeastern Amazon craton is linked to southwestern

Baltica (e.g., Zhao et al., 2002, 2006; Johansson, 2009). According to this last author, this connection must have existed from at least 1.8 Ga to at least 0.8 Ga.

Others paleogeographic configurations for the Paleo-Mesoproterozoic are suggested by Kusky et al., (2007), Bispo-Santos et al, (2008), and D'Agrella Filho et al., (2012). These authors suggested that North China was located between Baltica and Amazonia.

Otherwise, Alvarez and Cordani (1980), Kroonenberg (1982), Priem et al., (1989), Brito Neves and Cordani (1991) and Dalziel (1992b) suggest a possible link between Amazonia and Laurentia mainly based on geochronological data, except for the latter author, who suggested only a geometrical link between Amazonia and Laurentia, while Sadowski and Bettencourt (1996) argued that Laurentia and Amazonia were already close together, as parts of the same continental mass, whose evolution includes consumption of large ocean floor, at ca. 1500 Ma.

More recently, in global terms, the involvement of Amazonia in Rodinia is, in general, a well accepted hypothesis (e.g. Tohver et al., 2002, 2006; Boger et al., 2005; Li et al., 2008; Ibanez-Mejia et al., 2011). The correlation between Amazonia and Laurentia especially involves the comparison of orogenic events that took place between ca. 1200 and 970 Ma. This hypothesis is contested by Santos et al., (2008), who suggested that Amazonia-Laurentia amalgamation happened during the Candeias collisional orogeny at 1370-1320 Ma.

In the southern portion of the western margin of the Amazon craton, several geological and geochronological summaries were presented over the last two decades, which reflect significant advances in geological knowledge. These reviews attempted to develop evolutionary models consistent with the geology and geochronology of the southwestern margin of the Amazon craton (Table 1). However, the models proposed outline some mega-features delimiting tectonic provinces, terranes and orogens, which still require further study to assess their real tectonic significance.

In this respect, Hasui et al., (1984) were pioneers in the development of a geotectonic framework that used geophysical elements to define major features and structures in an attempt to sketch out the structural framework of the Amazon craton. However these authors only recognize collisional processes in the evolution of the region and also postulate that limits between provinces and blocks are made of large collisional belts, limits that have not been confirmed by the geological mapping projects of the Geological Survey of Brazil-CPRM. On the other hand, studies based on U-Pb zircon age data coupled with Nd isotopic data have been used to document crustal accretion processes, leading to an increasing recognition of overlap between domains. So, the exact locations of terranes and orogen boundaries may have been rendered more diffuse due to the polycyclic nature of the southwestern Amazon basement. The main questions remain in establishing a reference tectonic framework and are related the lack of identification of oceanic crust and their corresponding sutures zones.

A more detailed discussion about the tectonic evolution of the southwestern Amazon craton based on geochronological, structural and metamorphic data for basement rocks was presented by Tohver et al., (2005a) and Boger et al., (2005). These authors suggested the existence of a suture zone resulting from the accretion of the Paraguá craton to the Amazon craton during late Mesoproterozoic times (ca. 1.1-1.0 Ga) along the E–W trending Nova Brasilândia Belt.This suture model contradicts an earlier suggestion by Rizzotto (1999) that the Nova Brasilândia Group formed in an intracontinental rift setting that was followed by a proto-oceanic opening, synchronous to the development of the Grenvillian-age orogeny (Sunsás Orogeny) but not implying in tectonic connection with the Grenville orogeny in Laurentia. Another tectonic model presented by Bettencourt et al., (2010) suggests that the Rondonian-San Ignácio Orogen is composite, multi-stage affair formed reactivation of an older accretionary margin (1556-1430 Ga) during the terminal microcontinent-continent

collision at 1.34-1.32 Ga involving the oblique collision of the Paraguá Block and the proto-Amazon craton.

The recent recognition of the middle-Mesoproterozoic Trincheira ophiolitic Complex (Rizzotto and Hartmann, 2012) exposed between the southern boundary of the SW Amazon craton basement and the Paraguá Block suggests an alternative model for consideration. These new observations require a reevaluation of previous Amazon craton tectonic models in pre-Rodinia times. The present study addresses the question of defining a new suture zone in the southwestern margin of the Amazon craton and its geotectonic implications for the evolution of the craton, predating the formation of Rodinia. This new interpretation is based on zircon geochronology and isotopic geochemistry, supported by field geology and aeromagnetometric data. With these data we are able to better define the formation age of the ophiolitic complex which integrates the Guaporé suture zone, a key tectonic structure for testing the inferred Mesoproterozoic connection between SW Amazon craton and Paraguá Block.

2. Geological setting

The southern portion of the southwestern Amazon craton is characterized by a number of lithospheric blocks with distinct structural, isotopic and geochronological characteristics (Quadros and Rizzotto, 2007; Bettencourt et al., 2010). The basement rocks of the Amazon craton lie north of the Nova Brasilândia belt, and constitute the Rondônia-Juruena province (RJP) while south of this belt lies the Paleoproterozoic Paraguá craton (cf. Litherland et al., 1989). The region we have studied lies along the northern margin of the Paraguá Block (Fig.1). These blocks are placed adjacent to a frontal/oblique thrust system, whose limit is characterized by tectonic discontinuities. This limit is well defined by gravimetric and magnetic discontinuities, interpreted as deep tectonic features of the first order, represented by compressional shear zones of great magnitude associated with ophiolitic sequences (Rizzotto and Hartmann, 2012). These rocks are here interpreted as

representing the Guaporé suture zone. This suture zone represents a major paleo-plate boundary in southwestern Amazon craton that separates two continental blocks (Fig. 1).

A summary of the geology of the relevant continental blocks, previous regional evolutionary models and published age data is presented below (Table 1).

2.1. *The northeastern continental block*

The northeastern block of the Amazon craton is represented by the RJP (Santos et al., 2008) and includes six major Paleo-Mesoproterozoic terranes and events: Juruena magmatic arc, Jamari magmatic arc, Alto Jauru Terrane, Quatro Cachoeiras orogeny, Cachoerinha orogen and Anorogenic magmatism (Table 1).

The boundaries of the RJP (1820-1537 Ma) extend from the extreme west of Rondônia and eastern Acre states in its western portion, until the watershed area of the upper course of the Teles Pires river (Mato Grosso state), to the east. The Rondônia-Juruena basement comprises a continuous EW trending exposure of rocks approximately 1150km long and 300km wide (Fig. 1). The orientation of the RJP differs significantly from the NW-SE orientation suggested by Tassinari et al., (2000). The basement (Table 1) in the central-eastern sector of the RJP consists predominantly of granitoid rocks of the Juruena magmatic arc (e.g. São Romão, São Pedro, Paranaíta Suites) and their corresponding volcanic and volcano-sedimentary rocks (Colíder and Roosevelt Groups) as well as quartz-diorite to tonalitic constituents (Vitória Suite) and the Vespor high-K calc-alkaline mafic rocks, originated in the time interval between 1820 and 1740 Ma (Ribeiro and Duarte, 2010).

These rocks show $\varepsilon_{Nd(t)}$ values ranging from -1.37 to + 0.61 and model ages from 2.10 to 2.28 Ga. The structural framework, in general, is characterized by shear zones marked by high-angle mylonitic foliation and gneissic banding, with the dominant trend between N40-60W and EW. A tectono-metamorphic event (collisional?), not yet well defined, originated amphibolite facies conditions, was superimposed on rocks on the eastern sector of

the RJP in the time interval between 1.67 and 1.63 Ga (Table 1). The last large granitic magmatism in the northern-eastern of the RJP occurred around 1570-1530 Ma with the intrusions of the Serra da Providência and Aripuanã Granites (1537 Ma; Rizzotto et al., 2002b).

On the other hand, the basement of the western sector of the province is represented by the Jamari Complex (1.76 to 1.74 Ga), comprising predominantly tonalitic, quartz-diorite, granitic ortogneiss, amphibolites and minor supracrustal sequences. These lithostratigraphic units occur as inliers, partially preserved during crustal reworking triggered by collisional events and/or subsequent orogenies (Quatro Cachoeiras, Rondonian-San Ignacio and Nova Brasilândia orogenies). The Nd isotopic composition of the tonalite indicates values of $\varepsilon_{Nd(t)}$ ranging from -1.50 to +0.20 and T_{DM} from 2.10 to 2.20 Ga (Table 1). Granites, charnockites, mangerites and gabbros of the Serra da Providência Intrusive Suite (Ga 1.57 to 1.53) are intrusive into the basement.

The structural geometry of the western RJP was established by tectono-magmatic and metamorphic high-grade events, accompanied by voluminous syn to late tectonic granite intrusion which took place in the time interval from 1.35 to 1.32 Ga. These events comprise the Rondonian-San Ignacio orogen (Tassinari et al., 2000) or the Candeias orogeny (Santos et al., 2008).

This event was first recognized by Amaral (1974), who named it the Madeira event, coeval with the San Ignacio Orogeny, defined in eastern Bolivia by Litherland et al., (1986, 1989). The tectonic regime is dominated by a directional regime characterized by sinistral transcurrent systems along which NNE symmetric and asymmetric transpressive duplexes developed. This event of high grade metamorphic overprinted in the RJP rocks is revealed by U-Pb SHRIMP ages (1.33 - 1.35 Ga) on zircon overgrowths and monazite (Payolla et al., 2002, Santos et al., 2008). Another metamorphic event in the western sector of the RJP was detected by Tohver et al., (2005) in the age range of 1.15-1.2 Ga based on integration of

$^{40}Ar/^{39}Ar$ data and feldspar thermometry data from regionally extensive strike-slip mylonitic shear zones (Ji-Paraná shear zone network).

The RJP extends to the south under the Parecis Basin (Fig. 1), where the basement is represented by the Alto Jauru Terrane (1.79-1.75 Ga) (Geraldes et al., 2001) and the Cachoeirinha Orogen (Bettencourt et al., 2010). The Alto Jauru Terrane includes volcano-sedimentary sequences, tonalitic gneisses and intrusives granitoids. The supracrustal rocks forms, from east to west, the Cabaçal, Araputanga and Jauru volcano-sedimentary belts, separated by gray and pink orthogneisses. Nd isotopic data of the volcano-sedimentary and orthogneiss rocks indicate that the sources of these rocks were largely juvenile, with ε_{Nd} between +2.8 to +2.2 and T_{DM} between 2.1 and 1.93 Ga). The Cachoeirinha Orogen, is interpreted by Bettencourt et al., (2010) as an accretionary orogen that includes tonalites and granites gneisses metamorphosed under amphibolite facies conditions between 1.56 and 1.52 Ga (Ruiz et al., 2004, Geraldes et al., 2001). Nd T_{DM} model ages varying from 1.8 to 1.7 Ga and ε_{Nd} between +0.5 and -1.3 suggest mixing of juvenile magmas with older crustal material (Ruiz, 2005).

2.2. *The southwestern continental block*

The Paraguá Block lies to the south and southwest of the Guaporé suture zone, amalgamated to the Rondônia-Juruena Province. Litherland et al., (1986) defined the metamorphic Precambrian basement of eastern Bolivia as the Paraguá craton on the basis of a structurally coherent unit unaffected by the Sunsás-aged deformation at ca. 1.1-1.0 Ga. The northern and eastern limits of the craton are unclear because they are covered by Cenozoic sedimentary sequences (Fig. 1). The rocks that define the Paraguá Block remain poorly known due to limited exposure in a flat to undulating region that is mostly covered by a Late Tertiary-Quaternary lateritic peneplain. Rock exposures are limited to isolated elevated outcrops or along rivers. However, the available field and geochronological data of Santos et al., (2008), Matos et al., (2009) and Boger et al., (2005) demonstrate that most of the northern

part of the “Block” is formed by arc-related granites of the Candeias orogeny (1370-1330 Ma). Correlations with the Proterozoic of Eastern Bolivia are very difficult because the existing geological map of this region (Litherland et al., 1986, 1989) requires a detailed and careful review. The stratigraphy is constrained by the metamorphic grade where higher grade rocks are interpreted to be the oldest units. Santos et al., (2008), however, demonstrated that several rock units previously considered to form the basement (supposedly as old as 1960 Ma; Litherland et al., 1989) were formed during the Candeias (1370-1330 Ma) and Sunsás-Nova Brasilândia (1180-1100 Ma) orogenies.

The Paleoproterozoic basement rocks comprises the Lomas Manechi Complex, marked by the granulitic metamorphism at ca. 1330-1350 Ma (Santos et al., 2008), the Chiquitania Complex and San Ignacio Group which were subsequently deformed and metamorphosed during the San Ignacio Orogeny (~1350 Ma), by means of three successive phases of deformation accompanied by voluminous syn-tectonic granite intrusion (Litherland et al., 1986). Granulitic gneisses belonging to the Lomas Manechi Complex present the oldest age (1818 Ma) in Bolívia (Santos et al., 2008) whereas an orthopyroxene bearing granitoid (1663 Ma) provided the youngest age for the basement rock units (Boger et al., 2005). Nd T_{DM} model ages of the magmatic rocks varying from 2.07 to 1.74 Ga and ε_{Nd} between +0.5 and +4, suggest a juvenile mantle derived magmas.

Structural data from the San Ignacio region show four phases of deformation for the basement rocks. These data show fold axes trends to the north-northeast, and to the north-west (for more structural details see Boger et al., 2005).

3. Geological features of the Guaporé suture zone

The high-grade mafic-ultramafic rocks forming the Trincheira complex at the southern edge of the Parecis Basin, together with the mafic rocks that constitutes the Rio Alegre terrane

in Mato Grosso, represent a dismembered ophiolite that marks a paleosuture. Tentatively, part of this sequence may be preserved to the north of the Phanerozoic Parecis basin, where a discontinuous mafic-ultramafic belt and granitoids form the São Felipe Complex, which most likely constitutes the largest ophiolitic complex, which was then dismembered during the opening of the Paleozoic Parecis basin. These rock units constitute the Calymmian/Ectasian Guaporé suture zone (Fig.1).

A possible Mesoproterozoic suture zone represented by rocks of the Santa Luzia Granulitic Complex was suggested in the southern-central Rondônia by Scandolara and Rizzotto (1998). Similarly, Saes and Cesar (1996) suggested that the Mesoproterozoic accretion terranes (Rio Alegre terrane) in the southwestern margin of the Amazon craton represent a suture zone between the Jauru and Paraguá terranes. Similarly, Tohver et al., (2004, 2005b) identified the Nova Brasilândia belt as a suturing belt, based on the contrasting metamorphic history with the Amazon basement to the north.

Despite its tectonic importance, the architecture and evolution of the Guaporé suture zone are poorly known, largely because the ophiolites in the suture zone have not been studied. This framework changed after the recognition of fragments of oceanic crust preserved as ophiolites in the southern sector of southwestern Amazon craton (Rizzotto and Hartmann, 2012).

The Guaporé suture zone is identified by the presence of mafic-ultramafic rocks, associated with strong magnetic anomalies between two crustal blocks whose boundaries are represented by thrusts and shear zones (Fig. 2). To the north of the Guaporé magnetic anomaly lies a second paired set of anomalies that coincides with the younger 1.2-1.0 Ga Nova Brasilândia belt. Both sets of magnetic anomalies are attributed to the large amount of mafic-ultramafic rocks (mostly mafic, in the case of the Nova Brasilândia belt), which have high magnetic susceptibility and form pairs of high and low magnitudes and bipolar anomalies parallel to the EW mega-structural trend along the suture zone (Fig. 2). The

continuity of magnetic anomalies over 1000 km to the west suggests that this zone continues below the Phanerozoic cover until truncation by the Andean Cordillera.

The Guaporé suture zone is marked by rocks of the Trincheira mafic-ultramafic Complex, which represents an accretionary phase and is composed of several imbricated thrust slices that form a dismembered, incomplete ophiolitic sequence (Rizzotto and Hartmann, 2012). The sequence includes mafic-ultramafic plutonic bodies as well as extrusive mafic rocks with an interbedded sedimentary clastic-chemical sequence subdivided into three units: a) Layered mafic-ultramafic lower unit (granulite-facies metamorphism): olivine-orthopyroxenite, bronzitite, websterite,; b) an Intermediate unit: mafic plutonics (amphibolite-facies metamorphism) including norite, gabbronorite, gabbro, anorthosite, gabbroanorthosite and rare plagiogranite, and c) an Upper unit formed by extrusive mafic rocks (amphibolite-facies metamorphism) represented by fine-grained amphibolites (massive and pillowed basalts) with intercalations of chemical and detrital sedimentary sequence consisting of metachert, banded iron formation (BIF), calc-silicate rocks and aluminous schist/quartzite. Syn-tectonic tonalites to granites occur as intrusions within the ophiolites.

Metamorphic conditions range from granulite facies in the basal portions of the complex to amphibolite facies in the upper zone of the complex, with retrogression to middle amphibolite facies restricted to an anastomosing network of mylonitic shear zones. The deformation is heterogeneous, as indicated by highly deformed zones adjacent to areas with poorly developed foliation or partially preserved primary textures. The mylonitic foliation has a high dip (> 60 °) to SSW and down-dip mineral lineation (> 50º). Metamorphic banding and tight isoclinal and asymmetric folds are generally associated with the tectonic foliation. The structural framework shows that the thrust structures were generated through a system of thrusts with tectonic transport towards the NNE. Geotermobarometry data presented by Rizzotto and Hartmann (2012) indicate temperatures of 780-853°C in mafic granulites and 680-720°C in amphibolites under an overall pressure of 6.8 kbar.

Correlative rocks of the Guaporé suture zone are found 200 km to the SE where mafic-ultramafic rocks of the Rio Alegre terrane (Saes, 1999) are exposed. The Rio Alegre terrane rocks crop out in a large NNW trending area with approximately 50×200 km^2 in southwest Mato Grosso, and comprise volcanic/pyroclastic rocks ranging in composition from basic to intermediate, associated with iron-rich sedimentary rocks and quartzites (Geraldes et al., 2001). This sequence is metamorphosed under granulite-amphibolite facies conditions. The Santa Bárbara amphibolite is a geological unit of the Rio Alegre terrane, which yielded zircons with the age of 1494 ± 10 Ma and isotopic Sm-Nd data indicating that the source for this rocks was juvenile ($\varepsilon_{Nd(t)}$= +2.5 and T_{DM}=1.68 Ga) (Geraldes et al., 2001). Intrusive rocks into the Rio Alegre terrane range from tonalite/granodiorite to granite. Two samples of the tonalitic rocks yield U-Pb ages of 1465 ± 4 Ma and 1481 ± 7 Ma, with $\varepsilon_{Nd(t)}$ = +3.8 to +4.1 and T_{DM} = 1.53 to 1.50 Ga (Geraldes et al., 2001). These authors have interpreted the Rio Alegre terrane as representative of an oceanic island arc between 1515-1460 Ma.

The collisional phase in the building of the Guaporé suture zone is represented by a minor volcano-sedimentary sequence and significant bimodal mafic-felsic magmatism, which is composed of syntectonic granites as well as coeval mafic rocks (mainly amphibolites). This unit was defined by Rizzotto et al., (2002) as Colorado Metamorphic Suite (Fig. 3). This suite consists of amphibolite facies monzonitic gneiss associated with amphibolite, metagabbro and metadiabase, that were originated in a forearc setting (Rizzotto et al., 2002), intercalated with sillimanite-quartz schist, paragneiss and rare BIF's. The mylonitic zones shown trend ENE-WSW, and strong dip SSE. It is suggested that the originally subhorizontal structures (thick-skin style) would be associated with a crustal shortening SWW-NEE and evolved into a pop-up in regional scale. Radiometric and isotopic data from felsic and mafic intrusives rocks indicate their contemporaneity, and short crustal residence for the felsic suite protolith. One metagabbro yields a U/Pb TIMS zircon

crystallization age of 1352 ± 3 Ma. The coeval monzonitic gneiss yields a Rb/Sr whole rock isochron age of 1.36 Ga, and $\varepsilon_{Sr(t)}$ and $\varepsilon_{Nd(t)}$ values of +6.5 and +1.4, respectively. The granitic rocks have U/Pb TIMS zircon ages between 1346 and 1337 Ma (Rizzotto et al., 2002a).

The $^{40}Ar/^{39}Ar$ ages in the range 1327 - 1315 Ma in the amphibolites and schists reflect the regional cooling following this major event. (Rizzotto et al., 2002a, Teixeira et al., 2006).

4. Sampling and analytical methods

Samples were collected during geological mapping. Our sampling covers most lithologies of the mafic and ultramafic rocks as well as the tonalite-granite intrusions. These samples were crushed, milled, and split into fractions for whole rock isotope geochemistry, zircon and titanite dating. Zircons were separated from 16 samples using heavy liquid and magnetic separation techniques. Titanite and baddeleyite were found only in some mafic rocks. All rocks were investigated in thin section and have chemical analyses, and ten samples have Sm-Nd and Sr isotope data. Fourteen samples were analyzed by SHRIMP in the Curtin University of Technology-Australia and 2 samples analyzed by LA-MC-ICP-MS plus 10 samples of the mafic-ultramafic rocks for isotopic investigation (Sm-Nd-Sr) in the Isotope Geology Laboratory of the Rio Grande do Sul Federal University in Brazil. All grains used for zircon, baddeleyite and titanite dating were imaged with backscattered electrons at the Centre for Microscopy Characaterization and Analysis at the University of Western Australia to determine their internal structure and igneous or metamorphic growth (Figs. 4 and 5). Sampling sites are shown in Figs. 1 and 3 and general data for each sample (coordinates, rock name, stratigraphic unit,) are described in the next item.

The analytical procedures are presented in Appendix A and the isotopic data are presented in Tables 2, 3, 4 and 5.

5. Sample descriptions and U-Pb zircon geochronology by SHRIMP and LA-ICPMS

The recognition of the oceanic crust and juvenile terranes in the Alto Guaporé belt was based on whole-rock geochemistry, Nd-Sr isotopes for mafic rocks, diorites, trondhjemites and tonalites. Geraldes et al., (2001) had already established the magmatic ages of one example of oceanic crust and related rocks represented by dacitic pyroclastics, tonalites and amphibolites in the Rio Alegre terrane at 1517, 1465 and 1494 Ma respectively.

Our geochronological investigation included the study of the internal structure of the zircon and titanite crystals back-scattered electrons (BSE) imaging, prior to isotopic study (Figs. 4 and 5). The ages reported in the following text represent mean-weighted $^{207}Pb/^{206}U$ ages for a single population.

5.1. *Accretionary phase*

5.1.1. *Trincheira mafic-ultramafic Complex*

The ophiolitic rocks in the Trincheira Complex comprises slices of mafic granulites, amphibolites, metagabbros and serpentinites that are thrust over the arc metavolcanic-metasedimentary sucession (basalt massive and pillowed, calc-silicate rocks and aluminous schist/quartzite) and intruded by tonalitic-plagiogranite plutons (Rizzotto and Hartmann, 2012). Eleven samples selected for age determination were collected during field studies and isotopic results are presented in Tables 2 and 3.

Sample GP4-110 consisted of a half drill-core collected from the core of a mafic granulite found at the depth of 110 meters in drill-hole GP4 (S 12º49’30”; W 61º18’ 30”) . This rock is comprised of metamorphic orthopyroxene, plagioclase, diopside, minor amphibole and magnetite. It has a coarse-grained, granoblastic and nematoblastic texture, and locally exhibits mafic and felsic minerals forming bands parallel to the dominant foliation as well as amphibole segregations that cross-cut this foliation.

Seven zircon grains were analyzed. These grains have 150–200 μm in length with length-to-width ratios of 1:1 to 2:1. Grain shapes varied from rounded to subhedral prismatic with partly broken terminations. BSE images revealed that some grains have irregular zoning pattern (Fig. 4a-b). U–Pb isotope analyses (Table 2) yield concordant to slightly discordant analyses with an average $^{207}Pb/^{206}Pb$ age of 1447 ± 12 Ma and MSWD of 1.8 (Fig. 6a) which is interpreted as the igneous crystallization age.

Sample SJ-2430a (S 12º49'51"; W 61º17'49") is a medium-grained dark gray mafic granulite, with granoblastic texture and regular, centimetric banding, locally preserving the original igneous texture. It consists mainly of zoned plagioclase with altered cores and less altered rims, porphyroblastic orthopyroxene with minor clinopyroxene and magnesio-hornblende. These characteristics suggest norite as the protolith. A mylonitic foliation that has trends N40ºE; dipping 80°SE, cross-cuts the primary foliation and was developed at lower metamorphic grade.

Zircon grain shapes vary from rounded to subhedral prismatic (120-150 μm), unzoned or with irregular zoning pattern (Fig. 4c-d) and low U and Th contents. Th/U ratios (0.16-0.36) are consistent with a magmatic origin. Most analyses plot on or near concordia (Fig. 6b) and using all data we obtain an average $^{207}Pb/^{206}Pb$ age of 1468 ± 24 Ma (MSWD=0.072). On the basis of zircon morphology and the absence of metamorphic overgrowths, this age is interpreted as the protolith crystallization age.

Sample GR 793 (S 13º06'25"; W 60º49'16"), is a banded and folded amphibolite collected to the east of the granulites within a transpressive sinistral zone. This amphibolite is fine to medium grained and has thicker centimetric bands (N30ºW; 80º SW) of mafic (amphibole and clinopyroxene) and thin felsic (plagioclase and minor quartz) zones, suggesting a transposed primary layer. The mylonitic foliation overprinting these rocks trends N45ºE; dips 80ºNE (S_n+1) with a mineral lineation trending 20º and plunging N50ºE. The

asymmetry of folds indicates sinistral movement. Felsic minerals (quartz and plagioclase) form subparallel bands that cross-cut this mylonitic foliation.

Zircons obtained from this amphibolite are between 120 and 200 μm long and have aspect ratios close to 4:1. They show rounded forms with internal structures displaying dark grey cores surrounded by light grey narrow rims (Fig. 4e-f). The U content is variable from 27 to 613 ppm, while Th/U ratios are very low (0.004-0.022), indicative of a metamorphic origin. The age is 1435 ± 6 Ma (MSWD =1.6; - Fig. 6c) which is taken as the timing of growth of cooling through the titanite blocking temperature of 600˚C following amphibolite-facies metamorphism. However, some dark grey cores have older ages (1446-1442 Ma), which are similar igneous ages in the previous example (GP4-110).

Sample GR 737 (S 12º37'38"; W 61º27'35") is a dark gray, fine-grained amphibolite, which locally presents partially preserved igneous textures and structures and can be characterized as a metabasalt. Millimeter to centimeter veinlets and cavities are filled with an aggregate of epidote, garnet and quartz which may correspond to deformed amygdules in relict pillow lavas. Mylonitic fabric is defined by a preferred orientation of amphibole or by sub-centimeter to centimeter scale epidote veinlets. Their mylonitic foliation trends N40E, dips 70NW with a mineral lineation trending 70º and plunging N70ºW.

Zircons from this sample are of variable size with partly rounded or broken terminations (Fig. 4g-h). The U content of the grains is generally lower than 320 ppm and Th content is highly variable (0.016 to 217 ppm). Th/U ratios are bimodal with some grains presenting Th/U ratios < 0.01 (metamorphic) and the remaining with Th/U ratios near 0.7 (magmatic?). In the BSE imagens, the zircons grains are homogeneous, unzoned and rounded (Fig. 4g-h). This feature is typical of metamorphic zircons where recrystallization caused partial to complete rounding of the original crystals. Mineral inclusions are common, and some are probably apatite.

Three of the four zircon grains analyzed form a tightly clustered population with a weighted mean $^{207}Pb/^{206}Pb$ age of 1435 ± 9 Ma (MSWD =0.16- Fig. 6d), interpreted to be the metamorphic age. This age is the same as the age obtained from sample GR-793 described above and suggests a discrete metamorphic event overprinting the ophiolitic rocks at this time.

5.1.2. *Syntectonic tonalites (Rio Galera and São Felipe Complexes)*

Calc-alkaline plutons mark a second magmatic stage in the development of the Trincheira ophiolite. These gneissic plutons are diorite-tonalite-trondhjemite in composition and were emplaced syn-tectonically with some late-tectonic features. The intrusive rocks form stocks, dikes, lens-shaped and tabular bodies and are commonly discordant with older MORB-like layered rocks. These rocks record a polyphase deformational history under medium-pressure, upper amphibolite facies metamorphism.

In *sample NM-189* (S 13º29'29"; W 60º08'36"), the Rio Galera tonalitic gneisses (previously mapped as the Alto Guaporé Complex) are pale grey, coarse-grained, with regular banding, folded, continuous and ranges in thickness from millimeters to centimeters. Trondhjemites gneisses form thin (1-5 cm) bands in the tonalites. Three progressive deformational phases are recognized in the orthogneisses. The metamorphic banding (S_n) strikes N90ºE dips 65ºS trend and mineral lineation trending 50º with a plunge S30ºW. The banding was later folded in asymmetric chevron folds. This fold generation is characterized by a penetrative axial-planar foliation (S_{n+1}) with N10ºE; 60ºSE orientation and S-C structure indicate sinistral displacement. Further far south of this outcrop, these gray tonalitic gneisses are cut by younger granitic late-tectonic plutons (Rio Piolho and Praia Alta granites) which show well preserved cross-cutting intrusive relationships and truncate the fabric of the older tonalitic gneisses.

The zircon crystals from these samples are 100-250 μm long, with an aspect ratio of 3:1. Although magmatic euhedral faces are present in some crystals, rounding is a common feature in many crystals. Several radial and cross cutting fractures are restricted to the dark grey core (magmatic?) of the crystal and sealed by metamorphic zircon. The recrystallized zircons are homogeneous and forms large rims with faint to non existent fractures (light gray to medium gray portion in BSE) (Fig. 5a-b).

Five zircon analyses mostly show high U contents, between 1593 and 2445 ppm although one zircon analysis yields a U content of only 98 ppm. Th contents are low varying between 40 and 72 ppm. The Th/U ratio varies between 0.025 and 0.030, which are suggestive of a metamorphic growth, except for one grain with a Th/U ratio of 0.6. U–Pb isotope analyses of six zircon and 2 titanite grains yield an average $^{207}Pb/^{206}Pb$ age of 1433 ± 2 Ma with an MSWD of 1.4 (Fig. 6e) which indicates the age of metamorphism. Excluding the titanite analyses yields an identical age of 1434 ± 5 Ma (Figure 6e.1). However, one zoned zircon with dark grey core (Th/U= 0.6) show the age of 1463 ± 70 Ma, which is similar to the age of crystallization of mafic granulite SJ 2430a and of orthogneiss GR 750 described below.

Sample GR-337 (S 12º00’22”; W 61º27’29”) is a dark gray, coarse-grained, tonalitic orthogneiss of the São Felipe Complex, intercalated with decimeter to meter-thick, lens-shaped amphibolites and bondinaged quartz veins. Granoblastic plagioclase and quartz predominate in bands which are intercalated with nematoblastic to lepidoblastic hornblende and biotite bands. The main mineral assemblage is plagioclase, quartz, hornblende, biotite and minor epidote, indicative of lower to middle amphibolite facies metamorphism. Mylonitic textures developed in high strain portions show consistent mineral stretching and banding striking N25ºW; dipping 30°NE with a mineral lineation trending 30º that plunges N20ºE. Granite dyke swarms and veins cut the gneissic banding with formation of chlorite, epidote, white mica and cassiterite.

Zircons from this tonalitic gneiss display patchy and widely spaced zoning but some grains are internally homogeneous, possibly indicating recrystallization during metamorphism. Radial and cross cutting fractures occur mostly in the dark grey core of the crystals. The grains are mostly prismatic in shape, with 1:2 to 1:5 width:length ratios and generally smaller than 250 μm in size (Fig. 5c-d).

The U content of zircon is high but variable from 3800 a 960 ppm. Th contents are high (66-633 ppm), and Th/U ratios vary between 0.05 and 0.08, with two grains having a Th/U ratio close to 0.1. Analyses from six crystals show a distribution of discordant data which produced the upper intercept age of 1435 ± 2 Ma with an MSWD of 0.8 (Fig. 6f). This age is similar to the age obtained from sample NM 189 and is interpreted to be the metamorphic age.

Subhedral, light color, cassiterite crystals from intrusive granite dyke within the tonalitic gneiss yielded the average $^{207}Pb/^{206}Pb$ age of 1012 ± 22 Ma with an MSWD of 0.34 (Fig. 6f.1). The age of the cassiterite will probably reflect the age of cooling from metamorphism related to Nova Brasilândia-Aguapeí belt.

Sample GR-750 (S 13º 21’ 36”; W 60º 32’ 42”) is a heterogeneous equigranular medium-grained (3-5mm grain size) biotite-bearing tonalitic gneiss intercalated with trondhjemite .The trondhjemite crops out as small (10 cm to a few meters wide) tabular to lenticular light-gray felsic bodies emplaced concordantly with the banding of the tonalitic gneiss. The metamorphic banding consistently strikes to N30º-70ºW, and dips 80º to the northeast and is cut by pegmatite dike. Mineral lineations have high plunges, indicating the predominance of oblique thrust. Pronounced foliation and extensive grain-size reduction characterize the more intense mylonitic deformation, and there are zones with enrichment in biotite. With increased strain, destruction of feldspar and micas is accompanied by a small but markedly greater abundance of retrometamorphic products such as fine-grained muscovite

and epidote-group minerals, and hence probably indicates an increased water content of the total rock.

Zircons are prismatic with slightly rounded edges. Both elongate and more equant grain shapes show BSE images with a mostly zoned igneous internal structure, and no metamorphic overgrowths (Fig. 5g). Measured U contents range from 100 to 247 ppm, whereas Th contents ranges from 34 to 135 ppm. Th/U ratios vary between 0.28 and 0.57, suggesting a magmatic origin. The isotope analyses of six zircon grains yield an average $^{207}Pb/^{206}Pb$ age of 1459 ± 9 Ma with an MSWD of 0.9 (Fig. 7a), which is interpreted as the age of igneous crystallization.

5.1.3. Syn to *late-tectonic granites (Praia Alta and Rio Piolho granites)*

The Praia Alta and Rio Piolho granites form a group of porphyritic to equigranular granites that intrude the tonalitic-trondhjemitic-dioritic orthogneiss of the Rio Galera Complex. Centimeter scale phenocrysts of K-feldspar, the presence of quartz-diorite enclaves, a magmatic foliation and the absence of both leucosomes and folds differentiate these rocks from the Rio Galera and São Felipe granitoids. These characteristics suggest that the Praia Alta and Rio Piolho granites are younger than the granitoids in the Rio Galera and São Felipe complexes. We consider that these granites were emplaced after the obduction of the ophiolites.

Previously inserted into the Praia Alta granite unit, the rock unit represented by sample *F1GR1* (S 13º46'14"; W 60º20'41") is a drill core collected at the depth of 184 meters and consists of a biotite syenogranite intruded into serpentinized dunite of the Morro Sem Boné unit. It is pinkish to reddish, coarse-grained, equigranular, with a weakly-developed magmatic foliation. The rock has one population of magmatic zircon, and no metamorphic rims or zones were detected. Zircons are prismatic (aspect ratio 4:1), weakly zoned and generally of the 100 to 200 μm in size (Fig. 5e-f), with U contents ranging from 469 to 1084 ppm and Th contents

is variable, from 158 to 615 ppm. Th/U ratios vary between 0.13 and 0.59, suggestive of a magmatic origin. Most analyses from these zircons plot on or near the concordia (Fig. 7b) indicating the average $^{207}Pb/^{206}Pb$ age of 1436 ± 7 Ma (MSWD=2.8) interpreted as the age of igneous crystallization.

The Praia Alta granite (*sample NM-318* - S 13º43'23"; W 60º 04'17") is a stock elongated in the N20ºW direction. It is a coarse-grained pinkish porphyritic syenogranite, with a magmatic foliation and an overprinting mylonitic foliation developed along the margins of the body. It contains tabular phenocrysts of perthitic microcline (5-15mm) that occur in a matrix of medium-grained K-feldspar, plagioclase altered to epidote, quartz, biotite and minor magnetite. Zircons from this sample are large (> 200 μm) and commonly show well-formed, euhedral terminations. These grains were analysed by LA-MC-ICP-MS (Table 3) and Th/U ratios vary between 0.24 and 0.42, indicative of a magmatic origin. All analyses plot on the concordia curve (Fig. 7c) indicating a Concordia age of 1426 ± 5 Ma. Given the relatively simple zoned structure of the zircons, together with the single age population obtained, we interpret the age of 1426 ± 5 Ma as representative of the emplacement of the Praia Alta granite.

The Rio Piolho granitoid stocks are elongated parallel to the NNE transpressional shear zones. They are biotite-bearing syenogranite to monzogranite with porphyritic to granular textures with subordinate coarse-grained inequigranular phases. The rocks are, in general, massive, but they locally show a magmatic flow overprinted by a mylonitic foliation along the margins of the body. Centimeter- to decimeter-wide enclaves of quartzite and tonalitic to dioritic composition and aggregates of mafic minerals are commonly observed.

Sample NM-177 (S 13º22'59"; W 60º10'05") is a syenogranite (Rio Piolho unit) which show granular to porphyritic texture defined by the contact of subhedral microcline, anhedral plagioclase, and quartz grains. The K-feldspar forms always the largest crystals that are locally prismatic up to 5 cm in size with a preferred orientation. The biotite flakes form small

aggregates scattered in the matrix. Discrete ductile shears are present in the core of the stock and mylonitic structures are observed along the edges of the body.

Zircon grains range mostly from 0.15 to 0.3mm in the longest dimension. They are prismatic with sharp to slightly rounded pyramids. CL imaging showed that some of the grains have igneous growth-zoning patterns, but lack evident metamorphic overgrowths or extensive recrystallization. From a population of 14 analyzed crystals, 11 crystals gave interpretable isotopic results indicating an upper intercept age of 1442 ± 16 Ma (MSWD = 0.25) (Table 3 and Fig. 7d). The inherited zircon (c-v-1a; Table 3) has an age comparable to the age of granitic rocks of Serra da Providência Suite. No significant morphological differences have been observed for zircon crystals of this population. This age is similar to that of 1436 ± 7 Ma obtained for granite sample F1GR1, described above.

5.1.4. *Amphibolite - Rio Alegre terrane*

Published results from previous studies (Geraldes et al., 2001; Matos et al., 2004) assigned a Mesoproterozoic age for the mafic rocks of the Rio Alegre terrane. The Santa Bárbara amphibolitic gneiss is part of the Rio Alegre terrane, yielded zircons with ages of 1494 ± 10 Ma (Geraldes et al., 2001). However, this age has a high MSWD of 9 and must be regarded with caution. Isotopic Sm-Nd data from this sample indicate that the source for this rocks was juvenile ($\varepsilon_{Nd(T)}$ =+2.5 and T_{DM}=1.68 Ga).

Sample GRT-06 (S 15º34’35”; W 59º23’04”) was collected along the western side of the Rio Alegre valley. The sample consists of a melanocratic banded amphibolite, medium to fine-grained, showing a strong vertical to sub-vertical mylonitic foliation.

Macroscopically, amphibole + plagioclase+ clinopyroxene layers and granoblastic to stretched clusters of plagioclase + clinopyroxene ± amphibole are visible. Leucocratic layers with quartz are rare. In thin section, the leucocratic parts consist of plagioclase, quartz and titanite. Greenish-brown hornblende and clinopyroxene form granoblastic aggregates and in

high strain zone the hornblende + plagioclase + clinopyroxene are stretched parallel to the banding, trending N20ºW. The plagioclase has straight to lobate grain boundaries, often recrystallized to small subgrains. The clinopyroxene occur as porphyroblasts and contain inclusions of the plagioclase + quartz. Subhedral to anhedral titanite are observed as inclusions plagioclase or aggregated mats of anhedral grains. The concordant orientation of these mats with the metamorphic foliation and inclusions of metamorphic quartz and epidote indicates that these grains grew during metamorphism.

Individual titanites display no internal zoning, possibly indicating growth or recrystallization during metamorphism (Fig. 5h). As shown in Table 2, metamorphic titanite sometimes contains extremely low concentrations of U. In backscatter-electron image (Fig. 5h) red dots represent the areas tested and avoided due to low contents in U (below 20-30 ppm). Thus, brown titanite grains contain 37-116 ppm U and have relatively high uniform Th/U rations between1.0 and 1.03.

The isotopic data for seven titanite grains from this sample are very simple, ranging from concordant to slightly discordant (MSWD=0.83) and yielded the mean age of 1399 ± 7 Ma (Fig. 7e). We interpret these data as a minimum estimate for the age of metamorphism. The metamorphic zircons of other ophiolitic rocks mentioned above yielded ages which are approximately 30 Ma older. The difference in age may only reflect the differences in closure temperatures of the U-Pb system between zircon and titanite. Alternatively, this age can represent a later deformational/metamorphic event.

5.2. *Collisional phase*

5.2.1. *Syn- to late- kinematic bimodal magmatism*

The collisional phase in building the Guaporé suture zone is represented by Colorado Complex that consists of an association of igneous, metamorphic and metasedimentary rocks, represented by porphyritic metamonzogranites and coeval amphibolites and mafic rocks

(bimodal magmatism). One high-grade metamorphism overprinted allowed a pervasive migmatization followed by mylonitic sigmoidal foliation and boudinage of amphibolites. Within the Complex, hornblende gabbros and diorites associated with syeno to monzogranites occur as small pods or scattered mafic enclaves. Field evidence suggests that most of the mafic rocks are temporally related to the granites.

Sample GR 127 (S 13º 16' 01"; W 60º 27' 03") is a syn-kinematic fine-grained banded dioritic gneiss, dark gray color, that occur as tabular to lenticular bodies, tens to hundreds of meters thick, rarely reaching more than 500m. They are intercalated with amphibolites and rare psamo-pelitic metasedimentary rocks. Banding is regular with folded quartz-K-feldspar veins. Show a high-angle foliation subparallel to the compositional banding. The foliation has an E-W to WNW-trending and high dip angle lineation.

Dioritic gneiss contain three zircon populations: a metamorphic age and two inherited. Zircons in this sample mostly display patchy and widely spaced zoning. Generally, crystals are prismatic to rounded and fragmented and their widths vary between 100 and 250 μm. The rock has three ages - one at 1344 ± 7 Ma; 1469 ± 5 Ma and the other at 1539 ± 9 Ma (Table 4; Fig. 8a). The younger is a metamorphic age, with Th/U ratios from 0.02 to 0.07 and suggests that the rock was metamorphosed during the collisional phase. The older inherited age of 1469 ± 5 and 1539 ± 9 Ma are correlated with the Trincheira Complex and Serra da Providência Suite, respectively.

Sample NM 42 (S 13º 11' 32"; W 60º 34' 15") is coarse-grained porphyritic monzogranite, whith a pronounced alignment of the feldspar megacrysts (2–4 cm in length). Is this a magmatic fabric (lathe-like crystals entrained and oriented by flow in a "mushy" magma) overprinted by mylonitic foliation. Rounded or lens-shaped aplitic felsic inclusions (< 50 cm in mean diameter) and occasional small mafic autoliths occur in the granite suggests the mingling between the two magmas with contrasting compositions, resulting in a hybrid rock ranging in composition from granodiorite to tonalite.

Zircons are mostly prismatic (aspect ratio 4:1), zoned and unzoned, with well-formed, euhedral terminations and no evidence of either metamorphic rims or zones and older cores. U contents ranging from 88 to 892 ppm and Th contents is variable, from 49 to 210 ppm. Th/U ratios vary between 0.15 and 0.58, suggestive of a magmatic origin. Most analyses plot on the concordia curve (Fig. 8b) indicating a Concordia age of 1340 ± 5 Ma. Isotopic Sm-Nd data from this sample indicate that the source for this rocks was juvenile ($\varepsilon_{Nd(t)}$ =+2.84 and T_{DM}=1.51 Ga).

Sample GR 143 (S 13° 15’ 14”; W 60° 34’ 05”) is a dark gray metagabbro with a well-preserved igneous texture. This body is weakly deformed in its interior, but solid-state deformation increases outwards where rocks have recrystallised amphibole and plagioclase. External foliation is concordant with the subcircular shape of the pluton. Their mylonitic foliation trends N40W, dips 85SW.

A total of 10 analyses were performed (Table 4). Of these, 8 analyses were performed in baddeleyite crystals and 2 in zircon. Baddeleyite in this sample are short prism, subhedral surfaces and no sector zoning. Zircon crystals are mostly elongate and 100-300 μm long, with aspect ratios of 1:1 to 3:1, prismatic, and grains with weakly sector zoning. Analyses from ten crystals (2 zircon + 8 baddeleyite) show a distribution of discordant data which produced the upper intercept age of 1354 ± 11 Ma with an MSWD of 2.5 (Fig. 8c) and interpreted as the age of igneous crystallization.

Correlative rocks of the metagabbro GR 143 are found 100 m to the SW where there are two different types of rocks representing a combination of melts mixed. Mafic microgranular enclaves represent the most common heterogeneities present in the granite pluton, whereas in metagabbro contain fine- to medium-grained granitic veins. However, the most common rock type is a medium- to coarse grained, foliated metagabbro (*Sample GR 145* (S 13° 15’ 59”; W 60° 34’ 54”). Also present within the metagabbro are concordant metre-scale sheets of fine- to medium-grained granitic veins that are mainly developed on the

centimeter-decimeter scale but can range up to 2-3 m in thickness. This complex textures are indicative of mingling between the two parent magmas. The metagabbro body is only partly recrystallized and retains some relict igneous textural and mineralogical features.

The majority of the zircons in the sample are partially rounded to subhedral prismatic (100-150 μm) shape, unzoned or with irregular zoning pattern and low U and Th contents. Th/U ratios (0.15-0.30) are consistent with a magmatic origin. Six of the seven zircon grains analyzed form a tightly clustered population with a weighted mean $^{207}Pb/^{206}Pb$ age of 1344 ± 8 Ma (MSWD =0.54- Fig. 8d), which was obtained from the most concordant data, excluding grain L.7-1 (Table 4), and interpreted to be the magmatic age. The geochronological data presented above are consistent with synchronous emplacement of mafic and felsic plutons (GR 145 and NM 42, respectively).

Sample NM 166 (S 13º 25' 17"; W 60º 15' 46") is massive, coarse-grained hornblende metagabbro. Although the rocks of the mafic sequence were metamorphosed and show secondary mineral paragenesis, ranging from low- to middle metamorphic grade, preserved igneous textures and structures can be recognized. This rock consists mainly of amphiboles (66 vol. %) and plagioclase (30 vol. %). The generally subhedral amphibole grains are mainly hornblende and they are typically larger (up to several millimetres) than the interstitial, anhedral plagioclase. Variably chloritized biotite makes up as much as 3 vol. %. Irregular patches of the hornblende grains are replaced by actinolite.

The zircon grains in the metagabbro are mostly prismatic in shape with 100-130 μm in length and a number of them display simple internal structures where some grains show a weak oscillatory zonation. Th/U ratios vary between 0.28 and 0.51, suggestive of a magmatic origin. From a population of 4 analyzed crystals, 3 crystals gave interpretable isotopic results indicating a Concordia age of 1347 ± 8 Ma (Table 4 and Fig. 8e), interpreted as the age of igneous crystallization.

6. Sm–Nd and Sr isotope results

The measured and initial isotopic ratios for samples from Trincheira mafic-ultramafic Complex are reported in Table 5. Initial $^{87}Sr/^{86}Sr$ (Sr_i) and $^{143}Nd/^{144}Nd$ (Nd_i) ratios as well as $\varepsilon_{Sr(t)}$ and $\varepsilon_{Nd(t)}$ values were calculated using a crystallization age of 1460 Ma. For the mafic-ultramafic rocks, Sr_i varies from 0.7002 to 0.7033 and Nd_i from 0.5120 to 0.5133. Positive $\varepsilon_{Nd(t)}$ values (+2.6 to +8.8) of the Trincheira mafic-ultramafic Complex signify that the basaltic precursors were derived from a depleted mantle source. Plotted in the $\varepsilon_{Nd(t)}$ - $^{87}Sr/^{86}Sr$ diagram (Fig. 9) the mafic-ultramafic rocks exhibits limited dispersion in both ε_{Nd} and $^{87}Sr/^{86}Sr$ values and most of the samples lie roughly along the mantle array. Only a few samples are displaced to the right of the mantle array showing more radiogenic Sr isotopic compositions.

7. Discussion and conclusions

Zircon U-Pb geochronological and Nd-Sr data presented in this contribution comprise the first evidence for the existence of an oceanic crust represented by a Mesoproterozoic ophiolite assemblage in southwestern Amazon craton which began to form at ca. 1470 Ma. This pre-Rodinia ophiolite forms the Guaporé suture zone and was obducted soon after it formed. The collision between the Paraguá Block and Amazon craton (more specifically the Rondônia and Mato Grosso regions) and subsequent final docking occurred around 1350-1330 Ma.

Dating of 91 zircon, 9 titanite and 8 baddeleyite crystals from sixteen rocks established the time frame for the evolution of the Rondonian-San Ignacio Orogeny, particularly the Guaporé suture zone defined by the Trincheira mafic-ultramafic Complex, syntectonic tonalites of the Rio Galera and São Felipe Complexes, and intrusives granites and gabbros of the Praia Alta, Rio Piolho Suites and Colorado Complex. The tectonic scenario

includes the generation of juvenile ultramafic and mafic rocks during accretionary phase, deformation and metamorphism of this oceanic crust and related sedimentary rocks, as well as generation of magmas in arc/back-arc setting (Rizzotto and Hartmann, 2012) in the collisional phase.

A mixture between MORB-like and arc-like signatures is not uncommon in ophiolitic sequences (e.g. Stern and Bloomer, 1992; Shervais, 2001; Ishikawa et al., 2002). This is generally considered to reflect melting of a MORB mantle source that has been contamined with fluids released from the subducting slab and/or sediment-derived melts (Fig. 10).

Different mantle processes have been proposed for the generation of the different isotopic reservoir end-members. There is a general consensus that the major source of arc magmas lies in the mantle wedge (Perfit et al., 1980; Gill, 1981; Plank and Langmuir, 1998) and that the subducting slab provides the components that initiate the melting process. Components from the subducting slab that contribute to the subarc mantle include hydrous fluids and silicate melts from altered oceanic basalt and sediment. Subducted oceanic crust and sediment have different isotopic and incompatible trace element compositions, and by considering these differences it is possible to identify contributions from different components. Otherwise, Nd-Sr isotopes compositions provide a useful discriminant of tectonic setting.

Thus, N-type MORB magmas generally has ε_{Nd} values of from +8 to +12 and have very low $^{87}Sr/^{86}Sr$, in the range 0.7024-0.7030, whereas island-arc rocks have ε_{Nd} lower than +9 and a larger range in $^{87}Sr/^{86}Sr$ values (0.7030-0.710). Back-arc basin basalts are normally characterized by lower $^{87}Sr/^{86}Sr$ ratios (0.7028-0.7033) than volcanics from the associated island arc (Stern, 1992). Thus, the large range of ε_{Nd} values (+2.6 to +8.8) and low to medium $^{87}Sr/^{86}Sr$ ratios (0.7013-0.7033) exhibited by the Trincheira rocks differs from mid-ocean ridge rocks but is compatible with an island-arc or back-arc basin setting. This is in agreement

with trace element geochemical characteristics of the investigated mafic-ultramafic rocks. In the ε_{Nd} versus La/Yb diagram (Fig. 11) the Trincheira samples have higher $\varepsilon_{Nd\,(t)}$ and with some samples slightly displaced to the right of primitive mantle values, suggesting that the mantle sources of the Trincheira complex rocks were not substantially contaminated by fluids released from the subducting slab and/or sediment-derived melts. Likewise, in the Th/Yb and Rb/Sr versus $^{87}Sr/^{86}Sr$ diagrams (Fig. 12) the samples display roughly positive trends revealing the influence of components derived from the subducted slab such as enrichments in Rb, Th and Sr. The elements with low ionic potential are most readily mobilized by a fluid phase, and their enrichment in island-arc basalts has been explained by metasomatism of their mantle source region by hydrous fluids derived from the subducted oceanic crust. Thus, the Sr and Nd isotopic data indicate that the original magma of the Trincheira Complex was derived from a depleted source.

Twelve samples have Nd isotopic compositions consistent with modern depleted MORB mantle (DMM), although two of these (GR-694 and GP3-117) have Sr isotopic compositions which are more radiogenic than DMM. In this way, the coherent Sm-Nd systematics combined with measured $\varepsilon_{Nd\,(t)}$ that are slightly more positive than MORB values indicate that the Trincheira Complex rocks has undergone melt extraction from a DMM-type source, where secondary metasomatic enrichment of incompatible lithophile trace elements commonly results in a time-integrated isotopically enriched environment in the sampled lithospheric mantle. The progressive depletion in the increasingly incompatible elements is attributed to repeated melting of a hydrous mantle above a subduction zone, and the characteristic negative anomalies, particularly of Ta and Nb, are related to the stability of certain minerals (e.g. titanite and zircon) during melting or extraction of hydrous fluids from the subducted slab (e.g. Saunders et al., 1991).

Thus, combined strontium and neodymium isotope studies of the Trincheira mafic-ultramafic Complex demonstrate that the observed isotope variations in these rocks can be

generated by a single mantle process where oceanic slab subduction below the peridotite wedge were enriched by percolation of metasomatic suprasubduction fluid in an arc/back-arc setting. The geochemical evidence for the island arc/back-arc magmatic fingerprint in the Trincheira ophiolites has been demonstrated by Rizzotto and Hartmann (2012). The Trincheira mafic-ultramafic Complex, therefore, represents the remnants of an oceanic lithosphere produced in a arc/back-arc setting that includes the subduction of oceanic lithosphere and terminal collision of a microcontinent (Paraguá Block) – with the proto-Amazon craton (Fig. 10). The suturing of the Paraguá Block and proto-Amazon craton was achieved during the Ectasian, at ca. 1.35-1.33 Ga with the production of mafic and felsic melts during this time. In addition, the similar $^{40}Ar/^{39}Ar$ ages reported by Rizzotto et al., (2002a) in amphibole and muscovite from amphibolites and granites suggests a fast cooling rate following the 1.35-1.32 Ga orogenic phase.

The Guaporé suture zone is also defined by magnetometric lineaments associated with distinct and well marked Analytical Signal Amplitudes (ASA), which discriminated magnetometric domains with approximately linear and parallel boundaries, as shown in Figure 2. This pattern and the very strong magnetic susceptibility contrast in geophysical signature are typical of suture zones, well recognized in other sutures elsewhere (Thomas, 1992; Mishra and Kumar, 2006). The depicted feature is at least 950 km long and 80 km wide, displaying a regional character, as identified in aeromagnetic products presented in this paper. The adjoining areas display distinct magnetometric signatures, suggesting distinct tectonic compartments.

This observation is also supported when one compares the tectonic framework from Rondônia and Mato Grosso to that from Eastern Bolivia. It is clear from geochemical and isotopic data that the 1.76-1.73 Ga basement rocks from Rondônia and Mato Grosso originated in a magmatic arc setting, predating those basement rocks of Eastern Bolivia (Paraguá Block), where the main crust-formation event occurred between 1690-1660 Ma

(Boger et al., 2005). We conclude, therefore, that the Paraguá Block accreted to the Amazon craton preceding or during an early phase of the Rondonian-San Ignacio orogeny, at ca. 1470-1350 Ma. In our tectonic reconstruction (Fig. 10), we suggest that the initial evolution of the western margin of the Amazon craton took place in the early Mesoproterozoic. This scenario is supported by recent paleomagnetic results from 1.42 Ga mafic rocks of the Indiavaí Suite in Mato Grosso, that demonstrate the latitudinal proximity of the Amazon craton north of the Nova Brasilândia belt and Guaporé suture zones and the Paraguá craton basement to the south of this suture zone by 1.42 Ga (D'Agrella Filho et al., 2012)

Some of the most significant results of this work can be summarized as follows:

1. Characterization of a Mesoproterozoic suture zone (Guaporé suture zone) between the proto-Amazon craton and the Paraguá Block represented by an ophiolitic assemblage.
2. The accretionary phase of the Rondonian-San Ignacio orogeny occurred between 1.47 and 1.43 Ga, as registered by the Trincheira mafic-ultramafic Complex. This is in partial agreement with the original ideas of Bettencourt et al., (2010). The collisional phase and final docking of the Paraguá Block and proto-Amazon craton occurred around 1350-1330 Ma.
3. The mafic-ultramafic magmatism was followed by syntectonic tonalitic-dioritic intrusions.
4. The ages of crystallization and metamorphism of ophiolitic and associated rocks show that these events occurred within a short time interval of approximately 25 m.y.
5. Sr-Nd isotopic compositions indicate that the original magma of the Trincheira Complex was formed by the melt extraction from a DMM-type source with secondary and poor metasomatic enrichment of incompatible lithophile trace elements, consistent with oceanic crust in suprasubduction setting.
6. Mafic-ultramafic rocks of Rio Alegre terrane is interpreted here as part of the Guaporé suture zone.
7. A significant syn to late-tectonic tonalitic-granitic magmatism occurred between 1439-1432 Ma.

8. Timing of peak metamorphism and deformation along the southwestern margin of the proto-Amazon craton occurred during the collisional phase that resulted of tectonic emplacement of the bimodal mafic/felsic plutons, around 1350 Ma.

9. Definition of the minimum age of crystallization of the ultramafic rocks of the Morro Sem Boné (Mato Grosso State) indicated by the intrusive granite, which gave a crystallization age of 1436 ± 7 Ma.

Acknowledgements

This work was supported by CNPq (Conselho Nacional de Desenvolvimento Científico e Tecnológico) grant 140917/2008-0. The authors thank CPRM/Geological Survey of Brazil office in Porto Velho, Rondônia, for assistance in the fieldwork and access to sample preparation. We are thankful to Marcus Chiarini by interpretation of the geophysical data. We thank also Marcos Luiz Quadros, Maria Rosalva Coelho and Pamela Emanuelle Silva for help with sample preparation. SEM images were obtained at the UWA Centre for Microscopy and Microanalysis, an Australian Microscopy & Microanalysis Research Facility. U-Pb zircon analyses were performed on the sensitive high-resolution ion microprobes (SHRIMP II) located at the John de Laeter Centre of Mass Spectrometry, which is operated by Curtin University, the University of Western Australia and the Geological Survey of Western Australia. Constructive reviews of this manuscript by anonymous reviewer are gratefully acknowledged. Anglo American Brasil Ltda are thanked by unlimited access to mines and prospects.

Appendix A. Analytical procedures

A.1. *U–Pb SHRIMP methodology*

Grains from the non-magnetic fractions were hand-picked, mounted on epoxy discs with fragments of standards, grains of Sri Lanka zircon standard (CZ3) which has a

conventionally measured age of 564 Ma. ($^{206}Pb/^{238}U$ ratio = 0.0914; 551 ppm U) and BR 266 zircon (559 Ma, 903 ppm U). Titanite standard is Namibia Khan (518 Ma; $^{206}Pb/^{238}U$ ratio = 0.083671; 700 ppm U). The mounted zircons and titanites were polished to effectively cut them in half and zircons were imaged by Back Scatterd Electrons (BSE) using a scanning electron microscope prior to gold coating.

U–Th–Pb analyses were performed using the SHRIMP II ion microprobe at Curtin University-Australia following techniques described by Williams (1998) utilizing five-cycle runs through the mass stations. Corrections for common Pb were made using the measured ^{204}Pb and the Pb isotopic composition of Broken Hill galena. Before each spot analysis, 60–90 s were used for pre-sputtering to remove the gold, avoiding the analysis of common Pb from the coatings. Results with more than 0.50% common lead correction are presented but not used in age calculations. Zircon and titanite data are reduced using SQUID (Ludwig, 2002). Data were plotted on concordia diagrams using ISOPLOT/ Ex software (Ludwig, 1999), and error ellipses on Concordia plots are shown at the 95% confidence level (2σ). The ages given in text are concordia and weighted mean $^{207}Pb/^{206}Pb$ ages.

Analytical results for zircons, baddeleyites and titanites are listed in Tables 2, 3 and 4.

A.2. *LA-MC-ICP-MS methodology*

All zircons were mounted in epoxy in 2.5-cm-diameter circular grain mounts and polished until the zircons were just revealed. Images of zircons were obtained using the optical microscope (Leica MZ 125) and back-scatter electron microscope (Jeol JSM 5800). Zircon grains were dated with laser ablation microprobe (New Wave UP213) coupled to a MC-ICP-MS (Neptune) at the Isotope Geology Laboratory of the Rio Grande do Sul Federal University in Brazil. Isotope data were acquired in static mode with spot size between 15 and 40 μm. Laser-induced elemental fractional and instrumental mass discrimination were corrected using reference zircon (GJ-1) (Jackson et al., 2004). Two GJ-1 analyses were

carried out after every ten sample zircon spots. The external error was calculated after propagation error of the GJ-1 mean and the individual sample zircon (or spot).

A.2.1. Collector configuration

The collector configuration used for simultaneous measurements of Th, U, Pb and Hg isotopes is as follows:

^{202}Hg	$^{204}Hg+ ^{204}Pb$	^{205}Pb	^{206}Pb	^{207}Pb	^{208}Pb		^{232}Th	^{238}U
MIC3	MIC4	MIC5	L4	MIC6	L3	Axial	H2	H4

The gain calibration of Faraday cups as well the cross calibration between the L4 cup against the MIC 3, 4 and 6 were carried out before the laser section. The MIC3 to MIC 5 are attached to the L4 faraday cup, and the MIC6 is attached to the L3.

Because the multicollector system involves 3 ion counters and 5 conventional Faraday collectors, the gain and cross calibration has to be performed routinely. The gain factor to calibrate Faraday measurements is calculated applying a constant signal of 33.0 V. The cross calibration used to calculate necessary conversion factors (voltage to cps) is achieved using a 220 ppt Neptune solution with addition of 200 ppt Th and an efficient nebulizer system. A calculated convertion value of 62,500 cps/mV was used.

The various ratios are obtained simultaneously and appropriately corrected. However, because of inherent fractionations during laser ablation, these ratios vary during analysis and require different approaches to estimate reliable data. As illustrated for the standard zircon, the $^{207}Pb/^{206}Pb$ ratios do not fractionate visibly like the $^{206}Pb/^{238}U$ ratios, which involve two different elements with own chemical and physical properties. Pb is more volatile than U, which condensates progressively on the walls of the pit formed during the laser ablation process. We routinely adopt the average of the $^{207}Pb/^{206}Pb$ determinations as the representative value of the sample, and for $^{206}Pb/^{238}U$, we assume the extrapolated value for t (time)=0. Outliers that do not show good alignment are also discarded. Other ratios such as

$^{206}Pb/^{207}Pb$ and $^{232}Th/^{238}U$, are also taken into account in the extrapolated ratios when they are applicable or exhibit the same trend of fractionation. These ratios are usually quite close to the expected values.

The conversion factors are calculated based on available data for standard used and applied for unknown samples. Thus, a homogeneous standard is of paramount importance. The GJ-1 standard (GEMOC ARC National Key Center) meets the requirements for the methods used in our laboratory, and the ratios $^{206}Pb^*/^{238}U$, $^{207}Pb^*/^{206}Pb^*$ and $^{232}Th/^{238}U$ are homogeneous during the entire "bracket" technique, a standard-samples-standard analysis.

A. 2.2. Mass bias correction, External correction and laser conditions

The isotope ratios and inter-element fractionation of data obtained by MC-ICP-MS instrument were evaluated by interspersing the GJ-1 standard zircon on every set of 4, 6, 8 or 10 zircon samples (spots). The number of analyzed spots varied depending on the zircon homogeneity and the amount of Pb and U in the zircon. The GJ-1 standard zircon was used to estimate the necessary corrections for the external corrections and internal instrumental fractionation. The GJ-1 zircon and sample were assembled in the same mounting. The spot size of laser herein used was mostly of 25 μm, but the spot sizes were 40 μm and 15 μm for the zircon phases with a low amount of ^{207}Pb (under 10,000 cps) and for small zircon grains (<30 μm of diameter), respectively.

The repetition rate of the laser was 10 Hz. The energy varied from 0.3 to 1.1 mJ/ pulse, and the corresponding spot size from 25μm to 40 μm. The data acquisition occurred in 50 cycles of 1.048s of integration time, and the masses 202, 204, 206,207, 208, 232, and 238 were collecting simultaneously. For every standard and sample set, blank values in same conditions as the standard and sample were also measured. The average blank values were subtracted from all individual cycle measurements. The ^{204}Pb value was corrected for ^{204}Hg by assuming a $^{202}Hg/^{204}Hg$ ratio equal to 4.355.

A.2.3. Operation conditions for LA-MC-ICP-MS

Laser operating conditons	
Laser type: New Wave UP213	MC-ICP-MS Neptune
Laser output power: 6j/cm^2 Shot repetition rate:10 Hz Laser spot: 25 and 40 μm	Cup configuration: Faradays ^{206}Pb, ^{208}Pb, ^{232}Th, ^{238}U MIC's ^{202}Hg, ^{204}Hg+^{204}Pb, ^{20}7Pb Gas input: Coolant flow (Ar) 15 l/min Auxiliary flow (Ar) 0.8 l/min Carrier flow 0.75 l/min (Ar) + 0.45 l/min (He) Acquisition: 50 cycles of 1.048 s

A.2.4. Common Pb correction

The usual method for common-lead corrections on zircons (based on the non-radiogenic ^{204}Pb isotope) is not appropriate when using the laser technique, because the ^{204}Pb signal is strongly affected by ^{204}Hg. The majority of the ^{204}Hg comes from gases (Ar and He) that are required in the ICP and ablation procedure. After the Hg correction based on ^{202}Hg is measured, the common ^{204}Pb is insignificant in most situations. For instance, a typical signal intensity of the ^{204}Hg during laser ablation of the standard zircon is the 600-1000 cps range, and the calculated count rate for ^{204}Pb is less than statistical error of ca. 25-33 cps. We assume that the ^{204}Pb values obtained from zircons grains contain some common Pb, and we also assume a concordant age of ^{206}Pb/^{238}Pb and ^{207}Pb/^{206}Pb as the estimated age. In this case, we estimate the radiogenic composition of ^{206}Pb and Pb^{207} using the following equation for a fraction (f) of non-radiogenic ^{206}Pb (Williams, 1998):

$$f_{206} = \frac{[^{206}\mathrm{Pb}/^{204}\mathrm{Pb}]_c}{[^{206}\mathrm{Pb}/^{204}\mathrm{Pb}]_s}$$

$$f_{207} = \frac{[^{207}\mathrm{Pb}/^{204}\mathrm{Pb}]_c}{[^{207}\mathrm{Pb}/^{204}\mathrm{Pb}]_s}$$

For the common lead isotope composition, we assume the isotope composition evolve as proposed by Stacey and Kramers (1975). This assumption is required to determine an initial estimated age.

The $^{207}Pb/^{206}Pb$ and $^{206}Pb/^{238}U$ ratios were corrected after the the f_{206} and f_{207} were determined for each cycle. The cycles with values of f_{206} above 0.0025 are not usually included in the age calculation.

A.2.5. Calculation of the ratios and error estimation

After blank and common Pb corrections, the ratios and their absolute errors (one sigma level) of $^{206}Pb^*/^{238}U$, $^{232}Th/^{238}U$ and $^{206}Pb^*/^{207}Pb^*$ were calculated, using a Excel sheet. Because the $^{206}Pb^*/^{238}U$ usually produces a linear fractionation, we used the intercept method for laser induced Pb/U fractionation to correct the ratio according to the formulation proposed by Youden (1951) and adopted by Kosler et al., (2002)**.** The uncertainty of the fractionation-corrected ratio was calculated as one SD of the intercept ($\sigma R(o)$), which is the isotope ratio at the start of laser ablation.

The internal derived errors were calculated in the conventional way by taking account the uncertainties (1 SD) on the respective background signals.

For the $^{232}Th/^{238}U$ and $^{207}Pb^*/^{206}Pb^*$ ratios, the mean values were used after discarding the outliers. In some cases, the $^{232}Th/^{238}U$ and $^{207}Pb^*/^{206}Pb^*$ ratios show a slightly fractionation. Laser-induced fractionation was applied to obtain the R(o) of these ratios.

A.3. *Sm–Nd methodology*

Whole-rock powders were spiked with mixed ^{149}Sm–^{150}Nd tracer and dissolved in a Teflon vial using an HF–HNO3 mixture and 6N HCl until complete material dissolution. Column procedures used cationic AG-50W-X8 (200–400 mesh) resin in order to separate REE, followed by Sm and Nd separation using anionic poly-Teflon HDEHP LN-B50-A (100–200 mesh), resin according to Patchett and Ruiz (1987). Each sample was dried to a solid and then loaded with $0.25NH_3PO_4$ on an double filament assemblys. Isotopic ratios were measured in static mode with a Thermo*Finnigan* TRITON multi-collector mass spectrometer at the Laboratório de Geologia Isotópica of the Universidade Federal do Rio Grande do Sul (Brazil). We normally collected 100–120 ratios with a 1-V 88Sr beam and a 0.5–1-V ^{144}Nd

beam. Nd ratios were normalized to $^{146}Nd/^{144}Nd= 0.7219$. All analyses were adjusted for instrumental bias due to periodic adjustment of collector positions as monitored by measurements of our internal standards. Measurements for the Nd Spex $^{143}Nd/^{144}Nd=$ 0.511130 (±0.000010). Total blanks average were <100 pg for Sm and <500 pg for Nd. Correction for blank was insignificant for Nd isotopic compositions and generally insignificant for Sm/Nd ratios. Neodymium crustal residence ages (T_{DM}) were calculated following the depleted mantle model of De Paolo (1981). Nd_t values were calculated using the U–Pb SHRIMP or U–Pb LA-ICP-MS ages from this work (Table 5).

A.4. *Sr isotopes methodology*

Samples for Rb-Sr isotopic analysis were mixed with solutions of ^{84}Sr and ^{87}Rb tracer in order to determine the concentrations of two elements. Rb and Sr were separated from samples using conventional cation exchange techniques. About 100 mg of powder sample was mixed with the tracer solution and dissolved in HF:HNO_3 in Tefloncapsules Savillex. The ion separation was performed on columns packed with AG 50W 8X resin previously equilibrated with HCl 2.5N. The Rb and Sr fractions were separately deposited on Re filaments and analyzed in static mode in the mass spectrometer VG Sector multicoletor, the LGI. Corretion for mass fractionation is carried out using $^{88}Sr/^{86}Sr$ of 8.37521. σ 2 errors in $^{87}Sr/^{86}Sr$ and $^{87}Rb/^{86}Sr$ ratios were always better than 0.01% and 0.1% respectively.

References

Almeida, F.F.M., 1974. Evolução tectônica do Craton do Guaporé comparada com a do Escudo Báltico. Revista Brasileira de Geociências 4, 191-204 (in Portuguese).

Alvarez, J., Cordani, U.G., 1980. Precambrian basement within the septentrional Andes: age and geological evolution. 26th International Geological Congress, Abstract 1, 10.

Amaral, G., 1974. Geologia pré-cambriana da Região Amazônica. Tese de Livre Docência, Instituto de Geociências, Universidade de São Paulo, 212 p (in Portuguese).

Bettencourt, J.S., Dall'Agnol, R., 1987. The rondonian tin-bearing anorogenic granites and associated mineralization, in: International Symposium on Granites and Associated Mineralization. Excursion Guide. Salvador: SME-BA, pp. 49-87.

Bettencourt, J.S., Leite Jr. W.B., Ruiz, A.S., Matos, R., Payolla, B.L., Tosdal, R.M., 2010. The Rondonian-San Ignacio Province in the SW Amazonian Craton: An overview. Journal of South American Earth Sciences 29, 28-46.

Boger, S.D., Raetz, M., Giles, D., Etchart, E., Fanning, C.M., 2005. U–Pb age data from the Sunsas region of eastern Bolivia, evidence for the allochtonous origin of the Paraguá Block. Precambrian Research 139, 121-146.

Brito Neves, B.B., Cordani, U.G., 1991. Tectonic evolution of South America during the Late Proterozoic. Precambrian Research 53, 23-40.

Cordani, U.G., Teixeira, W., 2007. Proterozoic accretionary belts in the Amazonian Craton, in: Hatcher, R.D., Jr. Carlson, M.P., McBride, J.H., Martinez Catalan, J.R. (Eds.), 4-D Framework of Continental Crust: Geological Society of America Memoir 200, 297-320.

Cordani, U.G., Teixeira, W., D'Agrella-Filho, M.S., Trindade, R.I., 2009. The position of the Amazonian Craton in supercontinents. Gondwana Research 15, 396-407.

D'Agrella-Filho, M.S., Trindade, R.I. F., Elming, S.A., Teixeira, W., Yokoyama, E., Tohver, E., Geraldes, M.C., Pacca, I.G., Barros, M.A.S., Ruiz, A.S., 2012. The 1.42 Ga Indiavaí Mafic Intrusive (SW Amazonian Craton): Paleomagnetic results and implications for the Columbia supercontinent configuration. Gondwana Research (in press).

Dalziel, I., 1992b. Antarctica; a tale of two supercontinents? Earth and Planetary Science Letters 20, 501-526.

De Paolo, D.J., 1981. A neodymium and strontium isotopic study of the Mesozoic calc-alkaline granitic batholiths of the Sierra Nevada and Peninsular Ranges, California. Journal of Geophysical Research 86, 10470-10488.

Geraldes, M.C., Van Schmus, W.R., Condie, K.C., Bell, S., Teixeira, W., Babinski, M., 2001. Proterozoic Geologic Evolution of the SW part of the Amazonian Craton in Mato Grosso State, Brazil. Precambrian Research 111, 91-128.

Gill, J.B., 1981. Orogenic Andesites and Plate Tectonics, Springer-Verlag, Berlin.

Hasui, Y., Haralyi, Nicolau, E., Schhobbenhaus, C. 1984. Elementos geofísicos e geológicos da Região Amazônica: Subsídios para o modelo geodinâmico, in: Symposium Amazonico 2, Manaus. Anais: DNPM, p.129-47 (in Portuguese).

Ibanez-Mejia, M., Ruiz, J., Valencia, V.A., Cardona, A., Gehrels, G., Mora, A., 2011. The Putumayo Orogen of Amazonia and its implications for Rodinia reconstructions: New U-Pb geochronological insights into the Proterozoic tectonic evolution of northwestern South America. Precambrian Research 191, 58-77.

Ishikawa, T., Nagaishi, K., Umino, S., 2002. Boninitic volcanism in the Oman ophiolite: implications for thermal conditions during transition from spreading ridge to arc. Geology 30, 899-902.

Jackson, S.E., Pearson, N.J., Griflin, W.L., Belousova, E.A., 2004. The application of laser ablation-inductively coupled plasma-mass spectrometry to in situ U–Pb zircon geochronology. Chemical Geology 211, 47-69.

Johansson, A., 2009. Baltica, Amazonia and the SAMBA connection—1000 million years of neighbourhood during the Proterozoic? Precambrian Research 175, 221-234.

Kosler, J., Fonneland, H., Sylvester, P., Tubrett, M., Pedersen, R.B., 2002. U-Pb dating of detrital zircons for sediment provenance studies—a comparison of laser ablation ICPMS and SIMS techniques. Chemical Geology 182, 605-618.

Kroonenberg, S.B., 1982. A Grenvillian Granulite Belt in the Colombian Andes and its relation to the Guiana Shield. Geologie en Mijnbouw 61, 325-333.

Li, Z.X., Bogdanova, S.V., Collins, A.S., Davidson, A., De Waele, B., Ernst, R.E., Fitzsimons, I.C.W., Fuck, R.A., Gladkochub, D.P., Jacobs, J., Karlstrom, K.E., Lu, S.,

Natapov, L.M., Pease, V., Pisarevsky, S.A., Thrane, K., Vernikovsky, V., 2008. Assembly, configuration, and break-up history of Rodinia: a synthesis. Precambrian Research 160, 179-210.

Litherland, M., Annels, R.N., Appleton, J.D., Berrange, J.P., Bloomfield, K., Darbyshire, D.P.F., Fletcher, C.J.N., Hawkins, M.P., Klinck, B.A., Mitchell, W.I., O'Connor, E.A., Pitfield, P.E.J., Power, G., Webb, B.C., 1986. The geology and mineral resources of the Bolivian Precambrian Shield. Overseas Memoir British Geological. Survey 9, 153 pp.

Litherland, M., Annels, R.N., Darbyshire, D.P.F., Fletcher, C.J.N., Hawkins, M.P., Klink, B.A., Mitchell, W.I., O'Connor, E.A., Pitfield, P.E.J., Power, G., Webb, B.C., 1989. The Proterozoic of eastern Bolivia and its relationship to the Andean mobile belt. Precambrian Research 43, 157-174.

Ludwig, K.R., 1999. Using ISOPLOT/Ex, version 2: a geochronological toolkit for Microsoft Excel. Berkeley Geochronological Center Special Publication Ia, 47 pp.

Ludwig, K.R., 2002. Squid 1.02, a user's manual. Berkeley Geochronological Center, Special Publication 2 (Berkeley, California, USA), 21 pp.

Matos, J.B., Schorscher, J.H.D., Geraldes, M.C., Souza, M.Z.A., Ruiz, A.S. 2004. Petrografia, geoquímica e geocronologia das rochas do Orógeno Rio Alegre, Mato Grosso: um registro de crosta oceânica Mesoproterozóica no SW do Cráton Amazônico. Geologia USP – Série Científica 4, 75-90 (in Portuguese).

Matos, R., Teixeira, W., Geraldes, M.C., Bettencourt, J.S., 2009. Geochemistry and isotopic evidence of the Pensamiento Granitoid Complex, Rondonian–San Ignacio province, eastern Precambrian Shield of Bolivia: petrogenetic constraints for a Mesoproterozoic magmatic arc setting. Revista Geologia USP série científica 9 (2), 89-117.

Mishra D.C., Vijaya Kumar, V., 2005. Evidence for Proterozoic collision from airborne magnetic and gravity studies in southern granulite terrain, India and signatures of recent tectonic activity in the Palghat Gap. Gondwana Research 8, 43-54.

Patchett, P.J., Ruiz, J., 1987. Nd isotopic ages of crust formation and metamorphism in the Precambrian of eastern and southern Mexico. Contributions to Mineralogy and Petrology 96, 523-528.

Payolla, B.L., Bettencourt, J.S., Kozuch, M. Leite Jr., W. B., Fetter, A.H., Van Schmus, W.R., 2002. Geological evolution of the basement rocks in the east-central part of the Rondonia Tin Province, SW Amazonian Craton, Brazil: U-Pb and Sm-Nd isotopic constraints. Precambrian Research 119, 141-169.

Perfit, M.R., Gust, D.A., Bence, A.E., Arculus, R.J., Taylor, S.R., 1980. Chemical characteristics of island arc basalts: implications of mantle sources. Chemical Geology 30, 227-256.

Plank, T., Langmuir, C.H., 1998. The chemical composition of subducting sediment and its consequences for the crust and mantle. Chemical Geology 145, 325-394.

Priem, H.N.A., Kroonenberg, S.B., Boelrijk, N.A.I.M., Hebeda, E.H., 1989. Rb-Sr and K-Ar evidence for the presence of a 1.6 Ga basement underlying the 1.2 Ga Garzón-Santa Marta granulite belt in the Colombian Andes. Precambrian Research 42, 315-324.

Quadros, M.L.E.S., Rizzotto, G.J., 2007. Geologia e Recursos Minerais do Estado de Rondônia. Texto Explicativo do Mapa Geológico e de Recursos Minerais do Estado de Rondônia, escala 1:1.000.000. Sistema de Informações Geográficas – SIG. Serviço Geológico do Brasil – CPRM, Porto Velho, 154 p (in Portuguese).

Ribeiro, P.S.E., Duarte, T.B., 2010. Geologia e Recursos Minerais das Folhas Rio Guariba e Rio Aripuanã: escala 1:250.000. Projeto Noroeste -Nordeste de Mato Grosso; Programa Geologia do Brasil – PGB. Goiânia: CPRM, Relatório Interno, 248pp (in Portuguese).

Rizzotto, G.J., 1999. Petrologia e geotectônica do Grupo Nova Brasilândia, Rondônia. MSc. Dissertation. Federal University of Rio Grande do Sul. Porto Alegre, Brazil (in Portuguese).

Rizzotto, G.J., Bettencourt, J.S., Teixeira, W., D'Agrella-Filho, M.S., Vasconcelos, P., Basei, M.A.S., Onoe, A., Passarelli, C.R., 2002a. Geologia e Geocronologia da Suíte Metamórfica Colorado e suas encaixantes, SE de Rondônia: implicações para a evolução mesoproterozóica do Craton Amazônico. Geologia USP, Série Científica 2, 41-56.

Rizzotto G.J., Quadros M.L.E.S., Silva, L.C., Armstrong, R., Almeida, M., 2002b. O Granito Aripuanã: datação U-Pb (Shrimp) e implicações metalogenéticas, in: Sociedade Brasileira de Geologia, Congresso Brasileiro de Geologia 41, Anais, p. 469 (in Portuguese).

Rizzotto, G. J., Quadros, M. L. E. S., 2007. Margem Passiva e Granitos Orogênicos do Ectasiano em Rondônia, in: Simpósio de Geologia da Amazônia 10. Porto Velho. Anais eletrônico, SBG-Núcleo Norte (in Portuguese).

Rizzotto, G.J., Hartmann, L.A., 2012. Geological and geochemical evolution of the Trincheira Complex, a Mesoproterozoic ophiolite in the southwestern Amazon craton, Brazil. Lithos (in press).

Rollinson, H., 1993. Using geochemical data: evaluation, presentation, interpretation: Pearson Education Limited, Longman, Singapore.

Ruiz, A.S., Geraldes, M.C., Matos, J.B., Teixeira, W., Van Schmus, W.R., Schmitt, R., 2004. The 1590-1520 Ma Cachoeirinha magmatic arc and its tectonic implications for the Mesoproterozoic. SW Amazonian Craton crustal evolution. Anais da Academia Brasileira de Ciências 76, 807-824.

Ruiz, A.S., 2005. Evolução geológica do sudoeste do Cráton Amazônico, região limítrofe Brasil-Bolívia, Mato Grosso. Ph.D. Thesis, São Paulo State University, Rio Claro, São Paulo, Brazil (in Portuguese).

Sadowski, G.R., Bettencourt, J.S., 1996. Mesoproterozoic tectonic correlations between eastern Laurentia and western border of the Amazon Craton. Precambrian Research 76, 213-227.

Saes, G.S., Fragoso Cesar, A.R.S., 1996. Acresção de terrenos mesoproterozóicos no

SW da Amazônia, in: 39th Congresso Brasileiro de Geologia, Boletim de Resumos Expandidos, Salvador, Brazil, SBG, pp. 124-126 (in Portuguese).

Saes, G.S., 1999. Evolução tectônica e paleogeográfica do Aulacógeno Aguapei (1.2–1.0 Ga) e dos terrenos do seu embasamento na porção sul do Cráton Amazônico. Ph.D. Thesis, University of São Paulo, São Paulo, Brazil (in Portuguese).

Santos, J.O.S., Rizzotto, G.J., Potter, P., Mcnaughton, N., Matos, R., Hartmann, L., Chemale jr, F., Quadros, M., 2008. Age and autochthonous evolution of the Sunsás Orogen in West Amazon Craton based on mapping and U Pb geochronology. Precambrian Research 165, 120-152.

Saunders, A.D., Norry, M.J., Tarney, J., 1991. Fluid influence on the trace element compositions of subduction zone magmas. Philosophical Transactions of the Royal Society of London 335, 377-392.

Scandolara, J.E., Rizzotto, G.J., 1998. Programa Levantamentos Geológicos Básicos do Brasil. Folha SC.20-Z-C-V-Paulo Saldanha. Estado de Rondônia. Escala 1:100.000. Brasilia: CPRM, (Convênio DNPM/CPRM). Relatório interno (in Portuguese).

Schobbenhaus, C., 2001. Geological map of South America. CGMW-CPRM Geological Survey of Brazil-DNPM co-edition.

Shervais, J.W., 2001. Birth, death and resurrection: the life cycle of suprasubduction zone ophiolites. Geochemistry, Geophysics, Geosystems 2: Paper 2000GC000080.

Stacey, J.S., Kramers, J.D., 1975. Approximation of terrestrial lead isotope evolution by a two-stage model. Earth and Planetary Science Letters 26, 207-221.

Stern, R.J., Bloomer, S.H., 1992. Subduction zone infancy: examples from the Eocene Izu–Bonin–Mariana and Jurassic California. Geological Society of America Bulletin 104, 1621-1636.

Sun, S.S., McDonough, W.E., 1989. Chemical and isotopic systematics of oceanic basalts: implications for mantle composition and processes, in: Saunders, A.D., Norry, M.J. (Eds.), Magmatism in the Ocean Basins. Geological Society, (London) Special Publication 42, pp. 313-345.

Tassinari, C.C.G., Macambira, M.J.B., 1999. Geochronological provinces of the Amazonian Craton. Episodes 22, 174-182.

Tassinari, C.C.G., Bettencourt, J.S., Geraldes, M.C., Macambira, M.J.B., Lafon. J.M., 2000. The Amazonian Craton, in: Cordani, U.G., Milani, E.J., Thomaz Filho, A., Campos, D.A. (Eds.), Tectonic evolution of South America. 31st International Geological Congress, Rio de Janeiro, Brazil, pp. 41-95.

Teixeira, W., Bettencourt, J.S., Girardi, V.A.V., Onoe, A.T., Sato, K., 2006. Mesoproterozoic mantle heterogeneity in SW Amazonian Craton: $^{40}Ar/^{39}Ar$ and Nd-Sr evidence from mafic–felsic rocks, in: Hansji, E., Mertanen, S., Rämö, T., Vuollo, J. (Orgs.), Dyke Swarms – Time Markers of Crustal Evolution. Proceedings of the V International Dyke Conference, 2006, vol. 1, Taylor and Francis Group, London, pp. 113-129.

Thomas, M.D. (1992). Ancient collisional continental margins in the Canadian shield: geophysical signatures and derived crustal transects, in: Bartholomew, M.J., Hyndman, D.W., Mogk, D.W., Mason, R. (Eds.), Basement tectonics, Kluwar Academic Publ., Dordrecht, The Netherlands, v. 8, pp. 5-25.

Tohver, E., van der Pluijm, B., Van der Voo, R., Rizzotto, G.J., Scandolara, J.E., 2002. Paleogeography of the Amazon craton at 1.2 Ga: Early Grenvillian collision with the Llano segment of Laurentia, Earth and Planetary Science Letters 199, 185-2000.

Tohver, E., van der Pluijm, B.A., Mezger, K., Scandolara, J.E., Essene, E.J., 2004. Significance of the Nova Brasilândia Metasedimentary Belt in western Brazil: Redefining the Mesoproterozoic boundary of the Amazon craton. Tectonics 23, TC6004, doi:10.1029/2003TC001563.

Tohver, E., van der Pluijm, B.A., Scandolara, J.E., Essene, E.J., 2005a. Late Mesoproterozoic Deformation of SW Amazonia (Rondônia, Brazil): Geochronological and Structural Evidence for Collision with Southern Laurentia. Journal of Geology 113, 309-323.

Tohver, E., van der Pluijm, B.A., Mezger, K., Scandolara, J.E., Essene, E.J., 2005b. Two stage tectonic history of the SW Amazon craton in the late Mesoproterozoic: identifying a cryptic suture zone. Precambrian Research 137, 35-59.

Tohver, E., Teixeira, W., van der Pluijm, B., Geraldes, M., Bettencourt. J.S., Rizzotto, G.J., 2006. Restored transect across the exhumed Grenville orogen of Laurentia and Amazonia, with implications for crustal architecture. Geology 34, 669-672.

Williams, I.S., 1998. U-Th-Pb geochronology by ion microprobe, in: McKibben, M.A., Shanks III, W.C., Rydley, W.I. (Eds.), Applications of Microanalytical Techniques to Understanding Mineralizing Processes. Reviews in Economic Geology 7, 1-35.

Youden, W. J., 1951. Statistical methods for chemists. Journal of the Royal Statistical. New York, Wiley.

Zindler, A., Hart, S., 1986. Chemical geodynamics. Annual Review of Earth and Planetary Sciences 86, 493-570.

FIGURE CAPTIONS

Figure 1- Simplified map of the southwestern Amazon craton showing the approximate boundaries of the main terranes and belts, tectonic elements, lithologic units, and location of dated samples (modified after Schobbenhaus, C., 2001 and Rizzotto and Hartmann, 2012). Guaporé suture zone is indicating by hatched zone.

Figure 2- Aeromagnetic anomaly data (Image of the Analytical Signal Amplitude) for the southwestern Amazon craton. The Guaporé suture (white line) is marked by a strong magnetic anomalies whith 1000 km long, approximately.

Figure 3- Simplified geological map of our study area in southeastern region of Rondônia and southwestern of Mato Grosso, Brazil and location of dated samples.

Figure 4- Back-scattered electron images of analyzed zircon crystals. (a, b) Sample GP4-110, mafic granulite, Trincheira Complex; (c, d) Sample SJ-2430a, mafic granulite, Trincheira Complex; (e, f) Sample GR-793, banded amphibolite, Trincheira Complex; (g, h) Sample GR-

737, fine-grained amphibolite, Trincheira Complex. Black circles indicate SHRIMP analysis position; spot number and age (Ma) shown.

Figure 5- Back-scattered electron images of analyzed zircon and titanite crystals. (a, b) Sample NM-189, tonalitic gneiss, Rio Galera Complex; (c, d) Sample GR-337, tonalitic orthogneiss of the São Felipe Complex; (e, f) Sample F1GR1, biotite syenogranite, Praia Alta granite; (g) Sample GR-750, tonalitic gneiss, and (h) Sample GRT-06, Santa Bárbara amphibolitic gneiss, Rio Alegre terrane.

Figure 6 – U-Pb concordia diagrams of the samples analyzed: (6a) Sample GP4-110; (6b) Sample SJ-2430a; (6c) Sample GR-793; (6d) Sample GR-737; (6e) Sample NM-189; (6f) Sample GR-337. $^{206}Pb/^{207}Pb$ ages are stated to 2σ (95%) confidence limits while the illustrated error ellipses reflect 1 σ confidence limits (68%).

Figure 7 - U-Pb concordia diagrams of the samples analyzed: (7a) Sample GR-750; (7b) Sample F1GR1; (7c) Sample NM-318; (7d) Sample NM-177; (7e) Sample GRT-06.

Figure 8- U-Pb concordia diagrams of the samples of the collisional phase: (8a) Sample GR-127; (8b) Sample NM 42; (8c) Sample GR-143; (8d) Sample GR-145; (8e) Sample NM 166.

Figure 9 – Nd and Sr isotopic data for the Trincheira mafic-ultramafic Complex.

Figure 10 – Simplified geodynamic model for the evolution of the Trincheira ophiolite (see text for explanation).

Figure 11 – $\varepsilon_{Nd(t)}$ versus La/Yb diagram for select samples of the Trincheira mafic-ultramafic Complex. PM = primitive mantle, after Sun and McDonough (1989).

Figure 12 – Diagrams $^{87}Sr/^{86}Sr$ versus Th/Yb and $^{87}Sr/^{86}Sr$ versus Rb/Sr showing that the samples of the Trincheira Complex form a crude positive array.

TABLE CAPTIONS

Table 1 – Summary of the main geological, geochronological and tectonic characteristic of the Rondônia-Juruena Province and Paraguá Terrane.

Table 2- U-Pb zircon and titanite SHRIMP isotopic data from Trincheira ophiolite and related rocks.

Table 3- U-Pb zircon data from the Praia Alta and Rio Piolho granites. Data were obtained by LA-MC-ICP-MS.

Table 4- U-Pb zircon and baddeleyite SHRIMP isotopic data from dacite, granite and gabbro of the collisional phase.

Table 5- Sr, Nd isotopic and incompatible trace element data for the select samples of Trincheira mafic-ultramafic Complex.

Table 1

Provinces/ Terranes	Major tectonic events	Geological unit	Lithological association	U-Pb age (Ma)	T_{DM} (Ga)	Tectonic environments
Rondônia-Juruena Province[a]	Anorogenic magmatism	Serra da Providência Intrusive Suite	AMCG associations	1570-1537	1.89 -1.76	Anorogenic intrusives (AMCG- type)
	Cachoerinha orogen	Alvorada and Santa Cruz Intrusive Suite	Syenogranite, monzogranite and granodiorite	1560-1520	1.83-1.77	Continental magmatic arc (Andean-type)
	Quatro Cachoeiras orogeny	Quatro Cachoeiras Metamorphic Suite	Migmatites, paragneiss and calc-silicatic rocks	1670-1630	2.05-1.85	High-grade orogenic terrain
	Alto Jauru Terrane	Alto Jauru Group, Santa Fé, Aliança and Cabaçal orthogneisses	volcano-sedimentary sequences and tonalitic gneiss	1790-1750	2.1-1.93	Greenstone belt and related rocks
	Jamari magmatic arc	Jamari Complex, Mutum-Paraná Formation	Qz-dioritic, amphibolitic and tonalitic gneiss, volcano-sedimentary sequences	1760-1730	2.2-1.96	Continental magmatic arc, arc related basin
	Juruena magmatic arc	Colíder Group, Paranaíta Intrusive Suíte, Juruena Complex, Roosevelt Group	Plutonic-volcanic acid, tonalitic and granodioritic gneiss, mafic rocks, monzogranite and granodiorite	1820-1740	2.2-2.1	Continental magmatic arc, retroarc basin
Paraguá Terrane[b]	Basement rocks (pre-San Ignacio orogeny)	San Ignacio Group	Quartzite, feldspathic psammites and pelitic schist	< 1690	?	Low to medium-grade orogenic belt
		Chiquitania Complex	Migmatitic semipelitic gneisses and granite gneisses	1764-1678	1.86-1.74	
		Lomas Manechi Complex	Calc-silicate and psammitic gneiss, granulitic gneiss, granitic sills	1818-1663	2.07-1.74	High to medium-grade orogenic terrain

References: [a] Payolla et al. (2002), Silva et al. (2002), Rizzotto & Quadros (2005),Tohver et al. (2005), Scandolara (2006), Ruiz (2006), Cordani and Teixeira, 2007,Quadros and Rizzotto (2007), Santos et al. (2008). [b] Litherland and Bloomfield (1981), Berrangé and Litherland (1982), Litherland et al. (1986), Boger et al. (2005), Ruiz et al. (2007), Santos et al. (2008), Matos et al. (2009).

Table 2

Spot	U ppm	Th Ppm	Th U	^{206}Pb ppm	4f^{206} %	Isotopic ratios ^{207}Pb/^{206}Pb	^{207}Pb/^{235}U	^{206}Pb/^{238}U	^{208}Pb/^{232}Th	Ages ^{206}Pb/^{238}U	^{207}Pb/^{206}Pb	Disc %
GP4-110, Trincheira Complex, mafic granulite, zircon												
C.3-1	249	119	0.49	52.8	0.04	0.0912 ± 0.7	3.1069 ± 1.59	0.2470 ± 1.40	0.0712 ± 2.58	1423 ± 18	1451 ± 14	2
C.3-2	98	56	0.59	20.3	0.01	0.0918 ± 1.1	3.0684 ± 1.48	0.2424 ± 0.94	0.0699 ± 1.72	1399 ± 12	1464 ± 22	4
C.4-1	234	83	0.37	48.8	0.06	0.0903 ± 0.9	3.0213 ± 1.14	0.2428 ± 0.71	0.0704 ± 1.37	1401 ± 9	1431 ± 17	2
C.5-1	134	69	0.53	28.9	0.06	0.0913 ± 1.0	3.1673 ± 1.79	0.2517 ± 1.47	0.0720 ± 2.32	1447 ± 19	1452 ± 19	0
C.1-1	117	76	0.67	24.3	0.00	0.0919 ± 1.3	3.0622 ± 1.87	0.2416 ± 1.33	0.0693 ± 2.06	1395 ± 17	1466 ± 25	5
C.6-1	199	62	0.32	41.4	0.00	0.0907 ± 1.0	3.0304 ± 1.29	0.2424 ± 0.80	0.0698 ± 1.62	1399 ± 10	1440 ± 19	3
C.5-2	74	35	0.49	16.1	0.05	0.0904 ± 1.2	3.1428 ± 2.12	0.2522 ± 1.75	0.0714 ± 2.38	1450 ± 23	1433 ± 23	-1
SJ-2430a, Trincheira Complex mafic granulite, zircon												
B.1-1	44	9	0.20	9.5	0.83	0.0917 ± 4.2	3.1564 ± 4.41	0.2497 ± 1.38	0.0794 ± 14.3	1437 ± 18	1461 ± 80	2
B213	16	3	0.18	3.2	2.51	0.0905 ± 13	2.8823 ± 13.2	0.2309 ± 2.98	0.0635 ± 58.1	1339 ± 36	1437 ± 246	7
B.4-1	85	30	0.36	17.1	0.00	0.0921 ± 1.3	2.9773 ± 1.76	0.2345 ± 1.13	0.0697 ± 2.4	1358 ± 14	1469 ± 26	8
B.6-1	11	2	0.16	2.7	3.30	0.0900 ± 13	3.2897 ± 13.7	0.2651 ± 3.10	0.0717 ± 69.7	1516 ± 42	1426 ± 256	-6
GR-793, Trincheira Complex banded amphibolite, zircon												
I.8-1	613	2.43	0.004	127.8	0.02	0.0908 ± 0.5	3.0370 ± 0.79	0.2427 ± 0.59	0.1402 ± 4.94	1401 ± 7	1442 ± 10	3
I.3-1	457	1.94	0.004	86.5	0.00	0.0895 ± 2.8	2.7192 ± 3.06	0.2204 ± 1.23	0.3133 ± 7.50	1284 ± 14	1415 ± 54	9
I.4-1	398	1.69	0.004	86.2	0.05	0.0901 ± 0.7	3.1256 ± 1.10	0.2516 ± 0.83	0.1505 ± 5.90	1447 ± 11	1428 ± 14	-1
I.9-1	86	0.02	0.000	18.5	0.02	0.0916 ± 1.4	3.1543 ± 2.19	0.2499 ± 1.66	0.7047 ± 28.2	1438 ± 21	1458 ± 27	1
I.7-1	511	1.72	0.003	109.6	0.05	0.0900 ± 0.7	3.0952 ± 1.41	0.2495 ± 1.24	0.1011 ± 7.34	1436 ± 16	1425 ± 13	-1
I.2-1	56	1.94	0.036	11.6	0.14	0.0906 ± 2.2	3.0096 ± 2.95	0.2409 ± 1.97	0.0931 ± 7.49	1391 ± 25	1439 ± 42	3
I4-23	27	0.56	0.022	5.6	0.00	0.0907 ± 3.5	3.0166 ± 4.62	0.2412 ± 2.98	0.2301 ± 11.1	1393 ± 37	1441 ± 67	3
I.11-1	137	0.58	0.004	29.7	0.00	0.0910 ± 1.2	3.1606 ± 1.92	0.2520 ± 1.53	0.1067 ± 12.1	1449 ± 20	1446 ± 22	0
GR-737, Trincheira Complex fine-grained amphibolite, zircon												
B.1-1	27	0.03	0.001	5.7	0.27	0.0904 ± 4.45	3.0193 ± 5.09	0.2423 ± 2.47	3.2133 ± 52.3	1399 ± 31	1433 ± 85	2
B.2-1	100	0.02	0.000	21.8	0.04	0.0908 ± 1.42	3.1963 ± 1.97	0.2552 ± 1.37	1.193 ± 31.2	1465 ± 18	1440 ± 25	-1
B.2-2	320	222	0.717	69.9	0.05	0.0903 ± 0.81	3.1661 ± 1.34	0.2542 ± 1.07	0.0746 ± 1.39	1460 ± 14	1433 ± 15	-2
B.2-3	303	217	0.740	67.5	0.07	0.0904 ± 0.74	3.2336 ± 1.45	0.2593 ± 1.24	0.0741 ± 1.49	1486 ± 17	1435 ± 14	-4
NM-189, Rio Galera Complex tonalitic gneiss, zircon and titanite^{T}												
1-11^{T}	9	10	1.09	1.6	12.2	0.0916 ± 31.2	2.2384 ± 31.4	0.1773 ± 3.86	0.0674 ± 18.6	1052 ± 37	1459 ± 593	28
4-14^{T}	12	15	1.23	2.3	4.97	0.0938 ± 12.1	2.6371 ± 12.2	0.2040 ± 1.91	0.0148 ± 32.8	1197 ± 21	1504 ± 229	20
G7-1	2277	63	0.03	487.2	0.02	0.0903 ± 0.23	3.0996 ± 0.80	0.2490 ± 0.76	0.0679 ± 2.24	1433 ± 10	1431 ± 4	0
G7-2	2445	61	0.03	510.7	0.00	0.0902 ± 0.23	3.0237 ± 0.79	0.2432 ± 0.76	0.0710 ± 1.74	1403 ± 10	1430 ± 4	2
G8-1	1593	40	0.03	348.3	0.02	0.0906 ± 0.30	3.1790 ± 0.83	0.2544 ± 0.78	0.0695 ± 4.14	1461 ± 10	1439 ± 6	-2
G8-2	1604	42	0.03	341.3	0.01	0.0906 ± 0.29	3.0944 ± 0.83	0.2478 ± 0.77	0.0751 ± 2.35	1427 ± 10	1438 ± 6	1
G8-3	2329	72	0.03	504.8	0.04	0.0903 ± 0.26	3.1381 ± 0.80	0.2521 ± 0.76	0.0699 ± 3.44	1449 ± 10	1431 ± 5	-1
11-1	98	57	0.60	21.2	1.12	0.0918 ± 3.69	3.1590 ± 3.90	0.2496 ± 1.27	0.0455 ± 5.94	1436 ± 16	1463 ± 70	2

Table 2_continued

						Isotopic ratios				Ages		
	U	Th	Th	^{206}Pb	4f^{206}	^{207}Pb	^{207}Pb	^{206}Pb	^{208}Pb	^{206}Pb	^{207}Pb	Disc.
Spot	ppm	ppm	U	ppm	%	^{206}Pb	^{235}U	^{238}U	^{232}Th	^{238}U	^{206}Pb	%
GR-337, São Felipe Complex, tonalitic orthogneiss, zircon												
A.4-1	1979	113	0.06	434.2	0.02	0.0904 ± 0.25	3.1810 ± 0.91	0.2553 ± 0.88	0.0719 ± 1.31	1466 ± 12	1433 ± 5	-2
A.4-2	1979	113	0.06	434.2	0.02	0.0904 ± 0.25	3.1810 ± 0.91	0.2553 ± 0.88	0.0719 ± 1.31	1466 ± 12	1433 ± 5	-2
A4-21	3848	435	0.12	801.7	0.00	0.0904 ± 0.23	3.0246 ± 0.91	0.2425 ± 0.88	0.0695 ± 1.35	1400 ± 11	1435 ± 4	2
A.3-1	3706	633	0.18	778.0	0.01	0.0904 ± 0.22	3.0478 ± 0.91	0.2444 ± 0.88	0.0687 ± 1.04	1410 ± 11	1435 ± 4	2
A2-13	1363	66	0.05	283.4	0.02	0.0906 ± 0.34	3.0200 ± 0.97	0.2420 ± 0.90	0.0688 ± 1.89	1397 ± 11	1439 ± 7	3
A.6-1	958	72	0.08	201.9	0.00	0.0907 ± 0.35	3.0695 ± 0.97	0.2454 ± 0.91	0.0718 ± 1.45	1415 ± 12	1440 ± 7	2
GR-750, tonalitic gneiss, zircon												
f.2-1	100	34	0.35	21.3	0.16	0.09095 ± 1.40	3.0875 ± 1.91	0.2462 ± 1.29	0.0665 ± 2.94	1419 ± 16	1445 ± 27	2
f.2-2	128	40	0.32	26.6	0.23	0.09213 ± 1.35	3.0518 ± 1.74	0.2402 ± 1.09	0.0694 ± 2.89	1388 ± 14	1470 ± 26	6
f.3-1	152	42	0.28	33.4	0.17	0.09114 ± 1.18	3.1955 ± 1.55	0.2543 ± 1.01	0.0707 ± 2.79	1461 ± 13	1449 ± 23	-1
f.4-1	247	135	0.57	55.5	0.11	0.09212 ± 0.95	3.3152 ± 1.85	0.2610 ± 1.59	0.0724 ± 2.16	1495 ± 21	1470 ± 18	-2
f.4-2	187	78	0.43	40.6	0.05	0.09163 ± 1.05	3.1945 ± 1.95	0.2528 ± 1.64	0.0709 ± 2.26	1453 ± 21	1460 ± 20	0
f.8-1	164	49	0.31	34.8	0.18	0.09117 ± 1.19	3.0927 ± 1.56	0.2460 ± 1.00	0.0692 ± 2.62	1418 ± 13	1450 ± 23	2
F1GR1, Praia Alta, equigranular syenogranite, zircon												
C.1-1	469	158	0.35	100.2	0.00	0.09044 ± 0.48	3.1036 ± 1.08	0.2489 ± 0.96	0.0729 ± 1.21	1433 ± 12	1435 ± 9	0
C4-1-4	697	200	0.30	144.1	0.00	0.08976 ± 0.49	2.9776 ± 1.13	0.2406 ± 1.01	0.0722 ± 1.30	1390 ± 13	1420 ± 9	2
C.5-1	1574	10	0.01	329.9	0.01	0.09058 ± 0.31	3.0465 ± 1.01	0.2439 ± 0.96	0.0646 ± 9.73	1407 ± 12	1438 ± 6	2
C5-2-3	536	79	0.15	111.0	0.00	0.09100 ± 0.61	3.0238 ± 1.23	0.2410 ± 1.06	0.0714 ± 1.74	1392 ± 13	1447 ± 12	4
C.6-1	1076	136	0.13	227.5	0.01	0.09047 ± 0.33	3.0694 ± 0.96	0.2461 ± 0.90	0.0705 ± 1.24	1418 ± 12	1435 ± 6	1
C.7-1	327	73	0.23	71.2	0.03	0.09064 ± 0.78	3.1608 ± 1.33	0.2529 ± 1.08	0.0742 ± 2.16	1454 ± 14	1439 ± 15	-1
C.8-1	1084	615	0.59	227.9	0.01	0.09070 ± 0.33	3.0609 ± 0.98	0.2447 ± 0.92	0.0691 ± 1.77	1411 ± 12	1440 ± 6	2
GRT-06, Rio Alegre, banded amphibolite, titanite												
j.1-1	101	98	1.00	20.5	0.08	0.08845 ± 1.11	2.8854 ± 1.61	0.2366 ± 1.17	0.1884 ± 1.37	1369 ± 14	1392 ± 21	2
j.2-1	54	53	1.03	11.0	0.18	0.08952 ± 1.90	2.9569 ± 2.25	0.2396 ± 1.20	0.1613 ± 1.59	1384 ± 15	1415 ± 36	2
j.2-2	111	108	1.00	22.7	0.01	0.89105 ± 0.80	2.9061 ± 1.43	0.2368 ± 1.17	0.1888 ± 1.96	1370 ± 14	1405 ± 16	2
j.3-1	37	37	1.02	7.6	0.02	0.08984 ± 1.55	2.9188 ± 2.00	0.2356 ± 1.26	0.1640 ± 1.71	1364 ± 15	1422 ± 30	4
j.3-2-1	90	89	1.02	18.3	0.00	0.08840 ± 0.91	2.8679 ± 1.47	0.2353 ± 1.16	0.1515 ± 1.45	1362 ± 14	1391 ± 17	2
j.3-3	107	107	1.03	21.1	0.11	0.08866 ± 1.03	2.7958 ± 1.53	0.2287 ± 1.12	0.1601 ± 1.33	1328 ± 13	1397 ± 20	5
j.4-1	116	112	1.00	23.1	0.16	0.08866 ± 0.97	2.8352 ± 1.47	0.2319 ± 1.11	0.1512 ± 1.30	1345 ± 13	1397 ± 19	4

Notes: Isotopic ratios errors in %. All Pb in ratios are radiogenic component. Most are corrected from ^{204}Pb and some for ^{208}Pb (metamorphic, Th-poor grains or rims). Analyses lacking ^{208}Pb/^{232}Th ratio were corrected using ^{208}Pb.
Disc. = discordance, as $100-100\{t[^{206}Pb/^{238}U]/t[^{207}Pb/^{206}Pb]\}$; f206 = (common ^{206}Pb)/(total measured ^{206}Pb) based on measured ^{204}Pb. Uncertainties are 1σ.

Table 3

Spot	Isotopic ratios $^{207}Pb/^{235}U$		$^{206}Pb/^{238}U$		Rho	$^{207}Pb/^{206}Pb$		Ages $^{206}Pb/^{238}U$		$^{207}Pb/^{235}U$		$^{207}Pb/^{206}Pb$		f206	Disc %	$^{232}Th/^{238}U$
NM-318, Praia Alta porphyritic syenogranite, zircon																
B-II-01	3.09625	± 3.11	0.24718	± 1.49	0.48	0.09085	± 2.73	1424	± 21	1432	± 44	1443	± 39	0.0009	1	0.42
B-II-03	3.16801	± 2.06	0.24944	± 1.44	0.70	0.09211	± 1.47	1436	± 21	1449	± 30	1470	± 22	0.0009	2	0.31
B-II-04	3.15797	± 4.04	0.25189	± 2.53	0.63	0.09093	± 3.15	1448	± 37	1447	± 58	1445	± 45	0.0007	0	0.26
B-II-05	3.02932	± 3.02	0.24047	± 1.48	0.49	0.09137	± 2.63	1389	± 21	1415	± 43	1454	± 38	0.0014	4	0.29
B-II-06	3.19250	± 2.75	0.25107	± 1.36	0.49	0.09222	± 2.39	1444	± 20	1455	± 40	1472	± 35	0.0029	2	0.30
B-II-08	3.06922	± 2.75	0.24470	± 1.58	0.57	0.09097	± 2.25	1411	± 22	1425	± 39	1446	± 33	0.0004	2	0.24
B-II-09	3.05431	± 2.40	0.24096	± 1.44	0.60	0.09193	± 1.92	1392	± 20	1421	± 34	1466	± 28	0.0013	5	0.35
B-II-10	3.19491	± 2.63	0.25446	± 1.31	0.50	0.09106	± 2.29	1461	± 19	1456	± 38	1448	± 33	0.0002	-1	0.28
B-II-14	3.04431	± 2.32	0.24199	± 1.31	0.56	0.09124	± 1.92	1397	± 18	1419	± 33	1452	± 28	0.0008	4	0.38
B-II-15	3.09975	± 3.09	0.24450	± 1.45	0.47	0.09195	± 2.72	1410	± 20	1433	± 44	1466	± 40	0.0006	4	0.39
NM-177, Rio Piolho syenogranite, zircon																
C-IV-2	3.1239	± 1.67	0.2492	± 1.12	0.67	0.0909	± 1.24	1434	± 16	1439	± 24	1445	± 18	0.0004	1	0.40
C-IV-5	3.1722	± 1.73	0.2541	± 1.05	0.61	0.0905	± 1.37	1460	± 15	1450	± 25	1437	± 20	0.0006	-2	0.34
C-IV-6b	2.9979	± 2.47	0.2408	± 1.76	0.71	0.0903	± 1.74	1391	± 24	1407	± 35	1432	± 25	0.0005	3	0.31
C-VI-3	3.0769	± 2.73	0.2481	± 1.55	0.57	0.0900	± 2.25	1429	± 22	1427	± 39	1424	± 32	0.0016	0	0.31
C-VI-7	3.0967	± 2.36	0.2477	± 1.14	0.48	0.0907	± 2.06	1427	± 16	1432	± 34	1440	± 30	0.0008	1	0.42
C-VI-10	3.1532	± 2.16	0.2527	± 1.30	0.60	0.0905	± 1.72	1453	± 19	1446	± 31	1436	± 25	0.0010	-1	0.29
C-VI-11	3.1569	± 2.15	0.2514	± 1.10	0.51	0.0911	± 1.85	1446	± 16	1447	± 31	1448	± 27	0.0006	0	0.52
C-VI-13	2.8778	± 2.30	0.2294	± 1.27	0.55	0.0910	± 1.91	1332	± 17	1376	± 32	1446	± 28	0.0071	8	0.36
C-V1b	3.1620	± 3.14	0.2510	± 0.60	0.19	0.0914	± 3.08	1443	± 9	1448	± 45	1455	± 45	0.0038	1	0.19
C-V-2	3.0178	± 4.54	0.2431	± 0.62	0.14	0.0900	± 4.50	1403	± 9	1412	± 64	1426	± 64	0.0050	2	0.21
C-IV-4	3.4097	± 3.51	0.2670	± 1.58	0.45	0.0926	± 3.14	1525	± 24	1507	± 53	1480	± 46	0.0076	-3	0.35
C-IV6a	3.3913	± 2.82	0.2664	± 1.84	0.65	0.0923	± 2.14	1523	± 28	1502	± 42	1474	± 32	0.0013	-3	0.57
C-V-1a	3.6244	± 2.04	0.2763	± 0.76	0.37	0.0951	± 1.89	1573	± 12	1555	± 32	1531	± 29	0.0032	-3	0.25
C-V-7	2.9100	± 1.81	0.2458	± 1.11	0.62	0.0859	± 1.43	1417	± 16	1385	± 25	1335	± 19	0.0001	-6	0.13

Table 4

						Isotopic ratios				Ages		
	U	Th	Th	^{206}Pb	4f^{206}	^{207}Pb	^{207}Pb	^{206}Pb	^{208}Pb	^{206}Pb	^{207}Pb	Disc.
Spot	ppm	ppm	U	ppm	%	^{206}Pb	^{235}U	^{238}U	^{232}Th	^{238}U	^{206}Pb	%
GR-127, fine-grained banded dioritic gneiss. zircon												
h.1-1	1473	43	0.03	295.1	0.02	0.08590 ± 0.37	2.7628 ± 1.35	0.2333 ± 1.30	0.0716 ± 3.75	1352 ± 16	1336 ± 7	-1
h.1-2	1371	283	0.21	298.4	0.27	0.09186 ± 0.53	3.2014 ± 1.60	0.2527 ± 1.50	0.0840 ± 2.09	1453 ± 20	1465 ± 10	1
h.2-1	1003	18	0.02	204.3	0.01	0.08646 ± 0.45	2.8255 ± 1.39	0.2370 ± 1.31	0.0676 ± 3.36	1371 ± 16	1348 ± 9	-2
h.7-1	863	412	0.49	203.2	0.00	0.09601 ± 0.44	3.6303 ± 1.40	0.2742 ± 1.32	0.0783 ± 1.46	1562 ± 18	1548 ± 8	-1
h.6-1	2478	126	0.05	500.7	0.00	0.08597 ± 0.26	2.7880 ± 1.34	0.2352 ± 1.31	0.0669 ± 1.64	1362 ± 16	1338 ± 5	-2
h.3-1	1804	831	0.48	416.5	0.00	0.09544 ± 0.30	3.5367 ± 1.34	0.2688 ± 1.30	0.0776 ± 1.41	1534 ± 18	1537 ± 6	0
h.3-2	756	332	0.45	172.7	0.01	0.09521 ± 0.44	3.4921 ± 1.40	0.2660 ± 1.33	0.0759 ± 1.67	1521 ± 18	1532 ± 8	1
h.4-1	1266	21	0.02	252.9	0.03	0.08615 ± 0.37	2.7611 ± 1.37	0.2325 ± 1.32	0.0640 ± 3.81	1347 ± 16	1341 ± 7	0
h.6-2	1113	90	0.08	245.3	0.01	0.09217 ± 0.37	3.2603 ± 1.93	0.2566 ± 1.90	0.0740 ± 2.27	1472 ± 25	1471 ± 7	0
h.7-2	1624	63	0.04	326.7	0.01	0.08620 ± 0.34	2.7841 ± 1.44	0.2342 ± 1.40	0.0676 ± 2.64	1357 ± 17	1343 ± 6	-1
h.2-2	1015	65	0.07	198.2	0.00	0.08670 ± 0.47	2.7166 ± 1.41	0.2272 ± 1.33	0.0659 ± 2.06	1320 ± 16	1354 ± 9	3
NM-42, porphyritic monzogranite. zircon												
42-1.1	892	132	0.15	178	0.00	0.08604 ± 0.37	2.760 ± 10	0.2326 ± 0.93	- -	1348 ± 11	1339 ± 7.1	-1
42-2.1	88	49	0.58	16.7	0.10	0.0858 ± 1.3	2.604 ± 2.4	0.2202 ± 2.1	- -	1283 ± 24	1333 ± 25	4
42-2.2	361	103	0.29	71.2	0.00	0.08534 ± 0.58	2.705 ± 1.1	0.2299 ± 0.91	- -	1334 ± 11	1323 ± 11	-1
42-3.1	671	159	0.24	132	0.03	0.08641 ± 0.43	2.730 ± 0.9	0.2292 ± 0.85	- -	1330 ± 10	1347 ± 8.4	1
42-4.1	533	167	0.32	106	0.04	0.08648 ± 0.49	2.768 ± 0.9	0.2321 ± 0.87	- -	1346 ± 11	1349 ± 9.4	0
42-5.1	402	132	0.34	78	0.29	0.08672 ± 0.73	2.689 ± 1.1	0.2249 ± 0.88	- -	1308 ± 10	1354 ± 14	3
42-6.1	712	181	0.26	138	0.00	0.08658 ± 0.41	2.693 ± 0.9	0.2256 ± 0.85	- -	1311 ± 10	1351 ± 7.8	3
42-7.1	399	129	0.33	72	0.10	0.08555 ± 0.63	2.476 ± 1.1	0.2099 ± 0.88	- -	1228 ± 9.9	1328 ± 12	8
42-8.1	727	210	0.30	143	0.04	0.08575 ± 0.42	2.701 ± 0.9	0.2284 ± 0.85	- -	1326 ± 10	1333 ± 8.1	0
42-9.1	511	167	0.34	102	0.04	0.08604 ± 0.48	2.743 ± 1.1	0.2312 ± 0.94	- -	1341 ± 11	1339 ± 9.2	0
4210.1	173	58	0.34	34	0.00	0.08602 ± 0.79	2.704 ± 1.3	0.228 ± 0.99	- -	1324 ± 12	1339 ± 15	1
4211.1	229	59	0.27	46.3	0.00	0.08614 ± 0.7	2.791 ± 1.2	0.235 ± 0.96	- -	1360 ± 12	1341 ± 14	-1
4211.2	430	109	0.26	86.7	0.00	0.08635 ± 0.53	2.794 ± 1.0	0.2346 ± 0.89	- -	1359 ± 11	1346 ± 10	-1
4212.1	252	97	0.40	51.2	0.00	0.08696 ± 0.66	2.843 ± 1.2	0.2371 ± 0.98	- -	1372 ± 12	1360 ± 13	-1
4213.1	254	94	0.38	50.2	0.10	0.08597 ± 0.77	2.724 ± 1.2	0.2298 ± 0.97	- -	1333 ± 12	1337 ± 15	0
4214.1	383	104	0.28	77.6	1.79	0.08740 ± 3.5	2.790 ± 3.7	0.2316 ± 0.93	- -	1343 ± 11	1369 ± 68	2
GR-143, metagabbro, baddeleyite + zircon*												
B.10-1	139	0.89	0.01	28.2	0.01	0.0855 ± 0.9	2.800 ± 1.54	0.2372 ± 1.27	0.0887 ± 11.4	1372 ± 16	1330 ± 17	-3
B.10-2	82	0.24	0.00	17.0	0.03	0.0872 ± 1.1	2.919 ± 1.80	0.2421 ± 1.37	0.1003 ± 17.3	1397 ± 17	1370 ± 22	-2
B.10-4	251	1.31	0.01	50.0	0.05	0.0873 ± 0.8	2.774 ± 1.50	0.2318 ± 1.22	0.0733 ± 9.2	1344 ± 15	1356 ± 17	1
B.10-5	96	0.41	0.00	20.5	0.01	0.0869 ± 1.4	2.975 ± 2.14	0.2486 ± 1.46	0.0929 ± 16.9	1431 ± 19	1356 ± 30	-6
B.9-1	140	1.04	0.01	32.6	0.20	0.0874 ± 1.1	3.266 ± 1.67	0.2703 ± 1.27	0.0802 ± 10.9	1542 ± 17	1374 ± 21	-12
B.8-1	216	2.05	0.01	48.4	0.03	0.0876 ± 1.1	3.167 ± 1.69	0.2615 ± 1.28	0.0869 ± 9.2	1497 ± 17	1379 ± 21	-9
B.12-1	141	1.16	0.01	24.5	0.05	0.0866 ± 1.6	2.396 ± 2.15	0.2015 ± 1.33	0.0638 ± 12.1	1184 ± 14	1344 ± 33	12
B.12-2	126	1.02	0.01	25.1	0.09	0.0859 ± 1.3	2.780 ± 1.82	0.2327 ± 1.32	0.0781 ± 11.4	1347 ± 16	1353 ± 24	0
B.6-1*	279	213	0.79	54.0	0.03	0.0862 ± 0.7	2.667 ± 1.30	0.2252 ± 1.04	0.0654 ± 1.3	1313 ± 14	1336 ± 15	2
B.3-1*	1852	1808	1.01	364	0.01	0.0868 ± 0.3	2.743 ± 0.92	0.2290 ± 0.88	0.0667 ± 1.0	1333 ± 12	1358 ± 5	2

Table 4_continued

						Isotopic ratios									Ages			
	U	Th	Th	^{206}Pb	4f^{206}	^{207}Pb		^{207}Pb		^{206}Pb		^{208}Pb		^{206}Pb	^{207}Pb		Disc.
Spot	ppm	ppm	U	ppm	%	^{206}Pb		^{235}U		^{238}U		^{232}Th		^{238}U	^{206}Pb		%
GR-145, foliated metagabbro, zircon																	
L.4-1	292	43	0.15	56.8	0.02	0.0865	± 1.0	2.70	± 1.3	0.2268	± 0.8	0.0645	± 2.2	1319 ± 9.6	1346	± 20	2
L3-1-1	505	72	0.15	94.6	0.00	0.0861	± 0.7	2.59	± 0.9	0.2179	± 0.7	0.0647	± 1.6	1271 ± 7.9	1341	± 13	5
L.5-1	355	51	0.15	69.3	0.07	0.0863	± 1.7	2.73	± 2.9	0.2274	± 2.3	0.0728	± 3.7	1319 ± 28.1	1358	± 34	3
L6-1-4	171	26	0.16	34.0	0.21	0.0889	± 1.1	2.77	± 2.0	0.2305	± 1.0	0.0687	± 7.0	1337 ± 11.9	1363	± 34	2
L.7-1	189	38	0.21	36.7	0.22	0.0918	± 0.9	2.80	± 1.5	0.2256	± 0.8	0.0685	± 3.9	1311 ± 10.2	1425	± 25	8
L.2-1	202	58	0.30	39.6	0.59	0.0907	± 0.8	2.69	± 2.1	0.2272	± 1.4	0.0659	± 4.1	1321 ± 17.6	1333	± 31	1
L.1-1	197	33	0.17	39.2	0.08	0.0869	± 0.8	2.75	± 1.8	0.2316	± 1.4	0.0645	± 4.1	1345 ± 17.5	1342	± 21	0
NM-166, hornblende metagabbro, zircon																	
g.1-1	288	79	0.28	57.4	0.03	0.08627	± 0.84	2.7570	± 1.6	0.2318	± 1.4	0.0642	± 2.1	1344 ± 17	1344	± 16	0
g.1-2	173	63	0.38	34.9	0.00	0.08405	± 1.04	2.7274	± 1.8	0.2354	± 1.5	0.0667	± 2.1	1363 ± 18	1294	± 20	-5
g.2-1	145	71	0.51	29.3	0.06	0.08669	± 1.26	2.8074	± 1.9	0.2349	± 1.5	0.0687	± 2.4	1360 ± 19	1354	± 24	0
g.2-2	122	57	0.48	24.0	0.00	0.08729	± 1.23	2.7521	± 2.0	0.2287	± 1.6	0.0659	± 2.5	1328 ± 19	1367	± 24	3

Table 5

Sample	Age (Ga) zircon	Rb (ppm)	Sr (ppm)	$\frac{^{87}Rb}{^{86}Sr}$	$\frac{^{87}Sr}{^{86}Sr}$	Sr_i	εSr(T)	Sm (ppm)	Nd (ppm)	$\frac{^{147}Sm}{^{144}Nd}$	$\frac{^{143}Nd}{^{144}Nd}$	εNd0	εNd(t)[a]	$\frac{Rb}{Sr}$	La	Yb	Th	$\frac{Th}{Yb}$	$\frac{La}{Yb}$
GR558	1.46	4.2	207	0.05723	0.70336	0.70216	-16.2	4.112	13.12	0.1895	0.512922	5.55	+6.8	0.020	4.4	3.2	0.2	0.06	1.38
GR609	1.46	8.1	166	0.13764	0.70308	0.70019	-20.2	5.673	18.47	0.1856	0.512882	4.76	+6.6	0.049	8.8	5.5	0.6	0.11	1.60
GR737	1.46	5.5	90	0.17237	0.70448	0.70086	-0.4	3.579	10.77	0.2010	0.512931	5.71	+4.9	0.061	4.2	3	0.3	0.10	1.40
GR793	1.45	4.8	292	0.04637	0.70312	0.70214	-19.7	5.023	16.09	0.1887	0.512699	1.18	+2.6	0.016	8.1	3.5	0.6	0.17	2.31
GR775	1.46	3.5	161	0.06132	0.70372	0.70243	-11.2	1.795	4.232	0.2563	0.512788	2.92	+5.4	0.022	0.9	0.9	0.1	0.11	1.00
NM114	1.46	5.3	160	0.09343	0.70374	0.70179	-10.8	3.191	9.673	0.1994	0.512932	5.74	+5.2	0.033	6.3	4.6	0.5	0.11	1.37
SJ2430	1.47	5.7	188	0.08552	0.70447	0.70268	-1.3	3.618	10.02	0.2182	0.513337	13.6	+8.8	0.030	2.5	1.2	0.2	0.17	2.08
GP4112	1.45	3.5	113	0.08737	0.70416	0.70233	-4.8	1.417	6.840	0.1253	0.512091	-10.68	+5.5	0.031	2.6	2.4	0.3	0.13	1.08
GP3180	1.46	4.6	118	0.10996	0.70313	0.70083	-19.4	0.281	1.500	0.113	0.512052	-11.44	+7.5	0.039	2.9	2.4	0.1	0.04	1.21
GP4141	1.45	8	130	0.17358	0.70471	0.70107	-24.1	1.271	5.929	0.1296	0.512045	-11.56	+3.6	0.062	1.9	1.6	4.7	2.94	1.19
GR694	1.46	6.4	166	0.10875	0.70503	0.70275	-0.3	3.382	10.49	0.1950	0.512820	3.54	+3.8	0.039	2.3	1.9	0.1	0.05	1.21
GP3117	1.46	3.7	207	0.05042	0.70313	0.70207	-19.5	0.900	2.251	0.2398	0.513320	13.30	+5.9	0.018	3	2.3	0.2	0.09	1.30
GR719	1.46	2.7	197	0.03866	0.70406	0.70325	6.9	3.890	12.98	0.1813	0.512890	4.90	+7.6	0.014	2.8	2.2	0.3	0.14	1.27
F6GR25	1.46	2.3	120	0.05406	0.70433	0.70312	5.6	0.51	1.830	0.1681	0.512533	-2.06	+4.5	0.019	2.3	1.7	0.5	0.29	1.35

Note: Ratios were normalized to $^{146}Nd/^{144}Nd = 0.7219$ and $^{88}Sr/^{86}Sr = 8.375$. NBS987 Sr standard $^{87}Sr/^{86}Sr = 0.710248 \pm 0{,}000036$ (2σ).

[a] $\varepsilon_{Nd(t=1.46\ Ga)}$

Figure 1

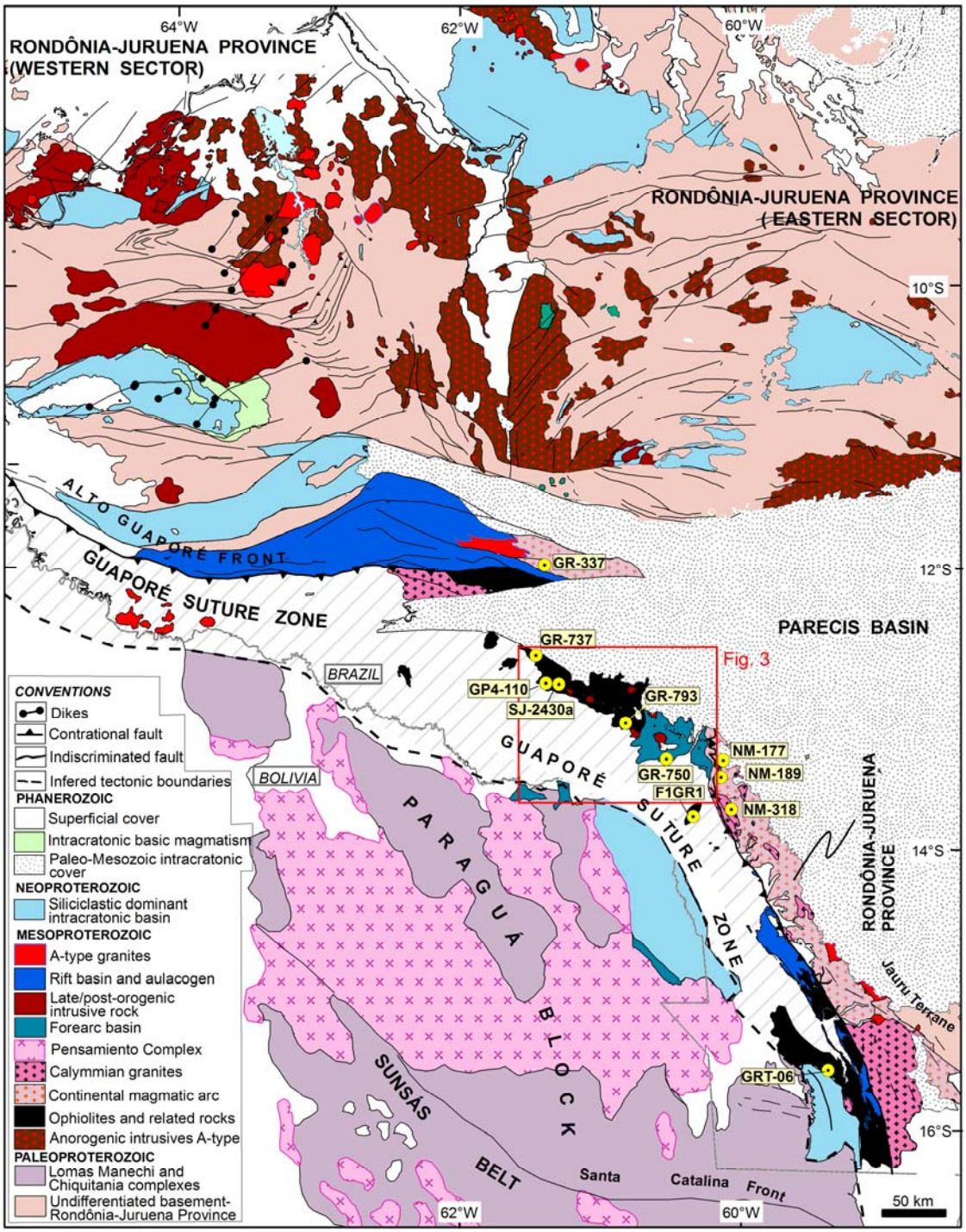
64°W
62°W
60°W
RONDÔNIA-JURUENA PROVINCE
(WESTERN SECTOR)
RONDÔNIA-JURUENA PROVINCE
(EASTERN SECTOR)
10°S
12°S
14°S
16°S
ALTO GUAPORÉ FRONT
GUAPORÉ SUTURE ZONE
GR-337
PARECIS BASIN
GR-737
Fig. 3
GP4-110
SJ-2430a
GR-793
BRAZIL
BOLIVIA
GUAPORÉ SUTURE ZONE
NM-177
NM-189
GR-750
F1GR1
NM-318
PARAGUA BLOCK
RONDÔNIA-JURUENA PROVINCE
Jauru Terrane
GRT-06
SUNSÁS BELT
Santa Catalina Front
50 km
CONVENTIONS
Dikes
Contrational fault
Indiscriminated fault
Infered tectonic boundaries
PHANEROZOIC
Superficial cover
Intracratonic basic magmatism
Paleo-Mesozoic intracratonic cover
NEOPROTEROZOIC
Siliciclastic dominant intracratonic basin
MESOPROTEROZOIC
A-type granites
Rift basin and aulacogen
Late/post-orogenic intrusive rock
Forearc basin
Pensamiento Complex
Calymmian granites
Continental magmatic arc
Ophiolites and related rocks
Anorogenic intrusives A-type
PALEOPROTEROZOIC
Lomas Manechi and Chiquitania complexes
Undifferentiated basement-Rondônia-Juruena Province

Figure 2

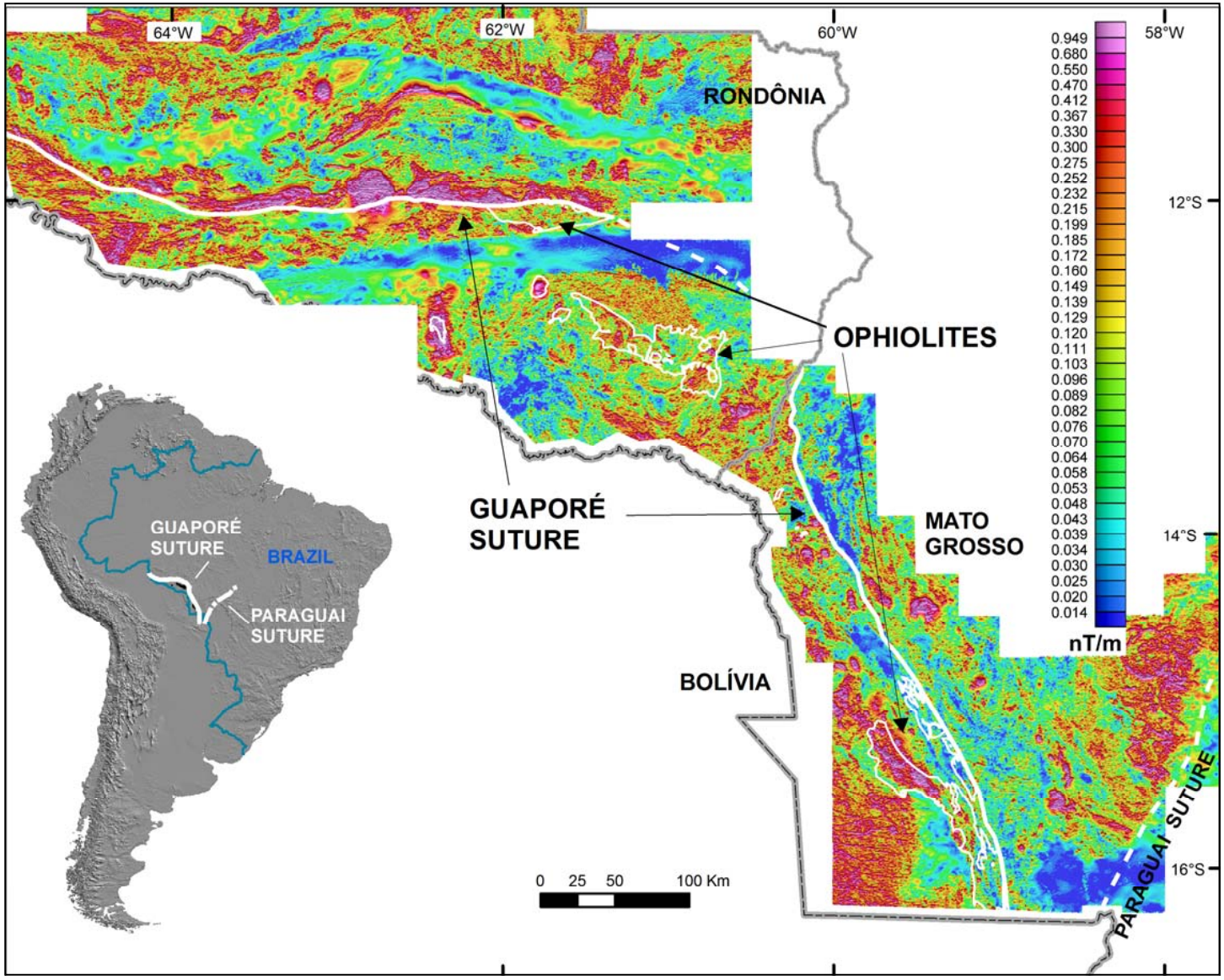
64°W
62°W
60°W
58°W
12°S
14°S
16°S
RONDÔNIA
OPHIOLITES
GUAPORÉ
SUTURE
MATO
GROSSO
BOLÍVIA
PARAGUAI SUTURE
0.949
0.680
0.550
0.470
0.412
0.367
0.330
0.300
0.275
0.252
0.232
0.215
0.199
0.185
0.172
0.160
0.149
0.139
0.129
0.120
0.111
0.103
0.096
0.089
0.082
0.076
0.070
0.064
0.058
0.053
0.048
0.043
0.039
0.034
0.030
0.025
0.020
0.014
nT/m
GUAPORÉ
SUTURE
BRAZIL
PARAGUAI
SUTURE
0 25 50 100 Km

Figure 3

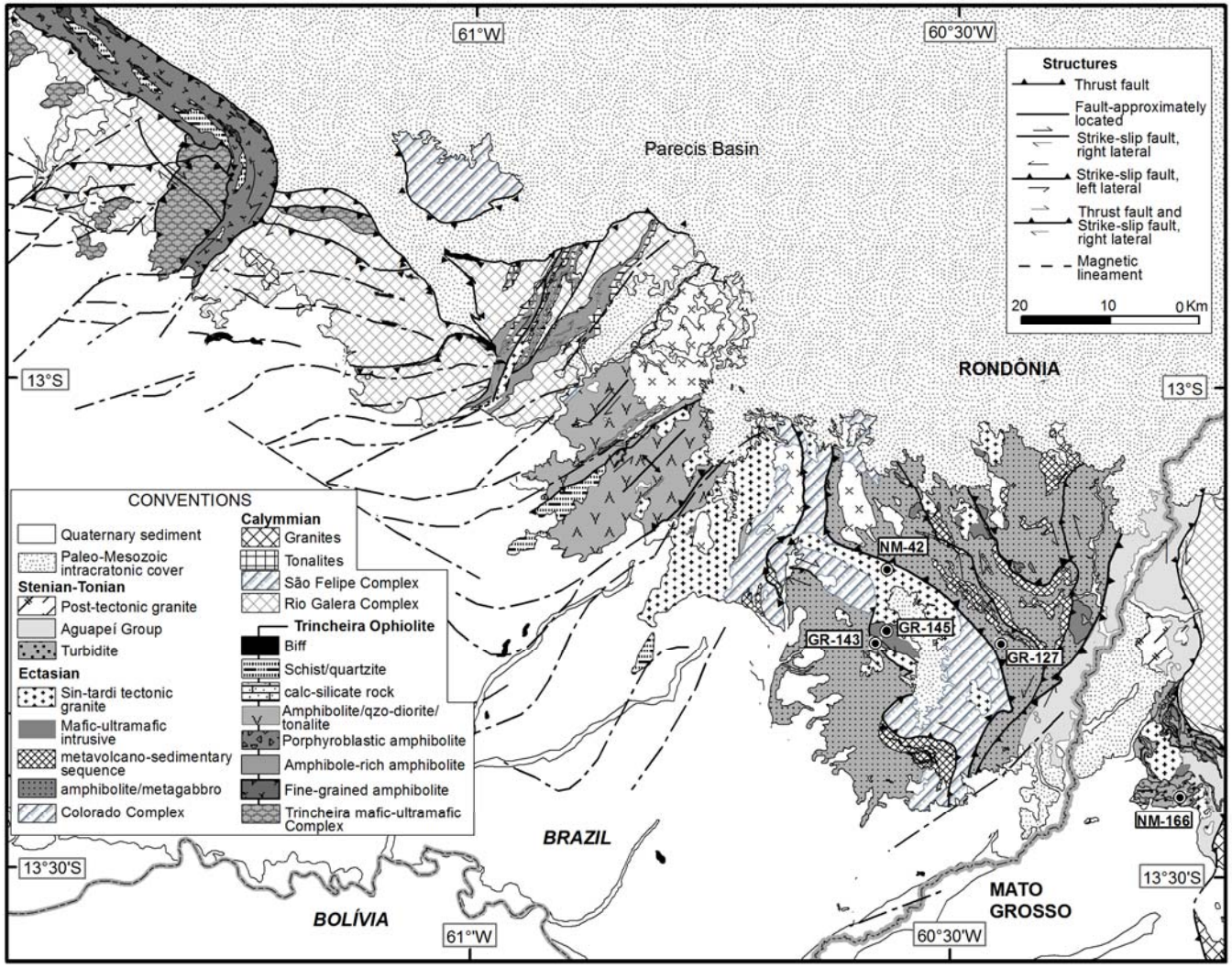
61°W
60°30'W
13°S
13°30'S
Parecis Basin
RONDÔNIA
BRAZIL
BOLÍVIA
MATO GROSSO
Structures
Thrust fault
Fault-approximately located
Strike-slip fault, right lateral
Strike-slip fault, left lateral
Thrust fault and Strike-slip fault, right lateral
Magnetic lineament
20 10 0 Km
CONVENTIONS
Quaternary sediment
Paleo-Mesozoic intracratonic cover
Stenian-Tonian
Post-tectonic granite
Aguapeí Group
Turbidite
Ectasian
Sin-tardi tectonic granite
Mafic-ultramafic intrusive
metavolcano-sedimentary sequence
amphibolite/metagabbro
Colorado Complex
Calymmian
Granites
Tonalites
São Felipe Complex
Rio Galera Complex
Trincheira Ophiolite
Biff
Schist/quartzite
calc-silicate rock
Amphibolite/qzo-diorite/ tonalite
Porphyroblastic amphibolite
Amphibole-rich amphibolite
Fine-grained amphibolite
Trincheira mafic-ultramafic Complex
NM-42
GR-143
GR-145
GR-127
NM-166

Figure 4

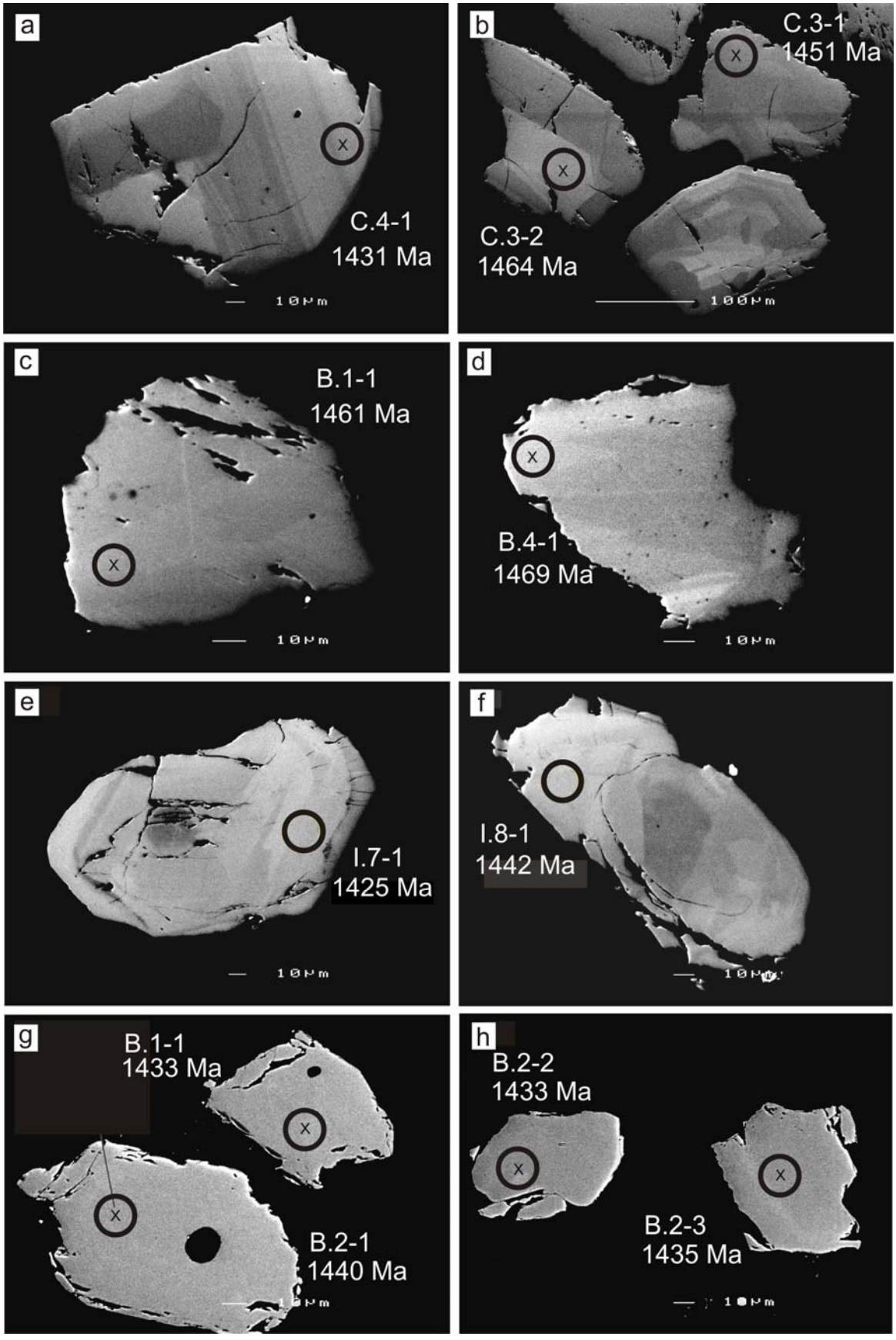
a
C.4-1
1431 Ma
10µm
b
C.3-1
1451 Ma
C.3-2
1464 Ma
100µm
c
B.1-1
1461 Ma
10µm
d
B.4-1
1469 Ma
10µm
e
I.7-1
1425 Ma
10µm
f
I.8-1
1442 Ma
10µm
g
B.1-1
1433 Ma
B.2-1
1440 Ma
h
B.2-2
1433 Ma
B.2-3
1435 Ma
10µm

Figure 5

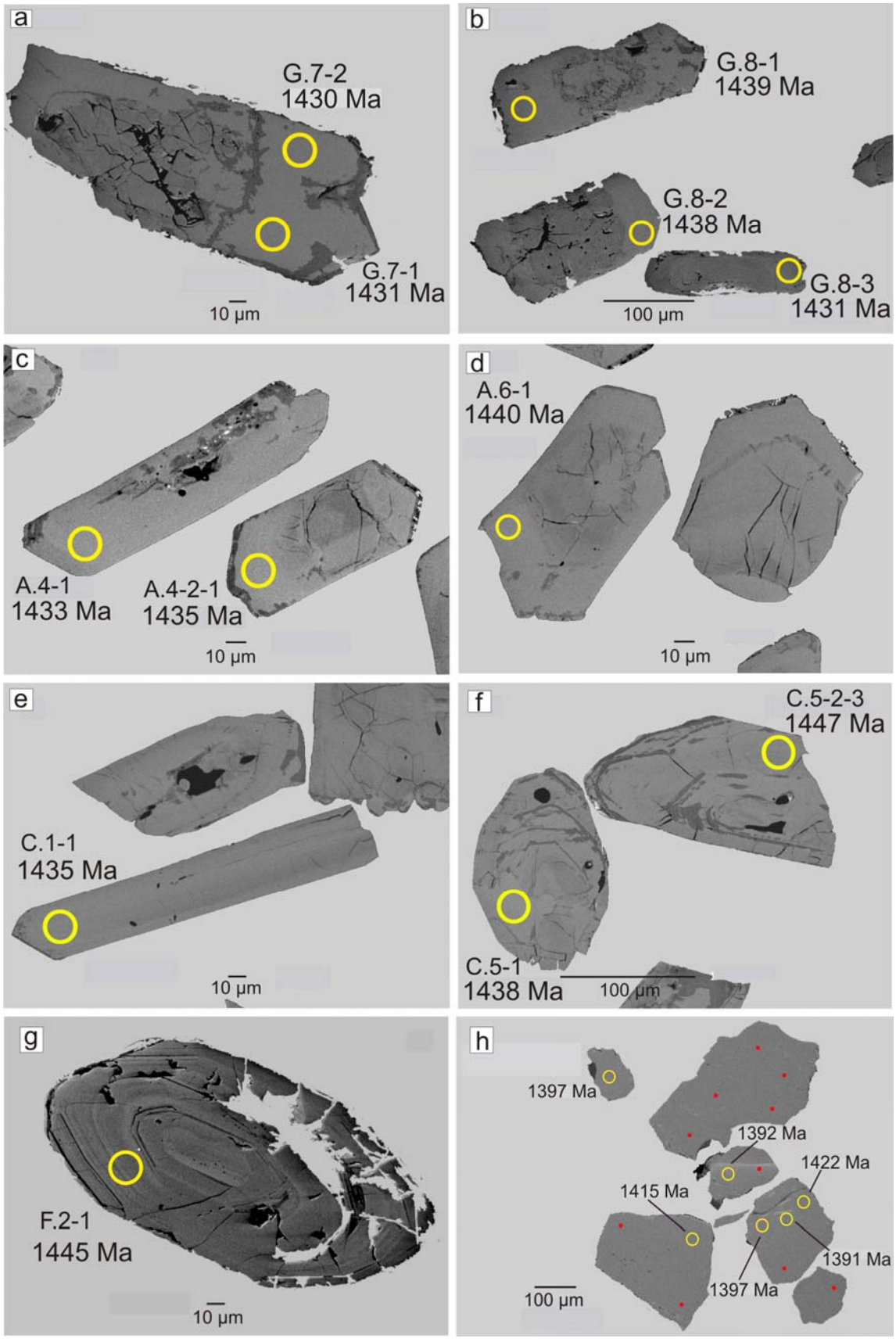
a
G.7-2
1430 Ma
G.7-1
1431 Ma
10 µm
b
G.8-1
1439 Ma
G.8-2
1438 Ma
G.8-3
1431 Ma
100 µm
c
A.4-1
1433 Ma
A.4-2-1
1435 Ma
10 µm
d
A.6-1
1440 Ma
10 µm
e
C.1-1
1435 Ma
10 µm
f
C.5-2-3
1447 Ma
C.5-1
1438 Ma
100 µm
g
F.2-1
1445 Ma
10 µm
h
1397 Ma
1392 Ma
1422 Ma
1415 Ma
1391 Ma
1397 Ma
100 µm

Figure 6

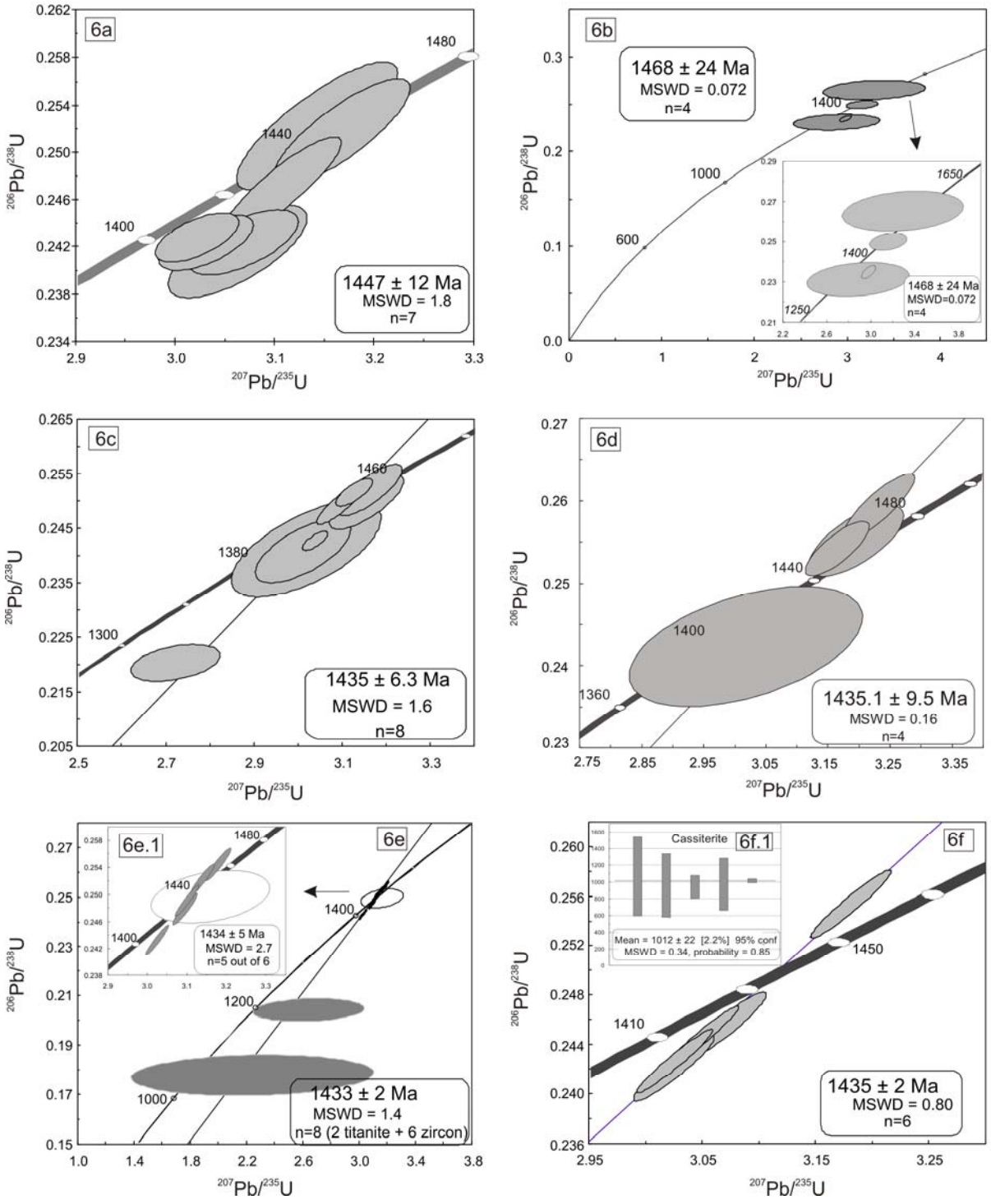
6a
1480
1440
1400
1447 ± 12 Ma
MSWD = 1.8
n=7
206Pb/238U
207Pb/235U
6b
1468 ± 24 Ma
MSWD = 0.072
n=4
1400
1000
600
1650
1400
1250
1468 ± 24 Ma
MSWD=0.072
n=4
6c
1460
1380
1300
1435 ± 6.3 Ma
MSWD = 1.6
n=8
6d
1480
1440
1400
1360
1435.1 ± 9.5 Ma
MSWD = 0.16
n=4
6e.1
1480
1440
1400
1434 ± 5 Ma
MSWD = 2.7
n=5 out of 6
6e
1400
1200
1000
1433 ± 2 Ma
MSWD = 1.4
n=8 (2 titanite + 6 zircon)
Cassiterite
6f.1
Mean = 1012 ± 22 [2.2%] 95% conf
MSWD = 0.34, probability = 0.85
6f
1450
1410
1435 ± 2 Ma
MSWD = 0.80
n=6

Figure 7

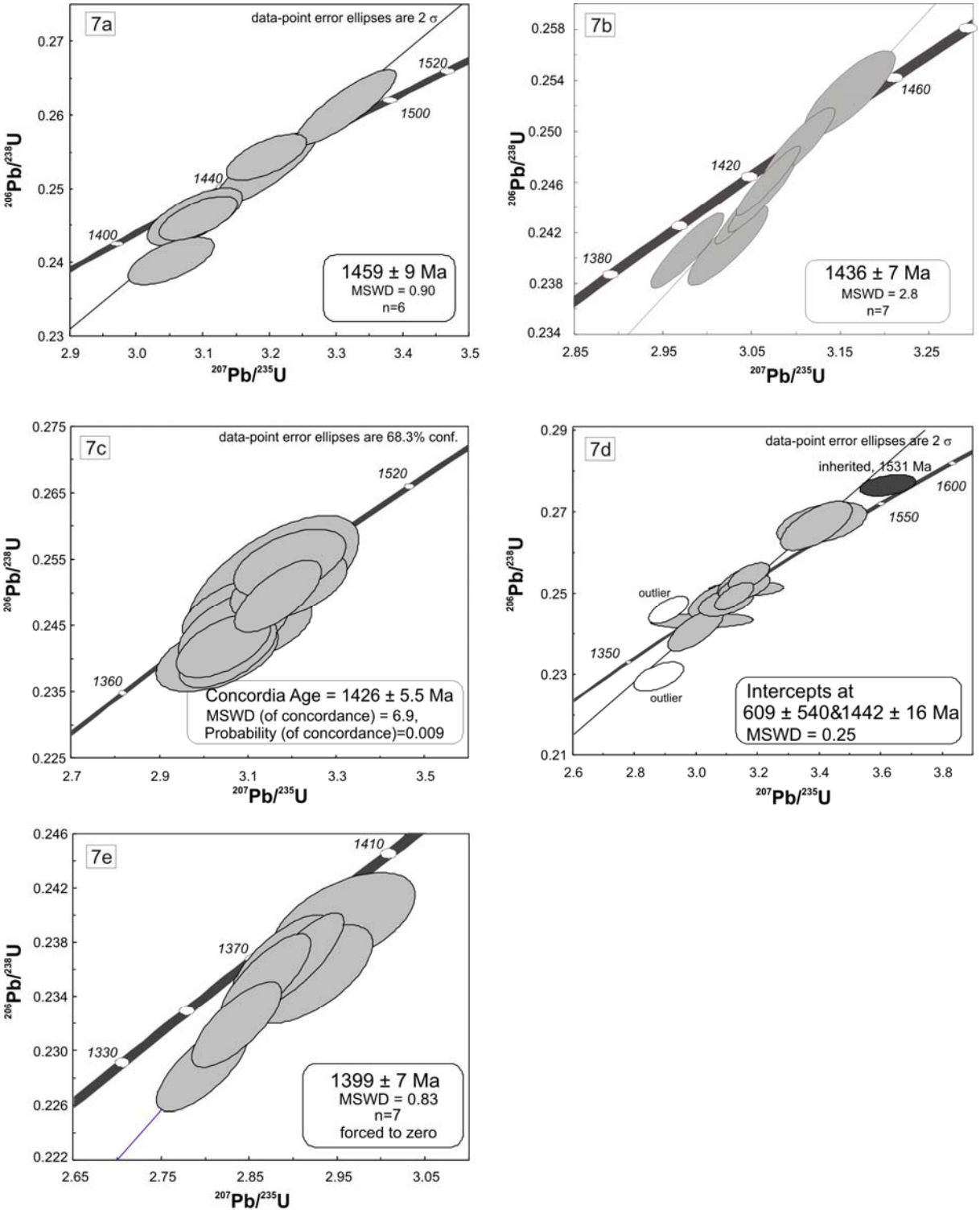
7a
data-point error ellipses are 2 σ
1520
1500
1440
1400
1459 ± 9 Ma
MSWD = 0.90
n=6
206Pb/238U
207Pb/235U
7b
1460
1420
1380
1436 ± 7 Ma
MSWD = 2.8
n=7
7c
data-point error ellipses are 68.3% conf.
1520
1360
Concordia Age = 1426 ± 5.5 Ma
MSWD (of concordance) = 6.9,
Probability (of concordance)=0.009
7d
data-point error ellipses are 2 σ
inherited, 1531 Ma
1600
1550
outlier
1350
outlier
Intercepts at
609 ± 540&1442 ± 16 Ma
MSWD = 0.25
7e
1410
1370
1330
1399 ± 7 Ma
MSWD = 0.83
n=7
forced to zero

Figure 8

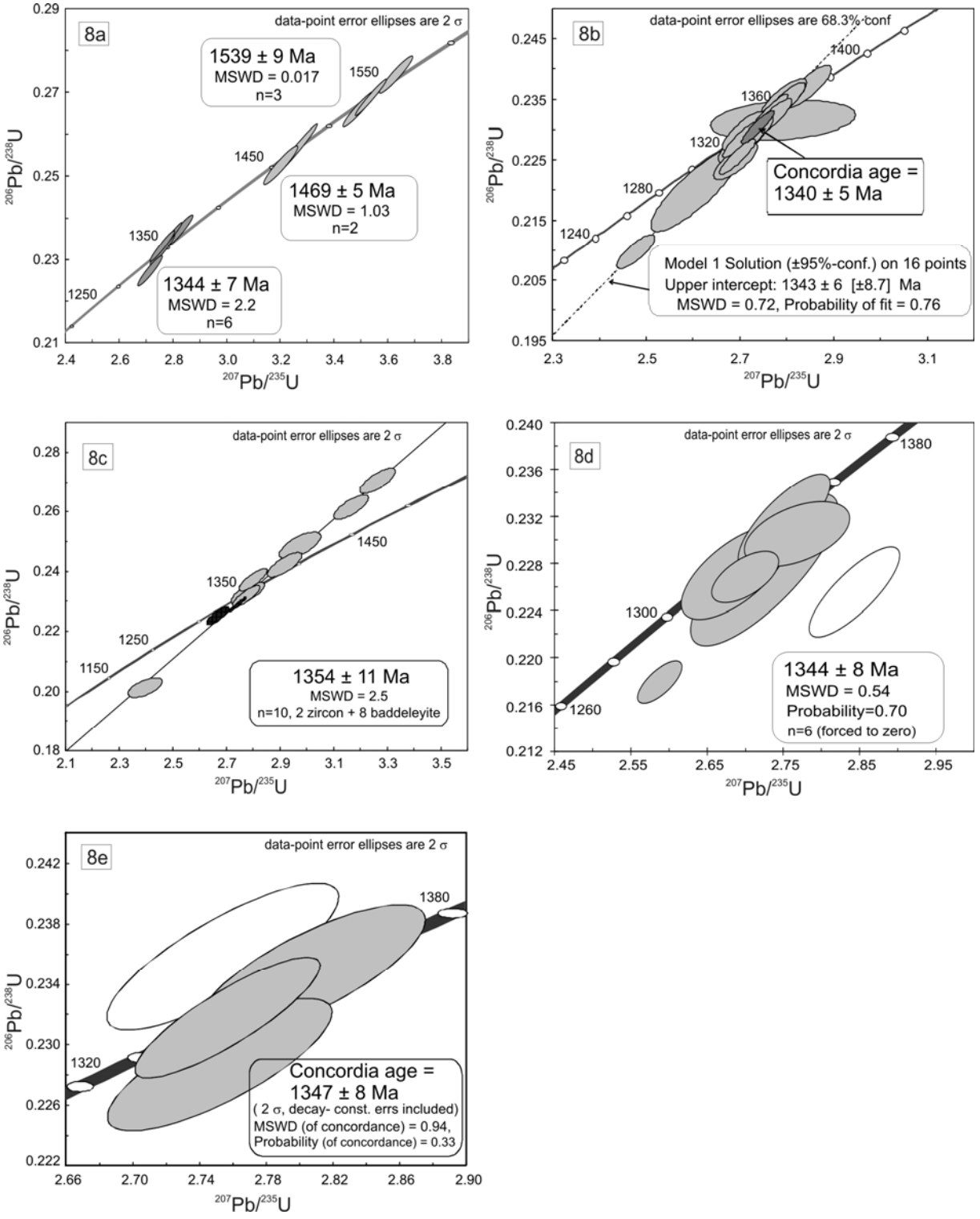
8a
data-point error ellipses are 2 σ
1539 ± 9 Ma
MSWD = 0.017
n=3
1469 ± 5 Ma
MSWD = 1.03
n=2
1344 ± 7 Ma
MSWD = 2.2
n=6
1250
1350
1450
1550
206Pb/238U
207Pb/235U
8b
data-point error ellipses are 68.3% conf
Concordia age =
1340 ± 5 Ma
Model 1 Solution (±95%-conf.) on 16 points
Upper intercept: 1343 ± 6 [±8.7] Ma
MSWD = 0.72, Probability of fit = 0.76
1240
1280
1320
1360
1400
8c
data-point error ellipses are 2 σ
1354 ± 11 Ma
MSWD = 2.5
n=10, 2 zircon + 8 baddeleyite
1150
1250
1350
1450
8d
data-point error ellipses are 2 σ
1344 ± 8 Ma
MSWD = 0.54
Probability=0.70
n=6 (forced to zero)
1260
1300
1380
8e
data-point error ellipses are 2 σ
Concordia age =
1347 ± 8 Ma
(2 σ, decay- const. errs included)
MSWD (of concordance) = 0.94,
Probability (of concordance) = 0.33
1320
1380

Figure 9

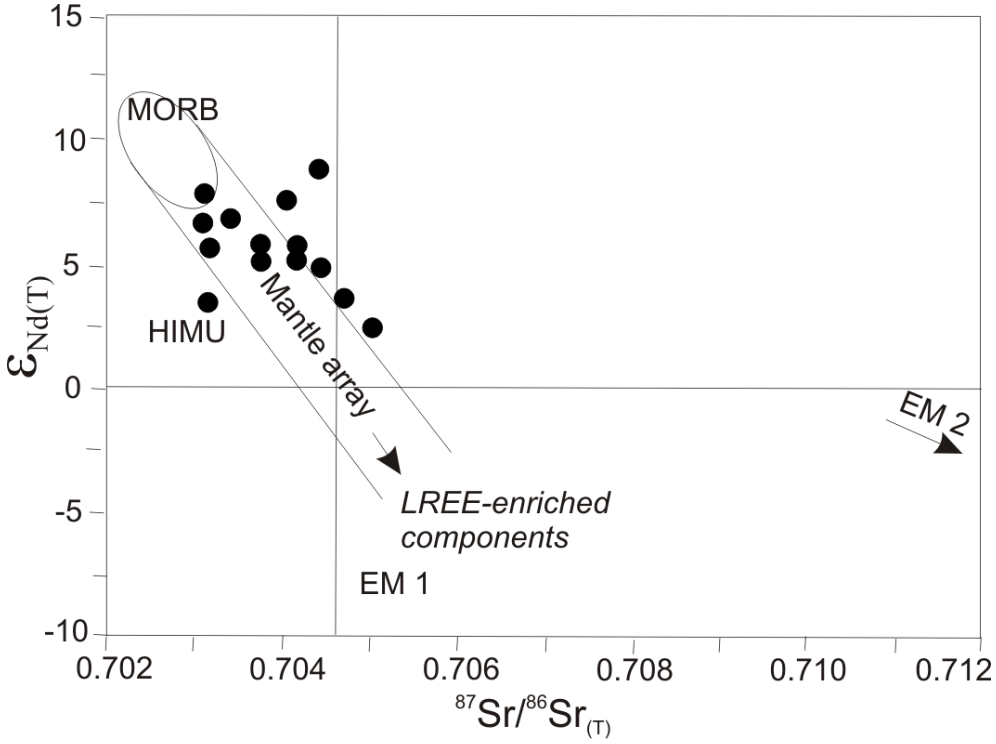
15
10
5
0
-5
-10
0.702
0.704
0.706
0.708
0.710
0.712
MORB
HIMU
Mantle array
EM 2
LREE-enriched components
EM 1
εNd(T)
87Sr/86Sr(T)

Figure 10

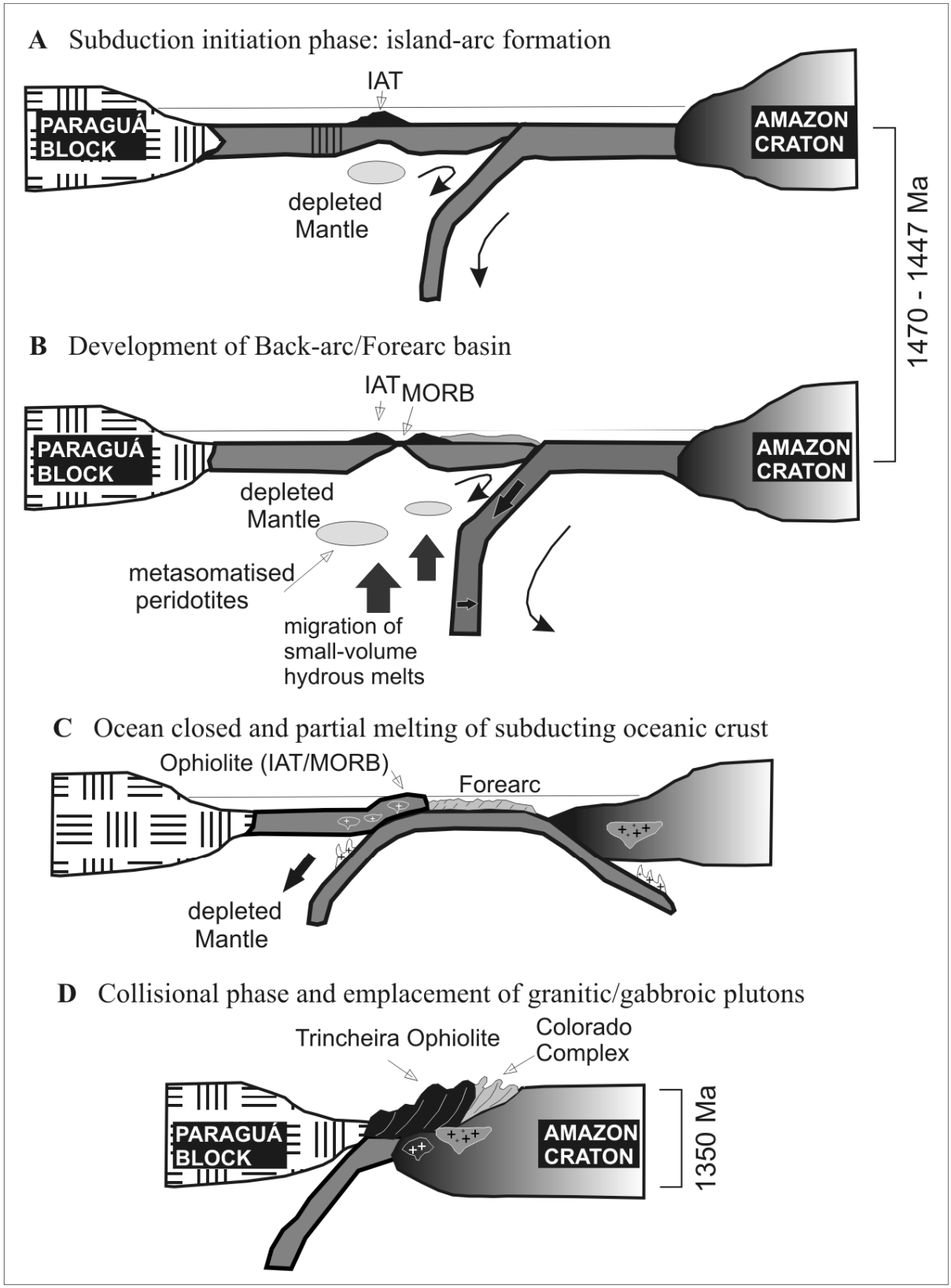
A Subduction initiation phase: island-arc formation
IAT
PARAGUÁ BLOCK
AMAZON CRATON
depleted Mantle
1470 - 1447 Ma
B Development of Back-arc/Forearc basin
IAT
MORB
PARAGUÁ BLOCK
AMAZON CRATON
depleted Mantle
metasomatised peridotites
migration of small-volume hydrous melts
C Ocean closed and partial melting of subducting oceanic crust
Ophiolite (IAT/MORB)
Forearc
depleted Mantle
D Collisional phase and emplacement of granitic/gabbroic plutons
Trincheira Ophiolite
Colorado Complex
PARAGUÁ BLOCK
AMAZON CRATON
1350 Ma

Figure 11

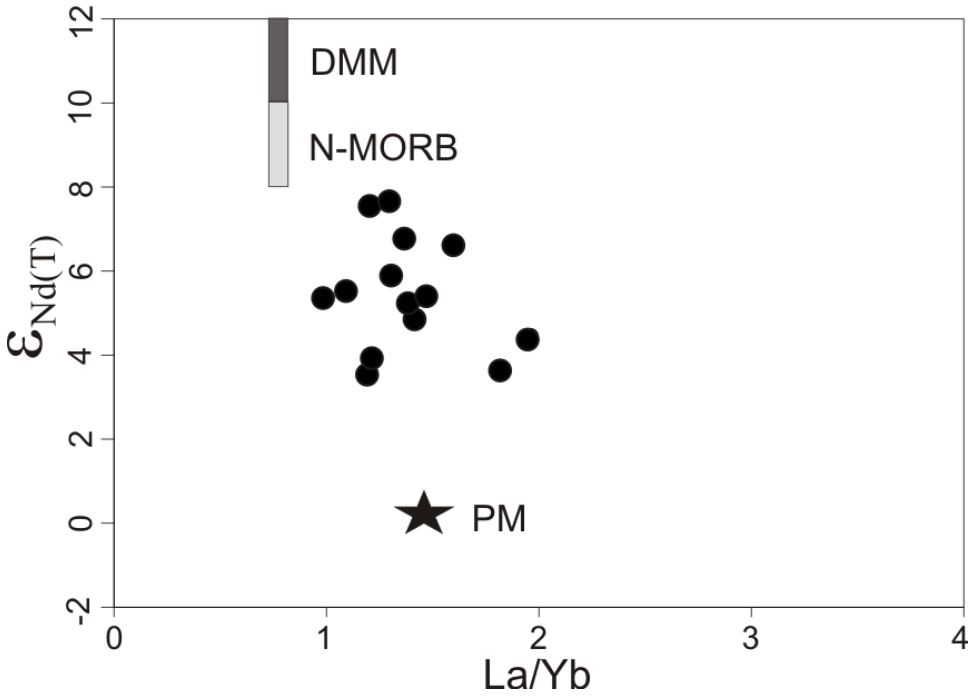

Figure 12

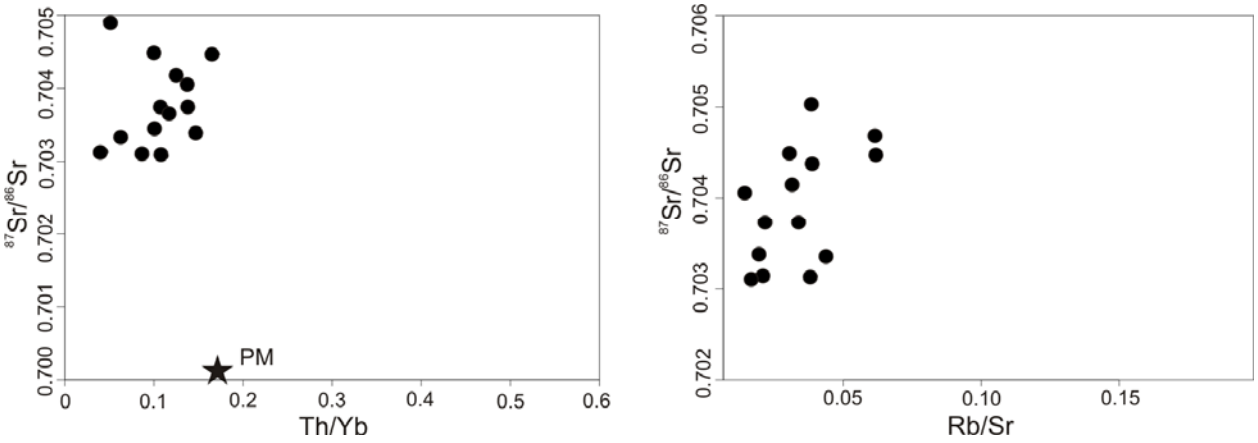
$^{87}Sr/^{86}Sr$
0.700
0.701
0.702
0.703
0.704
0.705
PM
0
0.1
0.2
0.3
0.4
0.5
0.6
Th/Yb
$^{87}Sr/^{86}Sr$
0.702
0.703
0.704
0.705
0.706
0.05
0.10
0.15
Rb/Sr

2.3. Artigo III

Rizzotto, G.J., Hartmann, L.A., Santos, J.O.S., McNaughton, N., 2012. Tectonic evolution of the southern margin of the Amazon craton in late Mesoproterozoic based on field relationships and zircon U–Pb geochronology. **Anais da Academia Brasileira de Ciências.** (Submetido).

31-May-2012

REF.: 2364

Dr. Rizzotto, Gilmar

Thank you for submitting your manuscript "Tectonic evolution of the southern margin of the Amazon craton in the late Mesoproterozoic based on field relationships and zircon U–Pb geochronology" for publication in our journal \\'Anais da Academia Brasileira de Ciências\\' (AABC).

Its reference code is 2364. Please always mention this number in any correspondence regarding this manuscript. It will be evaluated and you will be contacted in due course.

At any stage you may check the status of your manuscript logging into the AABC website http://aabc.abc.org.br. In case of any doubt, contact our Editorial Office at aabc@abc.org.br. For more information about AABC style, see latest papers published in www.scielo.br/aabc.

Tectonic evolution of the southern margin of the Amazon craton in the late Mesoproterozoic based on field relationships and zircon U–Pb geochronology

Gilmar José Rizzotto [a,*], Léo Afraneo Hartmann [b], João Orestes S. Santos [c], Neal J. McNaughton [d]

[a] Geological Survey of Brazil (CPRM), Rua 148, nº 485; 74170-110 Goiânia, Goiás, Brazil;

[b] Instituto de Geociências, Universidade Federal do Rio Grande do Sul, Avenida Bento Gonçalves, 9500; 91501-970 Porto Alegre, Rio Grande do Sul, Brazil;

[c] Redstone Resources, Suite 3 – 110 East Parade, East Perth, WA, 6004, Australia;

[d] Curtin University of Technology, GPO Box U1987, Bentley, WA, 6845, Australia

Abstract

New zircon U-Pb geochronological data integrated with field relationships and an airborne geophysical survey suggest that the Nova Brasilândia and Aguapeí belts are part of the same monocyclic, igneous and metasedimentary belt formed in the late Mesoproterozoic (1150 Ma-1110 Ma). This geological history is very similar to the within-plate origin of the Sunsás belt. Thus, we propose that the Nova Brasilândia, Aguapeí and Sunsás belts represent a unique geotectonic unit (here termed the Western Amazon belt) that became amalgamated at the end of the Mesoproterozoic and originated through the reactivation of a paleo-suture in an intracontinental rift environment. Therefore, its geological history involves a short, complete Wilson cycle of ca. 40 Ma. Globally, this tectonic evolution may be related with the final breakup of supercontinent Columbia. Mafic rocks and trondhjemites in the northernmost portion of the belt yield U-Pb zircon ages ca. 1110 Ma, which dates the high-grade metamorphism and the closure of the rift. This indicates that the breakup of supercontinent Columbia was followed in short sequence by the assembly of supercontinent Rodinia at ca. 1.1-1.0 Ga. This scenario suggests that the Western Amazon belt was formed during the accretion of the Arequipa-Antofalla basement to the Amazon craton.

Keywords: Amazon craton, intracontinental rift, Mesoproterozoic, Western Amazon belt, U-Pb geochronology

1. Introduction

The Amazon craton constitutes a central core of the South American continent and was formed by the amalgamation of Proterozoic accretionary belts that are successively younger toward the southwestern border of the craton (Santos et al. 2000, 2008, Cordani et al. 2000). This continental landmass has participated in major paleogeographic reconstructions, such as the formation of the Columbia and Rodinia supercontinents (e.g., Rogers and Santosh 2003, Li et al. 2008). The Rodinia supercontinent was formed in the late Mesoproterozoic to early Neoproterozoic by the agglutination of the existing cratonic fragments, such as Amazonia and Laurentia. In Amazonia, the records of this agglutination are present in the southwestern-most part of the Amazon craton. This region is composed of rocks belonging to the Sunsás Orogen, according to Santos et al. (2008), or the Rondonian-San Ignacio Province (Tassinari et al. 1996). The first authors proposed that the Sunsás Orogen is characterized by an autochthonous evolution that lasted for 360 m.y. (from 1465 to 1110 Ma) and was formed by four orogenies: Santa Helena (1460-1420 Ma), Candeias (1370-1320 Ma), San Andrés (1275 Ma) and Nova Brasilândia (1180-1110 Ma). They also postulated the nonexistence of the Paraguá craton, a cratonic fragment that consists of metamorphic basement rocks in the eastern Bolivia Precambrian shield, which was first defined by Litherland et al. (1986), and argued that Paraguá "craton" and Amazonia were already close together, as parts of the same continental masses in the middle to late Mesoproterozoic. In the same way, Sadowski and Bettencourt (1996) argued that there is no clear evidence that the Paraguá craton is a unit that is independent from the Amazon craton, and they consider it to be part of the Amazon craton that is defined as the Paraguá Block.

Additionally, Bettencourt et al. (2010), in a recent review of the evolutionary history of the Rondonian-San Ignacio Province, characterized the Rondonian-San Ignacio Province as a composite orogen, consisting of an older, complex accretionary orogen (1556-1430 Ma) that was followed by the collision of the Paraguá Block with the southern part of the cratonized Amazon craton at 1340-1320 Ma.

The proposal for the tectonic framework of the Amazon made by Tohver et al. (2004, 2005a, b, 2006) draws a comparison between the Grenville history recorded in the SW Amazon craton with that observed in southernmost Laurentia. They propose that during the late Mesoproterozoic, the SW Amazon craton was marked by two separate tectonic events, the first related to collision with southern Laurentia (ca. 1.2–1.15 Ga) and the second caused by suturing of the Paraguá craton (ca. 1.09 Ga). These researchers also suggest the existence of a suture belt (Nova Brasilândia belt) indicating that the initial docking of the Amazon craton with southern Laurentia (Llano uplift) at 1.2 Ga was followed by strike–slip motion, allowing for later suturing of the Paraguá craton in the final stages of the amalgamation of Rodinia. They also suggest that the Nova Brasilândia sedimentation occurred during a transtensional phase at <1.2 Ga.

In contrast, alternative positions of the Amazon craton in the Mesoproterozoic are envisaged to accommodate smaller crustal fragments, such as the Arequipa-Antofalla (i.e., Keppie and Ortega-Gutierrez 1999, Loewy et al. 2003, 2004, Casquet et al. 2006). In this way, Boger et al. (2005) present three possible scenarios for the accretion of the Paraguá Block and the Arequipa-Antofalla Basement to the western margin of the Amazon craton. Nevertheless, latest authors favor the tectonic model by which the Paraguá Block was accreted to the margin of a coherent Amazon craton during the Sunsás Orogeny.

The tectonic framework of the Amazon basement (Rondônia-Juruena Province) is of multi-orogenic nature, whereas the adjacent Nova Brasilândia Group in the Nova Brasilândia

belt most likely originated in an intracontinental rift setting. Rifting was followed by the opening of a proto-ocean at <1215 Ma as part of a single Wilson cycle (Rizzotto 1999).

With a similar geochronological and tectonic evolution, the Sunsás and Aguapeí belts occur along the southeastern rim of the Paraguá Block. These belts are most likely related to the timing of an intraplate extensional episode, a stage equivalent to the Nova Brasilândia belt passive margin. The deposition of the Aguapeí Group occurred between 1167 ± 27 Ma and 1149 ± 7 Ma (Santos et al. 2005). However, Tohver et al. (2004, 2005) and Teixeira et al. (2010) suggest the absence of physical and structural continuity between the northernmost extent of the Aguapeí belt and the E–W trending Nova Brasilândia belt. Teixeira et al. (2010) suggest that the Aguapeí belt is a late tectonic component of the Sunsás province as a result of the Sunsás collision.

The stratigraphic correlation between the Aguapeí and Sunsás Groups is in agreement with the idea that late Mesoproterozoic extensional dynamics produced a system of continental, aborted rifts over the cratonized SW margin of the Amazon craton, evolving to a wide intracratonic basin (e.g., Leite and Saes 2003).

Therefore, the inconsistencies regarding the collided Paraguá Block-Amazon craton and its geodynamic behavior during the Mesoproterozoic are under evaluation. However, Rizzotto and Hartmann (2012) suggested a new scenario for the operation of Mesoproterozoic plate tectonics, with the definition of the Guaporé suture zone, a mega-structure that marks the suturing of the proto-Amazon craton and the Paraguá Block in the late Calymmian to middle Ectasian, ca. 1470-1320 Ma. The Guaporé suture is a zone of crustal weakness reactivated during sedimentation and the proto-oceanic opening of the Nova Brasilândia basin.

In this paper, we present new zircon U-Pb geochronological results from the two Mesoproterozoic Nova Brasilândia and Aguapeí orogenies of the southwestern Amazon craton, coupled with field relationships, in a contribution to resolve some of these issues.

These results place new delimitations on the geologic evolution of the southwestern margin of the Amazon craton, and this sheds light on paleogeographic correlations between Amazonia and Laurentia.

2. Geological overview

The studied area is located between the Sunsás and Rondônia-Juruena Provinces (Santos et al. 2008), southwestern Amazon craton (Fig. 1). The basement rocks of the Rondônia-Juruena Province are included in six major Paleo-Mesoproterozoic terranes and events: the Juruena magmatic arc, the Jamari magmatic arc, the Alto Jauru Terrane, the Quatro Cachoeiras orogeny, the Cachoerinha orogen and the anorogenic magmatism (Fig. 1).

The Paleoproterozoic basement rocks of the Sunsás Province (Paraguá Block) (Fig. 1) comprise two main units. The Lomas Manechi Complex displays granulitic metamorphism generated during the Mesoproterozoic, at ca. 1330-1350 Ma (Santos et al. 2008). The Chiquitania Complex and San Ignacio Group subsequently deformed and metamorphosed during the San Ignacio Orogeny by means of three successive events of deformation accompanied by voluminous syn-tectonic granite magmatism (Litherland et al. 1986).

This Paleoproterozoic basement was amalgamated along WNW-trending Mesoproterozoic belts, described here from oldest to youngest. The Alto Guaporé belt (Rizzotto and Deller 2007) is a accretionary orogen formed by oceanic plate subduction between1.47-1.43 Ga (Rizzotto and Hartmann 2012). This constitutes the Guaporé suture zone between the proto-Amazon craton and the Paraguá Block. The rocks of the Alto Guaporé belt are exposed from the northwestern sector of Rondônia state to the southeastern and southwestern portion of Mato Grosso state. They are largely covered by the Cenozoic sedimentary rocks of the Parecis and Guaporé Basins, in an area of 200 x 60 km, with WNW-ESE trend marked by strong magnetic anomalies. This belt consists predominantly of plutonic, sedimentary and mafic-ultramafic volcanic rocks of the Trincheira Complex and calc-alkaline granitic rocks. The Colorado Complex is a meta-sedimentary sequence occurring

in the Guaporé suture and is composed of paragneiss, pelitic schist, calc-silicate gneiss, para-amphibolite and banded iron formation. The protolith of the paragneiss and pelitic schist is interpreted as a turbiditic sequence deposited in a passive margin (Rizzotto and Quadros 2007).

The Nova Brasilândia and Aguapeí belts (ca. 1150-950 Ma) are exposed along the Bolivia-Brazil border (Fig. 2). The Nova Brasilândia belt originated from the opening and closing of an ocean, whereas the Aguapeí belt is an aborted rift, both generated by reactivation along the Guaporé suture zone at ca. 1110-950 Ma.

The region being examined comprises the Nova Brasilândia and Aguapeí belts, with the integration of new field and geochronological data. The Sunsás belt is also described for comparison. The importance of the theme is centered on the register of the last orogenic phase in the southwestern border of the Amazon craton and its correlation with the Grenville province in southern Laurentia.

- *Grenvillian-age deformation in the basement of the Rondônia-Juruena Province*

The timing of deformation and generation of orogenic rocks of Grenvillian age in the southwestern Amazon craton was first estimated by Rizzotto (1999) using U-Pb geochronology in the Nova Brasilândia belt. To the north of this belt, the granitoid basement rocks of the Rondônia-Juruena Province record a polycyclic evolution characterized by the complex juxtaposition of distinct units and widespread shear zone structures.

The granitoid basement rocks were sheared by a wide network of sinistral, amphibolite-grade, strike-slip shear zones defined as the Ji-Paraná shear zone (Scandolara et al. 1999) which extends over hundreds of kilometers and cross-cuts all preexisting rock fabrics. According to Tohver et al. (2005a), metamorphism along the shear zone occurred at temperatures of 450-550ºC, and the timing of this deformation varies from ca. 1.18 to 1.15 Ga. Consistent with these findings, recent data from field work in central Rondônia by

Quadros et al. (2012) defined the Ji-Paraná-Cojubim transpressional sinistral system as extending to the northwest of the Ji-Paraná shear zone. Within this zone, the Igarapé Quinze Formation consists of paragneisses and schists that trend N40W. The dating of detrital zircon from the schist yielded U-Pb ages in the range of 1940-1367 Ma. The younger age is interpreted as the maximum age of sedimentation of the sedimentary protoliths of the Igarapé Quinze Formation (Quadros et al. 2012). This formation is interpreted as turbiditic deposits and the tectonic structures allow its correlation with the Nova Brasilândia Group (Quadros et al. 2012).

According to these authors, lenses and pods of anatectic granite were generated by partial melting of metapelites. Zircons from a locally-derived anatetic melt yield a U-Pb age of 1138 ± 8 Ma. This age represents the peak metamorphic conditions experienced by the sedimentary protolith along the Ji-Paraná-Cujubim belt.

- *Nova Brasilândia belt*

The Nova Brasilândia Group in the Nova Brasilândia belt consisted originally of a supracrustal unit of deep-sea turbidites with a siliceous-clastic-to-carbonatic composition. The unit was metamorphosed in upper amphibolite to granulite facies to produce quartz-feldspar gneisses, mica schists and minor calc-silicate gneisses. The metasedimentary package also includes metagabbro sills, amphibolites and scarce metabasalts. SHRIMP U-Pb analyses of detrital zircons from the Nova Brasilândia pelitic rocks yield ages that range from ca. 2090 ± 17 Ma to 1122 ± 12 Ma. The main population of zircon has an age of 1215 Ma, interpreted by Rizzotto (1999) as the maximum deposition age for the sequence. Sample reprocessing shows a youngest group of zircons with an age of 1122 ± 12 Ma, interpreted as the age of the basin opening (see section 4).

The other unit consists of mafic sills that outcrop in a narrow and elongated WNW-ESSE belt of voluminous plutonic mafic rocks with a strong, positive magnetic signature (Fig. 3). This magmatism is related to the successful initial rifting that formed a narrow proto-ocean

of approximately 12 km x 110 km during the evolution of continental to oceanic rift phase. These mafic rocks are here considered to record an extensional anorogenic magmatism associated with fragmentation of a pre-Rodinia supercontinent.

This mafic unit is bordered in the north by a transcurrent sinistral shear zone, which consists of mafic granulites (norite and gabbro as protoliths), rare acid granulites, banded amphibolites, porphyroblastic amphibolites, and interbedded trondhjemites, diabase dikes and lenses of calc-silicate gneisses. Rare and scattered basalts, metasedimentary and banded iron formation indicate a high degree of exhumation of the terrain with the accompanying erosion of the top portion of the volcano-sedimentary rocks. The Rio Branco monzogranitic orthogneiss was emplaced under a transpressive regime into the banded amphibolite at ca. 1113 Ma, with T_{DM}=1630 Ma (Rizzotto 1999).

The transtensional stage was succeeded by a transpressional regime accompanied by crustal shortening, as evidenced by regional EW- and WNW-ESE-trending structures, dominated by oblique thrust faults (D1). The northeast vergence and medium-to high-grade metamorphism correspond to a progressive thrust to transcurrent shear zones with tectonic transport from SSW to NNE. The main extensional structures are oriented in the N45°E direction, while the structures with a direction of N45°W correspond to a frontal thrust. The synkinematic emplacement of the Rio Branco granite and anatetic leucogranite (1110 ± 8 Ma) was contemporaneous with this compressional stage. These are the first Grenvillian-age orogenic rocks within the Nova Brasilândia belt described by Rizzotto (1999) within the southwestern margin of the Amazon craton.

The geological history of the Nova Brasilândia belt is supplemented with the emplacement of the Rio Pardo granite, which comprises a kilometer-size syn- to late transcurrent body with an age of the 1005 ± 41 Ma, injected during the development of transcurrent shear zones.

Thus, the Nova Brasilândia Group originated in an intracontinental rift setting

followed by the opening of a proto-ocean and was further subjected to crustal shortening, deformation and associated magmatism. This is suggested by detailed structural studies and metamorphic petrology coupled with chemical and petrogenetic constraints from the sedimentary and igneous rocks (Rizzotto 1999). This scenario is supported by recent paleomagnetic results reported by D'Agrella-Filho et al. (2012) where the 1420 Ma Indiavaí and Nova Guarita poles suggest that the Nova Brasilândia belt does not represent a suture zone, but rather an intracratonic structure.

In contrast, Tohver et al. (2004, 2005a) interpreted the Nova Brasilândia belt as the result of the crustal thickening through imbrication caused by the transpressive suturing of the Amazon and Paraguá cratons at ca. 1.09 Ga. They used detailed structural data, supported by thermobarometric calculations and geochronological information. Metamorphic ages (U-Pb in titanite and monazite; $^{40}Ar/^{39}Ar$ in amphibole and biotite) range from 1.09-1.06 Ga to 0.97-0.91 Ga throughout the belt (e.g., Thover et al. 2004, 2006). This age range reveals a long history of metamorphism, tectonic exhumation and cooling.

According to Rizzotto (2001), the distensional phase and final orogenic collapse (1005-970 Ma) of the Nova Brasilândia belt was accompanied by late to post-tectonic granites dated at 1.05 Ga ($\varepsilon Nd_{(T)} = +0.5$), with the generation of the foreland basins (Palmeiral Formation) in a cratonic stabilization phase accompanied by bimodal intraplate magmatism. This stage was accompanied by lateral movements of crustal blocks that generated large strike-slip zones (Rio Branco shear zone). This is in agreement with the $^{40}Ar/^{39}Ar$ and K-Ar analyses on amphibole from amphibolite (Tohver et al. 2004) and muscovite from mylonite granitic (Tassinari 1993), respectively, along this strike-slip zone. These analyses yielded a minimum age of metamorphism and deformation (D_2) at 970-966 Ma and 965 ±23 Ma. Similar ages were obtained by Fernandes et al. (2003) in sericites of the metarenites and metaconglomerates of the Aguapeí Group.

- *Aguapeí belt*

The Aguapeí belt consists of a narrow metasedimentary belt that borders the eastern margin of the Paraguá Block in southwestern Mato Grosso state. It comprises a folded metasedimentary unit (Aguapeí Group) deposited in an aulacogen NNW-SSE trend (Saes 1999) or in a rift environment (Saes et al. 1992). Souza and Hildred (1980) characterized the Aguapeí group as a thick sequence of siliciclastic rocks composed, from bottom to top, of the Fortuna, Vale da Promissão and Morro Cristalina formations. The Fortuna Formation shows thick packages of the oligomictic conglomerates and quartz sandstones with interbedded metassiltites/metapelites deposited in a shallow sea environment. The Vale da Promissão Formation displays a transitional interfingered contact with the underlying unit and comprises a sequence dominated by metapsamites, metapelites and rare metarenites deposited in a deep marine environment. The Morro Cristalina Formation is composed of fluvial sandstones and siltstones. The depositional age of the Aguapeí Group is estimated between 1167 ± 27 Ma and 1149 ± 7 Ma (Santos et al. 2005).

The Aguapeí Group overlies the Rio Alegre plutono-volcanic rocks, occurring discontinuously along more than 500 km between the northeastern/eastern margins of the Paraguá Block. The depocenter of the Aguapeí Group coincides with the paleo-suture previously established in the Rio Alegre terrane (Guaporé suture zone, Rizzotto and Hartmann 2012, Rizzotto et al. unpublished data). The pronounced magnetic low that characterizes the Aguapeí Group may be partially related to a failed rift that is filled with Mesoproterozoic sediments (Fig. 3). We suggest that the tectonic evolution of the Aguapeí Group was initiated by rifting that subsequently failed, allowing the development of a long-lived intracratonic sedimentary basin.

The Aguapeí Group exhibits pervasive deformation and low-grade metamorphism (e.g., Geraldes et al. 2001, Ruiz 2005) within a regional synform structure indicated by gentle

folds (upright to northeast-dipping) and NW-trending shears. Sinistral shearing and thrusts deformed this sequence. Recrystallized mylonites yielded K/Ar and $^{40}Ar/^{39}Ar$ mica ages between 960 and 910 Ma (e.g., Geraldes et al. 1997, Fernandes et al. 2006, Ruiz et al. 2007). Because of the occurrence side by side of folded and sheared rocks (Sunsás and Aguapeí Groups) and flat-lying and unmetamorphosed rocks (Huanchaca and Ricardo Franco ridges), Santos et al. (2002) prefer the usage of Aguapeí I for the folded and metamorphosed unit and Aguapeí II for the flat-lying cover.

- *Sunsás belt*

The sedimentary units of the Sunsás Group were deposited between 1300 and 1000 Ma and unconformably overlie the metamorphic rocks of the basement. They were deformed together with the basement during the subsequent Sunsás Orogeny at ca. 1000 Ma (Litherland et al. 1996).

The Sunsás Group comprises a sedimentary sequence up to 6 km thick, found mainly in the Serrania Sunsás, Bolivia (Litherland and Bloomfield 1981). In general, this group comprises a basal conglomerate overlain by psammitic units (arkoses, sandstones, quartzites), pelitic units (mudstones and siltstones), and a combination of feldspathic sandstones, pelites and quartzites (Berrrangé and Litherland 1982). Sedimentary structures, such as cross-beds and ripple marks, are common in the psammitic units, mainly in quartzites of the Los Tajibos serrania. Berrrangé and Litherland (1982) suggested that the sedimentary rocks of the Sunsás Group were deposited in an alluvial to deltaic environment. Later, Saes et al. (1992) referred to the sediments as deposited in an intra-continental rift.

The upper psammitic units (Vibosi Group) of the Sunsás Group were intruded by the layered Rincón del Tigre igneous complex (Prendergast 2000), which yielded a Rb–Sr age of ca. 990 Ma. This age is similar to that obtained for the late syn- to post-tectonic Sunsás granites (Litherland et al. 1996).

The Sunsás belt is structurally marked by upright NW-trending folds formed contemporaneously with extensive mylonitic shear zones that developed during low-to-medium grade metamorphism, active at ca. 1080-1050 Ma (Boger et al. 2005).

3. Analytical procedures

The samples were crushed, milled and split into fractions for whole rock isotope geochemistry, zircon, rutile and titanite dating. Zircon, titanite and rutile were separated from twelve samples using heavy liquid and magnetic separation techniques. All rocks were investigated in thin section, and their chemical compositions were determined. Nine rock samples were analyzed by SHRIMP at the Curtin University of Technology-Australia, and three samples were analyzed by LA-MC-ICP-MS. All grains used for zircon, titanite and rutile dating were imaged with backscattered electrons to determine their internal structure and the nature (igneous or metamorphic) of their growth zones. The sampling sites are shown in Figure 1, and general data for each sample (coordinates, rock name, and stratigraphic unit) are described in the next item.

The analytical procedures are described in appendix A in the online edition, and the isotopic data are presented in Table 1.

4. Samples, results and discussion

4.1. Nova Brasilândia belt

The samples were collected along an EW belt that contains primarily mafic rocks belonging to a proto-ocean, the Nova Brasilândia rift. These lithotectonics units were deformed by NW-SE (D_1) to E-W (D_2) transpressional phases, corresponding to progressive thrust to transcurrent shear zones. Generally, all localities preserve evidence of granulite facies metamorphism associated with ductile deformation; orthopyroxene often has an elongated granoblastic texture. However, later hydrous retrogression is widespread along

transcurrent shear zone, and the orthopyroxene shows various degrees of alteration to amphibole. The analyzed samples show minimal retrogression.

Sample GRT-01 (S 11°57'49"/W 61º44'58") is a dark gray, coarse-grained mafic granulite with granoblastic texture. It is fine-grained within mylonitic zones and displays several millimeter-to-centimeter-sized veinlets of amphibole that are randomly oriented and associated with sulfides, resulting from retrogressive amphibolite facies conditions. Their mylonitic foliation trends N60ºW; 30ºNE, with mineral lineation at 35º; N30ºW.

Zircons from this sample are generally 80 to 120 μm in size with partly rounded or broken terminations and are generally structureless or patchily zoned. Zircon grains reveal internal features characteristics of solid state recrystallization, even on grains from rocks in which igneous textures are partly preserved. This alteration process is pervasive through the mafic rocks of the belt.

The U content is highly variable (706 to 2254 ppm) as is the Th content which ranges between 254 and 2266 ppm (Table 1). From a population of 5 analyzed crystals, 4 crystals yielded suitable isotopic response, indicating the upper intercept age of 1114 ± 5 Ma, with an MSWD of 1.09 (Fig. 4a), which is interpreted as peak metamorphic age. This age is in agreement with the age measured in the anatetic melt (1110 ± 8 Ma) of the northern domain of the Nova Brasilândia belt (Rizzotto 1999). However, there is one zircon (grain h.1-3) with discordant ages near 1014 Ma, which may indicate Pb loss due to the superimposition of a later metamorphic event.

Sample GRT-02 (S 11º57'04"/W 61º45'01") is a banded leucocratic trondhjemite, fine- to medium-grained, and forms subconcordant lenses (ca. 300 m long and 50 m thick) intercalated with mafic granulite. It consists mainly of quartz and variably saussuritized plagioclase, with ≤10% interstitial mafic minerals (mostly amphibole and clinopyroxene, with titanite, magnetite and traces of zircon). Titanites contain inclusions of biotite, plagioclase, quartz and epidote. Titanite crystals develop along the foliation planes characterizing

synkinematic crystals. Much of the matrix titanite is aligned and concentrated in amphibole-rich bands that anastomose around granoblastic plagioclase/quartz-rich domains.

Zircons and titanite crystals were dated. Zircon grains are light tan to colorless, clear and show varied morphology with sizes ranging from 100 μm to 350 μm. Elongated prisms characterize the most frequent zircon type, but ovoid habits with rounded terminations are also observed. The zircon crystals reveal the most varied internal features, with a disruption of concentric oscillatory zonation resulting in irregular patches and ghost zoning. Some grains have fractured cores and homogeneous rims.

The U content of zircon varies from 509 to 1461 ppm (Table 1). Thirteen analyses in ten zircon grains were obtained from this sample. Eight of these analyses yielded a weighted mean $^{207}Pb/^{206}Pb$ age of 1089 ± 9 Ma (MSWD =1.5 - Fig. 4b), which is interpreted as the metamorphic age of the trondhjemite. The age of metamorphism is slightly younger than that of sample GRT-01, which may be due to Pb loss resulting from alteration processes such as metamictization.

Light tan to dark titanite grains are subhedral to rounded and unzoned, and generally crystals are fragmented with widths that vary from 120 to 200 μm. The U contents of the grains are generally lower than 300 ppm, and the Th content varies between 180 and 260 ppm. Regardless, the Th/U ratios are high, and their occurrence within metamorphic bands indicates that these grains grew in a metamorphic environment.

The five analyzed grains plot on concordia (Fig. 4b), indicating a concordant age of 986 ± 6 Ma. The large difference between the titanite age and zircon age suggests that there may have been a deformational phase at ~1.0 Ga. Another possibility is that titanite has a lower closure temperature than zircon, and thus, this age would represent the cooling after peak metamorphism. In this same area, Tohver et al. (2004) dated monazite crystals from a mylonitic gneiss, near GRT-01, which yielded the age of 993 ± 11 Ma. These authors argue that monazite grew below its closure temperature through dynamic recrystallization. This

interpretation is in agreement with the previous suggestion of a later phase deformation at ca. 1.0 Ga.

Sample GRT-03 (S 11º53'11"/W 62º29'11") is a light gray banded trondhjemite, medium-grained, in decametric lenses intercalated with mafic granulites. The mineralogy and texture of this trondhjemite are similar to sample GRT-02. However, its has higher content of mafic minerals (amphibole and clinopyroxene) and banding defined by the preferred orientation of these minerals. The metamorphic fabrics range in intensity from a well-developed foliation to gneissic banding in high strain zones. Lineation is characterized by high rake angle, suggestive of a strike-slip component of the motion.

Zircons crystals are slightly elongated and exhibit stubby habit with rounded terminations, which render oval morphologies to some grains. Generally, crystals are fragmented, and their length varies between 100 and 200 μm. Irregular light patches and ghost zoning are also commonly observed. Four zircons were analyzed and show high U contents between 217 and 1284 ppm, although one analysis yielded only 76 ppm. Th contents are mostly high, varying between 23 and 100 ppm. Low Th/U ratios (0.08 –Table 1) indicate a correlation with light patches, suggesting that these zones are metamorphic. One zircon grain with irregular concentric oscillatory zoning in the core yielded the oldest age (1229 Ma), either magmatic or inherited. In this scenario, the mafic rocks would have assimilated zircon from an older crust, although rocks of this age have not been discovered in the region.

In addition to of zircons, six titanite grains were analyzed. They are generally fragmented with various sizes and shapes, and their lengths vary between 200 and 500 μm. Most of the grains are unzoned or have faint, patchy zoning. Titanite crystals have U contents lower than 210 ppm, varying between 180 and 203 ppm, and have Th near 200 ppm. Combining the data from zircon and titanite, the metamorphic recrystallization in this sample is dated at 1103 ± 17 Ma (Fig. 4c) by nine analyses (3 zircon + 6 titanite).

Fine-grained amphibolite (*Sample GRT-04*; S 11º53'23"/W 62º29'16") of upper amphibolite facies with minor intercalations of trondhjemite dominates the central part of the mafic belt of the Nova Brasilândia proto-ocean. This sample is an amphibole-rich amphibolite that partially preserves primary igneous features. In thin section, brown and clear titanite grains occur primarily in amphibole–epidote-rich domains. The plagioclase has lobate grain boundaries, often recrystallized to small subgrains, and shows evidence of strong deformation. The mineralogical and textural features suggest gabbro as the protolith.

Zircons from this sample are colorless, clear, elongated, prismatic-to-rounded, and many contain numerous cracks. Most grains are structureless or patchily zoned. Irregular light patches occur in various parts of the crystals. The U content of the zircon varies between 37 and 527 ppm, and the Th contents between 21 and 298 ppm. Nine analyses this sample yield an intercept age of 1103 ± 7 Ma (MSWD= 1.3, Fig. 4d), which is interpreted as the age of peak metamorphism. This age is the same as that obtained from sample GRT-03 described above.

A coarse-grained amphibolite was collected at the westernmost part of the mafic belt of the Nova Brasilândia rift, near the contact with a porphyroblastic milonitic granite. *Sample GRT-05* (S 11º57'08"/W 63º05'57") has partially preserved igneous texture and zones with well-developed mylonitic foliation. The mylonitic fabric is defined by a preferred orientation of amphibole or by sub-centimeter-to-centimeter scale titanite-ilmenite veinlets. Their mylonitic foliation shows a W-E structural trend.

Zircon and rutile crystals were analyzed. Zircon crystals are weakly zoned (ghost zoning) and generally 100 to 200 μm in size. They exhibit stubby habit with rounded terminations, which provide oval-to-rounded morphologies to some grains. U contents range from 277 to 552 ppm, and Th contents are more uniform and vary from 57 to 89 ppm. U–Pb isotopic analyses of three zircon grains yield an average $^{207}Pb/^{206}Pb$ age of 1103 ± 5 Ma (Fig. 4e), which we interpret to be a metamorphic recrystallization age.

Rutile grains show an external morphology that varies from prismatic to slightly rounded, and these grains are 100-250 μm long. Six grains were dated and yielded a $^{207}Pb/^{206}Pb$ concordia age of 949 ± 9 Ma (Fig. 4e). Taking into account the analytical uncertainty, this age is similar to the titanite age of sample GRT-02. Generally, the U-Pb ages for rutile are younger than the age of peak metamorphism and younger than the U-Pb ages for zircon, titanite and monazite (Mezger et al. 1989). This result suggests that the rutile ages reflect cooling below closure temperatures. However, there is a large difference between the peak metamorphic age recorded by zircons (~1100 Ma) and the age of metamorphic rutile (~950 Ma). Another possible scenario is that the metamorphic rutile grew below its closure temperature through dynamic recrystallization, promoted by a later phase of deformation at ca. 1.0 Ga. This later phase of deformation is related to the Rio Branco transcurrent shear zone development in low amphibolite facies metamorphic conditions (Rizzotto 1999).

Sample GR-66 (S 11º43'33"/W 62º09'10") was previously dated by Rizzotto (1999) and has now been reprocessed. It is a fine-grained banded paragneiss, with well-defined felsic bands composed of quartz and plagioclase and mafic bands of biotite. The mineral assemblage is in metamorphic equilibrium compatible with upper amphibolite facies conditions.

Twenty-four grains from this sample were analyzed (Table 1). The largest population (9 grains) yield an age of 1215 ± 20 Ma. Five grains yield older ages of 1320 ± 20 Ma, while a group of three crystals has an age of 1417 ± 35 Ma. A younger population with an age of 1122 ±12 Ma was also obtained (2 grains). The remaining data yield a spread of ages between 2090 and 1505 Ma (Fig. 4f). These results suggest that the protolith of the Nova Brasilândia paragneiss was derived from a Paleoproterozoic/ Mesoproterozoic mixed source. These data further suggest that the sedimentary protolith of the Nova Brasilândia Group was not deposited prior to 1122 Ma, the youngest age obtained from the population of detrital zircons.

Therefore, all of the ages reported above are equivalent, within error ranges, and represent the timing of peak metamorphism (~1104 Ma) after the late Mesoproterozoic intraplate rifting (1150-1122 Ma).

4.2. Aguapeí belt

The sampled area is the most northwestern region of the belt, near the southwestern boundary of the Parecis Basin (Figs. 1 and 2). This area consists of a repetitive, intercalated sequence of pelitic and quartzose layers, suggesting a turbiditic sequence. In spite of the mid-to-low metamorphic grade of this area (greenschist to lower amphibolite facies), S_0 bedding is locally preserved and still distinguishable in some outcrops. The metasedimentary rocks of the area investigated in this work are structurally and lithologically distinct from the mature, continental sediments of the Aguapeí Group (e.g., Souza and Hildred 1980, Saes 1999). However, we propose that these metasedimentary rocks (sand-silt rhythmites) form part of the basal unit of the Aguapeí Group. In this way, this metasedimentary package is very similar structurally and lithologically to the metasedimentary rocks of the Nova Brasilândia Group.

Sample NM-165 (S 13º25'39"/W 60º15'20") is an aluminous metapsammite, which is interbedded with metapelitic layers, suggesting a turbiditic environment. It shows pervasive symmetrical folds with mainly quartz, biotite and garnet and fine veinlets of quartz along the axial plane.

Zircons from this sample are partly rounded or have broken terminations, and vary in size from 100-300 μm with an aspect ratio of 3:1 to 2:1. Although magmatic euhedral faces are present in some crystals, rounding is a common feature in many crystals, and all are detrital. The main population (n=6) has an age in the 1331-1354 Ma range (Table 1 and Fig. 5a) interpreted to have been derived from rocks of the Alto Guaporé belt, such as the granitoids of the Igarapé Enganado and Alto Escondido suites. Four grains have ages between 1506 and 1527 Ma, derived from rocks of the Rio Alegre terrane. One grain has an age of

1436 ± 6 Ma and derived from the Trincheira complex. The youngest zircon yielded an age of 1331± 8 Ma (Table 1), which is interpreted as the maximum sedimentation age of the sedimentary protolith.

Sample GR-752 (S 13º25'26"/W 60º15'40") is a banded phyllite interbedded with quartzite layers. It consists of quartz, biotite and garnet aggregates arranged along a well-developed vertical foliation. Many ptigmatic folds consist mainly of quartz, and the layers are cut cross-cut by a dense network of quartz veins. Folds axes are consistent with the mineral lineation at 70º; S80ºW.

Most zircon grains are short prisms with rounded edges and variable shapes and color and are all detrital. They present two main age populations, 1768 and 1451 Ma; the youngest grain has an age of 1390 Ma and the oldest grain 2027 Ma (Fig. 5b). The ages of the most representative zircon populations (1.45 Ga; 1.76 Ga) signify not only the different continental sedimentation sources (Leite and Saes 2003) but also the timing of the adjacent magmatic arcs (Jamari and Santa Helena magmatic arcs), which forms part of the basement in the Rondônia and Mato Grosso states of the southwestern margin of the Amazon craton.

Sample NM-182 (S 13º26'35"/W 60º09'25") is an impure quartzite (metagreywacke), which presents overturned and subvertical beds with metric to decimetric thickness and oriented banding at N05ºE/85ºSE, although it is strongly folded in the highest strain zones. This quartzite is interbedded with thin beds of biotite-rich metamudstones (phyllites).

Most zircon grains are small (80-120 μm) with rounded edges, and several types of shapes are present. The results obtained for the 10 analyzed zircon crystals (Table 1) show that the quartzite has a wide range of zircon provenances (Fig. 5c). Most of the crystals (n=7) have an age of 1508 Ma and may have been derived from rocks correlated to the Cachoeirinha orogeny (Ruiz 2005). Two grains yield older ages of 1938 and 1645 Ma and are interpreted to have been derived from rocks constituting the basement of the Rondônia-Juruena Province. One grain has a younger age (1255 Ma), which may indicate the maximum depositional age

of the protoliths of the Aguapeí belt and most likely was derived from rocks correlated to the San Andres Granite (Santos et al. 2008). This granite occurs in the easternmost part of Bolivia or the provenance is from another granitoid body within the basement of the Rondônia-Juruena Province.

Sample GR336 (S 11º59'02"/W 61º23'58") is a fine-grained dark banded gneiss, which contains abundant elongated quartz nodules, in a strongly foliated matrix of quartz–plagioclase–biotite–ilmenite, including significant areas of leucosome development. The zircon population is dominated by rounded grains, short prisms, and a very small proportion of prismatic grains. They present variable shapes and color and are all detrital. The main population (n=8) has an age of 1337 Ma (Fig. 5d) and is interpreted to have been derived from rocks of the Alto Guaporé belt, such as granitoids of the Igarapé Enganado and Alto Escondido suites. Four grains yield an age of 1512 Ma, and these grains are derived from rocks of Serra da Providência suite. One grain has an age of 1420 Ma and may be derived from the tonalitic rocks of the Trincheira complex. The youngest zircons (n=2) are most likely derived from granitic leucosome that has an age of 1068 ± 20 Ma. Considering the analytical uncertainty, this age is close to the age of the metamorphic climax of the Nova Brasilândia orogeny (~1110 Ma).

Sample GR-768 (S 13º15'30"/W 60º16'00") is from a slightly elliptical stock that is essentially undeformed. It is a fine-grained equigranular biotite syenogranite, with an elliptical to rounded mafic autolith, an isotropic structure and is intruded into metapsammites of the Aguapeí Group. Its average composition is microcline (36%), oligoclase (27%), quartz (30%), biotite (6%), zircon, apatite and fluorite (<1%). Zircon crystals are prismatic, with aspect ratios 2:1 to 4:1, and are 90-150 μm long and poorly zoned. There are two populations of zircon, zoned magmatic zircon formed at 1025 ± 6 Ma (date of emplacement) (Fig. 5e) and inherited grains with age of the 1569 ± 73 Ma, which is correlated to the Serra da Providência

granites. Given the post-tectonic timing implied for the granite, we interpret all of the observed stages of ductile deformation to have occurred prior to 1025 ± 6 Ma.

Sample GR 345 (S 12º05'49"/W 61º25'24") is part of small stocks that occur throughout the area and as intrusions in orthogneiss of the São Felipe complex. The rock is medium- to fine-grained, pink-colored monzogranite, with an equigranular-to-inequigranular texture. This rock contains biotite and/or hornblende as mafic minerals. Centimeter- to decimeter-wide granular enclaves of granodioritic orthogneiss are commonly observed. This rock is in general massive, but has locally magmatic foliation.

Zircon crystals are subhedral, prismatic, clear and of good quality and are 200-250 μm long with broad concentric oscillatory zoning. Of the ten crystals analyzed, nine group tightly, and one is discordant, producing the upper intercept age of 1010 ± 15 Ma (MSDW=0.67) (Fig. 5f). This age is interpreted to be the crystallization age of the granite and is similar to the ages obtained in other late-to post-tectonic granites within the Nova Brasilândia-Aguapeí belt.

5. Discussion

Main questions regarding the tectonic history and further characterization of the temporal evolution of Nova Brasilândia and Aguapeí belts: (1) Were the belts contiguous, did they form and evolve in the same interval of time, or were they geologically distinct belts? Did these belts form over an already-stabilized crust (craton), or do they represent a suture zone that marks a crustal boundary in the Amazon craton?

In light of the new geochronological data combined with field data, we suggest a geographical and lithotectonic connection between the Nova Brasilândia and Aguapeí metasedimentary belts. The two belts evolved together and were generated by the reactivation of the Guaporé paleo-suture (Rizzotto et al. unpublished data), positioned between the Amazon craton in the north and the Paraguá Block in the south.

The belts extend up to 900 km inside the cratonic area in SW Amazon craton (Fig. 1), and their curved shapes depict the ancient Guaporé suture zone.

The Nova Brasilândia belt records the processes of sedimentation, bimodal magmatism and high-grade metamorphism in a rift-basin environment during a very short time interval from 1122 to 1100 Ma. The orogeny lasted ca. 22 million years from the initial opening of the rift to the final shortening. The youngest zircon group (sample GR-66; 1122 Ma, Fig. 4) of the Nova Brasilândia turbiditic deposits marks the opening of the rift basin, whereas the anatetic melt leucogranitic (sample GR-20; 1110 ± 8 Ma), locally derived from the fusion of the turbidites, indicates the age of peak metamorphism and the closure of the basin (Rizzotto 1999). In this way, Tohver et al. (2004), using the U-Pb TIMS method, investigated monazite of the Nova Brasilândia metaturbidite, located near sample GR-20, which yielded an age of 1096 ± 5 Ma. The proto-oceanic-rift phase is marked by the emplacement of gabbros and trondhjemites prior to 1110 Ma, corresponding to the age of the peak metamorphism affecting these rocks, according to the results obtained from samples GRT-01 to GRT-05.

The Aguapeí belt in turn presents a wider age range, representating the beginning of sedimentation, but shows strong similarities between the ages of the main sources of deposition and the maximum age of sedimentary protoliths when compared with the protolith Nova Brasilândia belt. According to Santos et al. (2005), the deposition of the lower Aguapeí Group (Fortuna Formation) occurred between 1167 ± 27 Ma and 1149 ± 7 Ma. These authors argue that, considering the uncertainties in these ages, the deposition of the sediments of the Fortuna Formation occurred over a period of 46 Ma (maximum) to 12 Ma (minimum). This period is roughly in accordance with the interval associated with the opening and closure of the Nova Brasilândia rift, as noted above. Table 2 shows the main populations of zircon analyzed to date, in this paper and from previous work.

In the northernmost portion of the Aguapeí belt, the sedimentary rocks are characterized by a gneissic foliation with lower-to-middle amphibolite facies metamorphism and a tight style of folding, and their protoliths are greywackes of the turbiditic environment. Deep-sea turbiditic deposits were also described by Saes (1999) in the Santo Corazón region, where a deep marine submarine turbiditic deposit that comprises deformed immature sedimentary rocks has been deposited into the central rift zone.

These geological features, except for the metamorphic grade, are also found in metaturbidites of the Nova Brasilândia Group (Rizzotto 1999). On the eastern margin of the Serra da Borda, the central portion of the Aguapeí belt, metapelites of the low Fortuna Formation (Souza 2011) have the same structural and lithological characteristics of the northern portion of the Aguapeí belt and have similar detrital zircons ages (Table 2). These sedimentary sequences could represent the same lithotectonics unit with little differences in the degrees of deformation and metamorphism and deposited under the same tectonic environments, at the same time. The Aguapeí belt is confined in a narrow aborted rift, whereas the Nova Brasilândia belt was deposited in a proto-oceanic rift environment.

Additionally, providing direct evidence indicating a clear linkage between the two belts, both the Nova Brasilândia belt and Aguapeí belt were involved in a reactivation of the orogenic zone characterized by shear zone of the large-scale sinistral strike-slip motion at ca. 1.0 Ga. This structure was characterized as transcurrent shear zone of the D_2-phase by Rizzotto (1999), and it is recognizable on regional LANDSAT images as large-scale lineaments that extend over hundreds of kilometers. This event is recorded by zircon, titanite and rutile of the mafic rocks (GRT-01, GRT-02 and GRT-05) of the Nova Brasilândia belt (Fig. 4). Tohver et al. (2004) found similar ages in monazite (993 Ma-U/Pb) and hornblende (983 Ma-$^{40}Ar/^{39}Ar$) from the samples collected along the transcurrent shear zone of the Nova Brasilandia belt. Similar ages were found in shear zones that affected the metasedimentary

rocks of the Aguapeí Group and neighboring country rocks in the time interval between 1030 and 920 Ma (e.g., Geraldes et al. 1997, Ruiz 2005, Fernandes et al. 2006).

The Sunsás belt, in the southeastern Bolivia shield, presents the same features and geological evolution compared with the Nova Brasilândia-Aguapeí belt. Sedimentary rocks of the Sunsás Group were deposited between 1300 and 1000 Ma. Sunsás deformation show upright NW trending folds formed contemporaneously with low-to-medium grade metamorphism and is structurally well marked by mylonitic shear zones that show preferential sinistral offsets active at ca. 1080-1050 Ma. According to Boger et al. (2005), the stages of ductile deformation must have occurred prior to 1074 Ma, but tectonic reactivation along the shear zones is marked by pegmatite injections (997 ± 3 Ma) and Au-rich zones with molibdenite that yielded a Re/Os age of 994 ± 3 Ma (Isla-Moreno 2009).

On the basis of our findings, we conclude that the Nova Brasilândia, Aguapeí and Sunsás metasedimentary and igneous belts were linked in the late Mesoproterozoic at ca. 1.2 Ga to 0.95 Ga, forming what is here called the Western Amazon belt (WAB). This belt overprints the ca. 1350 crust formed by the Paraguá Block and the basement rocks of the Rondônia-Juruena Province. The main orogenic phase occurred at 1110 Ma (peak metamorphism). The dominant metamorphic grades are high (upper amphibolite to granulite) in the northern part of the belt in Rondônia and low to medium grade (green schist to lower amphibolite facies) in the eastern zone in Bolivia and in southern Mato Grosso (Sunsás and Aguapeí Groups). Reactivation in this belt occurred through extension, uplift and exhumation after ~ 1.0 Ga.

New field geology data coupled with robust geochronology indicate that the Paraguá Block accreted to the southwest margin of Amazonia at ca. 1.47-1.32 Ga (Rizzotto and Hartmann 2012; Rizzotto et al. unpublished data). Considering this scenario, we suggest that the Nova Brasilândia, Aguapeí and Sunsás groups have a within-plate origin. This scenario is supported by recent paleomagnetic results from 1.42 Ga mafic rocks of the Indiavaí Suite in

Mato Grosso, that demonstrate the latitudinal proximity of the Amazon craton north of the Nova Brasilândia belt and Guaporé suture zones and the Paraguá craton basement to the south of this suture zone by 1.42 Ga (D'Agrella-Filho et al. 2012). Globally, the tectonic evolution of the Nova Brasilândia, Aguapeí and Sunsás Groups may be related with the final breakup of the supercontinent Columbia, which occurred at about 1.3-1.2 Ga, marked by a major episode of plate-wide extension and rifting, whit the emplacement of the gabbros, trondhjemites and volcano-sedimentary rocks. This geological evolution is similar with Laurentia in North America, where occurred the emplacement of the McKenzie, Sudbury, Seal Lake, Harp and Mealy mafic dike swarms and coeval Coppermine River basalts at about 1.3-1.2 Ga.

Saes et al. (1992) interpreted the terrestrial or shallow marine to deep sedimentary rocks of the Aguapeí and Sunsás Groups to be deposited in rift environment. Sedimentary rocks of the Sunsás Group comprise a basal conglomerate overlain successively by two psammitic sequences and an intervening pelitic unit that were deposited in an alluvial-to-deltaic environment (Berrrangé and Litherland 1982). Subsequently, Saes et al. (1992) suggested that the deposition of the Sunsás Group has an intra-continental rift environment. These lithotectonics units differ from Nova Brasilândia Group because, in this Group, igneous rocks occur temporally and genetically associated with turbidites, reflecting the deposition of these rocks in the rift depocenter. Our theory is that when the reactivation of the Guaporé paleo-suture to generated the Nova Brasilândia-Aguapeí rift, the stretch rate (opening) of the rift, which is now the Nova Brasilândia rift, was high enough to generate a narrow ocean (proto-oceanic rift), while in the other two belts (Aguapeí and Sunsás), there was less opening, less sediment filling, and no ocean development (Fig. 2).

Therefore, over the cratonic area formed by the amalgamation of the Paraguá Block and Amazon craton during the early-middle Mesoproterozoic, the Nova Brasilândia, Aguapeí and Sunsás belts would then reflect zones of intense transpression, within-plate shortening and bimodal mafic-felsic intrusion due to the collisional dynamics, localized along the axis of

an intraplate Nova Brasilândia-Aguapeí rift. This tectonic cycle occurred between approximately 1150 and 1100 Ma. Deformation at this time would presumably have been driven by the collision and accretion of the Arequipa-Antofalla Basement to the western margin of the Paraguá Block (Loewy et al. 2004). As reported by previously published studies, the Proterozoic tectonic evolution of the Arequipa-Antofalla Basement suggests an allochthonous origin, and this microcontinent must have been part of a larger continent before 1.0 Ga. Thus, the Arequipa-Antofalla Basement, a Proterozoic crustal block exposed along the modern central Andean margin, is considered to have accreted to the margin of the Amazon craton during the Sunsás Orogeny, at approximately 1.2-0.94 Ga (Loewy et al. 2004). According to Dalziel (1994), pervasive metamorphism at 1.2–1.0 Ga in the northern and central domains of the Arequipa-Antofalla Basement supports accretion of the Arequipa-Antofalla Basement to the Amazon craton during the Sunsás Orogeny. Therefore, the late Mesoproterozoic orogenic event recorded in the northern and central domains of the Arequipa-Antofalla Basement is coeval with events in the southwestern margin of the Amazon craton. This indicates that the breakup of the supercontinent Columbia was followed rapidly by the assembly of another supercontinent Rodinia, which was assembled along the globally distributed Grenvillian orogens at ca. 1.0 Ga.

We partially agree with the models proposed by Loewy et al. (2004) and Boger et al. (2005) and suggest a tectonic evolution according to the framework depicted in Figure 6.

6. Conclusions

Zircon U-Pb geochronological data and field relationships presented in this contribution are strong evidence for the existence of a continuous intracratonic late Mesoproterozoic orogenic belt (Western Amazon belt) in the southwestern margin of the Amazon craton.

Considering the final docking of the Paraguá Block and the proto-Amazon craton during the middle-Mesoproterozoic time (1470-1330 Ma, Rizzotto et al. unpublished data), the youngest orogenic belt (WAB) of the Amazon craton is formed by the previously defined Nova Brasilândia, Aguapeí and Sunsás belts, which became interconnected at the end of the Mesoproterozoic, and has a curvilinear shape of approximately 1000 km in length. The continuity of magnetic anomalies and structural trends suggests that this belt is continuous below the Phanerozoic cover of the Parecis basin.

The opening of the rift that preceded the development of the Nova Brasilândia-Aguapeí belts originated from the reactivation of a paleo-suture (Guaporé suture zone). We propose that the sedimentary and igneous protoliths for the three orogenic belts exposed in the southwestern margin of the Amazon craton formed during the late Mesoproterozoic in an intracontinental rift, opening ca. 1150 Ma and closing at 1110 Ma. Therefore, Western Amazon belt's geological history has evolved from the development of a complete Wilson cycle at 50 Ma. Both the Nova Brasilândia-Aguapeí and the Sunsás belts were involved in an orogenic zone characterized by a transtensional stage that was succeeded by a transpressional regime accompanied by crustal shortening that allows the accommodation of N45ºE compressional stress field (Rizzotto 1999). This deformation occurred during the accretion of the Arequipa-Antofalla Basement to the proto-Amazon craton.

The latest tectonic movements, before the effective cratonization of the southeastern margin Amazon craton, occurred at approximately 1.0 Ga when the reactivation of the previous zone of weakness allowed the development of transcurrent zones, which favored the plutonic activity through the emplacement of the Rio Pardo granites in the Nova Brasilândia region, anorogenic plutons in the Rondônia Tin Province (Bettencout et al. 1999), post-tectonic granite in Sunsás belt (Litherland et al. 1986, Isla-Moreno 2009) and in the Arequipa-Antofalla Basement (Wasteneys et al. 1995, Wörner et al. 2000, Loewy et al. 2004). Soon

after this phase, uplift, exhumation and extension culminated in the generation of intracontinental basins (e.g., Palmeiral Formation and Huanchaca Group).

Acknowledgements

This work was supported by CNPq (Conselho Nacional de Desenvolvimento Científico e Tecnológico) grant 140917/2008-0. The authors thank CPRM/Geological Survey of Brazil office in Porto Velho, Rondônia, for assistance in the fieldwork and access to sample preparation. We thank also Marcos Luiz Quadros, Maria Rosalva Coelho and Pamela Emanuelle Silva for help with sample preparation. SEM images were obtained at the UWA Centre for Microscopy and Microanalysis, an Australian Microscopy & Microanalysis Research Facility. U-Pb zircon analyses were performed on the sensitive high-resolution ion microprobes (SHRIMP II) located at the John de Laeter Centre of Mass Spectrometry, which is operated by Curtin University, the University of Western Australia and the Geological Survey of Western Australia. Constructive reviews of this manuscript by anonymous reviewer are gratefully acknowledged.

Resumo

Novos dados de U-Pb em zircão e relações de campo, aliados aos dados de levantamento aerogeofísico permitiu-nos sugerir que os Grupos Nova Brasilândia e Aguapeí fazem parte de uma única faixa móvel constituída por rochas metaígneas e metassedimentares do final do Mesoproterozóico (1150 Ma -1110 Ma). Esta história geológica é muito semelhante com a evolução intraplaca da Faixa Sunsás, no oriente Boliviano. Assim, propomos que os cinturões Nova Brasilândia, Aguapeí e Sunsás constituem uma única unidade geotectônica (aqui denominada de Faixa Móvel Amazônia Ocidental) desenvolvida no final do Mesoproterozóico, a qual instalou-se num ambiente de rift intracontinental por reativação de uma paleo-sutura (zona de sutura Guaporé). Portanto, a sua história geológica

evoluiu a partir do desenvolvimento de um completo Ciclo de Wilson em cerca de 40 Ma. Globalmente, essa evolução tectônica pode estar relacionada com a fragmentação final do supercontinente Columbia. Rochas máficas e trondhjemitos da porção mais setentrional da faixa móvel forneceram idades U-Pb em zircão de ~1110 Ma, as quais datam o pico do metamorfismo de alto grau e o fechamento do rift. Isso indica que a fragmentação do supercontinente Columbia foi seguida rapidamente pela montagem do supercontinente Rodínia (~1,1-1,0 Ba) e que a Faixa Móvel Amazônia Ocidental foi construída durante a acresção do Cráton Arequipa- Antofalla ao Cráton Amazonas.

Palavras-chave: Cráton Amazonas, rift intracontinental, Mesoproterózoico, Faixa Móvel Amazônia Ocidental, geocronologia U/Pb.

References

BERRANGÉ JP AND LITHERLAND M. 1982. Sinopsís de la geologia y potencial de minerales del area del Proyecto Precambrico. Boletin del Servicio Geológico de Bolivia, Informe 21, 120 p.

BETTENCOURT JS, TOSDAL RM, LEITE JR, WB AND PAYOLLA BL. 1999. Mesoproterozoic rapakivi granites of the Rondônia Tin Province, southwestern border of the Amazonian Craton, Brazil–I. Reconnaissance U–Pb geochronology and regional implications. Precam Res 95: 41–67.

BETTENCOURT JS, LEITE JR. WB, RUIZ AS, MATOS R, PAYOLLA BL AND TOSDAL RM. 2010. The Rondonian-San Ignacio Province in the SW Amazonian Craton: An overview. Journ South Am Ear Sci 29: 28–46.

BOGER SD, RAETZ M, GILES D, ETCHART E AND FANNING CM. 2005. U–Pb age data from the Sunsas region of eastern Bolivia, evidence for the allochtonous origin of the Paraguá Block. Precam Res 139: 121–146.

CORDANI UG, SATO K, TEIXEIRA W, TASSINARI CG AND BASEI MA. 2000. Crustal Evolution of the South American Platform. In: CORDANI UG, MILANI EJ, THOMAZ FILHO A AND CAMPOS DA (Eds.), Tectonic Evolution of South America, 31st. International Geological Congress, Rio de Janeiro, Brazil, p. 19–40.

CASQUET C, PANKHURS, RJ, FANNING M, BALDO E, GALINDO C, RAPELA CW, CASADO JG AND DAHLQUIST JA. 2006. U–Pb SHRIMP zircon dating of Grenvillian metamorphism in Western Sierras Pampeanas (Argentina): correlation with the Arequipa-Antofalla Craton and constraints on the extent of the Precordillera Terrane. Gond Res 9 (4): 524–529.

CORDANI UG AND TEIXEIRA W. 2007. Proterozoic accretionary belts in the Amazonian Craton, In: HATCHER RD, CARLSON MP, MCBRIDE JH AND MARTINEZ CATALAN JR eds., 4-D Framework of Continental Crust: Geol Soc Am Memoir 200: 297-320.

D'AGRELLA-FILHO MS, TRINDADE, RIF, ELMING SA., TEIXEIRA W, YOKOYAMA E, TOHVER E, GERALDES MC, PACCA IG, BARROS MAS AND RUIZ AS. 2012. The 1.42 Ga Indiavaí Mafic Intrusive (SW Amazonian Craton): Paleomagnetic results and implications for the Columbia supercontinent configuration. Gond Res (in press).

DALZIEL IW. 1994. Precambrian Scotland as a Laurentia-Gondwana link: Origin and significance of cratonic promontories. Geology 22: 589–592.

DE PAOLO DJ. 1981. A neodymium and strontium isotopic study of the Mesozoic calc-alkaline granitic batholiths of the Sierra Nevada and Peninsular Ranges, California. J Geophys Res 86: 10470–10488.

FERNANDES CJ, KUYUMJIAN RM, PULZ GM, GERALDES MC AND PINHO FE. 2006. Geologia estrutural e idade $^{40}Ar/^{39}Ar$ do depósito de ouro Pau-a-Pique, Faixa Móvel Aguapeí, sudoeste do Estado do Mato Grosso. Rev Bras Geoc 36: 3–15.

GERALDES MC, FIGUEIREDO BR, TASSINARI CC AND EBERT HD. 1997. Middle Proterozoic vein-hosted gold deposits in the Pontes e Lacerda region, southwestern Amazonian Craton, Brazil. Int Geol Rev 39: 438–448.

GERALDES MC, VAN SCHMUS WR, CONDIE KC, BELL S, TEIXEIRA W AND BABINSKI M. 2001. Proterozoic Geologic Evolution of the SW part of the Amazonian Craton in Mato Grosso State, Brazil. Precam Res 111: 91–128.

ISLA-MORENO L. 2009. Distrito Don Mario, un deposito de Au-Cu hidrotermal asociado a zonas de cizalla. XVIII Congreso Geológico de Bolivia, Potosi, Bolívia. Memorias del Colegio de Geólogos, p. 85–92.

JACKSON SE, PEARSON NJ, GRIFLIN WL AND BELOUSOVA EA. 2004. The application of laser ablation-inductively coupled plasma-mass spectrometry to in situ U–Pb zircon geochronology. Chem Geol 211: 47–69.

KEPPIE JD AND ORTEGA-GUTIERREZ FO. 1999. Middle American Precambrian basement: a missing piece of the reconstructed 1 Ga orogen. Geol Soc Am, Sp Paper 336: 199–210.

KOSLER J, FONNELAND H, SYLVESTER P, TUBRETT M AND PEDERSEN RB. 2002. U-Pb dating of detrital zircons for sediment provenance studies—a comparison of laser ablation ICPMS and SIMS techniques. Chem Geol 182: 605–618.

Li ZX et al. 2008. Assembly, configuration, and break-up history of Rodinia: a synthesis. Precam Res 160: 179–210.

LITHERLAND M AND BLOOMFIELD K. 1981. The Proterozoic history of eastern Bolivia. Precam Res 15: 157–179.

LITHERLAND M et al. 1986. The geology and mineral resources of the Bolivian Precambrian Shield. Overseas Memoir British Geological Survey 9, 153 pp.

LEITE AD AND SAES GS. 2003. Geocronologia Pb/Pb de zircões detríticos and análise estratigráfica das coberturas sedimentares proterozóicas do sudoeste do Cráton Amazonas. Rev Geol USP Série Científica 3: 113–127.

LOEWY S, CONNELLY JN, DALZIEL IW AND GOWER CF. 2003. Eastern Laurentia in Rodinia: Constraints from whole-rock Pb and U-Pb geochronology, in: SIRCOMBE KN AND MCELHINNY MW eds. Orogenic belts, regional and global tectonics: A memorial volume to Chris McAulay Powell. Tectonophys 375: 169–197.

LOEWY SL, CONNELLY JN AND DALZIEL IW. 2004. An orphaned basement block: the Arequipa-Antofalla Basement of the central Andean margin of South America. Geol Soc Am Bull 116: 171–187.

LUDWIG KR. 1999. Using ISOPLOT/Ex, version 2: a geochronological toolkit for Microsoft Excel. Berkeley Geochronological Center Spec Public Ia, 47 pp.

MEZGER K, HANSON GN AND BOHLEN SR. 1989. Highprecision U-Pb ages of metamorphic rutile: application to the cooling history of high-grade terranes. Earth Plan Sci Lett 96: 106-118.

PATCHETT PJ AND RUIZ J. 1987. Nd isotopic ages of crust formation and metamorphism in the Precambrian of eastern and southern Mexico. Cont Mineral Petrol 96: 523–528.

PRENDERGAST MD. 2000. Layering and precious metals mineralization in the Rincón del Tigre Complex, Eastern Bolivia. Econ Geol 95: 113–130.

QUADROS ML, PALMEIRA LC AND CASTRO CC. 2012. Geologia e Recursos Minerais da Folha Rio Machadinho (SC.20-X-C), escala 1:250.000: Sistema de Informações Geográficas-SIG: Texto Explicativo do Mapa Geológico e de Recursos Minerais da Folha Rio Machadinho. Porto Velho: CPRM, 203 p.

RIZZOTTO GJ. 1999. Petrologia e Geotectônica do Grupo Nova Brasilândia, Rondônia. MSc. Dissertation. Federal University of Rio Grande do Sul. Porto Alegre, Brazil (in Portuguese).

RIZZOTTO GJ. 2001. Reavaliação do Ciclo Orogênico Sunsas/Aguapeí no Sudoeste do Cráton Amazônico. In: Workshop on Geology of the SW Amazonian Craton: state of the art, IGC Project 426, Extended Abstracts p. 66-67.

RIZZOTTO GJ AND QUADROS ML. 2007. Margem Passiva e granitos Orogênicos do Ectasiano em Rondônia. In: X Simpósio de Geologia da Amazônia. Porto Velho, CD-ROM.

RIZZOTTO GJ AND DEHLER NM. 2007. Arcabouço Estrutural da Faixa Alto Guaporé e o Regime Tectônico do Ectasiano na borda SW do Craton Amazônico. XI Simpósio Nacional de Estudos Tectônicos – V International Symposium on Tectonics of the SBG, Natal, p.130-132.

RIZZOTTO GJ AND HARTMANN LA. 2012. Geological and geochemical evolution of the Trincheira Complex, a Mesoproterozoic ophiolite in the southwestern Amazon craton, Brazil. Lithos (in press).

ROGERS JJ AND SANTOSH M. 2003. Supercontinents in Earth history. Gond Res 6: 357–368.

RUIZ AS. 2005. Evolução geológica do sudoeste do Cráton Amazônico, região limítrofe Brasil-Bolívia, Mato Grosso. PhD Thesis, São Paulo State University, Rio Claro, São Paulo, Brazil (in Portuguese).

RUIZ AS, SIMÕES LS, ARAUJO LM, GODOY AM, MATOS JB AND SOUZA MZ. 2007. Cinturão Orogênico Aguapeí (1025–900 Ma): Um exemplo de Faixa Móvel Intracontinental

no SW do Cráton Amazônico. In: XI Simpósio Nacional de Estudos Tectônicos, Natal. Anais, p. 116-118.

SADOWSKI GR AND BETTENCOURT JS. 1996. Mesoproterozoic tectonic correlations between eastern Laurentia and western border of the Amazon Craton. Precam Res 76: 213–227.

SAES GS. 1999. Evolução tectônica e paleogeográfica do Aulacógeno Aguapeí (1.2–1.0 Ga) e dos terrenos do seu embasamento na porção sul do Craton Amazônico. Doctoral thesis, Institute of Geociences, University of São Paulo, São Paulo, Brazil, p. 135.

SAES GS, LEITE JA AND ALVARENGA CJ. 1992. Evolução tectono-sedimentar do Grupo Aguapeí, Proterozóico Médio na porção meridional do Cráton Amazônico: Mato Grosso e Oriente Boliviano. Rev Bras Geoc 23 (1): 31–37.

SANTOS JOS, HARTMANN LA, GAUDETTE HE, GROVES DI, McNAUGHTON NJ AND FLETCHER IR. 2000. A new understanding of the provinces of Amazon craton based on integration of field mapping and U–Pb and Sm–Nd geochronology. Gond Res 3: 489–506.

SANTOS JOS, RIZZOTTO GJ, EASTON MR, POTTER PE, HARTMANN LA AND MCNAUGHTON NJ. 2002. The Sunsás Orogen in Western Amazon Craton, South America and correlation with the Grenville Orogen of Laurentia, based on U-Pb isotopic study of detrital and igneous zircons. In: Geological Society of America, 2002. Denver Annual Meeting (October 27–30, 2002), Precam Geol, paper 122-8.

SANTOS JOS, MCNAUGHTON NJ, HARTMANN LA, FLETCHER IR AND SALINAS RM. 2005. The age of the deposition of the Aguapeí Group, Western Amazon Craton, based

on U–Pb study on diagenetic xenotime and detrital zircon. In: Latin American Congress, Quito, Equador, Extended Abstracts, p. 1–4.

SANTOS JOS, RIZZOTTO GJ, POTTER P, MCNAUGHTON N, MATOS R, HARTMANN LA, CHEMALE JR F AND QUADROS ML. 2008. Age and autochthonous evolution of the Sunsás Orogen in West Amazon Craton based on mapping and U-Pb geochronology. Precam Res 165: 120-152.

SCANDOLARA JE, RIZZOTTO GJ, AMORIM JL, BAHIA RB, QUADROS ML AND SILVA CR. 1999. Geological map of Rondônia. 1:1.000.000. Companhia de Pesquisa de Recursos Minerais, Brasilia.

SOUZA AE AND HILDRED PR. 1980. Contribuição ao estudo da geologia do Grupo Aguapeí, Mato Grosso. 31º Congresso Brasileiro de Geologia 2: 587–598.

TASSINARI CC, CORDANI UG, NUTMAN AP, VAN SCHMUS WR, BETTENCOURT JS AND TAYLOR PN. 1996. Geochronological systematics on basement rocks from the Rio Negro-Juruena Province (Amazonian Craton) and tectonic implications. Int Geol Rev 38: 161–175.

TEIXEIRA W, GERALDES MC, MATOS R, RUIZ AS, SAES G AND VARGAS-MATTOS G. 2010. A review of the tectonic evolution of the Sunsás belt, SW Amazonian Craton. Journ South Am Earth Sci 29(1): 47-60.

TOHVER E, VAN DER PLUIJM BA, MEZGER K, ESSENE E, SCANDORALA JE AND RIZZOTTO GJ. 2004. Significance of the Nova Brasilândia metasedimentary belt in western

Brazil: redefining the mesoproterozoic boundary of the Amazon Craton. Tectonics. doi:10.1029/2003TC001563 (TC6004).

TOHVER E, VAN DER PLUIJM BA, SCANDOLARA JE AND ESSENE E. 2005a. Late Mesoproterozoic deformation of SW Amazonia (Rondonia, Brazil): geochronological and structural evidence for collision with Southern Laurentia. J Geol 113: 309–323.

TOHVER E, VAN DER PLUIJM BA, MEZGER K, SCANDOLARA JE AND ESSENE EJ. 2005b. Two stage tectonic history of the SW Amazon craton in the late Mesoproterozoic: identifying a cryptic suture zone. Precamb Res 137: 35–59.

TOHVER E, TEIXEIRA W, VAN DER PLUIJM B, GERALDES M, BETTENCOURT JS AND RIZZOTTO GJ. 2006. Restored transect across the exhumed Grenville orogen of Laurentia and Amazonia, with implications for crustal architecture. Geology 34: 669-672.

WASTENEYS HA, CLARK AH, FARRAR E AND LANGRIDGE RJ. 1995. Grenvillian granulite-facies metamorphism in the Arequipa Massif, Peru: A Laurentia-Gondwana link: Earth Plan Sci Lett 132: 63–73.

WILLIAMS IS. 1998. U-Th-Pb geochronology by ion microprobe. In: MCKIBBEN MA, SHANKS III WC, RYDLEY WI (Eds.). Applications of Microanalytical Techniques to Understanding Mineralizing Processes. Rev Econ Geol 7: 1-35.

WÖRNER G, LEZUAN J, BECK A, HEBER V, LUCASSEN R, ZINNGREBE E, RÖSSLING R AND WILKE HG. 2000. Geochronology, petrology and geochemistry of

basement rocks from Belen (N. Chile) and C. Uyarani (W. Bolivian Altiplano): Implications for the evolution of the Andean basement: Journ South Am Earth Sci 13: 717–737.

YOUDEN WJ. 1951. Statistical methods for chemists. J. R. Stat. Soc. New York, Wiley.

FIGURE CAPTIONS

Figure 1- Simplified map of the southwestern Amazon craton showing the approximate boundaries of the main provinces, belts, tectonic elements, lithologic units, and location of dated samples.

Figure 2- Geotectonic map of the southwestern Amazon craton highlighting the Nova Brasilândia, Aguapeí and Sunsás rifts.

Figure 3- Airborne analytical signal amplitude map of southwestern margin of the Amazon craton. The highlighted (white line) magnetic lineaments indicate the rift zones and areas with mafic rocks outcrops of the Nova Brasilândia proto-oceanic rift phase.

Figure 4- Concordia diagrams of dated samples of the Nova Brasilândia belt.

Figure 5- U-Pb concordia plots and relative probability plots of zircons ages from samples of the Aguapeí belt and intrusive rocks.

Figure 6- Model tectonic evolution of the southwestern Amazon craton in the Mesoproterozoic (modified from Boger et al. 2005).

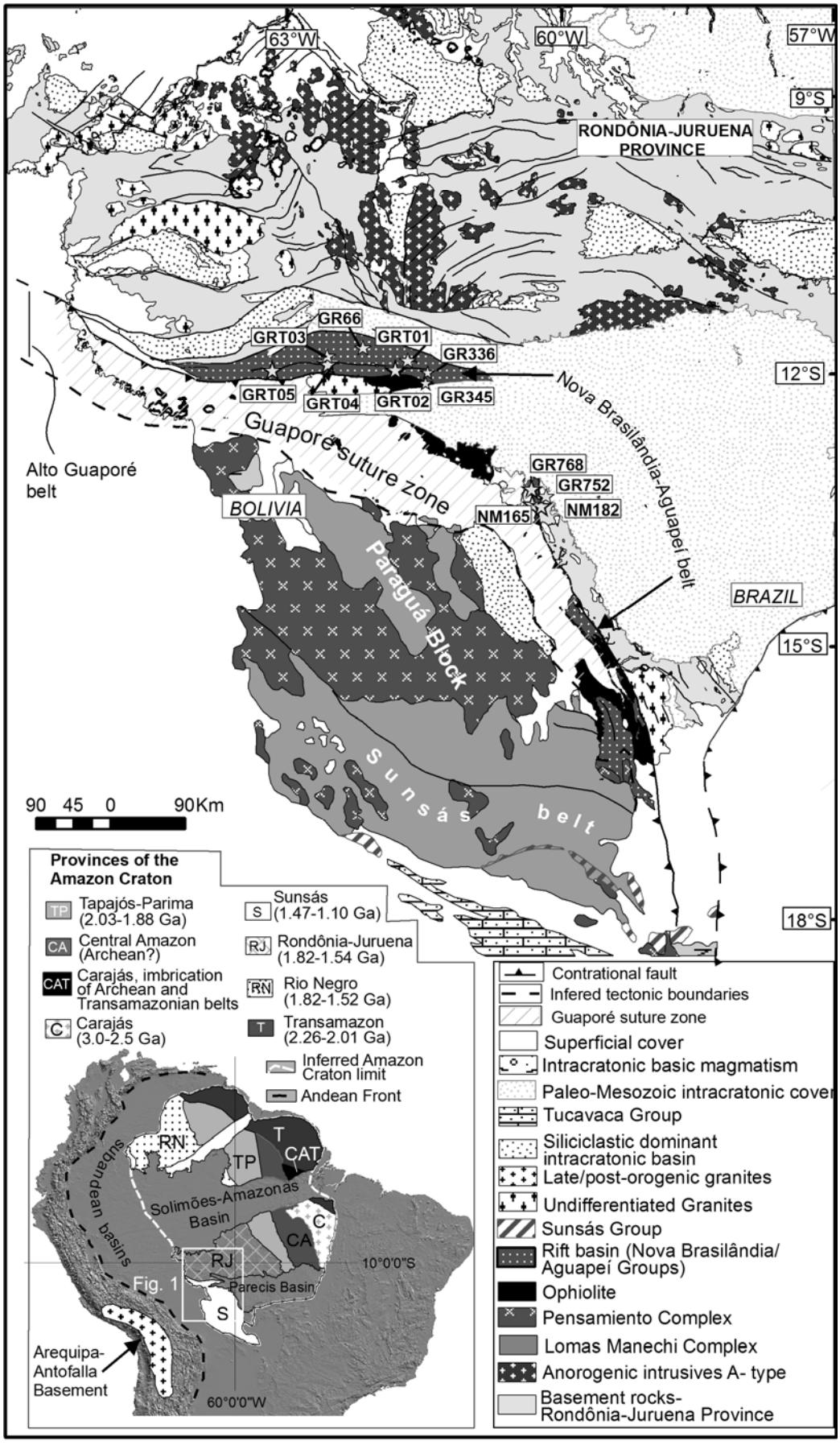

Figure 1- Simplified map of the southwestern Amazon craton showing the approximate boundaries of the main provinces, belts, tectonic elements, lithologic units, and location of dated samples.

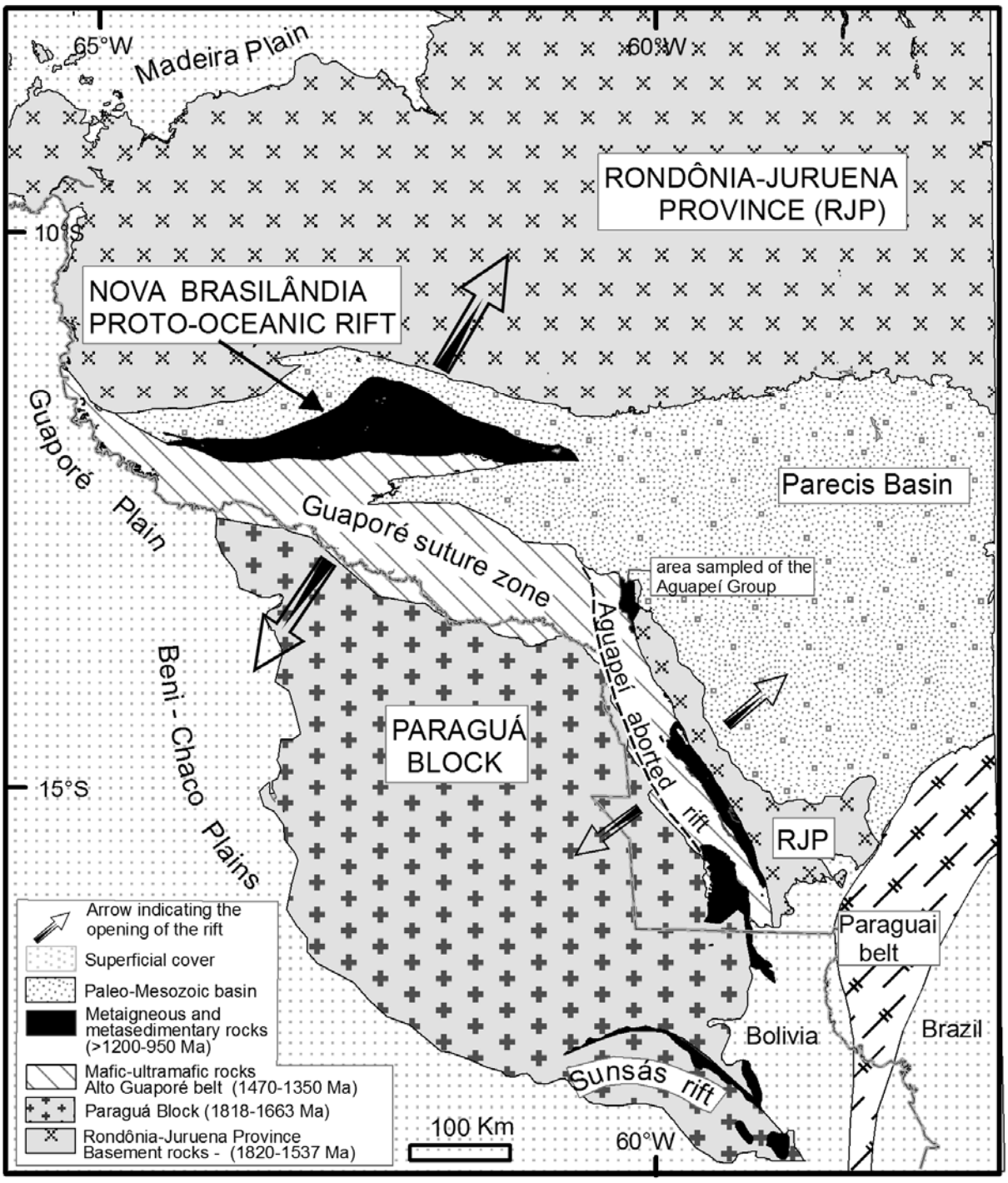

Figure 2- Geotectonic map of the southwestern Amazon craton highlighting the Nova Brasilândia, Aguapeí and Sunsás rifts.

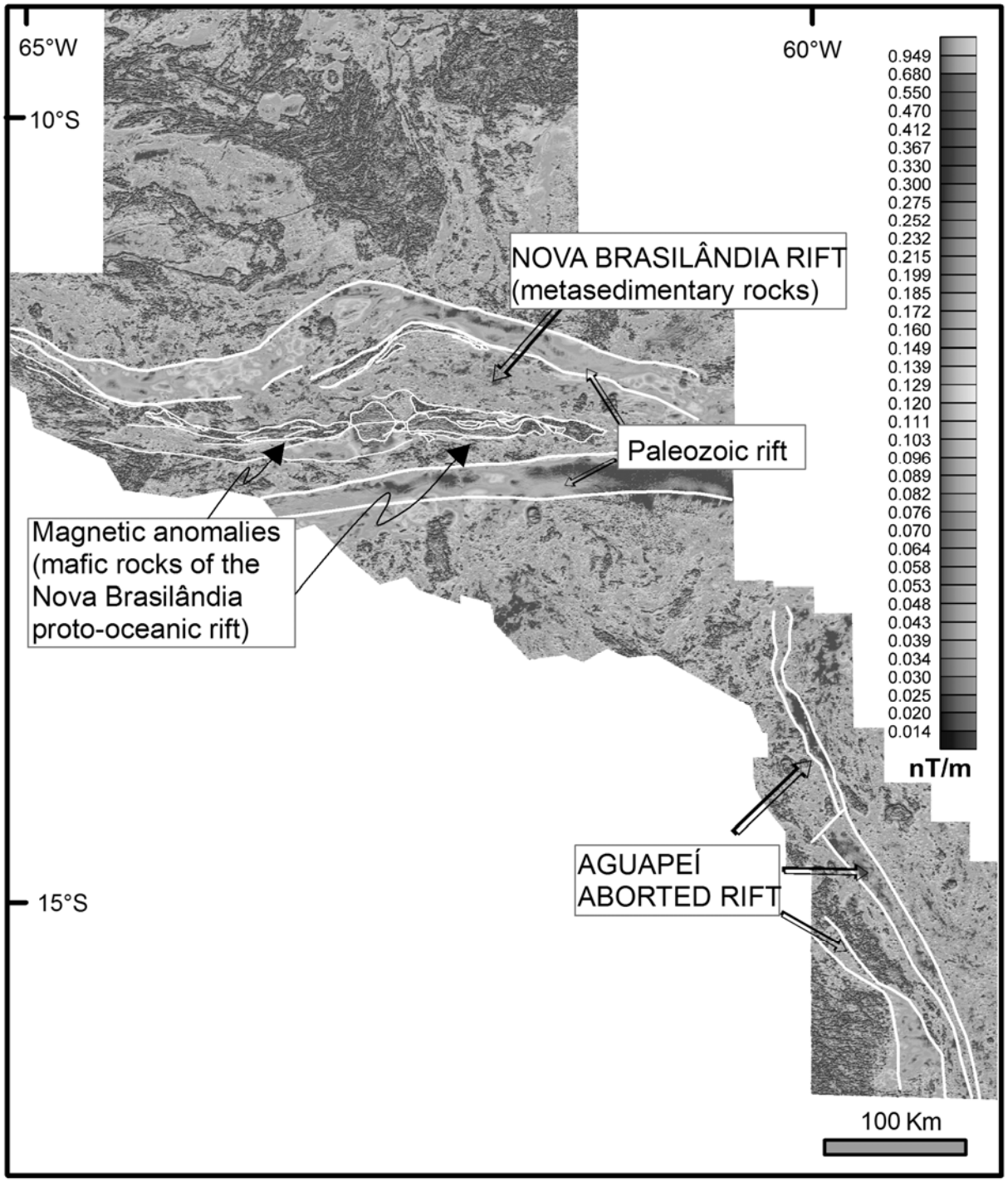

Figure 3- Airborne analytical signal amplitude map of southwestern margin of the Amazon craton.
The highlighted (white line) magnetic lineaments indicate the rift zones and areas with mafic rocks outcrops of the Nova Brasilândia proto-oceanic rift phase.

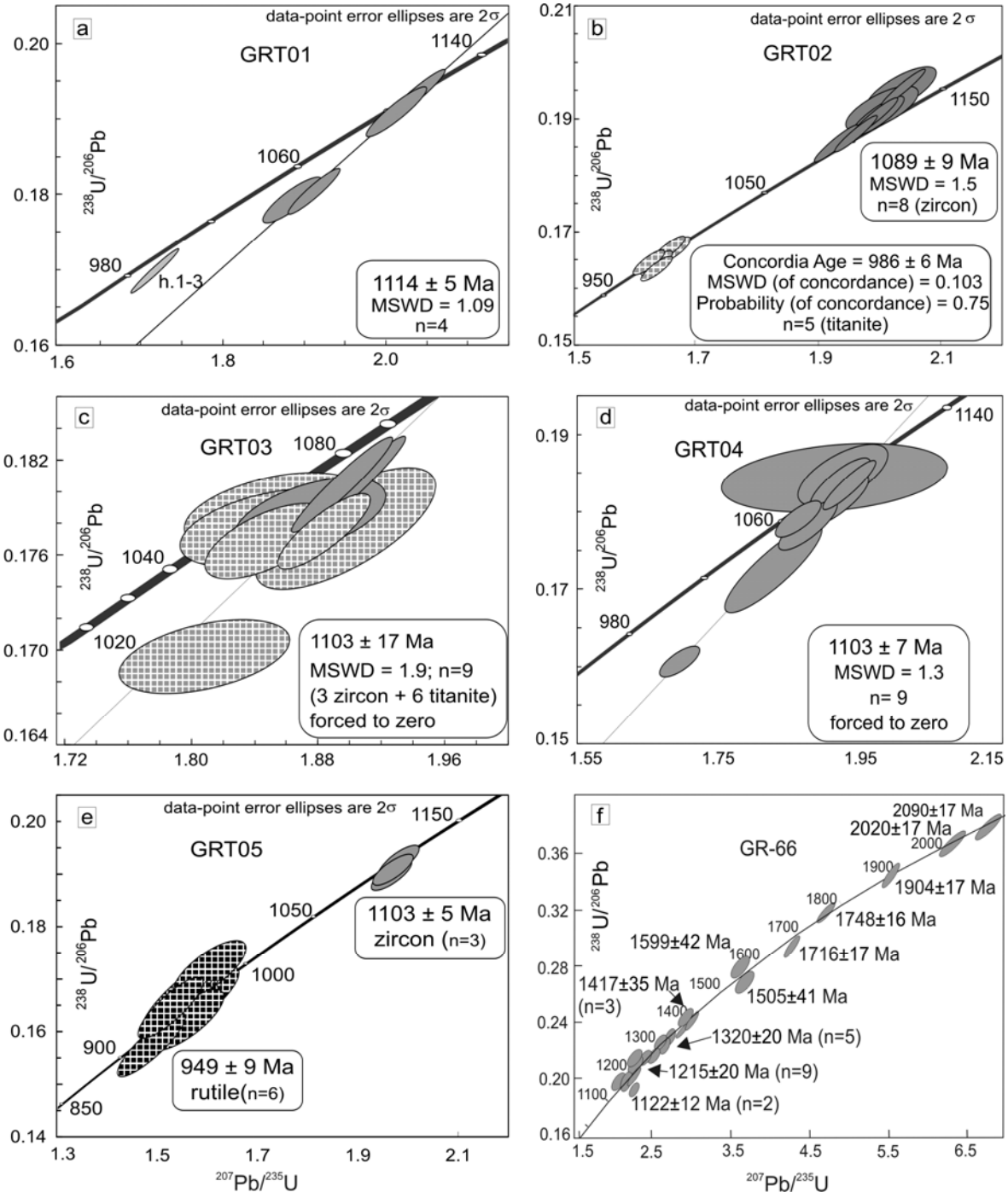

Figure 4- Concordia diagrams of dated samples of the Nova Brasilândia belt.

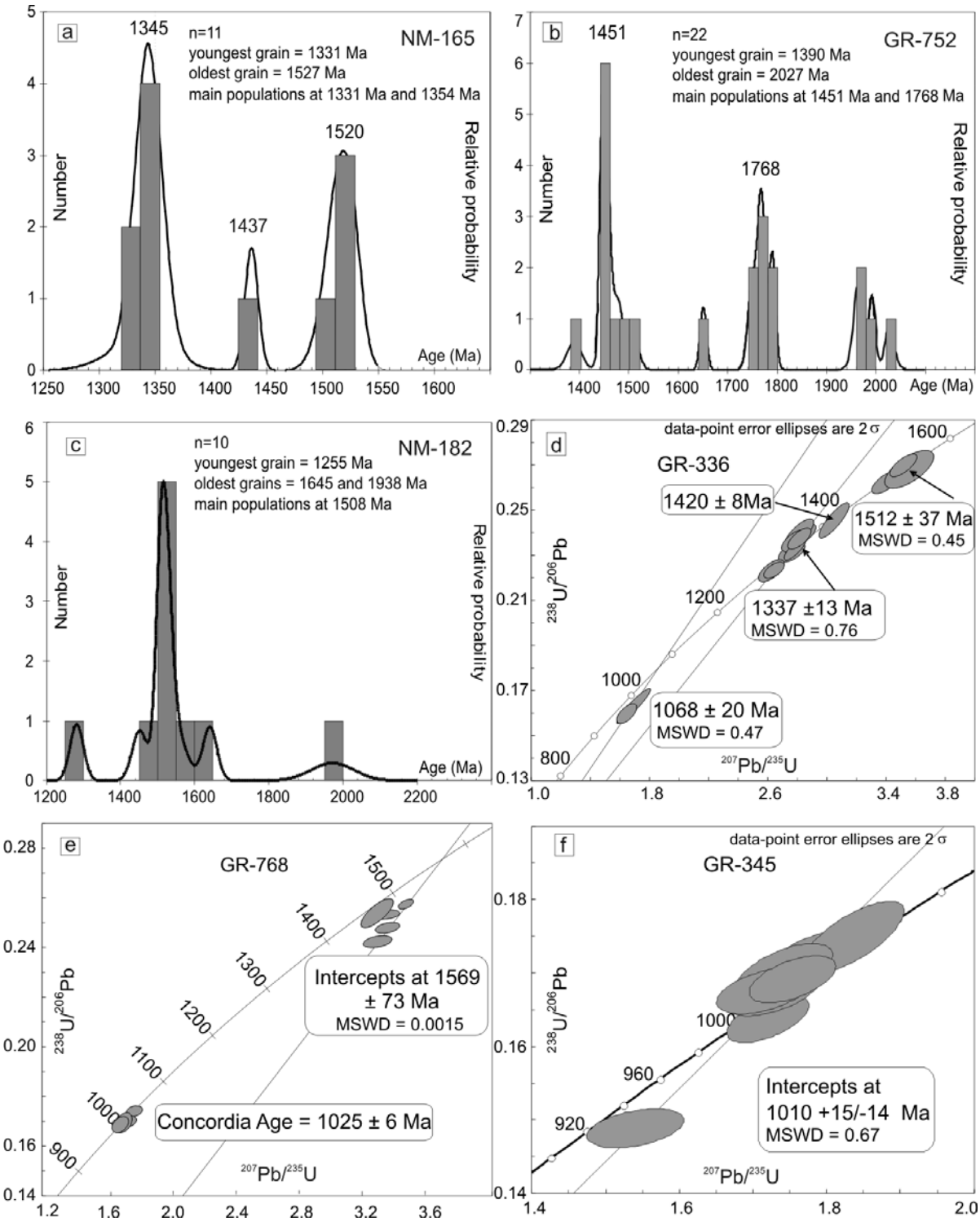

Figure 5- U-Pb concordia plots and relative probability plots of zircons ages from samples of the Aguapeí belt and intrusive rocks.

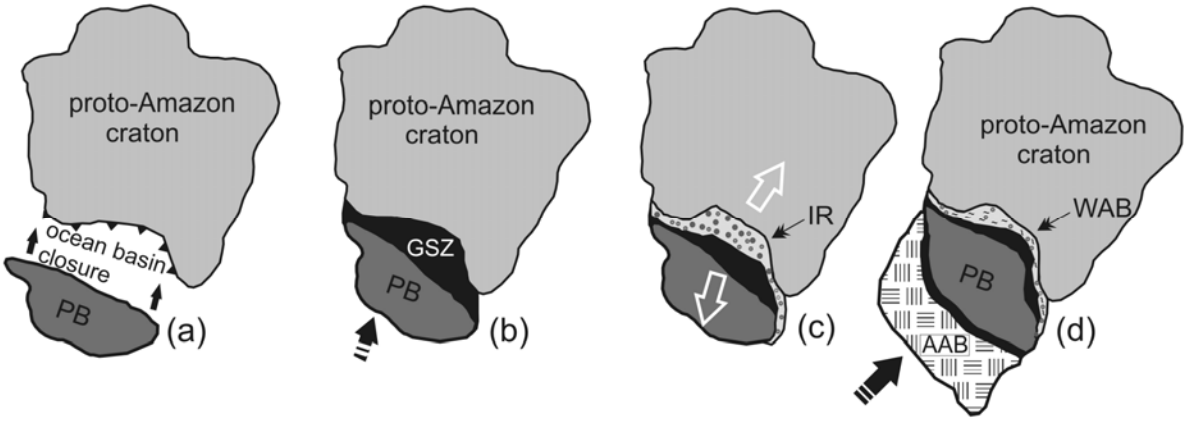

(a) Subduction of oceanic crust and start of building of Guaporé suture zone (GSZ) (1.47-1.43 Ga)

(b) Collision and docking final of the Paraguá Block (PB) with the proto-Amazon craton (1.35-1.33 Ga)

(c) Intraplate extensional tectonics. Reactivation of the Guaporé suture zone and intraplate rifting (IR) and concurrent sedimentation: Nova Brasilândia, Aguapeí and Sunsás Groups (1150- 1110 Ma)

(d) Collision-related deformation in a transpressional orogeny (Western Amazon belt-WAB). Collision of the Arequipa-Antofalla Basement (AAB) with the proto-Amazon craton (1100-950 Ma)

Figure 6- Model tectonic evolution of the southwestern Amazon craton in the Mesoproterozoic (modified from Boger et al. 2005).

Table 1- SHRIMP and LA-MC-ICP-MS zircon and titanite U-Pb analytical results for the samples studied.

						Ratios					Ages		
spot	U ppm	Th ppm	Th/U	^{206}Pb ppm	4f ^{206} %	^{207}Pb/^{206}Pb	^{207}Pb/^{235}U	^{206}Pb/^{238}U	err. corr.	^{208}Pb/^{232}Th	^{206}Pb/^{238}U	^{206}Pb/^{207}Pb	Disc. %
GRT1, zircon													
h.1-1	706	254	0.37	105.7	0.10	0.07548 ± 0.88	1.8118 ± 1.68	0.1741 ± 1.43	0.851	0.0523 ± 1.76	1035 ± 14	1081 ± 18	4
h.1-2	1056	821	0.80	159.1	-0.01	0.07696 ± 0.50	1.8613 ± 1.48	0.1754 ± 1.40	0.942	0.0512 ± 1.48	1042 ± 13	1120 ± 10	7
h.1-3	2254	501	0.23	319.2	0.00	0.07301 ± 0.32	1.6593 ± 1.50	0.1648 ± 1.47	0.978	0.0504 ± 2.81	984 ± 13	1014 ± 6	3
h.2-1	2021	2266	1.16	322.8	0.00	0.07667 ± 0.63	1.9654 ± 1.59	0.1859 ± 1.47	0.920	0.0551 ± 1.60	1099 ± 15	1113 ± 12	1
h.3-1	779	426	0.57	125.8	0.00	0.07669 ± 0.47	1.9886 ± 1.56	0.1881 ± 1.49	0.954	0.0551 ± 1.58	1111 ± 15	1113 ± 9	0
GRT2, titanite													
a.1-1	254	244	0.99	35.7	0.02	0.07229 ± 0.65	1.6302 ± 1.28	0.1636 ± 1.10	0.860	0.2735 ± 1.23	976 ± 10	994 ± 13	2
a.1-2	268	260	1.01	37.9	0.08	0.07152 ± 0.72	1.6231 ± 1.30	0.1646 ± 1.09	0.834	0.1574 ± 2.42	982 ± 10	972 ± 15	-1
a.2-1	234	225	0.99	33.1	-0.05	0.07218 ± 0.74	1.6358 ± 1.32	0.1644 ± 1.09	0.830	0.1723 ± 1.21	981 ± 10	991 ± 15	1
a.3-1	186	180	1.00	26.8	0.13	0.07191 ± 0.68	1.6553 ± 1.30	0.1670 ± 1.11	0.852	0.1672 ± 1.25	995 ± 10	983 ± 14	-1
a.3-2	215	211	1.02	30.8	0.00	0.07231 ± 0.80	1.6619 ± 1.41	0.1667 ± 1.16	0.823	0.1663 ± 1.29	994 ± 11	995 ± 16	0
GRT2, zircon													
a.5-1	509	66	0.13	80.2	0.01	0.07363 ± 0.86	1.8597 ± 1.70	0.1832 ± 1.47	0.864	0.0537 ± 2.55	1084 ± 15	1031 ± 17	-5
a.5-2	112	40	0.37	18.8	0.07	0.07571 ± 1.57	2.0354 ± 2.34	0.1950 ± 1.73	0.740	0.0590 ± 2.79	1148 ± 18	1087 ± 31	-6
a.9-1	1201	40	0.03	191.5	-0.01	0.07537 ± 0.52	1.9295 ± 1.54	0.1857 ± 1.44	0.940	0.0581 ± 2.42	1098 ± 15	1078 ± 11	-2
a.10-1	141	50	0.37	23.3	0.00	0.07575 ± 1.72	2.0036 ± 2.40	0.1918 ± 1.68	0.699	0.0575 ± 2.51	1131 ± 17	1089 ± 34	-4
a.10-2	398	202	0.53	65.1	0.06	0.07606 ± 0.89	1.9973 ± 1.74	0.1905 ± 1.50	0.859	0.0590 ± 1.82	1124 ± 15	1097 ± 18	-2
a.11-1	1461	753	0.53	245.4	0.02	0.07565 ± 0.43	2.0391 ± 1.45	0.1955 ± 1.39	0.956	0.0575 ± 1.48	1151 ± 15	1086 ± 9	-6
a.11-2	1036	521	0.52	169.5	0.01	0.07593 ± 0.51	1.9936 ± 1.48	0.1904 ± 1.39	0.939	0.0565 ± 1.67	1124 ± 14	1093 ± 10	-3
a.13-1	1231	668	0.56	198.2	0.01	0.07596 ± 0.46	1.9621 ± 1.46	0.1873 ± 1.38	0.949	0.0569 ± 1.99	1107 ± 14	1094 ± 9	-1
GRT3, zircon													
g.1-1	217	77	0.37	37.3	0.68	0.08133 ± 4.30	2.2308 ± 4.57	0.1989 ± 1.53	0.335	0.0603 ± 8.28	1170 ± 16	1229 ± 84	5
g.2-1a	1284	100	0.08	199.0	0.03	0.07621 ± 0.40	1.8954 ± 1.42	0.1804 ± 1.36	0.959	0.0514 ± 2.83	1069 ± 13	1101 ± 8	3
g.2-1b	1284	100	0.08	199.0	0.00	0.07650 ± 0.38	1.9032 ± 1.42	0.1804 ± 1.36	0.963	0.0531 ± 2.60	1069 ± 13	1108 ± 8	4
g.2-2	76	23	0.31	11.6	0.26	0.07748 ± 1.80	1.8978 ± 2.52	0.1776 ± 1.76	0.700	0.0553 ± 3.45	1054 ± 17	1134 ± 36	7
GRT3, titanite													
d.4-1	226	203	0.93	33.0	0.18	0.07726 ± 2.22	1.8064 ± 2.48	0.1696 ± 1.11	0.449	0.1179 ± 1.82	1010 ± 10	1128 ± 44	10
d.4-2	180	160	0.92	27.5	-0.01	0.07698 ± 0.72	1.8837 ± 1.31	0.1775 ± 1.10	0.835	0.1152 ± 1.27	1053 ± 11	1121 ± 14	6
d.4-3	210	195	0.96	32.4	0.92	0.07621 ± 1.84	1.8748 ± 2.15	0.1784 ± 1.10	0.513	0.0754 ± 1.86	1058 ± 11	1101 ± 37	4
d.5-1	203	192	0.98	31.3	0.45	0.07511 ± 2.30	1.8508 ± 2.55	0.1787 ± 1.11	0.434	0.1208 ± 1.96	1060 ± 11	1072 ± 46	1
d.5-2	215	197	0.95	32.7	0.25	0.07573 ± 1.37	1.8468 ± 1.76	0.1769 ± 1.10	0.627	0.1049 ± 1.33	1050 ± 11	1088 ± 27	4
d.5-3	184	178	1.00	28.3	0.69	0.07537 ± 2.21	1.8468 ± 2.48	0.1777 ± 1.13	0.454	0.0802 ± 1.63	1054 ± 11	1078 ± 44	2
GRT4, zircon													
e.2-1	129	99	0.79	19.2	0.12	0.07679 ± 1.50	1.8281 ± 3.09	0.1727 ± 2.70	0.874	0.0529 ± 3.04	1027 ± 26	1116 ± 30	8
e.3-1	394	146	0.38	62.2	0.13	0.07595 ± 1.04	1.9228 ± 1.80	0.1836 ± 1.47	0.816	0.0539 ± 2.03	1087 ± 15	1094 ± 21	1
e.3-2	59	30	0.54	9.4	0.95	0.07531 ± 6.50	1.9145 ± 6.79	0.1844 ± 1.97	0.291	0.0526 ± 8.40	1091 ± 20	1077 ± 130	-1.3
e.4-1	527	177	0.35	72.8	0.08	0.07656 ± 0.94	1.6958 ± 1.38	0.1607 ± 1.01	0.733	0.0484 ± 1.48	960 ± 9	1110 ± 19	13
e.4-2	155	76	0.51	23.9	0.02	0.07549 ± 0.90	1.8634 ± 1.41	0.1790 ± 1.09	0.770	0.0545 ± 1.52	1062 ± 11	1082 ± 18	2
e.5-1	297	87	0.30	46.4	0.02	0.07673 ± 1.07	1.9196 ± 1.84	0.1814 ± 1.49	0.812	0.0520 ± 2.48	1075 ± 15	1114 ± 21	4
e.6-1	468	163	0.36	73.7	0.03	0.07653 ± 0.64	1.9355 ± 1.57	0.1834 ± 1.43	0.913	0.0544 ± 1.70	1086 ± 14	1109 ± 13	2
e.7-1	299	298	1.03	45.8	0.13	0.07640 ± 1.07	1.8766 ± 1.82	0.1782 ± 1.47	0.809	0.0530 ± 1.75	1057 ± 14	1105 ± 21	4
e.7-2	37	21	0.60	5.8	0.00	0.07560 ± 2.05	1.9262 ± 2.70	0.1848 ± 1.76	0.651	0.0571 ± 2.83	1093 ± 18	1085 ± 41	-1
GRT5, zircon													
h.1-1	305	57	0.19	48.7	-0.01	0.07661 ± 0.74	1.9625 ± 1.20	0.1858 ± 0.95	0.788	0.0574 ± 1.65	1098 ± 10	1111 ± 15	1
h.2-1	552	89	0.17	89.3	0.01	0.07594 ± 0.79	1.9708 ± 1.26	0.1882 ± 0.98	0.781	0.0544 ± 1.69	1112 ± 10	1093 ± 16	-2
h.2-2	277	70	0.26	44.1	-0.02	0.07645 ± 0.78	1.9568 ± 1.26	0.1856 ± 0.98	0.781	0.0550 ± 1.61	1098 ± 10	1107 ± 16	1

GRT5, rutile																
h.3-3	35	0.893	0.026	4.6	0.39	0.06964	± 1.4	1.487	± 3.7	0.1523	± 3.3	0.92	0.0430	± 1.29	912 ± 28	953 ± 38	4
h.3-4	35	0.01	0.003	4.8	0.47	0.07388	± 1.5	1.557	± 4.0	0.1570	± 3.0	0.90	0.0513	± 1.94	942 ± 27	983 ± 52	5
h.6-1	91	0.003	0.003	12.6	0.70	0.07106	± 2.2	1.588	± 3.8	0.1610	± 3.1	0.87	0.0490	± 1.96	962 ± 39	973 ± 45	1
h.6-2	70.8	0.012	0.001	10.16	0.18	0.07169	± 2.0	1.604	± 3.7	0.1667	± 2.7	0.80	0.0535	± 1.38	996 ± 25	922 ± 52	-8
h.7-1	85	0.056	0.006	11.8	0.26	0.07114	± 1.0	1.536	± 3.7	0.1612	± 3.2	0.96	0.0540	± 1.66	966 ± 29	901 ± 35	-7
h.7-2	82	0.056	0.007	11.3	0.43	0.07111	± 1.0	1.521	± 3.5	0.1596	± 3.0	0.95	0.0514	± 1.35	956 ± 27	903 ± 38	-6
GR752, zircon																	
i.2-1	574	131	0.24	134.2	0.15	0.1014	± 0.7	3.80	± 1.3	0.2715	± 1.1	0.84	0.0763	± 1.6	1552 ± 15	1650 ± 13	6
i.3-1	268	134	0.52	78.9	0.03	0.1203	± 0.8	5.69	± 1.4	0.3428	± 1.2	0.84	0.0976	± 1.6	1901 ± 21	1960 ± 14	3
i.1-1	605	29	0.05	160.8	0.14	01079	± 0.7	4.59	± 1.3	0.3086	± 1.1	0.84	0.1274	± 2.8	1732 ± 16	1764 ± 13	2
i.1-2	236	98	0.43	62.2	0.10	0.1069	± 1.0	4.51	± 1.6	0.3059	± 1.2	0.79	0.0867	± 2.3	1724 ± 20	1747 ± 18	2
i.14-1	185	52	0.29	40.7	0.21	0.0883	± 1.5	3.11	± 2.3	0.2550	± 1.8	0.76	0.0738	± 2.7	1468 ± 24	1390 ± 29	-5
i.14-2	198	218	1.14	62.9	0.23	0.1249	± 1.1	6.35	± 1.7	0.3691	± 1.3	0.77	0.1020	± 1.6	2039 ± 26	2027 ± 19	0
i.2-2	508	155	0.31	99.8	0.09	0.0915	± 1.0	2.88	± 1.2	0.2285	± 0.7	0.55	0.0673	± 1.4	1328 ± 8	1457 ± 19	9
i.2-3	319	1	0.00	71.5	0.16	0.0926	± 0.8	3.33	± 1.1	0.2608	± 0.7	0.64	0.1892	± 7.3	1495 ± 9	1480 ± 16	-1
i.2-4	355	341	0.99	89.5	0.03	0.1095	± 0.6	4.42	± 1.0	0.2930	± 0.7	0.75	0.0849	± 1.7	1658 ± 13	1791 ± 12	7
i.7-1	580	201	0.36	112.4	0.01	0.0911	± 0.7	2.83	± 1.0	0.2256	± 0.7	0.66	0.0654	± 1.2	1313 ± 8	1449 ± 14	9
i.7-2	512	254	0.51	124.5	0.04	0.1093	± 0.9	4.26	± 1.1	0.2828	± 0.6	0.57	0.0826	± 1.6	1606 ± 9	1788 ± 16	10
i.8-1	165	107	0.67	41.5	0.00	0.1072	± 0.9	4.33	± 1.3	0.2929	± 1.0	0.72	0.0789	± 3.5	1666 ± 16	1753 ± 17	6
i.8-2	627	180	0.30	120.8	0.04	0.0915	± 0.7	2.83	± 0.9	0.2243	± 0.7	0.69	0.0715	± 1.7	1302 ± 8	1457 ± 13	10
i.8-3	250	67	0.28	51.1	0.16	0.0940	± 1.2	3.09	± 1.5	0.2387	± 0.9	0.58	0.0735	± 1.9	1376 ± 11	1508 ± 23	8
i.9-1	329	144	0.45	67.5	0.01	0.0912	± 0.8	3.00	± 1.1	0.2386	± 0.8	0.70	0.0708	± 1.3	1379 ± 10	1451 ± 15	5
i.3-2	35	18	0.53	10.8	0.19	0.1208	± 1.8	6.05	± 2.8	0.3629	± 2.1	0.76	0.0984	± 3.2	2006 ± 39	1968 ± 33	-1
i.6-1	250	96	0.40	66.3	0.04	0.1083	± 0.7	4.60	± 1.5	0.3081	± 1.3	0.88	0.0890	± 1.7	1733 ± 21	1772 ± 13	2
i.5-1	175	159	0.94	56.0	0.04	0.1224	± 0.7	6.30	± 1.5	0.3736	± 1.4	0.89	0.1076	± 2.1	2045 ± 27	1991 ± 12	-3
i.15-1	249	189	0.78	69.5	0.13	0.1081	± 0.7	4.83	± 1.5	0.3244	± 1.3	0.87	0.0929	± 1.7	1815 ± 23	1767 ± 14	-2
i.13-1	405	174	0.44	90.1	0.05	0.0909	± 0.6	3.24	± 1.4	0.2587	± 1.2	0.89	0.0733	± 1.5	1487 ± 17	1444 ± 12	-3
i.13-2	240	71	0.31	46.5	0.21	0.0919	± 1.2	2.85	± 1.8	0.2252	± 1.3	0.74	0.0766	± 1.8	1305 ± 17	1465 ± 23	11
i.10-1	455	217	0.49	101.4	0.03	0.0910	± 0.6	3.26	± 1.4	0.2594	± 1.2	0.90	0.0713	± 1.4	1493 ± 17	1448 ± 11	-3
NM165, zircon																	
a.2-1	389	92	0.24	80.3	-0.01	0.08647	± 0.74	2.8678	± 1.65	0.2405	± 1.48	0.895	0.0660	± 2.14	1390 ± 19	1349 ± 14	-3
a.3-1	745	387	0.54	168.0	0.29	0.09420	± 0.50	3.3994	± 1.10	0.2616	± 0.99	0.894	0.0731	± 1.27	1498 ± 13	1513 ± 9	1
a.3-2	781	336	0.44	178.3	0.13	0.09457	± 0.56	3.4592	± 1.13	0.2652	± 0.99	0.871	0.0744	± 1.22	1516 ± 13	1520 ± 11	0
a.5-1	930	550	0.61	214.6	0.01	0.09495	± 0.45	3.5162	± 1.09	0.2686	± 0.99	0.911	0.0765	± 1.10	1534 ± 14	1527 ± 8	0
a.8-1	1324	41	0.03	258.2	0.00	0.08673	± 0.44	2.7150	± 1.54	0.2270	± 1.48	0.959	0.0621	± 3.65	1319 ± 18	1354 ± 8	3
a.11-1	1171	11	0.01	232.3	0.03	0.08615	± 0.34	2.7408	± 1.02	0.2307	± 0.97	0.944	0.0576	± 7.99	1338 ± 12	1342 ± 7	0
a.12-1	993	102	0.11	196.2	0.05	0.08569	± 0.40	2.7147	± 1.05	0.2297	± 0.97	0.926	0.0633	± 2.04	1333 ± 12	1331 ± 8	0
a.13-1	474	162	0.35	107.9	-0.01	0.09389	± 0.63	3.4342	± 1.14	0.2653	± 0.95	0.834	0.0782	± 1.28	1517 ± 13	1506 ± 12	-1
a.13-2	1218	185	0.16	262.7	0.04	0.09051	± 0.31	3.1307	± 1.01	0.2509	± 0.96	0.952	0.0756	± 1.25	1443 ± 12	1436 ± 6	0
a.14-1	1088	38	0.04	213.9	0.01	0.08637	± 0.42	2.7245	± 1.07	0.2288	± 0.98	0.919	0.0659	± 2.86	1328 ± 12	1346 ± 8	1
a.16-1	90	33	0.38	17.8	0.00	0.08583	± 1.41	2.7313	± 2.07	0.2308	± 1.52	0.732	0.0682	± 2.51	1339 ± 18	1334 ± 27	0
GR768, zircon																	
d-iv-2	1817	188	0.10	384	0,003	0.0979	± 0.77	3.4721	± 0.92	0.2573	± 0.50	0.55	1476	± 7	1476 ± 7	1584 ± 12	7
d-iv-3	352	98	0.28	80	0,001	0.0983	± 1.34	3.3567	± 1.47	0.2477	± 0.60	0.41	1427	± 8	1427 ± 8	1592 ± 21	10
d-iv-4	1576	129	0.08	365	0,017	0.0986	± 1.67	3.2932	± 1.80	0.2421	± 0.67	0.37	1398	± 9	1398 ± 9	1599 ± 27	13
d-iv-5	2197	217	0.10	491	0,002	0.0958	± 1.75	3.3416	± 1.82	0.2530	± 0.52	0.29	1454	± 8	1454 ± 8	1544 ± 27	6
d-iv-7	1556	137	0.09	337	0,001	0.0944	± 0.87	3.3152	± 1.07	0.2548	± 0.61	0.57	1463	± 9	1463 ± 9	1516 ± 13	3
e-v-2	1870	348	0.19	350	0,002	0.0941	± 1.33	3.2910	± 2.03	0.2536	± 1.53	0.76	1457	± 22	1457 ± 22	1510 ± 20	4
e-v-3	148	38	0.26	24	0,001	0.0737	± 1.26	1.7552	± 1.31	0.1727	± 0.34	0.26	1027	± 3	1027 ± 3	1033 ± 13	1
e-v-4	26	4	0.17	4	0,002	0.0731	± 2.80	1.7090	± 2.99	0.1696	± 1.04	0.35	1010	± 10	1010 ± 10	1017 ± 29	1
e-v-5	108	28	0.26	17	0,003	0.0735	± 1.40	1.6898	± 1.49	0.1667	± 0.52	0.35	994	± 5	994 ± 5	1028 ± 14	3
e-v-6	84	16	0.19	13	0,003	0.0731	± 1.49	1.6941	± 1.63	0.1680	± 0.65	0.40	1001	± 6	1001 ± 6	1018 ± 15	2

GR66, zircon																	
d.54-1	447	100	0.223	0.0001	0.085	0.0535	± 13	2.277	± 42	0.2039	± 29	0.90	0.0489	± 14	1196 ± 16	1222 ± 20	2
d.56-1	422	185	0.438	0.0001	0.093	0.1300	± 17	2.453	± 56	0.2165	± 42	0.74	0.0643	± 15	1263 ± 22	1250 ± 19	-1
d.57-1	255	39	0.153	0.000	0.002	0.0460	± 20	2.729	± 70	0.2315	± 46	0.84	0.0696	± 33	1342 ± 24	1327 ± 27	-1
d.58-1	64	34	0.535	0.000	0.062	0.1583	± 64	2.326	± 102	0.2128	± 48	0.87	0.0630	± 30	1244 ± 26	1179 ± 69	-5
d.59-1	466	98	0.210	0.000	0.070	0.0618	± 12	2.916	± 64	0.2375	± 46	0.76	0.0699	± 20	1373 ± 24	1405 ± 16	2
d.60-1	845	162	0.192	0.000	0.001	0.0576	± 6	3.013	± 61	0.2430	± 46	0.70	0.0729	± 16	1402 ± 24	1424 ± 10	2
d.61-1	140	90	0.646	0.000	0.016	0.1787	± 23	6.288	± 150	0.3666	± 75	0.86	0.1015	± 25	2013 ± 35	2020 ± 17	0
d.62-1	61	21	0.350	0.000	0.000	0.1066	± 32	2.200	± 74	0.2002	± 46	0.63	0.0609	± 24	1177 ± 25	1189 ± 43	1
d.63-1	73	31	0.426	0.0003	0.405	0.1184	± 75	2.105	± 109	0.2001	± 45	0.75	0.0556	± 38	1176 ± 24	1103 ± 88	-7
d.64-1	103	62	0.598	0.0001	0.238	0.1712	± 44	2.532	± 84	0.2197	± 47	0.66	0.0629	± 22	1280 ± 25	1283 ± 44	0
d.65-1	71	43	0.604	0.000	0.075	0.1718	± 46	3.619	± 119	0.2797	± 61	0.57	0.0796	± 28	1590 ± 31	1505 ± 41	-6
d.67-1	113	37	0.326	0.0002	0.378	0.0936	± 63	2.644	± 111	0.2265	± 48	0.72	0.0650	± 46	1316 ± 25	1308 ± 66	-1
d.69-1	274	207	0.756	0.0001	0.147	0.1019	± 18	4.265	± 97	0.2943	± 58	0.69	0.0396	± 11	1663 ± 29	1716 ± 17	3
d.70-1	672	332	0.495	0.000	0.024	0.1438	± 12	2.217	± 47	0.1995	± 38	0.58	0.0580	± 12	1173 ± 21	1211 ± 14	3
d.71-1	99	56	0.571	0.000	0.069	0.1675	± 44	2.292	± 78	0.2151	± 46	0.76	0.0631	± 22	1256 ± 24	1122 ± 48	-11
d.73-1	226	65	0.285	0.000	0.059	0.0840	± 23	2.406	± 63	0.2163	± 43	0.79	0.0637	± 22	1262 ± 23	1213 ± 29	-4
d.75-1	224	95	0.389	0.0001	0.000	0.1020	± 16	1.991	± 48	0.1817	± 36	0.88	0.0476	± 12	1076 ± 20	1184 ± 22	9
d60.11	179	37	0.209	0.0004	0.616	0.0559	± 45	2.929	± 90	0.2429	± 39	0.55	0.0649	± 53	1402 ± 20	1370 ± 47	-2
d.61.2	171	75	0.440	0.000	0.008	0.1318	± 22	6.746	± 131	0.3781	± 59	0.84	0.1133	± 27	2068 ± 28	2090 ± 17	1
d65.11	76	52	0.683	0.0001	0.108	0.1959	± 53	3.687	± 117	0.2709	± 52	0.89	0.0777	± 27	1546 ± 26	1599 ± 43	3
d69.11	291	123	0.422	0.000	0.050	0.1130	± 18	4.706	± 87	0.3191	± 48	0.74	0.0854	± 20	1785 ± 23	1748 ± 16	-2
d.74-1	288	93	0.321	0.000	0.068	0.0933	± 24	2.281	± 50	0.1940	± 29	0.90	0.0564	± 17	1143 ± 16	1322 ± 27	13
d.76-1	237	95	0.399	0.0001	0.093	0.1211	± 22	2.648	± 57	0.2244	± 35	0.84	0.0681	± 17	1305 ± 18	1329 ± 25	2
d.77-1	215	185	0.858	0.000	0.047	0.2491	± 26	5.515	± 105	0.3432	± 53	0.57	0.0996	± 100	1902 ± 25	1904 ± 17	0

Table 1 (continued)

	Isotopic ratios								Ages							
spot	$^{207}Pb/^{235}U$		$^{206}Pb/^{238}U$		Rho	$^{207}Pb/^{206}Pb$			$^{206}Pb/^{238}U$		$^{207}Pb/^{235}U$		$^{207}Pb/^{206}Pb$		f206	Dis %	$^{232}Th/^{238}U$
NM182, zircon																	
cv-01	2.53454	± 1.41	0.21420	± 0.52	0.37	0.08582	± 1.31		1251	± 7	1282	± 18	1334	± 18	0.0004	6	0.38
cv-02	3.17845	± 1.40	0.24659	± 0.45	0.32	0.09348	± 1.32		1421	± 6	1452	± 20	1498	± 20	0.0001	5	0.43
cv-04	5.97356	± 2.94	0.35067	± 0.32	0.11	0.12355	± 2.93		1938	± 6	1972	± 58	2008	± 59	0.0000	4	0.50
cv-39	3.46876	± 1.21	0.26243	± 0.64	0.53	0.09586	± 1.02		1502	± 10	1520	± 18	1545	± 16	0.0006	3	0.20
cv-40	3.40291	± 0.87	0.26381	± 0.46	0.53	0.09355	± 0.74		1509	± 7	1505	± 13	1499	± 11	0.0001	-1	0.35
cv-42	3.44029	± 0.94	0.26608	± 0.56	0.59	0.09377	± 0.75		1521	± 8	1514	± 14	1504	± 11	0.0001	-1	0.50
cv-43	4.03463	± 1.16	0.29477	± 0.81	0.70	0.09927	± 0.83		1665	± 13	1641	± 19	1610	± 13	0.0002	-3	0.69
cv-48	3.63067	± 1.76	0.27049	± 0.77	0.44	0.09735	± 1.59		1543	± 12	1556	± 27	1574	± 25	0.0006	2	0.72
cv-51	3.49946	± 1.24	0.27216	± 0.95	0.77	0.09325	± 0.79		1552	± 15	1527	± 19	1493	± 12	0.0001	-4	0.34
cv-56	3.47862	± 1.01	0.26923	± 0.54	0.53	0.09371	± 0.86		1537	± 8	1522	± 15	1502	± 13	0.0008	-2	0.34
GR336, zircon																	
b-ii-1	3.39949	± 1.13	0.26236	± 0.76	0.68	0.09397	± 0.83		1502	± 11	1504	± 17	1508	± 12	0.0003	0	0.30
b-ii-3	3.48677	± 0.95	0.26728	± 0.72	0.76	0.09462	± 0.62		1527	± 11	1524	± 14	1520	± 9	0.0003	0	0.25
b-ii-5	3.55896	± 1.91	0.26826	± 1.28	0.67	0.09622	± 1.42		1532	± 20	1540	± 29	1552	± 22	0.0014	1	0.51
b-ii-6	2.84822	± 1.15	0.23945	± 0.78	0.68	0.08627	± 0.84		1384	± 11	1368	± 16	1344	± 11	0.0001	-3	0.32
b-ii-7	1.66614	± 0.98	0.16179	± 0.63	0.64	0.07469	± 0.75		967	± 6	996	± 10	1060	± 8	0.0001	9	0.06
b-ii-2	2.76130	± 1.34	0.23151	± 0.77	0.58	0.08650	± 1.09		1342	± 10	1345	± 18	1349	± 15	0.0005	1	0.33
b-iii-3	2.81367	± 1.44	0.23971	± 1.11	0.77	0.08513	± 0.92		1385	± 15	1359	± 20	1319	± 12	0.0003	-5	0.78
b-iii-6	2.78383	± 1.32	0.23658	± 0.84	0.63	0.08534	± 1.03		1369	± 11	1351	± 18	1323	± 14	0.0003	-3	0.28
biii7a	3.52090	± 1.05	0.27001	± 0.77	0.73	0.09457	± 0.72		1541	± 12	1532	± 16	1520	± 11	0.0001	-1	0.35
biii7b	1.68423	± 1.84	0.16244	± 1.73	0.94	0.07520	± 0.64		970	± 17	1003	± 18	1074	± 7	0.0001	10	0.04
biii11	2.62565	± 1.36	0.22332	± 0.91	0.67	0.08527	± 1.02		1299	± 12	1308	± 18	1322	± 13	0.0001	2	0.44
b-iv-1	2.64334	± 1.09	0.22359	± 0.65	0.60	0.08574	± 0.88		1301	± 8	1313	± 14	1332	± 12	0.0001	2	0.25

b-iv-3	3.03591	±	1.18	0.24366	±	1.00	0.85	0.09037	±	0.62	1406	±	14	1417	±	17	1433	±	9	0.0003	2	0.27
b-iv-5	2.78782	±	1.12	0.23325	±	0.92	0.83	0.08669	±	0.63	1351	±	12	1352	±	15	1354	±	9	0.0001	0	0.28
b-iv-7	2.81440	±	1.15	0.23754	±	0.79	0.69	0.08593	±	0.83	1374	±	11	1359	±	16	1337	±	11	0.0003	-3	0.28
GR345, zircon																						
a-i-3	1.71977	±	1.33	0.16868	±	0.77	0.58	0.07394	±	1.08	1005	±	8	1016	±	13	1040	±	11	0.0061	3	0.74
a-i-5	1.76550	±	1.23	0.17646	±	0.49	0.40	0.07257	±	1.13	1048	±	5	1033	±	13	1002	±	11	0.0001	-5	0.35
a-i -7	1.76088	±	1.26	0.17620	±	0.74	0.59	0.07248	±	1.02	1046	±	8	1031	±	13	999	±	10	0.0008	-5	0.62
a-i 12	1.53957	±	1.75	0.15376	±	0.71	0.41	0.07262	±	1.60	922	±	7	946	±	17	1003	±	16	0.0003	8	0.46
a-i 13	1.76515	±	1.42	0.17634	±	0.99	0.70	0.07260	±	1.02	1047	±	10	1033	±	15	1003	±	10	0.0002	-4	0.75
a-i 16	1.72609	±	1.59	0.17265	±	0.83	0.52	0.07251	±	1.36	1027	±	8	1018	±	16	1000	±	14	0.0009	-3	0.50
a-i 25	1.83594	±	1.54	0.17989	±	1.12	0.73	0.07402	±	1.06	1066	±	12	1058	±	16	1042	±	11	0.0144	-2	0.51
a-i 28	1.74057	±	1.57	0.17504	±	0.93	0.59	0.07212	±	1.27	1040	±	10	1024	±	16	989	±	13	0.0001	-5	0.50
a-i 32	1.71426	±	1.53	0.17251	±	0.74	0.48	0.07207	±	1.34	1026	±	8	1014	±	16	988	±	13	0.0001	-4	0.99
a-i-34	1.75302	±	1.37	0.17414	±	0.75	0.55	0.07301	±	1.14	1035	±	8	1028	±	14	1014	±	12	0.0004	-2	0.75

Notes: Isotopic ratios errors in %; All Pb in ratios are radiogenic component. Most are corrected for ^{204}Pb and some for ^{208}Pb (metamorphic, Th-poor grains or rims). disc. = discordance, as 100 - 100{t[^{206}Pb/^{238}U]/t[^{207}Pb/^{206}Pb]}; f206 = (common ^{206}Pb) / (total measured ^{206}Pb) based on measured ^{204}Pb. Uncertainties are 1σ.

Table 2- Summary of U–Pb detrital zircons data of the Nova Brasilândia and Aguapeí Groups.

Sample	Rock	Method	Zircon population (* xenotime)	Younger Zircon (m.a)	References
NM-165	Meta-psammite	U/Pb (shrimp)	1331, 1334, 1342, 1346,1349,1354, 1436, 1506, 1513, 1520,1527,	1331 ± 8	This work
GR-752	phyllite banded	U/Pb TIMS	1390,1444,1448,1449, 1451,1457, 1465, 1480, 1508, 1650, 1747,1753, 1764, 1767, 1772, 1788, 1791,1960 1968, 1991, 2027,	1390 ± 29	This work
NM-182	quartzite	U/Pb TIMS	1334, 1493, 1498, 1499, 1502, 1504, 1545, 1574 1610, 2008	1255 ± 7	This work
AS-88	Meta-siltstone	U/Pb TIMS	1366, 1447, 151,1617,1658, 1780, 1894	1299 ± 25	Souza 2011
AS-28	muscovite schist	U/Pb TIMS	1333, 1411,1521,1533,1604, 1607, 1644, 1816	1333 ± 22	Souza 2011
CL-1	Conglome-rate	Pb/Pb	1389, 1397, 1432,1437, 1442, 1496, 1450,1461, 1463, 1489, 1499, 1507	1319 ± 36	Leite and Saes 2003
MT-1	quartzite	U/Pb (shrimp)	1453, 1420, 1350, 1327, 1271, 1231	1231 ± 14	Santos et al. 2001
JO-02	sandstone	U/Pb (shrimp)	1145*, 1153*	1167 and 1149*	Santos et al. 2005
GR-66	paragneiss	U/Pb (shrimp)	1215, 1320, 1417, 1505, 1599, 1716, 1748, 1904, 2020, 2090	1122 ± 12	This work

Appendix A. Analytical procedures

A.1. *U–Pb SHRIMP methodology*

Grains from the non-magnetic fractions were hand-picked, mounted on epoxy discs with fragments of standards, grains of Sri Lanka zircon standard (CZ3) which has a conventionally measured age of 564 Ma ($^{206}Pb/^{238}U$ ratio = 0.0914; 551 ppm U) and BR 266 zircon (559 Ma, 903 ppm U). Titanite standard is Namibia Khan (518 Ma; $^{206}Pb/^{238}U$ ratio = 0.083671; 700 ppm U). Rutile standard is WH (Windmill Hill, 2629 Ma, U = 168 ppm). The mounted zircons, titanites and rutiles were polished to effectively cut them in half and these crystals were imaged by Back Scatterd Electrons (BSE) using a scanning electron microscope prior to gold coating.

U–Th–Pb analyses were performed using the SHRIMP II ion microprobe at Curtin University of Technology (Australia) following techniques described by Williams (1998) utilizing five-cycle runs through the mass stations. Corrections for common Pb were made using the measured ^{204}Pb and the Pb isotopic composition of Broken Hill galena. Before each spot analysis, 60–90 s were used for pre-sputtering to remove the gold, avoiding the analysis of common Pb from the coatings. Results with more than 0.5% common lead correction are presented but are not used in age calculations. Zircon and titanite data are reduced using SQUID (Ludwig 2002). Data were plotted on concordia diagrams using ISOPLOT/ Ex software (Ludwig, 1999), and error ellipses on Concordia plots are shown at the 95% confidence level (2σ). The ages given in the text are concordia and weighted mean $^{207}Pb/^{206}Pb$ ages.

A.2. *LA-MC-ICP-MS methodology*

All zircons were mounted in epoxy in 2.5-cm-diameter circular grain mounts and polished until the zircons were just revealed. Images of zircons and titanites were obtained using the optical microscope (Leica MZ 125) and back-scatter electron microscope (Jeol JSM

5800). Zircon grains were dated with laser ablation microprobe (New Wave UP213) coupled to a MC-ICP-MS (Neptune) at the Laboratório de Geologia Isotópica, Universidade Federal do Rio Grande do Sul, Brazil. Isotope data were acquired in static mode with spot size between 15 and 40 μm. Laser-induced elemental fractional and instrumental mass discrimination were corrected using reference zircon (GJ-1) (Jackson et al. 2004). Two GJ-1 analyses were carried out after every ten sample zircon spots. The external error was calculated after propagation error of the GJ-1 mean and the individual sample zircon (or spot).

A.2.1. Collector configuration

The collector configuration used for simultaneous measurements of Th, U, Pb and Hg isotopes is as follows:

^{202}Hg	$^{204}Hg+ ^{204}Pb$	^{205}Pb	^{206}Pb	^{207}Pb	^{208}Pb		^{232}Th	^{238}U
MIC3	MIC4	MIC5	L4	MIC6	L3	Axial	H2	H4

The gain calibration of Faraday cups as well the cross calibration between the L4 cup against the MIC 3, 4 and 6 were carried out before the laser section. The MIC3 to MIC 5 are attached to the L4 faraday cup, and the MIC6 is attached to the L3.

Because the multicollector system involves 3 ion counters and 5 conventional Faraday collectors, the gain and cross calibration has to be performed routinely. The gain factor to calibrate Faraday measurements is calculated applying a constant signal of 33.0 V. The cross calibration used to calculate necessary conversion factors (voltage to cps) is achieved using a 220 ppt Neptune solution with addition of 200 ppt Th and an efficient nebulizer system. A calculated convertion value of 62,500 cps/mV was used.

The various ratios are obtained simultaneously and appropriately corrected. However, because of inherent fractionations during laser ablation, these ratios vary during analysis and require different approaches to estimate reliable data. As illustrated for the standard zircon, the $^{207}Pb/^{206}Pb$ ratios do not fractionate visibly as the $^{206}Pb/^{238}U$ ratios, which involve two

different elements with particular chemical and physical properties. Pb is more volatile than U, which condensates progressively on the walls of the pit formed during the laser ablation process. We routinely adopt the average of the $^{207}Pb/^{206}Pb$ determinations as the representative value of the sample, and for $^{206}Pb/^{238}U$, we assume the extrapolated value for t (time)=0. Outliers that do not show good alignment are also discarded. Other ratios such as $^{206}Pb/^{207}Pb$ and $^{232}Th/^{238}U$, are also taken into account in the extrapolated ratios when they are applicable or exhibit the same trend of fractionation. These ratios are usually quite close to the expected values.

The conversion factors are calculated based on available data for standard used and applied for unknown samples. Thus, a homogeneous standard is of paramount importance. The GJ-1 standard (GEMOC ARC National Key Center) meets the requirements for the methods used in our laboratory, and the ratios $^{206}Pb^*/^{238}U$, $^{207}Pb^*/^{206}Pb^*$ and $^{232}Th/^{238}U$ are homogeneous during the entire "bracket" technique, a standard-samples-standard analysis.

A. 2.2. Mass bias correction, External correction and laser conditions

The isotope ratios and inter-element fractionation of data obtained by MC-ICP-MS instrument were evaluated by interspersing the GJ-1 standard zircon on every set of 4, 6, 8 or 10 zircon samples (spots). The number of analyzed spots varied depending on the zircon homogeneity and the amount of Pb and U in the zircon. The GJ-1 standard zircon was used to estimate the necessary corrections for the external corrections and internal instrumental fractionation. The GJ-1 zircon and sample were assembled in the same mounting. The spot size of laser herein used was mostly of 25 μm, but the spot sizes were 40 μm and 15 μm for the zircon phases with a low amount of ^{207}Pb (under 10,000 cps) and for small zircon grains (<30 μm of diameter), respectively.

The repetition rate of the laser was 10 Hz. The energy varied from 0.3 to 1.1 mJ/ pulse, and the corresponding spot size from 25μm to 40 μm. The data acquisition occurred in 50 cycles of 1.048s of integration time, and the masses 202, 204, 206,207, 208, 232, and 238

were collecting simultaneously. For every standard and sample set, blank values in same conditions as the standard and sample were also measured. The average blank values were subtracted from all individual cycle measurements. The ^{204}Pb value was corrected for ^{204}Hg by assuming a $^{202}Hg/^{204}Hg$ ratio equal to 4.355.

A.2.3. Operation conditions for LA-MC-ICP-MS

Laser operating conditons	
Laser type: New Wave UP213	MC-ICP-MS Neptune
Laser output power: 6j/cm^2 Shot repetition rate:10 Hz Laser spot: 25 and 40 μm	Cup configuration: Faradays ^{206}Pb, ^{208}Pb, ^{232}Th, ^{238}U MIC's ^{202}Hg, $^{204}Hg+^{204}Pb$, $^{20}7Pb$ Gas input: Coolant flow (Ar) 15 l/min Auxiliary flow (Ar) 0.8 l/min Carrier flow 0.75 l/min (Ar) + 0.45 l/min (He) Acquisition: 50 cycles of 1.048 s

A.2.4. Common Pb correction

The usual method for common-lead corrections on zircons (based on the non-radiogenic ^{204}Pb isotope) is not appropriate when using the laser technique, because the ^{204}Pb signal is strongly affected by ^{204}Hg. The majority of the ^{204}Hg comes from gases (Ar and He) that are required in the ICP and ablation procedure. After the Hg correction based on ^{202}Hg is measured, the common ^{204}Pb is insignificant in most situations. For instance, a typical signal intensity of the ^{204}Hg during laser ablation of the standard zircon is the 600-1000 cps range, and the calculated count rate for ^{204}Pb is less than statistical error of ca. 25-33 cps. We assume that the ^{204}Pb values obtained from zircons grains contain some common Pb, and we also assume a concordant age of $^{206}Pb/^{238}Pb$ and $^{207}Pb/^{206}Pb$ as the estimated age. In this case, we estimate the radiogenic composition of ^{206}Pb and Pb^{207} using the following equation for a fraction (f) of non-radiogenic ^{206}Pb (Williams, 1998):

$$f_{206} = \frac{[^{206}Pb/^{204}Pb]_c}{[^{206}Pb/^{204}Pb]_s}$$

$$f_{207} = \frac{[^{207}Pb/^{204}Pb]_c}{[^{207}Pb/^{204}Pb]_s}$$

For the common lead isotope composition, we assume the isotope composition evolve as proposed by Stacey and Kramers (1975). This assumption is required to determine an initial estimated age.

The $^{207}Pb/^{206}Pb$ and $^{206}Pb/^{238}U$ ratios were corrected after the the f_{206} and f_{207} were determined for each cycle. The cycles with values of f_{206} above 0.0025 are not usually included in the age calculation.

A.2.5. Calculation of the ratios and error estimation

After blank and common Pb corrections, the ratios and their absolute errors (one sigma level) of $^{206}Pb^*/^{238}U$, $^{232}Th/^{238}U$ and $^{206}Pb^*/^{207}Pb^*$ were calculated, using a Excel sheet. Because the $^{206}Pb^*/^{238}U$ usually produces a linear fractionation, we used the intercept method for laser induced Pb/U fractionation to correct the ratio according to the formulation proposed by Youden (1951) and adopted by Kosler et al. (2002)**.** The uncertainty of the fractionation-corrected ratio was calculated as one SD of the intercept ($\sigma R(o)$), which is the isotope ratio at the start of laser ablation.

The internal derived errors were calculated in the conventional way by taking account the uncertainties (1 SD) on the respective background signals.

For the $^{232}Th/^{238}U$ and $^{207}Pb^*/^{206}Pb^*$ ratios, the mean values were used after discarding the outliers. In some cases, the $^{232}Th/^{238}U$ and $^{207}Pb^*/^{206}Pb^*$ ratios show a slightly fractionation. Laser-induced fractionation was applied to obtain the R(o) of these ratios.

ANEXOS

Table 1-Representative microprobe mineral analyses from the Trincheira mafic-ultramafic Complex.

Mineral	Amphiboles													
Rock	mafic granulite						fine-grained amphibolite				rich amphibole-amphibolite			
	GP4-110	GR-145	SJ-2430	GR-790	GR-793	NM-224	GR-710-1	GR-710-3	GR-646-1	GR-646-6	GR-609-1	GR-609-2	GR-609-4	GR-609-5
SiO_2	44.55	42.28	43.04	43.75	43.05	45.77	45.26	44.41	45.03	45.91	45.910	43.920	43.670	43.530
TiO_2	1.153	1.68	1.81	1.451	0.921	0.64	0.41	0.417	0.636	0.572	0.572	0.918	0.880	0.827
Al_2O_3	11.60	11.64	11.96	13.07	12.79	11.30	14.54	14.61	12.31	11.51	11.510	11.860	12.030	11.930
Cr_2O_3	0.055	0.129	0.056	0.023	0.011	0.057	0.042	0.006	0.029	0.053	0.053	0.009	0.032	0.021
$FeO_{(tot)}$ [a]	14.43	18.92	16.79	18.24	18.10	14.56	14.02	14.77	14.57	13.89	13.890	19.260	19.080	19.150
MnO	0.139	0.259	0.105	0.296	0.235	0.239	0.257	0.257	0.108	0.124	0.124	0.320	0.357	0.342
MgO	12.41	8.30	9.69	8.65	8.89	11.41	10.380	10.01	11.43	11.92	11.92	8.590	8.50	8.590
CaO	10.52	11.59	11.41	11.29	10.96	11.79	11.350	11.92	12.29	12.37	12.370	11.440	11.520	11.170
Na_2O	1.302	1.93	2.23	1.42	1.43	1.42	1.228	1.266	1.760	1.940	1.940	1.710	1.680	1.580
K_2O	0.694	0.47	0.315	0.943	0.628	0.126	0.141	0.194	0.249	0.197	0.197	0.297	0.293	0.317
Total	96.85	97.20	97.41	99.13	97.01	97.31	97.63	97.86	98.41	98.49	98.487	98.324	98.041	97.457
Cations calculated on the bases of 23 oxigens														
Si	6.449	6.408	6.423	6.416	6.403	6.686	6.527	6.456	6.552	6.674	6.531	6.505	6.491	6.480
Ti	0.126	0.192	0.203	0.160	0.103	0.070	0.044	0.046	0.070	0.063	0.098	0.102	0.098	0.093
Al	1.551	1.592	1.577	1.584	1.597	1.314	1.473	1.544	1.448	1.326	1.469	1.495	1.509	1.520
Cr	0.006	0.015	0.007	0.003	0.001	0.007	0.005	0.001	0.003	0.006	0.005	0.001	0.004	0.002
Fe^{3+}	1.111	0.285	0.284	0.461	0.721	0.420	0.505	0.389	0.269	0.114	0.399	0.537	0.501	0.681
Fe^{2+}	0.636	2.114	1.812	1.776	1.530	1.358	1.186	1.407	1.504	1.575	1.906	1.849	1.871	1.703
Mn	0.017	0.033	0.013	0.037	0.030	0.030	0.031	0.032	0.013	0.015	0.042	0.040	0.045	0.043
Mg	2.678	1.875	2.156	1.891	1.971	2.485	2.232	2.169	2.479	2.583	1.928	1.897	1.884	1.906
Ca	1.632	1.882	1.824	1.774	1.747	1.845	1.754	1.857	1.916	1.927	1.848	1.815	1.835	1.782
Na	0.01	0.449	0.470	0.178	0.159	0.248	0.097	0.213	0.413	0.473	0.339	0.307	0.319	0.238
K	0.128	0.091	0.060	0.176	0.119	0.023	0.026	0.036	0.046	0.037	0.061	0.056	0.056	0.060
X_{Mg} [b]	0.707	0.470	0.543	0.516	0.563	0.646	0.653	0.606	0.622	0.621	0.503	0.506	0.502	0.528
Al^{IV}	1.125	1.106	1.052	0.911	0.954	0.684	0.476	0.587	0.787	0.682	0.847	0.921	0.912	0.949
Al^{vi}	0.426	0.486	0.525	0.673	0.643	0.630	0.997	0.957	0.661	0.644	0.622	0.574	0.597	0.571

Mineral	Amphiboles										Orthopyroxene			
Rock	porphyroblastic amphibolite										mafic granulite			
	GR-558-2	GR-558-4	GR-558-5	GR-558-8	GR-549-1	GR-549-3	GR-549-5	GR-549-9	GR-549-24	GR-549-26	GP3-180-1	GP3-180-2	GP3-180-3	¡GP3-180-4
SiO_2	43.840	43.150	44.050	44.280	47.920	44.610	45.990	45.620	48.490	44.870	53.09	53.00	52.97	53.29
TiO_2	0.371	0.267	0.275	0.227	0.361	0.526	0.514	0.486	0.319	0.460	0.015	0.046	0.055	0.053
Al_2O_3	14.330	14.470	13.710	13.480	10.440	14.340	12.820	13.400	10.610	13.980	1.725	1.768	1.92	1.83
Cr_2O_3	0.014	0.006	0.038	0.024	0.015	0.000	0.000	0.008	0.019	0.009	0.026	0.012	0.015	0.038
$FeO_{(tot)}$ [a]	17.570	17.730	16.550	17.630	13.670	14.740	14.600	14.490	13.150	14.320	19.75	20.20	20.15	19.83
MnO	0.342	0.292	0.229	0.298	0.241	0.258	0.276	0.237	0.259	0.248	0.331	0.342	0.353	0.328
MgO	8.460	7.880	8.670	8.070	12.150	10.110	10.840	10.890	12.420	10.350	23.95	23.79	23.96	24.27
CaO	12.070	11.800	11.780	11.910	12.170	11.790	12.010	12.100	12.070	11.700	0.239	0.218	0.243	0.276
Na_2O	0.955	1.178	1.148	1.220	0.933	1.104	1.099	1.181	0.785	1.205	0.006	0.000	0.000	0.004
K_2O	0.393	0.507	0.516	0.460	0.053	0.119	0.131	0.134	0.077	0.115	0.000	0.000	0.000	0.006
Total	98.344	97.281	96.967	97.598	97.951	97.598	98.279	98.546	98.200	97.256	99.132	99.376	99.666	99.925
Si	6.432	6.432	6.553	6.588	6.903	6.479	6.637	6.268	6.532	6.866	1.967	1.963	1.954	1.958
Ti	0.041	0.030	0.031	0.025	0.039	0.057	0.056	0.040	0.050	0.046	0.001	0.001	0.002	0.001
Al	1.568	1.568	1.447	1.412	1.097	1.521	1.363	1.732	1.468	1.134	0.033	0.037	0.046	0.042
Cr	0.002	0.001	0.004	0.003	0.002	0.000	0.000	0.000	0.001	0.000	0.001	0.000	0.001	0.001
Fe^{3+}	0.435	0.331	0.243	0.171	0.300	0.472	0.389	0.538	0.427	0.258	0.000	0.000	0.004	0.000
Fe^{2+}	1.721	1.879	1.816	2.023	1.347	1.318	1.373	1.319	1.317	1.390	0.612	0.626	0.618	0.609
Mn	0.043	0.037	0.029	0.038	0.029	0.032	0.034	0.044	0.031	0.028	0.01	0.011	0.011	0.010
Mg	1.850	1.751	1.923	1.790	2.609	2.189	2.332	1.973	2.246	2.552	0.956	0.958	0.956	0.96
Ca	1.897	1.884	1.877	1.899	1.878	1.835	1.857	1.794	1.825	1.871	0.01	0.009	0.009	0.011
Na	0.169	0.225	0.209	0.251	0.156	0.146	0.165	0.217	0.165	0.168	0.001	0.000	0.000	0.000
K	0.074	0.096	0.098	0.087	0.010	0.022	0.024	0.017	0.021	0.020	0.000	0.000	0.000	0.000
X_{Mg} [b]	0.518	0.482	0.514	0.469	0.659	0.624	0.629	0.599	0.630	0.647	0.610	0.605	0.607	0.612
Al^{IV}	0.659	0.597	0.493	0.462	0.423	0.589	0.547	0.646	0.539	0.408	0.033	0.037	0.046	0.042
Al^{vi}	0.909	0.971	0.954	0.950	0.674	0.932	0.816	1.086	0.929	0.726	0.043	0.04	0.038	0.037
Wo	n.d.	n.d.	n.d.	n.d.	n.d.	n.d.	n.d.	n.d.	n.d.	n.d.	0.487	0.446	0.484	0.562
En	n.d.	n.d.	n.d.	n.d.	n.d.	n.d.	n.d.	n.d.	n.d.	n.d.	67.676	67.065	67.237	67.825
Fs	n.d.	n.d.	n.d.	n.d.	n.d.	n.d.	n.d.	n.d.	n.d.	n.d.	31.837	32.489	32.279	31.612

Mineral	Orthopyroxene					Clinopyroxene						
Rock	mafic granulite											
	GP3-180-6	GP3-180-8	GP4-110-4	GP4-110-6	SJ-2430-1	SJ-2430-2	SJ-2430-5	SJ-2430--3	SJ-2430-4	GP-3180-6	GP3-180-8	GP3-180-1	GP3-180-3
SiO_2	53.61	53.04	52.07	52.19	50.95	51.23	51.03	51.82	51.12	50.74	50.48	52.81	53.04
TiO_2	0.000	0.041	0.016	0.000	0.079	0.219	0.267	0.197	0.181	0.01	0.01	0.04	0.10
Al_2O_3	1.513	1.844	1.69	1.586	1.076	2.353	2.343	2.147	2.259	1.02	1.19	0.62	0.73
Cr_2O_3	0.000	0.003	0.020	0.009	0.034	0.09	0.033	0.000	0.043	0.001	0.000	0.000	0.000
$FeO_{(tot)}$ [a]	19.95	20.10	24.12	23.52	31.09	11.34	12.36	12.68	12.14	17.83	17.31	11.00	11.73
MnO	0.328	0.343	0.413	0.434	0.721	0.269	0.319	0.314	0.266	0.210	0.180	0.390	0.400
MgO	24.07	23.56	21.10	20.87	15.57	12.06	11.82	12.01	11.83	8.43	8.20	11.70	11.45
CaO	0.204	0.393	0.288	0.371	0.523	22.34	21.85	21.77	22.16	21.14	20.92	22.54	22.07
Na_2O	0.007	0.008	0.009	0.000	0.018	0.497	0.468	0.427	0.450	0.350	0.350	0.140	0.08
K_2O	0.000	0.000	0.002	0.000	0.000	0.000	0.002	0.006	0.003	0.000	0.000	0.000	0.000
Total	99.682	99.332	99.728	98.98	100.06	100.39	100.50	101.39	100.47	99.74	98.64	99.24	99.60
Si	1.977	1.966	1.958	1.977	1.984	1.918	1,915	1,929	1,918	1.972	1.983	2.013	2.021
Al^{iv}	0.023	0.034	0.042	0.023	0.016	0.082	0,085	0,071	0,082	0.028	0.017	0.000	0.000
Ti	0.000	0.001	0.001	0.000	0.002	0,006	0,008	0,006	0,005	0.000	0.000	0.001	0.003
Al^{vi}	0.043	0.047	0.032	0.048	0.033	0,022	0,019	0,023	0,018	0.018	0.038	0.028	0.033
Cr	0.000	0.000	0.001	0.000	0.001	0,003	0,001	0.000	0,001	0.000	0.000	0.000	0.000
Fe^{3+}	0.000	0.000	0.009	0.000	0.000	0,080	0,084	0,067	0,085	0.035	0.005	0.000	0.000
Fe^{2+}	0.615	0.623	0.75	0.745	0.953	0,216	0,227	0,237	0,229	0.087	0.476	0.306	0.314
Mn	0.010	0.011	0.013	0.014	0.024	0,009	0,010	0,010	0,08	0.007	0.006	0.013	0.013
Mg	0.957	0.952	0.958	0.952	0.904	0,673	0,662	0,667	0,662	0.488	0.480	0.665	0.650
Ca	0.008	0.015	0.012	0.015	0.022	0,896	0,879	0,869	0,891	0.880	0.880	0.920	0.901
Na	0.001	0.001	0.001	0.000	0.002	0,036	0,034	0,031	0,033	0.026	0.027	0.010	0.006
K	0.000	0.000	0.000	0.000	0.000	0.000	0.000	0.000	0.000	0.000	0.000	0.000	0.000
Wo	0.404	0.794	0.594	0.769	1.106	46.363	45.330	44.774	45.877	45.024	45.495	47.240	46.489
En	67.626	66.725	60.161	60.362	46.074	34.828	34.128	34.366	34.076	24.981	24.812	34.119	33.559
Fs	31.970	32.481	39.244	38.869	52.821	18.809	20.542	20.860	20.047	29.994	29.693	18.641	19.952
X_{Mg} [b]	0.609	0.604	0.561	0.561	0.486	0.910	0.890	0.880	0.910	0.890	0.850	1.900	1.730

Mineral	Plagioclase											
Rock	mafic granulite				fine-grained amphib		rich amp.-amphibolite		porphyroblastic amphibolite			
	GP3-180-5	GP3-180-7	GP4-110-3	SJ2430	GR-646-4	GR-710-2	GR-609-3	GR-609-5	GR-549-12	GR-549-28	GR-549-4	GR-558-6
SiO_2	52.970	53.610	53.140	50.890	58.580	55.870	63.610	61.490	55.080	59.010	55.110	66.330
TiO_2	0.000	0.002	0.000	0.008	0.000	0.013	0.000	0.005	0.011	0.000	0.018	0.020
Al_2O_3	30.560	30.540	30.330	31.470	28.180	28.670	25.460	26.360	29.230	27.000	30.320	23.650
$FeO_{(tot)}$ [a]	0.085	0.011	0.003	0.121	0.112	0.601	0.163	0.052	0.004	0.042	0.071	0.245
MnO	0.000	0.000	0.003	0.000	0.013	0.002	0.001	0.000	0.000	0.001	0.011	0.000
MgO	0.000	0.003	0.000	0.000	0.007	0.373	0.000	0.000	0.000	0.000	0.021	0.014
CaO	13.150	12.930	12.710	14.160	10.040	11.050	6.460	7.710	11.370	8.430	11.230	4.600
Na_2O	4.430	4.020	4.400	3.690	5.030	4.680	5.860	6.020	5.210	6.570	4.170	6.170
K_2O	0.062	0.056	0.057	0.001	0.041	0.022	0.003	0.012	0.036	0.001	0.457	0.129
Total	101.26	101.17	100.64	100.36	102.03	101.28	101.55	102.63	100.96	101.06	101.43	101.15
Si	9.497	9.583	9.562	9.238	10.257	9.938	11.004	10.709	9.840	10.421	9.780	11.428
Al	6.453	6.429	6.427	6.727	5.811	6.006	5.187	5.406	6.150	5.615	6.336	4.799
Fe^{2+}	0.013	0.002	0.000	0.018	0.016	0.089	0.024	0.008	0.001	0.006	0.011	0.035
Ca	2.526	2.476	2.450	2.754	1.883	2.106	1.197	1.439	2.176	1.595	2.135	0.849
Na	1.540	1.393	1.535	1.299	1.708	1.614	1.966	2.033	1.805	2.250	1.435	2.061
K	0.014	0.013	0.013	0.000	0.009	0.005	0.001	0.003	0.008	0.000	0.103	0.028
An%	63.317	64.148	62.839	69.301	52.810	57.821	39.049	49.810	51.054	41.823	55.714	52.209
Ab%	35.586	34.016	37.232	29.452	45.562	41.601	53.586	42.562	48.070	55.594	35.285	43.821
Or%	0.366	0.331	0.337	0.007	0.242	0.130	0.018	0.242	0.135	0.006	2.701	0.762

[a] $FeO_{(tot)=}$ total iron on FeO
[b] Mg#=Mg/(Mg+Fe^{2+})
n.d.; no determined

Table 2- Major (wt%) and trace element (ppm) concentrations and significant element ratios for mafic-ultramafic rocks. Major elements oxides in wt.%. FeO_t is total Fe expressed as Fe^{2+}. Mg#=100 $Mg/(Mg+Fe^{2+})$ assuming $Fe_2O_3/FeO=0.15$. LDL= lower than detection limit

	Fine-grained amphibolites				Amphibole-rich amphibolites								
	GR 504	GR 610	GR 669	GR 737	GR 73	GR 151	GR 537	GR 542	GR 572	GR 609	GR 673	GR 770	GR 786
$SiO_{2\ (wt\ \%)}$	53.51	42.48	48.94	49.54	41.54	50.91	45.61	48.32	49.83	48.43	47.10	54.15	53.49
TiO_2	1.32	1.38	0.98	1.45	0.75	1.07	1.62	1.40	0.34	2.32	1.20	0.64	0.80
Al_2O_3	12.58	12.64	15.17	14.66	13.78	13.59	15.57	13.6	15.09	12.80	14.03	15.53	15.08
Fe_2O_3	16.25	17.99	15.45	12.80	10.85	13.19	14.67	12.7	10.82	15.75	16.36	11.64	12.58
MnO	0.24	0.42	0.26	0.24	0.18	0.17	0.20	0.21	0.18	0.24	0.28	0.27	0.21
MgO	4.28	7.93	4.93	6.73	8.69	6.75	6.22	7.65	8.25	5.86	6.95	4.36	5.02
CaO	6.97	10.78	9.57	10.44	10.65	11.78	11.93	12.49	12.02	9.89	10.53	7.73	7.49
Na_2O	2.68	1.93	2.78	3.03	1.70	1.05	1.72	1.82	1.73	2.44	1.46	3.21	3.83
K_2O	0.48	0.19	0.33	0.22	1.20	0.42	0.14	0.20	0.37	0.37	0.41	0.94	0.38
P_2O_5	0.21	0.27	0.80	0.12	0.15	0.12	0.103	0.14	0.041	0.371	0.233	0.21	0.10
LOI	1.30	3.30	0.80	0.50	10.40	0.70	2.00	1.10	1.10	1.20	1.10	1.10	0.80
Total	99.89	99.66	99.79	99.79	99.97	99.75	99.81	99.72	99.8	99.72	99.72	99.81	99.8
Mg #	34	47	39	51	61	50	46	54	60	42	46	43	44
Sc (ppm)	42	43	51	50	35	47	52	53	47	51	55	33	41
V	374	608	295	341	225	428	368	318	229	434	408	274	295
Cr	48	96	34	233	376	253	205	356	260	109	82	48	48
Co	40	50	38	44	47	46	50	50.4	43.8	47	54.6	27.9	35.9
Ni	18	80	12	56	77	53	73	80	70	54	86	12	19
Ga	18	19	17	15	15	16	19	15.8	11.8	19.6	17.2	16.7	16.4
Rb	9	1	1	6	32	8	4	3.5	4.6	8.1	7.5	21.4	6.6
Sr	73	146	183	90	234	172	168	113	118	165.6	199.6	291	214.5
Y	33.4	26.5	20.7	29.9	19	15.5	42.5	32.3	26.7	56.5	30	12.7	19.6
Zr	89.9	72.6	71.6	81.1	52.9	39.5	73	67.2	48.3	165.5	61.8	53.8	38.3
Nb	2.3	2.1	2	3.8	2.3	2.6	2.6	2.9	1.2	4.1	1.6	2.8	1.4
Ba	133	248	44	81	259	60	56	64	49	191	110	127	69
Ta	0.2	0.1	LDL	0.1	0.4	0.2	0.2	0.2	LDL	0.3	0.1	0.1	0.08
Th	1.1	0.3	0.4	0.7	0.6	0.5	0.4	0.3	0.18	0.6	0.3	0.8	0.2
Hf	2.8	2.2	1	2.3	1.4	1.4	2.7	1.8	0.9	5.1	2.1	1.9	0.8
U	0.6	0.2	0.2	0.3	0.2	0.3	0.2	LDL	0.2	0.3	0.2	0.3	0.1
La	7.3	4.2	3.5	4.2	5.3	4.6	7	5.3	5.1	8.8	3.8	8.4	3.8
Ce	17.1	10.2	10.4	11.6	13.7	11.9	10.9	10.5	10.6	26.3	9.6	18.4	9.3
Pr	2.79	1.71	1.71	2.03	1.99	1.75	2.21	1.75	1.65	4.45	1.62	2.56	1.46
Nd	14.5	8.6	9.6	11.4	10.3	9.0	11.7	9.8	7.0	22.5	9.1	11.9	7.2
Sm	4.1	2.81	2.78	3.4	2.7	2.33	3.8	3.08	2.4	6.99	2.87	2.66	2.05
Eu	1.53	1.06	1.08	1.2	0.91	0.90	1.57	1.27	0.52	2.33	1.13	0.88	0.78
Gd	5.39	3.7	3.38	4.53	3.04	2.80	5.99	4.31	3.01	8.67	3.91	2.57	2.83
Tb	0.97	0.70	0.59	0.84	0.55	0.47	1.12	0.88	0.6	1.63	0.8	0.39	0.51
Dy	6.2	4.15	3.44	5.39	3.18	2.40	7.13	5.21	4.11	9.47	4.81	2.28	3.35
Ho	1.27	0.94	0.76	1.15	0.69	0.56	1.48	1.2	0.87	2.01	1.08	0.44	0.68
Er	3.85	2.9	2.12	3.14	2.07	1.69	4.2	3.46	2.88	5.77	3.29	1.32	2.19
Tm	0.61	0.45	0.33	0.48	0.28	0.24	0.76	0.58	0.49	0.86	0.52	0.2	0.35
Yb	3.74	2.79	1.98	2.97	1.82	1.52	3.91	3.12	2.88	5.45	3.17	1.36	2
Lu	0.59	0.43	0.32	0.45	0.28	0.24	0.62	0.52	0.44	0.8	0.48	0.21	0.33
La/Yb_{cn}	1.4	1.08	1.27	1.01	2.09	2.17	1.28	1.22	1.27	1.16	0.86	2.43	1.36
La/Sm_{cn}	1.15	0.96	0.81	0.8	0.85	1.27	1.19	1.11	1.37	1.2	1.2	2.04	1.23
Gd/Yb_{cn}	1.19	1.1	1.41	1.26	1.23	1.38	1.27	1.14	0.86	1.32	1.02	1.56	1.17
$(Eu/Eu^*)_{cn}$	1.0	1.01	1.08	0.93	0.98	0.97	1.01	1.07	0.59	0.99	0.94	1.03	0.96
Al_2O_3/TiO_2	9.53	9.16	15.48	10.11	18.37	12.70	9.61	9.71	44.38	5.52	11.69	24.27	18.85
Zr/Y	2.69	2.74	3.46	2.71	2.78	2.55	1.72	2.08	1.81	2.93	2.06	4.24	1.95
Ti/Zr	88	114	82	107	85	162	133	125	42	84	116	71	125
$(Nb/Nb^*)_{pm}$	0.02	0.13	0.12	0.10	0.06	0.09	0.08	0.15	0.11	0.06	0.11	0.03	0.15
$(Zr/Zr^*)_{pm}$	0.07	0.14	0.13	0.10	0.09	0.09	0.08	0.11	0.14	0.05	0.11	0.08	0.12
$(Ti/Ti^*)_{pm}$	0.07	0.16	0.16	0.11	0.14	0.31	0.07	0.10	0.05	0.05	0.10	0.24	0.16

	Amphibole-rich amphibolites					Porphyroblastic amphibolites							
	GR 793	NM 67A	NM 114	NM 144	NM 166	GR 10	GR 695	GR 723	GR 724	SJ 2559	SJ 2560	SJ 2572	SJ 2585
SiO_2	50.00	48.30	47.21	49.97	43.10	46.27	47.13	47.55	46.73	48.32	46.51	47.87	47.75
TiO_2	1.75	1.09	1.87	1.46	1.41	0.58	0.89	0.95	0.80	1.29	0.90	0.90	1.23
Al_2O_3	13.80	14.68	13.66	14.77	14.95	18.14	15.89	15.41	16.22	16.46	17.02	16.12	15.09
Fe_2O_3	16.21	11.31	15.14	12.63	15.87	9.50	13.01	13.33	12.12	12.07	11.10	12.65	13.11
MnO	0.24	0.17	0.22	0.19	0.19	0.16	0.21	0.21	0.19	0.18	0.16	0.19	0.20
MgO	4.85	8.66	6.57	6.36	10.63	10.30	8.09	8.13	9.12	6.76	9.37	7.55	7.92
CaO	8.65	11.32	10.87	10.94	9.35	11.47	11.63	11.07	11.03	11.48	10.96	11.73	11.86
Na_2O	2.79	2.54	2.54	2.68	1.98	1.96	1.93	1.86	1.63	2.17	2.13	1.75	1.36
K_2O	0.36	0.27	0.32	0.36	0.31	0.21	0.17	0.15	0.29	0.25	0.13	0.23	0.35
P_2O_5	0.41	0.19	0.23	0.28	0.19	0.06	0.115	0.08	0.05	0.11	0.08	0.07	0.09
LOI	0.70	1.40	1.30	0.30	1.90	1.30	0.70	1.00	1.50	0.60	1.30	0.70	0.80
Total	99.76	99.99	99.97	99.97	99.94	100	99.8	99.76	99.76	99.75	99.74	99.75	99.75
Mg-#	37	60	46	50	57	68	55	55	60	53	63	54	54
Sc	42	38	49	44	23	26	41	45	39	41	33	44	46
V	426	236	372	290	251	188	277	286	244	281	214	280	315
Cr	41	315	151	96	123	205	144	260	144	226	157	144	151
Co	43.5	49.6	52.2	37.4	71.5	55.9	53.4	54.7	57.5	49.8	59.6	53.1	55.9
Ni	32	131	75	40	260	234	115	100	129	73	176	93	80
Ga	19.6	15.7	19.8	17.9	19.6	15	16	17	15.6	18.1	16.1	16.0	18.5
Rb	4.8	8.7	5.3	4.3	7.6	9.3	4.4	3	7.8	3.7	1.3	5.7	4.4
Sr	291.8	228	160.2	227.7	250.7	208.9	187.2	194.2	134.6	207.6	172.1	188.7	70.7
Y	33.3	27.7	46.4	35.1	23	16.3	21.5	23.1	19.2	24.4	16.5	21.7	24.4
Zr	76.7	66.9	109.7	85.9	82.1	31.5	44.5	44.9	36.7	68.3	43.1	44.2	64.4
Nb	3.8	1.5	3.6	3.1	4.2	1.7	1.2	1.4	1.1	1.5	1.0	1.2	2.4
Ba	48	106.2	70.7	105.2	261.1	75	49	30	69	38	20	51	29
Ta	0.2	0.1	0.4	0.3	0.4	0.4	0.05	0.1	0.06	0.1	0.1	0.1	0.1
Th	0.6	0.7	0.5	0.9	0.3	0.3	0.3	0.3	0.12	0.19	0.16	0.2	0.4
Hf	2.2	1.9	3.3	2.4	2.6	0.8	1.4	1.5	1.2	2.1	1.4	1.6	1.9
U	0.3	0.1	0.2	0.4	0.2	0.1	LDL	LDL	LDL	0.1	LDL	0.1	0.1
La	8.1	4.5	6.3	5.9	6.4	2.4	2.6	2.3	1.8	3.0	1.9	2.1	3.4
Ce	19.3	11.5	19.1	17.4	16.9	6	6.7	6.1	5.3	9.7	6.2	6.1	10.0
Pr	3.07	1.94	3.08	2.66	2.71	0.92	1.19	1.05	0.9	1.61	1.04	1.00	1.61
Nd	16.7	10.7	15	13.7	12.9	5	6.7	5.5	4.6	9.1	6.4	5.8	9.4
Sm	4.35	3.4	5.1	4	3.6	1.5	2.1	2.16	1.73	2.90	1.81	1.95	2.71
Eu	1.51	1.21	1.81	1.53	1.44	0.66	0.8	0.79	0.71	1.11	0.80	0.79	0.99
Gd	5.6	4.22	6.72	4.91	4.25	2.25	2.77	2.82	2.36	4.02	2.62	2.88	3.68
Tb	1.03	0.77	1.25	0.85	0.65	0.45	0.57	0.59	0.5	0.71	0.47	0.56	0.68
Dy	6.26	5	7.67	5.34	4.06	2.81	3.49	3.8	3.08	4.05	2.76	3.52	3.96
Ho	1.25	1.08	1.76	1.21	0.8	0.57	0.82	0.85	0.7	0.89	0.59	0.78	0.84
Er	3.63	3.06	5.1	3.65	2.28	1.92	2.39	2.5	2.16	2.58	1.73	2.30	2.41
Tm	0.56	0.48	0.73	0.61	0.4	0.26	0.38	0.36	0.32	0.39	0.25	0.36	0.37
Yb	3.5	2.83	4.6	3.36	2.1	1.58	2.34	2.41	2.1	2.32	1.62	2.30	2.34
Lu	0.53	0.44	0.75	0.49	0.3	0.25	0.36	0.37	0.32	0.37	0.25	0.35	0.35
La/Yb_{cn}	1.66	1.14	0.98	1.26	2.19	1.09	0.8	0.68	0.61	0.93	0.84	0.65	1.04
La/Sm_{cn}	0.8	0.85	0.95	0.81	1.27	1.03	0.8	0.69	0.67	0.67	0.68	0.7	0.81
Gd/Yb_{cn}	1.32	1.23	1.21	1.21	1.67	1.18	0.98	0.97	0.93	1.43	1.34	1.04	1.30
$(Eu/Eu^*)_{cn}$	0.95	1.06	1.13	1.08	1.03	1.1	1.01	0.98	1.07	0.99	1.12	1.02	0.96
Al_2O_3/TiO_2	7.89	13.47	7.30	10.12	10.60	21	18	16	20	13	19	18	12
Zr/Y	2.30	2.42	2.36	2.45	3.57	1.9	2.1	1.9	1.9	2.8	2.6	2.0	2.6
Ti/Zr	137	98	102	102	103	110	120	127	131	113	125	122	115
$(Nb/Nb^*)_{pm}$	0.06	0.04	0.09	0.05	0.18	0.19	0.12	0.16	0.41	0.21	0.27	0.23	0.14
$(Zr/Zr^*)_{pm}$	0.05	0.09	0.07	0.07	0.08	0.20	0.15	0.18	0.22	0.12	0.18	0.18	0.12
$(Ti/Ti^*)_{pm}$	0.09	0.09	0.06	0.11	0.18	0.15	0.15	0.14	0.17	0.15	0.23	0.15	0.15

	Mafic granulites			Ultramafic cumulus	Mafic cumulus (metagabbros)				
	GR 556	GR 719	SJ 2586	NM-241	GR-773	GR-774	GR-775	GR-776	NM-01
SiO_2	46.48	47.58	48.11	50.41	44.35	44.62	48.42	47.49	47.04
TiO_2	1.20	1.06	1.40	0.40	0.52	0.38	0.31	0.19	0.24
Al_2O_3	16.96	16.33	14.63	5.94	16.66	19.42	15.88	21.74	17.45
Fe_2O_3	12.91	11.03	13.01	7.93	10.03	7.75	5.56	4.29	6.32
MnO	0.22	0.18	0.20	0.15	0.17	0.12	0.11	0.08	0.14
MgO	6.94	8.33	6.75	16.26	12.07	11.11	10.98	7.54	11.63
CaO	9.89	10.68	11.03	15.32	11.87	11.22	16.01	15.36	13.03
Na_2O	2.27	2.66	2.73	0.83	1.26	1.81	1.24	1.61	1.44
K_2O	0.15	0.21	0.57	0.73	0.18	0.33	0.08	0.10	0.10
P_2O_5	0.218	0.09	0.11	0.10	0.03	0.02	0.008	LDL	0.02
LOI	2.60	1.50	1.20	1.30	2.50	2.90	0.90	1.30	2.40
Total	99.92	99.77	99.75	99.98	99.73	99.76	99.77	99.83	100
Mg-#	52	60	51	80	70	74	80	78	78
Sc	52	39	47	52	31	21	44	26	26
V	325	246	329	185	157	112	158	93	101
Cr	198	356	151	3770	246	164	1608	787	1020
Co	48.2	51.1	53.2	44.7	64.7	50.9	33.9	25.6	46.6
Ni	101	110	49	423	306	270	213	135	344
Ga	16	17	17.7	7.4	13.6	12.2	10.2	12	10.2
Rb	1.5	2.7	18.2	26.1	4.9	11.3	3.5	2.7	3.8
Sr	288	197.1	130.7	51.7	153.7	205.4	161.3	235.6	176
Y	21.9	23	26.5	19	11.7	8.6	8.9	5.4	7.6
Zr	63.2	61.5	78.2	29.3	24.3	17.4	13.7	9.1	10.8
Nb	1.2	1.0	3.5	1.8	0.5	0.6	0.4	0.4	0.6
Ba	94	42	99	106.2	25	69	26	36	79.5
Ta	LDL	0.1	0.16	0.1	0.1	LDL	0.1	LDL	0.1
Th	0.19	0.3	0.4	0.3	0.19	0.11	0.11	0.17	0.3
Hf	0.9	2	2.5	0.9	0.6	0.5	0.5	0.3	0.4
U	LDL	0.1	0.3	0.3	LDL	LDL	LDL	LDL	LDL
La	2.6	2.8	4.9	6.3	1.5	0.8	0.9	0.8	1.5
Ce	6.8	8	13.2	11	3.4	2	2.3	1.9	3.1
Pr	1.28	1.42	2.04	2.29	0.54	0.37	0.41	0.28	0.5
Nd	7.3	7.6	11.6	10.6	3.3	2	2.6	1.8	2.5
Sm	2.44	2.52	3.23	2.9	1.13	0.72	0.76	0.53	0.8
Eu	1.09	0.95	1.18	0.57	0.48	0.37	0.35	0.29	0.36
Gd	3.28	3.37	4.29	3.34	1.59	1.24	1.28	0.8	1.11
Tb	0.6	0.64	0.76	0.69	0.31	0.23	0.25	0.15	0.19
Dy	3.98	4.14	4.46	3.28	1.99	1.44	1.54	0.89	1.34
Ho	0.85	0.88	0.91	0.66	0.4	0.29	0.34	0.19	0.29
Er	2.57	2.4	2.70	1.82	1.31	0.92	0.96	0.55	0.84
Tm	0.39	0.38	0.41	0.3	0.2	0.15	0.15	0.09	0.14
Yb	2.4	2.24	2.52	1.59	1.21	0.83	0.9	0.5	0.77
Lu	0.36	0.37	0.39	0.23	0.19	0.14	0.14	0.09	0.1
La/Yb_{cn}	0.78	0.9	1.39	2.84	0.89	0.69	0.72	1.15	1.4
La/Sm_{cn}	0.69	0.72	0.98	1.4	0.86	0.72	0.76	0.97	1.21
Gd/Yb_{cn}	1.71	1.93	2.96	1.74	1.09	1.24	1.18	1.32	1.19
$(Eu/Eu^*)_{cn}$	1.18	1.0	0.97	0.56	1.09	1.2	1.08	1.36	1.17
Al_2O_3/TiO_2	14	15	10	87	32	51	51	114	73
Zr/Y	2.89	2.67	2.95	1.20	2.08	2.02	1.54	1.69	1.42
Ti/Zr	114	103	107	82	128	131	136	125	133
$(Nb/Nb^*)_{pm}$	0.20	0.10	0.14	0.08	0.14	0.55	0.33	0.24	0.11
$(Zr/Zr^*)_{pm}$	0.17	0.15	0.10	0.05	0.31	0.57	0.33	0.45	0.26
$(Ti/Ti^*)_{pm}$	0.17	0.13	0.14	0.06	0.28	0.38	0.27	0.47	0.31

Notes: $Eu/Eu^* = (Eu)_{cn}/[(Sm)_{cn} + (Gd)_{cn}]^{1/2}$; $Nb/Nb^* = Nb_{pm}/(Th_{pm} \times La_{pm})$; $Ti/Ti^* = Ti_{pm}/(Tb_{pm} \times Dy_{pm})$; $Zr/Zr^* = Zr_{pm}/(Nd_{pm} \times Sm_{pm})$.

Appendix A. Eletronic Supplementary Data. Accuracy and precision of the geochemical data

Method	Analyte	Unit	MDL	Rock Pulp (NM54)	REP. NM54	STD SO-18	STD SO-18	BLK	Blank_QZ	Blank_QZ
4A-4B	SiO2	%	0.01	46.1	46.45	58.2	58.19	<0.01	99.11	98.79
4A-4B	Al2O3	%	0.01	15.09	15.06	14.14	14.14	<0.01	0.03	0.02
4A-4B	Fe2O3	%	0.04	11.33	11.34	7.62	7.63	<0.04	0.59	0.74
4A-4B	MgO	%	0.01	9.34	9.3	3.32	3.33	<0.01	<0.01	<0.01
4A-4B	CaO	%	0.01	12.5	12.28	6.38	6.38	<0.01	<0.01	<0.01
4A-4B	Na2O	%	0.01	2.36	2.42	3.69	3.69	<0.01	0.04	0.04
4A-4B	K2O	%	0.01	0.27	0.26	2.16	2.16	<0.01	<0.01	<0.01
4A-4B	TiO2	%	0.01	1.44	1.41	0.69	0.69	<0.01	<0.01	<0.01
4A-4B	P2O5	%	0.01	0.12	0.12	0.83	0.83	<0.01	<0.01	<0.01
4A-4B	MnO	%	0.01	0.15	0.15	0.39	0.39	<0.01	<0.01	0.01
4A-4B	Cr2O3	%	0.002	0.048	0.048	0.549	0.55	<0.002	<0.002	<0.002
4A-4B	Ni	PPM	20	171	168	48	50	<20	<20	<20
4A-4B	Sc	PPM	1	37	37	23	25	<1	<1	<1
4A-4B	LOI	%	-5.1	1.2	1.1	1.9	1.9	0.0	0.2	0.4
4A-4B	Sum	%	0.01	99.97	99.97	99.87	99.88	<0.01	100.00	100.00
4A-4B	Ba	PPM	1	112.6	108.4	518.5	520.9	<1	1	2
4A-4B	Be	PPM	1	<1	<1	1	1	<1	<1	<1
4A-4B	Co	PPM	0.2	53.1	53.2	27	27	<0.2	0.5	0.7
4A-4B	Cs	PPM	0.1	0.6	0.6	7.5	7.4	<0.1	<0.1	<0.1
4A-4B	Ga	PPM	0.5	15.4	16.2	18.8	18	<0.5	<0.5	0.7
4A-4B	Hf	PPM	0.1	2.7	2.3	10.1	9.8	<0.1	<0.1	<0.1
4A-4B	Nb	PPM	0.1	0.9	1	19.7	19.7	<0.1	0.1	0.3
4A-4B	Rb	PPM	0.1	14.4	14.3	29.3	28.3	<0.1	0.4	0.4
4A-4B	Sn	PPM	1	17	25	14	12	<1	1	1
4A-4B	Sr	PPM	0.5	250.6	248.5	409.1	406.6	<0.5	1.9	2.2
4A-4B	Ta	PPM	0.1	0.2	0.2	7.7	7.7	<0.1	<0.1	<0.1
4A-4B	Th	PPM	0.2	0.5	0.4	10.4	10.8	<0.2	<0.2	<0.2
4A-4B	U	PPM	0.1	<.1	<.1	16.5	16.2	<0.1	0.3	0.1
4A-4B	V	PPM	8	229	219	194	199	<8	<8	<8
4A-4B	W	PPM	0.5	2.3	2.1	15.9	16.1	<0.5	<0.5	<0.5
4A-4B	Zr	PPM	0.1	78.3	81.7	281	279.4	1.4	0.3	<0.1
4A-4B	Y	PPM	0.1	33.4	33.7	33.7	33.7	<0.1	<0.1	<0.1
4A-4B	La	PPM	0.1	2.6	3.1	12.8	12.9	<0.1	0.1	<0.1
4A-4B	Ce	PPM	0.1	8.6	9.5	28	29.1	<0.1	0.2	0.1
4A-4B	Pr	PPM	0.02	1.65	1.71	3.53	3.48	<0.02	<0.02	<0.02
4A-4B	Nd	PPM	0.3	10.3	9.9	14.2	13.5	<0.3	<0.3	<0.3

Method	Analyte	Unit	MDL	Rock Pulp (NM54)	REP. NM54	STD SO-18	STD SO-18	BLK	Blank_QZ	Blank_QZ
4A-4B	Sm	PPM	0.05	3.8	3.9	3.1	2.9	<0.05	<0.05	<0.05
4A-4B	Eu	PPM	0.02	1.46	1.6	0.94	0.89	<0.02	<0.02	<0.02
4A-4B	Gd	PPM	0.05	4.95	4.96	2.98	2.97	<0.05	<0.05	<0.05
4A-4B	Tb	PPM	0.01	0.93	0.91	0.52	0.5	<0.01	<0.01	<0.01
4A-4B	Dy	PPM	0.05	6.31	5.67	3.13	3.03	<0.05	<0.05	<0.05
4A-4B	Ho	PPM	0.02	1.33	1.24	0.64	0.65	<0.02	<0.02	<0.02
4A-4B	Er	PPM	0.03	3.91	3.69	1.85	1.83	<0.03	<0.03	<0.03
4A-4B	Tm	PPM	0.01	0.57	0.51	0.28	0.3	<0.01	<0.01	<0.01
4A-4B	Yb	PPM	0.05	3.31	3.13	1.85	1.85	<0.05	<0.05	<0.05
4A-4B	Lu	PPM	0.01	0.49	0.47	0.29	0.29	<0.01	<0.01	<0.01
2A Leco	TOT/C	%	0.02	0.08	0.08	2.41	2.4	<0.02	<0.02	<0.02
2A Leco	TOT/S	%	0.02	0.08	0.08	5.31	5.28	<0.02	<0.02	<0.02
1DX	Mo	PPM	0.1	0.2	0.2	11.2	11.2	<0.1	0.7	0.9
1DX	Cu	PPM	0.1	79.9	76.9	118.8	125.2	<0.1	3.5	2.8
1DX	Pb	PPM	0.1	0.5	0.5	28.5	28.6	<0.1	0.3	0.3
1DX	Zn	PPM	1	19	18	138	146	<1	3	2
1DX	Ni	PPM	0.1	49.3	48.1	23	24.1	<0.1	1.5	0.9
1DX	As	PPM	0.5	<.5	<.5	21.1	21.1	<0.5	<0.5	0.7
1DX	Cd	PPM	0.1	<.1	<.1	5.8	5.9	<0.1	<0.1	<0.1
1DX	Sb	PPM	0.1	<.1	<.1	3.3	3	<0.1	<0.1	<0.1
1DX	Bi	PPM	0.1	<.1	<.1	4.8	4.8	<0.1	<0.1	<0.1
1DX	Ag	PPM	0.1	<.1	<.1	0.3	0.3	<0.1	<0.1	<0.1
1DX	Au	PPB	0.5	<.5	1.1	45.2	46.7	<0.5	0.9	<0.5
1DX	Hg	PPM	0.01	0.01	<.01	0.22	0.22	<0.01	<0.01	<0.01
1DX	Tl	PPM	0.1	<.1	<.1	1.6	1.6	<0.1	<0.1	<0.1
1DX	Se	PPM	0.5	<.5	<.5	4.3	4.2	<0.5	<0.5	<0.5

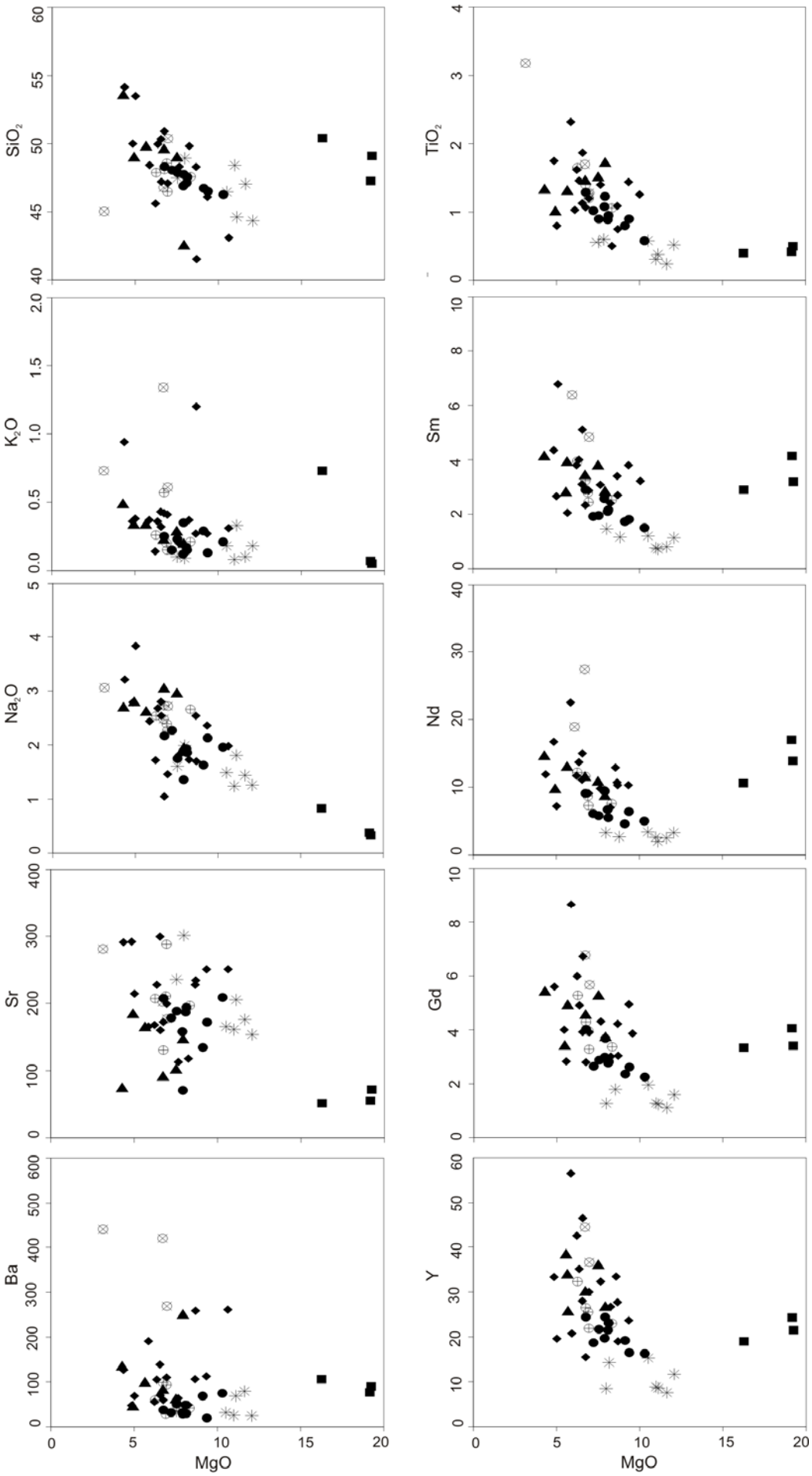

Fig. 1. Variations diagrams of MgO versus selected elements.

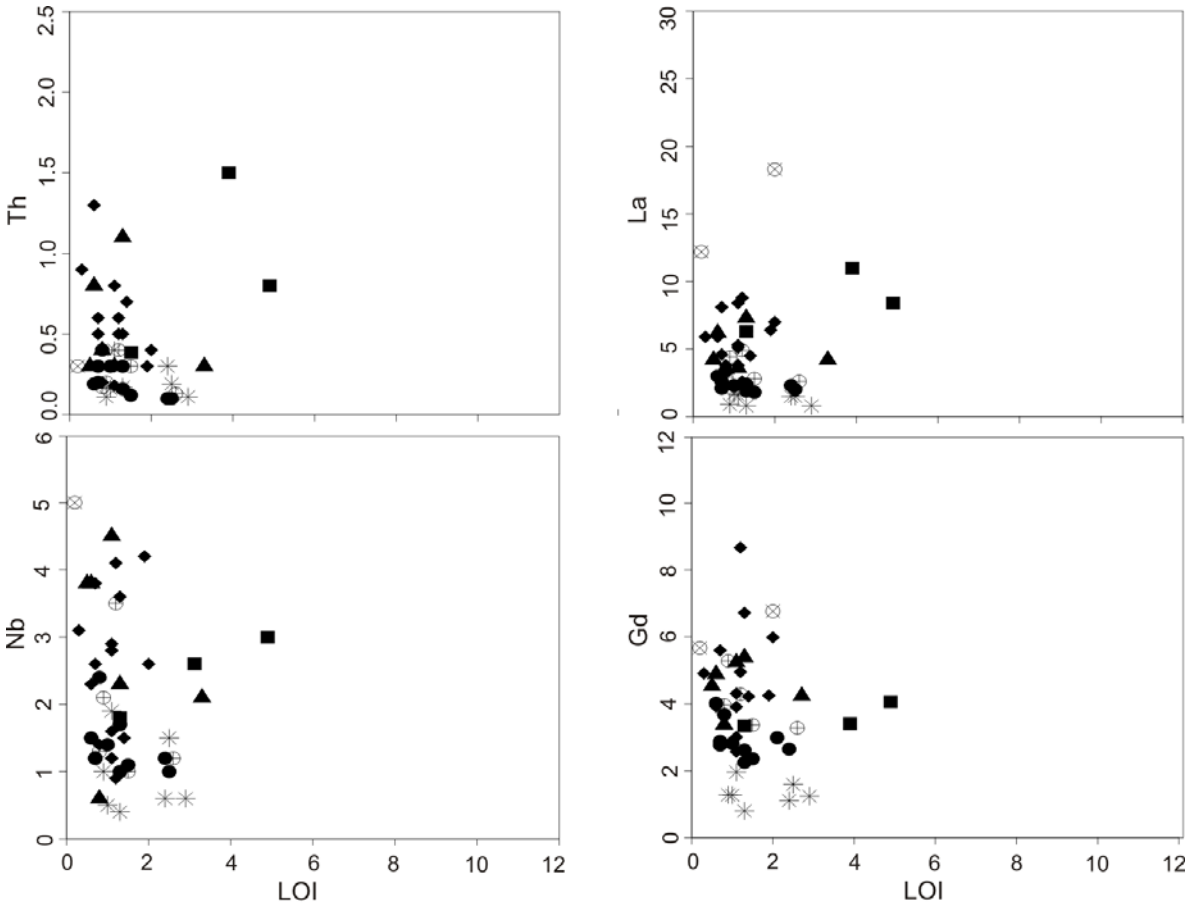

Fig. 2. Loss on ignition (LOI) versus trace elements and REE.

CIP - Catalogação na Publicação

Rizzotto, Gilmar José
PETROLOGIA E GEOCRONOLOGIA DO COMPLEXO MÁFICO-ULTRAMÁFICO TRINCHEIRA, SUDOESTE DO CRÁTON AMAZÔNICO: IMPLICAÇÕES TECTÔNICAS DO MESOPROTEROZÓICO / Gilmar José Rizzotto. -- 2012.
203 f.

Orientador: Léo Afraneo Hartmann.

Tese (Doutorado) -- Universidade Federal do Rio Grande do Sul, Instituto de Geociências, Programa de Pós-Graduação em Geociências, Porto Alegre, BR-RS, 2012.

1. Cráton Amazônico. 2. Geocronologia. 3. Ofiolito. 4. Mesoproterozóico. 5. Complexo máfico- ultramáfico. I. Hartmann, Léo Afraneo , orient. II. Título.

Elaborada pelo Sistema de Geração Automática de Ficha Catalográfica da UFRGS com os dados fornecidos pelo(a) autor(a).